University of Cambridge
Department of Engineering

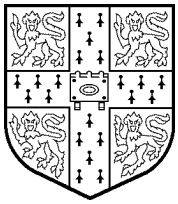

Shape Memory Alloys and their Application to Actuators for Deployable Structures

Dissertation submitted to the University of Cambridge
for the degree of Doctor of Philosophy

by

Weimin Huang

Peterhouse

March, 1998

Declaration

The author wishes to declare that, except for commonly understood ideas and concepts, or where specific reference is made to the work of other authors, the contents of this dissertation are original and include nothing that is the outcome of work done in collaboration. This dissertation has not been previously submitted, in part or whole, to any other University or institution for any degree, diploma or other qualification.

This dissertation is 175 pages long and contains approximately 38,600 words including appendices and bibliography.

Weimin Huang

To my parents

Acknowledgements

The work reported in this dissertation was carried out in the Department of Engineering of the University of Cambridge between October 1994 and March 1998.

First, and foremost, I extend the warmest and heartfelt thanks to my supervisor, Dr Sergio Pellegrino, for his inspiration, keen insight, unwaning enthusiasm and friendship.

Special gratitude must go to Professor C. R. Calladine, *FRS*, for his kindness and much help.

I am also grateful to Mr Roger Denston for his assistance with the experimental work, and to Dr Peter Long and Mr Roger Hume of the Design Office for lots of helpful advice on actuator design. Thanks are also due to the technicians of the Workshops of the Engineering Department for their assistance with various aspects of the construction of the test rigs, instrumentation and actuators. I am grateful to Matthew Jackson, who built the torsion testing machine during the course of his M.Eng. project, and to Mr David Bashford (ERA Technology) and Mr David Eaton (ESA-Estec) for their involvement during the early stages of my project. Their insistence on the importance of linking theory and practice in the field of shape memory alloys has left a clear and lasting mark on my research.

I would also like to thank all members of the Structures Group, and in particular Zhong You, Simon King, Riki Kangwai, David Miles, Thorsten Hack, Cheuk-Yan Lai, Khuram Iqbal, and Gopal Srinavasan, for their many constructive suggestions and friendships.

Finally, my most sincere thanks go to my parents and my wife, Xiaoqing, for their consistent love, support and encouragement. Without them, this dissertation would have been only a dream.

Financial support from the following sources is thankfully acknowledged: an ORS award from the Committee of Vice-Chancellors and Principals, a studentship from the Cambridge Overseas Trust, a Lundgren Research Award from the Board of Graduate Study, and a William George Collins Endowment Fund Grant from the Engineering Department. Travel grants were received from the Engineering Department and Peterhouse.

Abstract

Although it has been recognised that SMA materials have a significant potential for deployment actuators, the number of applications of SMA-based actuators to the present day is still quite small, since a deeper understanding of the thermomechanical behaviour of SMA and how it might be exploited in the design of working actuators is necessary.

In order to get a complete picture of the thermomechanical behaviour of Nitinol, one type of SMA, two kinds of experiment, purely thermal tests and thermomechanical tests, were carried out on Nitinol wire and bar.

In the purely thermal tests, a Differential Scanning Calorimeter was used to determine the phase transformation/temperature relation of Nitinol wire with diameter of 1 mm and Nitinol bar. The thermomechanical tests, including tension tests at different temperatures, tension tests under different strain rates, response to suddenly applied loads, thermal cycling under different loads and thermal cycling with fixed length were carried out on Nitinol wire. Torsional tests, thermal cycling under different torques, and normal tension and thermal cycling tests were carried out on Nitinol bar with diameter of 6.5 mm.

We have developed a thermo-micromechanical model based on complementary free energy and micromechanical transformation system to investigate the behaviour of shape memory under uniaxial load cycling and thermal cycling. Experimentally observed phenomena, such as V-shape of critical stress, non-symmetrical behaviour in tension and compression, transformation front behaviour, and multiphase transformation, were explained by this model.

We present a phenomenological model which is based on tension test, carried out at different constant temperatures, and thermal cycling test under different constant loads. We have shown that our model can reproduce accurately the stress-strain-temperature relationship for all the quasi-static tests we have carried out on Nitinol wires. This model has no difficulty in dealing with incomplete loading or thermal cycling. This model has been used to simulate thermal cycling behaviour with fixed length, strain rate effects, and phase transformation front behaviour.

Three Nitinol wire-based rotatory actuators, a one-way actuator, a biased actuator, and a two-way actuator, have been designed and tested. The behaviour of these actuators has been simulated by using the phenomenological model that we have developed. The power consumption to operate all actuators was measured. Two simple approaches were proposed to estimate the average power requirements. A preliminary study of a torsional actuator has been made. The general design procedure for Nitinol-based actuators is summarised.

The broad aim of this dissertation is also to provide a user's guide to the design of SMA-based actuators.

Keywords: shape memory alloy, Nitinol, phase transformation, martensite re-orientation, superelasticity, shape memory effect, deployable structures, actuator, thermomechanical model, thermo-micromechanical model, simulation, power requirement, phase transformation front, strain rate

Contents

List of Figures

List of Tables

Principal Nomenclature

A	Austenite/Area
A_f	Austenite finish temperature
A_s	Austenite start temperature
c	Specific heat
C_{ijkl}	Elastic Moduli
d	Diameter
D	Young's Modulus/Diameter
E	Energy
E_{fric}	Energy dissipation
E_{fric}^{total}	Total energy dissipation in a full transformation cycle
E_{ij}	Macroscopic strain tensor
F	Force
G_{ch}	Gibbs free energy/chemical free energy
h	Convection heat-transfer coefficient
I	Electrical current
k	Thermal conductivity of the material
l	Perimeter of the section of the wire
L	Length
M	Martensite/Torque
$M^m, (m = 1, 2, 3, ...)$	Martensite variant groups $1, 2, 3, ...$
$M^n, (n = i, j, k, ...)$	Martensite variant $i, j, k, ...$
M^{tim}	Thermal induced twinned martensite
M_d	The highest temperature where stress induced martensite can occur
M_f	Martensite finish temperature
M_s	Martensite start temperature
P	Power
q, Q	Heat source
r	Radius
R	Electrical resistance/Radius/R-phase
t	Time
T	Temperature of material
T_o	Ambient temperature
T_{equ}	Equilibrium temperature
U	Voltage
V	Volume
W_{int}	Internal energy
W_{mech}	Mechanical energy
W_{surf}	Surface energy on the interface

α	Angle
γ	Shear strain
ϵ	Axial strain along tensile direction
$\dot{\epsilon}$	Strain rate
ϵ_{ij}	Microscopic strain tensor
θ, ϕ, and ψ	Eulerian angles/Rotation angles
λ	Angle between the tensile axis and the $\boldsymbol{d}_i^p$ direction
μ	Static friction coefficient
ξ	Volume fraction
ρ	Density
σ	Tensile stress
$\bar{\sigma}$	Equivalent stress
σ_{ij}	Microscopic stress tensor
σ^{A-M}, σ^{M-X}	Maxwell stress
χ	Angle between the tensile axis and habit plane
Θ	Thermoelastic tensor
Σ_{ij}	Macroscopic stress tensor
Φ	Helmoltz's free energy
Ψ	Complementary free energy
Ω	Schmid factor/Transformation tensor

Subscript $init$,o	Initial state
Superscript e	Elastic
Superscript t	Transformation

Chapter 1

Introduction and Literature Review

1.1 Shape Memory Alloys

A **Shape Memory Alloy (SMA)** is able to memorise and recover its original shape, after it has been deformed by heating over its transformation temperature. This unique effect of returning to an original geometry after a large inelastic deformation (near 10%) is known as the **Shape Memory Effect (SME)**.

The SME had been found as early as 1932 and until 1971 it was believed to be common to all alloys that undergo thermoelastic martensitic transformations (Dye 1990). Many alloys displaying the SME have been found (see Table 1.1), and considerable effort is still being made to discover new materials. Of these alloys, however, only two alloy systems[1], CuZnAl and NiTi, and their combinations with minute quantities of other elements are presently of commercial importance. Other alloys are ill-suited to industrial manufacturing either because the constituent elements are too expensive or because they cannot be used unless they are in the form of single crystals (Funakubo 1987).

The properties of NiTi and CuZnAl alloys are fairly different, as shown in Table 1.2, due to their different micro-structure. Because NiTi alloys have much higher strength, larger recoverable strain, better corrosion resistance and most importantly higher reliability than CuZnAl, they are the standard choice for use in space and several other applications. So, the particular SMA that is studied in details in this dissertation is **Nitinol**[2], although some of the modelling work that is presented is valid more generally. Therefore, any results presented in this dissertation should be taken to be specific to Nitinol unless otherwise stated.

[1] Fe based alloys are only used as fasteners and in some other, very simple applications, due to their low price.

[2] The word Nitinol was derived by the initial letters of Nickel and Titanium, by its discoverers (Dye 1990) at the Naval Ordnance Laboratory.

Alloy	Composition	Range of transformation temperatures (A_s) ^{o}C	Transformation hysteresis, ^{o}C
AgCd	44 ∼49 at %Cd	-190 ∼50	∼15
AuCd	46.5∼50 at %Cd	30∼100	∼15
CuAlNi	14∼14.5 wt %Al 3∼4.5 wt % Ni	-140∼100	∼35
CuSn	∼15 at % X	-120∼30	
CuZn	38.5∼41.5 wt % Zn	-180∼-10	∼10
CuZn X (X=Si,Sn,Al)	small wt % X	-180∼200	∼10
InTl	18∼23 at %Tl	60∼100	∼4
NiAl	36∼38 at % Al	-180∼100	∼10
TiNi	46.2∼51 at % Ti	-50∼110	∼30
TiNi X (X=Pd,Pt)	50 at % Ni+X 5∼ 50 at % X	-200∼700	∼100
TiNiCu	∼15 at % Cu	-150∼100	∼50
TiNiNb	∼15 at % Nb	-200∼50	∼125
TiNiAu	50 at % Ni+Au	20∼610	
TiPd X (X=Cr,Fe)	50 at % Pd+X ∼15 at% X	0∼600	∼50
MnCu	5∼35 at % Cu	-250∼180	∼25
FeMnSi	32 wt%Mn, 6wt%Si	-200∼150	∼100
FePt	∼25 at % Pt	∼-130	∼4
FePd	∼30 at % Pd	∼50	
FeNi X (X=C,Co,Cr)	small wt% X		

Table 1.1: Shape memory materials (from Liang 1990).

	NiTi	CuZnAl
Recovery strain	max 8%	max 4%
Recovery stress	max 400 MPa	max 200 MPa
Number of cycles	10^5 ($\epsilon = 0.02$)	10^2 ($\epsilon = 0.02$)
	10^7 ($\epsilon = 0.005$)	10^5 ($\epsilon = 0.005$)
Corrosion resistance	good	problematic, especially stress corrosion cracking
Workability	poor	fair
SM processing	comparatively easy	fairly difficult

Table 1.2: Comparison of NiTi/CuZnAl alloys (from Funakubo 1987).

1.2 Brief Review of Applications of SMAs

SMAs have been used in a wide variety of applications because of their unique thermomechanical characteristics. We briefly review some of the applications in this section.

Two quite successful applications are SMA-made eyeglass frame and the antenna of mobile phone. The advantage of using SMA is that after severe deformation, SMA can still fully return its original shape due to its excellent superelasticity (refer to Section 2.1 for this terminology).

SMA couplings have been sold as products for many years (Nagaya and Hirata 1992). More than one hundred thousand of these fittings as shown in Fig. 1.1 have been installed in advanced air-planes such as the F-14 and there have been no reported failures (Liang 1990). Similar devices include SMA rivets, SMA clamps and SMA seals, etc. (Liang 1990).

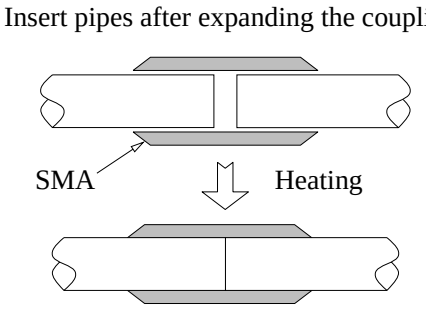

Figure 1.1: SMA coupling (from Funakubo 1987).

SMAs have been used in vibration dampers (Witting and Cozzarelli 1992) and isolators (Graesser and Cozzarelli 1992) due to SMAs' high internal friction. For example, Aiken *et al.* (1993) have suggested using SMA as passive energy dissipater to increase the hysteresis damping in structure under earthquake.

The more advanced applications are in passive/active control system (Baz *et al.* 1992, Kim 1995), smart/adaptive structures (Jia and Rogers 1990, Kakizawa and Ohno 1996), and composite structures (Sun and Sun 1993). Since it generally takes a comparatively long time to cool the SMA and hence for martensite transformation to occur, SMAs are not suitable for high-frequency control, but can be used for low-frequency and quasi-static response control. Maclean *et al.* (1990) have used SMA in feedback control of vibration and shape of large, adaptive space structures. Rogers (1992) has shown that the natural frequency of a cantilever beam with a SMA spring support at one end can be significently changed by significantly increasing the stiffness of SMA spring when SMA is heated. Hybrid composite embedded with SMA fibres can be used for vibration control and shape control by using the distributed force applied by SMA fibres.

Due to its excellent bio-compatibility, Nitinol has been used to make many medical instruments. For example, vascular stents (Whitcher 1997) made by fine Nitinol wires can be woven into cylindrical shapes to reinforce blood vessels.

The stent is crushed and inserted into the blood vessel through a cannula. As Nitinol is heated above its transformation temperature, the stent returns to its original cylindrical shape and provides reinforcement to the walls of the blood vessel. Other medical applications include vascular filters (Wang 1991), medical guide-wires and guide-pins for surgery, etc.

Readers may refer Venison (1986), Funakubo (1987), Duerig *et al.* (1990), Stoeckel (1991), Schetky (1991), Moorleghem (1993), Pelton *et al.* (1994, 1997), and Lipscomb and Nokes (1996) for more novel applications.

1.3 Applications to Deployable Structures

Future launchers will have larger envelope and mass capabilities, but large elements, such as solar arrays, antennas and large frames or masts etc., still cannot be taken into orbit in their operational configuration. The only solution is to make these structures foldable and to deploy them into their operational configuration in orbit. Furthermore, in the case of large structural elements the number of launches required to place them in orbit, and the number of in-orbit assembly operations, either by astronauts or by service vehicles, can be minimised if deployable structures are used (Unda *et al.* 1994).

Traditionally, there have been two methods to deploy a structure: **Controlled Deployment** and **Unconstrained Deployment** (or **Free Deployment**). The first method is to deploy the structure by means of actuators or cables which are linked to electrical motors. The second method uses the elastic strain energy stored in the folded structure to drive deployment. The most important difference between the two methods is that controlled deployment is often reversible while unconstrained deployment is usually irreversible, because it requires an external agent to initiate the folding procedure and to put strain energy back into the system.

Instead of traditional actuator, cable or folded structure, SMA can be used in these deployment schemes with very smooth motion due to its inherent damping properties. SMA based deployable structure can be folded easily by large deformation of SMA. During deployment, SMA is heated to above its transformation temperature to recover its original shape. This is exactly the idea of unconstrained deployable. Furthermore, reversible deployment can also be achieved by using two sets of SMA elements in the form of one against another, i.e. the structure is deployed by heating one set of SMA element and retracted by heating another set.

1.3.1 Basic Type of SMA-Based Actuators

Both one-way SMA and two-way SMA may be used for deployable structures. Although two-way SMA can perform in two directions due to its two-way shape memory mechanism, transformation strain associated with it is normally only half of that in one-way SMA. An alternative solution is to put two one-way SMA

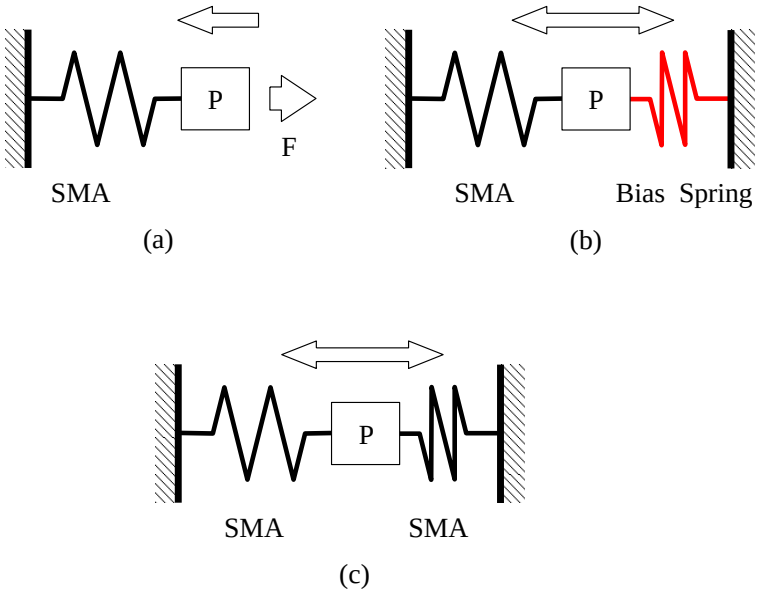

Figure 1.2: Basic types of SMA actuators using one-way SMAs. (a) One-way actuator; (b) biased actuator; (c) two-way actuator.

based actuators one against another to generate mechanical two-way performance, i.e. heating SMA in one actuator to get forward motion, and heating SMA in another actuator to reverse. The advantage of mechanical two-way actuator is higher motion and higher force than that in material two-way actuator, while the advantage of material two-way actuator is simpler, compacter and much less elements involved.

Figure 1.2 shows three basic types of SMA actuators using one-way SMAs.

- Figure 1.2(a) shows a **One-Way Actuator**. The SMA element is elongated initially, at low temperature, and is then heated to move element P in the direction of the arrow.
- Figure 1.2(b) shows a **Biased Actuator**, which is capable of moving the element P back and forth. The SMA element is deformed at low temperature, before being connected to the spring. When it is heated, the recovery force which is generated pulls the spring, thus storing energy in it. When the SMA element is cooled, the energy stored in the spring is released and the SMA element deforms back, thus completing the cycle.
- Figure 1.2(c) shows a **Two-Way Actuator** which includes two SMA elements. Two opposing SMA elements are used, instead of the SMA element and bias spring of the biased actuator. Any motion can be obtained by appropriately cooling or heating the two SMA elements.

Two-way SMA based actuator is similar to Fig. 1.2(a), one-way actuator, in shape, while its behaviour is more similar to Fig. 1.2(b), biased actuator.

The SMA elements have been made in the following shapes:

1. Straight wires in tension, for small linear motion/high force;
2. Helical elements, for large linear motion/small force, or large rotation/small torque;
3. Torsion bar/tube, for large rotation/small torque;
4. Cantilever strips, for large displacement/small force;
5. Belleville-type discs, for small linear motion/high force.

Generally speaking, only large deformations or large forces can be obtained from SMA, but not both.

1.3.2 Advantages of SMA-Deployed Structures

In recent years, the use of SMAs has been proposed as an alternative to electrical motors. The advantages of SMA-deployed structures over existing solutions are reported to be:

1. Mass and volume savings. Hirose *et al.* (1989) have compared the power/weight ratio vs. weight of a particular form of SMA actuator with many other conventional motors in Fig. 1.3. It suggests that SMA actuators have the potential capability to achieve an output/weight ratio which can not be realised by traditional actuators.
2. Avoidance of end-of-deployment shock loadings, which are always associated with spring-deployed structures. Therefore no more need for dampers, and hence overall system complexity can be reduced.
3. Retraction capability, usually available only in motor-deployed structures.
4. Noiseless operation, which removes the vibration disturbances to other payloads that are normally associated with motor-driven deployment.
5. Sensing capability. Both actuating and sensing functions can be combined by measuring changes in electrical resistance associated with the phase transformation.
6. Higher reliability. Deployment is triggered by a phase transformation and the speed of deployment is related to the temperature of the SMA element, which is itself determined by the thermal input and heat transfer. Therefore, it is possible to design systems with large torque margins without having to strike a balance between deployment torque and retarding, i.e. friction torque. The deployment torque of an SMA-deployed structure can be mobilised only in quasi-static conditions, and hence end-of-deployment shocks do not exist (see 2. above).

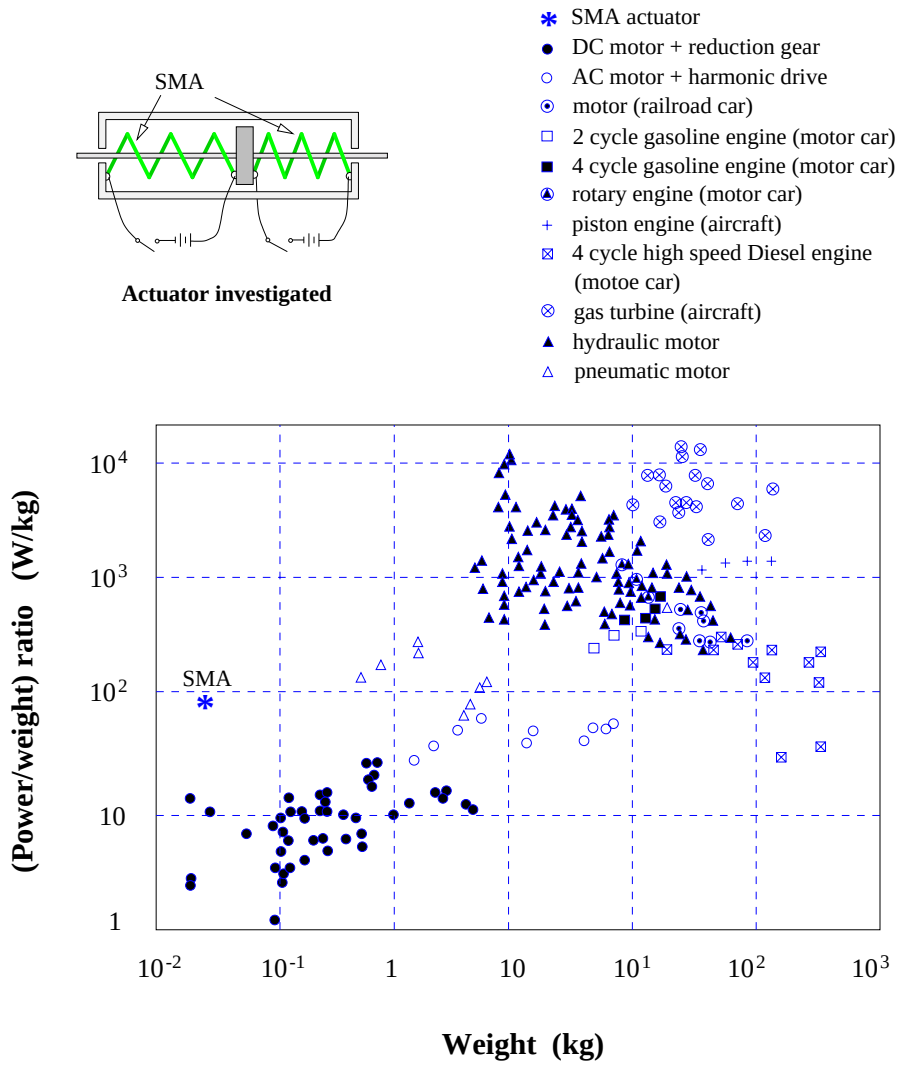

Figure 1.3: Power/weight ratio vs. weight diagram of different actuators (Hirose *et al.* 1989).

7. Large recoverable strains which permit extremely long strokes and the application of large forces when deformation is restrained.

8. High electrical resistivity means that the shape transformation can be activated by passing an electrical current through a SMA element, thus avoiding the need for separate heaters.

9. Design flexibility. Shape memory alloy actuators can be linear, rotary, or some combination of the two, as required, and can form an integral part of a component.

Thus, it would appear that SMA-deployed structures can combine practically all the advantages of controlled-deployed and free-deployed structures, without any of their disadvantages.

1.4 SMA-Based Actuators

This section reviews actuator concepts and existing actuators that are suitable for deployable structures.

To deploy a structure, it is necessary that a relative movement, i.e. a rotation or a linear motion, occurs between different parts of that structure. Such movement can be generated either by a specially designed actuator or simply by a part of the structure changing its shape.

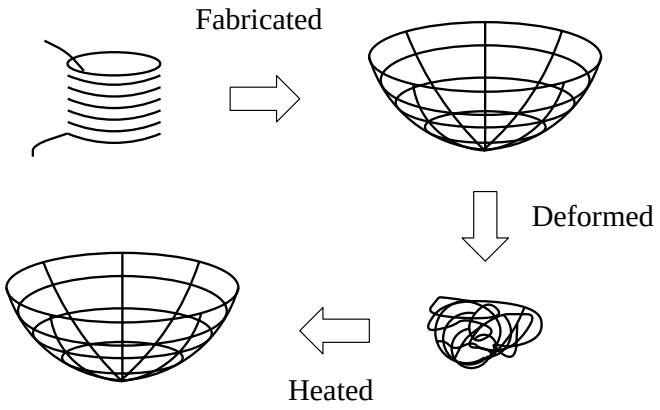

Figure 1.4: SMA satellite antenna (from Gandhi and Thompson 1992).

In the 1960's, Nitinol sheets and rods had been considered to unfurl satellite antennas upon exposure to solar heating, see Funakubo (1987) and Fig. 1.4. Figure 1.5 shows another simple SMA satellite antenna made of Nitinol wire, which was designed and tested in China.

In recent years, SMAs have been used for the following applications. To trigger the off-loading system of the Hubble Space Telescope solar array drive mechanism (Hostenkamp 1985); in a no-shock separation mechanism for spacecraft release

(Smith *et al.* 1997); in a multi-shot deployment mechanism for both release and spring recharge (Stella *et al.* 1991); to open the cover glass of a solar cell of NASA's Mars Pathfinder Rover, Fig. 1.6; and in a multi-axis ultra-lightweight gimbal drive, total weight 0.6 Kg, that can rotate from -100^o to +100^o at a rotation rate of 0.06^o/s, and has maximum output torque of 0.34 Nm, for solar array and antenna positioning applications (Carpenter *et al.* 1995).

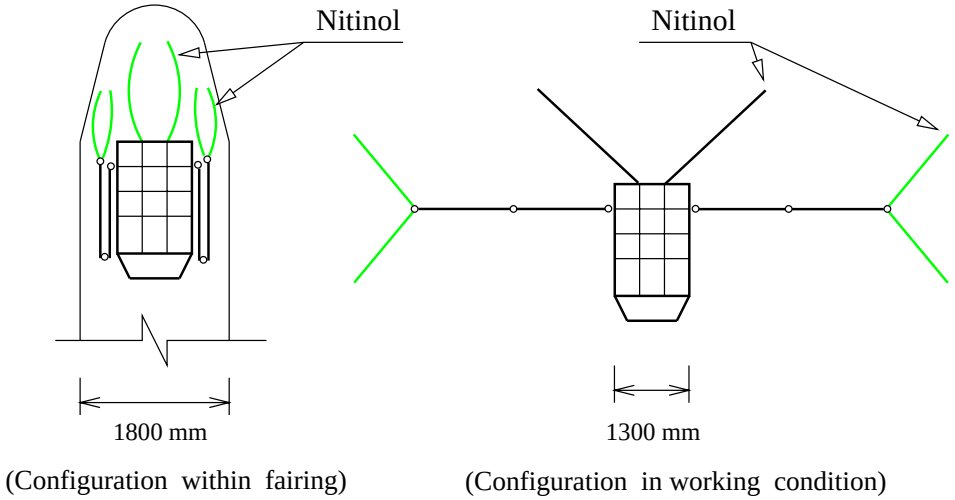

Figure 1.5: SMA satellite antenna (from Yang *et al.* 1985).

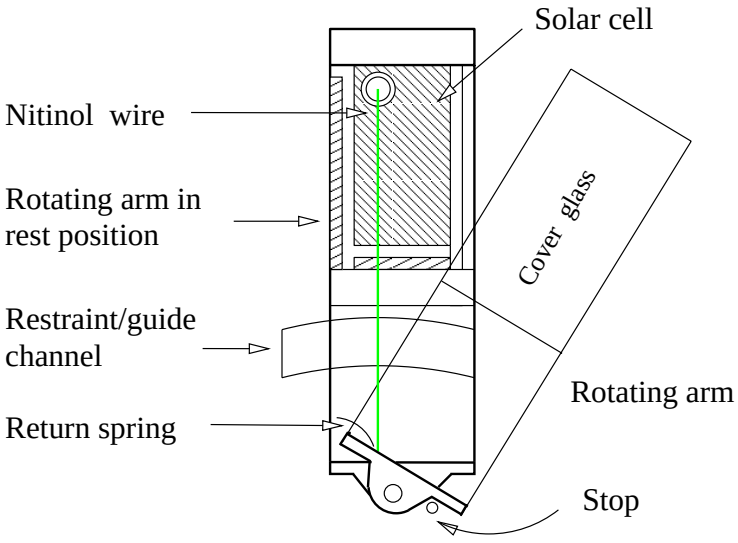

Figure 1.6: SMA-actuated rotating arm (from Jenkins and Landis 1995).

SMA elements have also been suggested as connections in the installation of large space platforms, or even as deployable shrouds to protect the equipment or personnel of a space station (Schetky 1991).

The feasibility of two concepts, a Nitinol mast, which is similar to the coilable masts made by the Astro Aerospace Corporation and by AEC-Able Engineering, but, instead of being driven by an electrical motor, have their vertical members released by Nitinol to provide recovery forces; and a Nitinol slit tube, similar to the Storable Tubular Extendible Member (STEM), have been investigated by Choi *et al.* (1996).

Anders and Rogers (1991) have studied a simple SMA wire hinge. The same concept was tested on board of the spacecraft PROGRESS-40 to assemble a space truss which contained five transformable units. Each unit consisted of four hinged panels, Fig. 1.7. The wire is a 2 mm diameter Nitinol heated by passing an electric current through it.

The use of SMA torsion springs, also heated by passing an electrical current through them has been suggested as a way of deploying solar panels (Moorleghem 1993).

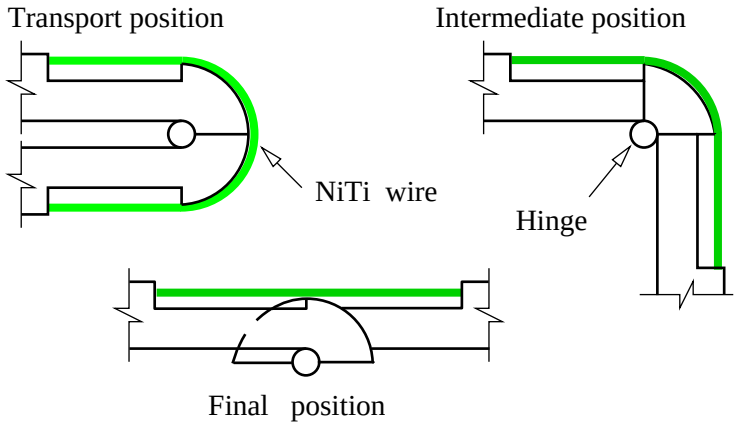

Figure 1.7: SMA hinge (from Likhachev *et al.* 1994).

Linear motion actuators, such as that shown in Fig. 1.8, are now commercially available. Coin-sized actuators can be produced with current technology. SMA micro-actuators and micro-machines are under study (Skrobanek *et al.* 1997).

Many exciting applications of SMAs come from the field of robotics which shares many common points with deployable structures. Many SMA-based joint actuators have been proposed. For example, Fig. 1.9, based on Bergamasco *et al.* (1989), shows a direct-drive robotic actuator. The joint can rotate back and forth by heating two Nitinol springs alternately. A cooling liquid was used to improve

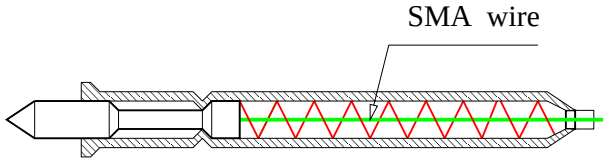

Figure 1.8: Linear motion SMA actuator (from Moorleghem 1993).

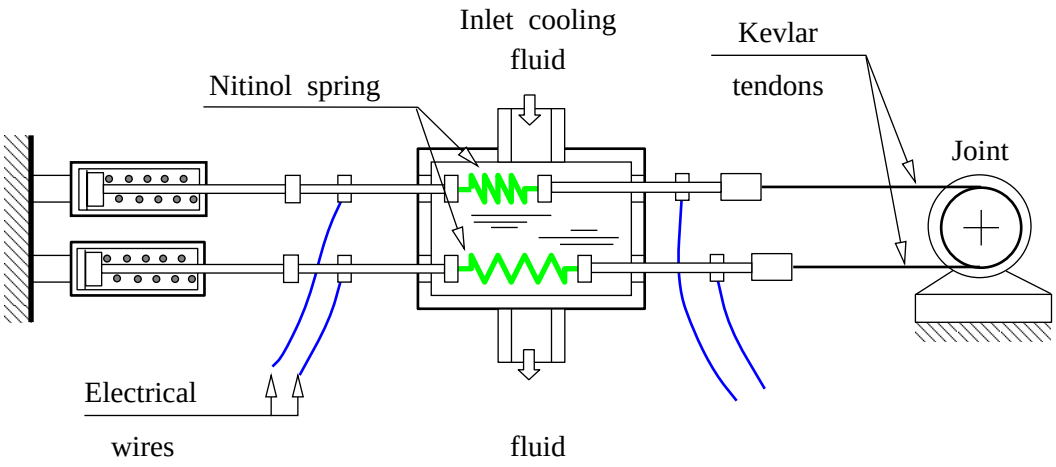

Figure 1.9: SMA actuator (from Bergamasco *et al.* 1989).

the usually limited bandwidth[3] of SMAs, and similar concepts have been used in many other actuators. Other technologies that have been used to rapidly cool SMAs include semiconductor (Thrasher *et al.* 1992, Bhattacharyya *et al.* 1995), mobile heat sinks (Gobert and Russell 1995), and pairs of agonistic-antagonistic wires (Ditman *et al.* 1994). Figure 1.10 shows a section of a 30×17×17 mm linear SMA actuator (Grant and Hayward 1995), which consists of twelve NiTi thin wires woven in a counter rotating helical pattern around supporting disks. When the wires are heated, they contract pulling the disks together.

An active endoscope using Nitinol coil springs has been designed and tested (Hirose *et al.* 1989). Position control of each section, see Fig. 1.11, is based on feedback of resistance change mainly caused by phase transformation during operation.

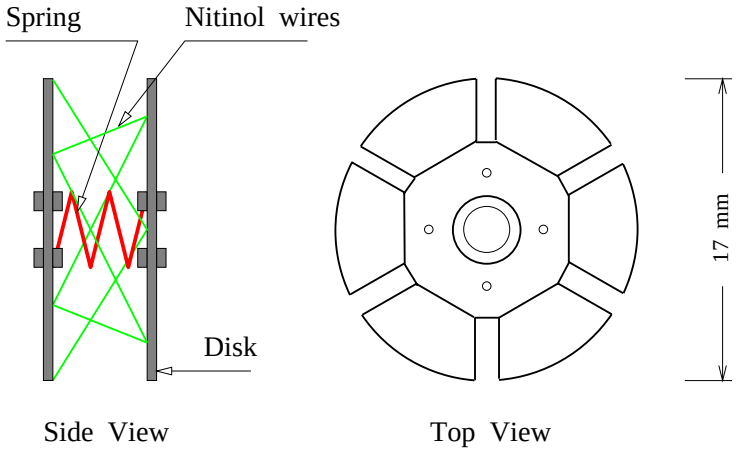

Figure 1.10: SMA actuator (from Grant and Hayward 1995).

[3]Actuation frequency.

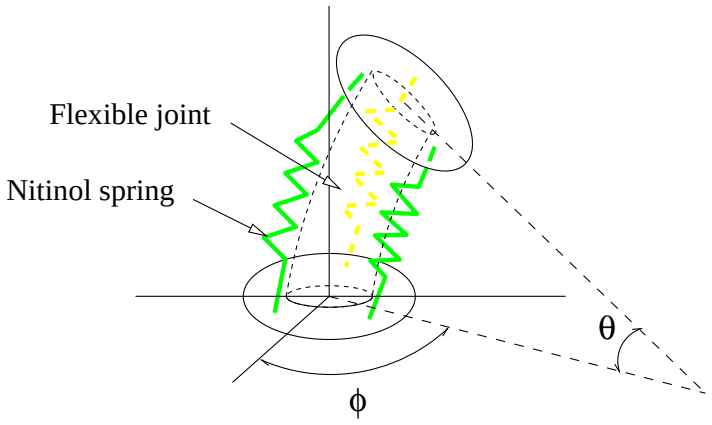

Figure 1.11: Nitinol endoscope (from Hirose *et al.* 1989).

While SMA wires in helical form (i.e. like springs) are commonly used for large displacement actuators, straight wires are often chosen when a bigger output force/torque is required.

Another popular configuration of SMA is torsion bar, which has been used in many cases to generate a rotation. Gabriel *et al.* (1988) tested a 0.04 cm^3 micro rotatory actuator using a 10 cm long, 100 μm diameter piece of Nitinol wire under torsion. A bandwidth of approximately 4 Hz was achieved. A similar idea has been used in the design of a 4 mm diameter Nitinol hinge which can deploy two panels by twisting 180^o against up to 2.2 Nm resistive torque (Jabs and Moignier 1996). Based on a slightly different idea, two 0.46 cm diameter, 38 cm long Nitinol torsion rods have been used to supply the torque required to unfold the backbone of a deployable solar array (Choi *et al.* 1996). Another concept (McCarty 1990) put one Nitinol tube inside another Nitinol tube that has bigger diameter but nearly equal polar moment of inertia to the first, to produce a two-position rotary actuator. By heating inner tube and outer tube alternately, this actuator can generate equal torques in both directions.

1.5 Heating Methods

Basically, SMAs can be heated by the following three different methods,

- By passing an electrical current through them, Figure 1.12(a). This method is only applicable where a small diameter SMA wire or spring is used, otherwise the electrical resistance is too small to produce enough heating. The main advantage is simplicity, while the big disadvantage is that the SMA element needs to be electrically insulated.

- By passing an electrical current through a high resistance wire or tape wrapped around the SMA element, Figure 1.12(b). This method is available for SMA bars or tubes. The electrical wire needs to be electrically insulated,

but the insulator should have good thermal conductivity to let the heat flow to the SMA element.

- By exposing the SMA component to thermal radiation, Figure 1.12(c). This may be the simplest way in space, since a component exposed to the light of the sun will heat to temperature of 150°C or more. No additional heating system is required. The main disadvantage of this method is that it is inflexible, and it could be very difficult to retract the structure.

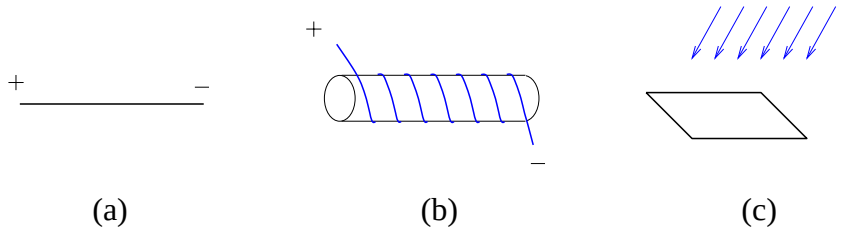

Figure 1.12: Heating methods. (a) Passing a current through; (b) external heating by wire; and (c) thermal radiation.

An advantage of using heating by electrical current is that by controlling the electrical current, deployment and retraction can be made controllable.

1.6 Aims of the Dissertation

Although it has been recognised that SMA materials have a significant potential for deployment actuators, the number of applications of SMA-based actuators to the present day is still quite small. This is mainly because of the following three reasons.

First, since SMAs are very different from traditional materials, a deeper understanding of their thermomechanical behaviour is essential for actuator design. Second, the predictive methods based on the available constitutive thermomechanical models for SMAs are, in most cases, far from reliable. Therefore the development of a robust predictive methodology to support the design process is required. Third, the design procedure for SMA-based actuators is different from ordinary design in many respects, and is insufficiently well understood.

Although some of the modelling work presented in this dissertation is valid more generally, the particular SMA that is studied is Nitinol because its properties are much better than other commercially available SMAs for our type of application.

Our aims of the study presented in this dissertation were twofold.

The first aim was to further investigate, both experimentally and theoretically, the thermomechanical behaviour of Nitinol, and to develop a phenomenological model for engineering design.

1. Experimental Work

   A lot of experimental work has been carried out on Nitinol. But all previous studies have considered only some of the aspects of its behaviour and hence had produced only an incomplete picture of it.

   Therefore, we will report on a testing program which included purely thermal tests and thermomechanical tests on Nitinol wires with diameters of 1 mm and 0.5 mm, and on Nitinol bar with diameter of 6.5 mm.

   In the purely thermal tests, a Differential Scanning Calorimeter was used to determine how heat treatment affects phase transformations. The difference in the transformation temperatures of twinned martensite and detwinned martensite was studied.

   The thermomechanical tests included tension tests at different temperatures, tension tests under different strain rates, response to suddenly applied loads, thermal cycling under different loads and thermal cycling with fixed length, all on Nitinol wires. These tests will tell us about subtle effects, such as the variation of the Young's Modulus during loading, the effects of strain rate on phase transformation fronts, the effects of temperature non-uniformity on thermal cycling. In particular, in our tension tests, we applied loads to the regime, which had been regarded as plastic regime in many previous studies.

   The torsional tests included thermal cycling under different torques (both positive and negative), uniaxial tension and thermal cycling tests. These tests will tell us about the two-way shape memory behaviour of Nitinol bars.

   After these tests, we were able to build a reasonably complete picture of the behaviour of Nitinol.

2. Theoretical Analysis

   Many constitutive models have been developed to describe the thermomechanical behaviour of SMAs. Each type of model is aimed to the different aspects of shape memory behaviour or to address the thermomechanical behaviour of SMA on a different level. Hence, most existing models cannot re-produce all features of SMA behaviour, not even qualitatively.

   In this research, we will develop a thermo-micromechanical model based on complementary free energy and micromechanical transformation systems that is able to re-produce the behaviour of SMAs undergoing uniaxial load cycling and thermal cycling.

   Phenomena such as the V-shape of the critical stress vs. temperature plot, the non-symmetrical behaviour in tension and compression, the transformation front behaviour, and the multi-phase transformation, are captured by this model.

3. Phenomenological Model

   Because of the very strong influence of micro-structure and processing on the mechanical properties, the theoretical model can only describe the shape memory performance qualitatively. For engineering applications, the most practical approach is based on phenomenological models, which fit the experimental data without attempting to capture the detailed underlying thermomechanical behaviour.

   In previous phenomenological models, the transformation fractions were assumed to be of certain functions. Since these functions were not based on the behaviour of material itself, i.e. they were not directly obtained from experiments, it turns out that they cannot describe the behaviour of SMAs accurately, and cannot be used in materials for which the transformation temperatures are ambiguous or not in the standard sequence $M_f \leq M_s \leq A_s \leq A_f$.

   In the present research, we have developed a phenomenological model, based on our tests, which is able to predict the experimentally observed thermal cycling behaviour with fixed length, the strain rate effects and the phase transformation front behaviour.

The second key aim was to design, test and simulate the behaviour of Nitinol-based actuators for deployable structures. Our final aim was to design an actuator which can rotate over 180^o against a torque of 2 Nm. These particular requirements were suggested by Mr David Eaton, of the European Space Agency, who was involved in this project, at its early stages.

As a first step, we will describe two Nitinol wire-based rotatory actuators based on different concepts, which were designed and tested. The first actuator is a biased actuator and the second one is a one-way actuator. The aim of this preliminary study was to explore different concepts and gain experience in the practical design of a complete working system.

As a second step, we will describe a two-way Nitinol wire-based actuator that uses the same concept as the second actuator concept studied in the previous phase, but designed much more carefully, to avoid the practical difficulties that had been encountered when testing the previous prototype. Also, two of these actuators were put together, one against the other, in order to obtain a two-way performance, i.e. to be able to rotate forward and backward by heating different Nitinol wires.

Simple methods for designing SMA actuators have been proposed by Waram (1988), Yaeger (1984), Stoeckel (1991) and Schmidt-Mende and Reiss (1991). These methods consider the SMA element in the actuator either fully in the high temperature, austenite phase or in the low temperature, martensite phase. The material characteristics, and especially the dependence of the phase transformation on temperature and stress are not taken into consideration. Hence, these methods are suitable only as preliminary design tools, but are insufficiently detailed if accurate prediction are required.

In this research, the behaviour of all actuators was simulated by using the phenomenological model that we had developed to see whether this model can be used in the real design.

In real application one is interested in the power consumption of an actuator, as well as its rotation range, speed, etc. We propose two prediction methods to calculate the power requirements of each actuator and we compare their estimates with experimental results.

1.7 Layout of the Dissertation

The dissertation is presented as follows:

In the present chapter, Chapter 1, we have introduced the concept of shape memory behaviour, and given a brief review of its applications. We had also summarised the basic type of SMA-based actuators and their advantages, and given a review of Nitinol-based actuator concepts and of existing actuators that are suitable for deployable structures. Heating methods have also summarised.

In Chapter 2, we give a compact, physically based explanation of the key aspects of the behaviour of shape memory alloys.

In Chapter 3, we present experimental work on Nitinol wires. These tests include Differential Scanning Calorimeter tests, tension tests at constant temperature, tension tests under constant strain rate, tension tests with suddenly applied loads, thermal cycling under constant load, and thermal cycling with fixed length.

In Chapter 4, after reviewing the constitutive models which are currently favoured, we propose a new experimental based thermomechanical model for Nitinol subject to uniaxial stress states. The predications of this model are compared with the experimental results presented in Chapter 3. This model is then used to simulate the thermal cycling with fixed length, the strain rate effects and the phase transformation front behaviour.

In Chapter 5, a thermo-micromechanical model based on complementary free energy and micromechanical transformation system is proposed, and the behaviour of shape memory under unaxial loading and thermal cycling were investigated.

In Chapter 6, as the first step in the design of wire-based actuators, the design and testing of two actuators based on different concepts is presented. The experimental behaviour of both actuators is compared with simulations based on the model presented in Chapter 4.

In Chapter 7, we present the design, testing and simulation of a two-way wire actuator. This actuator is based on the same concept as the second concept studied in Chapter 6, but was designed much more carefully. The power consumption of all three actuators is studied.

In Chapter 8, we present experimental results for a Nitinol bar. Differential Scanning Calorimeter tests, torsional tests, thermal cycling under constant torque, and uniaxial tension and thermal cycling tests are carried out.

The dissertation concludes with a summary of the achievements of the present work, and a general design procedure for Nitinol-based actuators. Some ideas for future work conclude the chapter.

Chapter 2

Shape Memory Behaviour

More than 60 years have passed since SMAs were first identified. The changes in micro-structure related to the phase transformation are now well understood, although the underlying microscopic mechanisms are still a research topic in materials science area, the connection between microscopic and macroscopic behaviour is still under investigation, and existing micro-structural thermomechanic models can describe the behaviour of SMAs only qualitatively.

An understanding of the micromechanical behaviour of SMA is necessary to understand their macroscopic behaviour. Our discussion is restricted to the elastic range, i.e. it is assumed that no plastic deformation takes place.

2.1 Memory Effect

At low temperature, a SMA can be seemingly "*plastically*" deformed, but this "*plastic*" strain can be recovered by increasing the temperature. This is called the **Shape Memory Effect (SME)**, Fig. 2.1(a).

At high temperature a large deformation can be recovered simply by releasing the applied force, and this behaviour is called **Superelasticity**, Fig. 2.1(b).

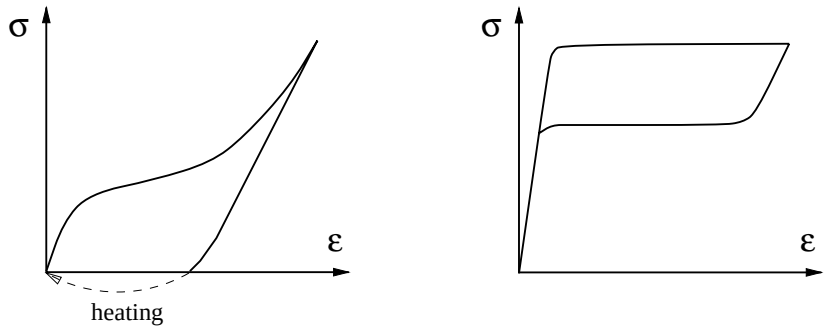

(a) SME (b) Superelasticity

Figure 2.1: Shape memory behaviour. (a) Shape memory effect; (b) superelasticity.

These two phenomena relate to two different micro-structural transformations (phase transformation and martensite re-orientation, respectively) that are described in the next two sections.

2.1.1 Phase Transformation

The **Martensitic Transformation** (from **Austenite** (A) to **Martensite** (M)) and its reverse transformation are lattice transformations involving a shearing deformation that results from cooperative atomic movements. Basically, this transformation is caused by the difference in free energy between the two phases (Nishiyama 1978, Funakubo 1987) as shown in Fig. 2.2.

Austenite is the high-temperature (high-energy) phase. In Nitinol, it is **Body-Centred Cubic (BCC)** lattice, which has a $B2$ structure with a_o= 0.3015 nm. The most common low-temperature (low-energy) phase, martensite, of Nitinol is monoclinic $2H$ structure with a= 0.2889 nm, b= 0.4120 nm, c= 0.4622 nm, and β= 96.8^o. Refer Fig. 2.2 for a schematic view of $B2$ and monoclinic $2H$ structures. For details of these structures reference may be made to Saburi and Nenno (1982), Funakubo (1987).

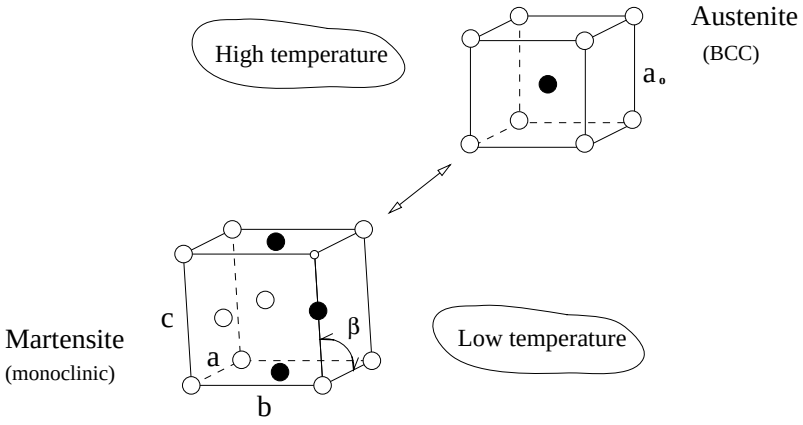

Figure 2.2: Phase transformation in Nitinol.

In order to induce the austenite to martensite transformation, the chemical free energy of the martensite phase must be lower than that of the austenite phase. However, since the transformation requires also non-chemical free energy, such as transformation strain energy, friction energy, etc., the transformation can happen only when the difference between the chemical free energies of the two phases is greater than the necessary non-chemical free energy[1]. Similarly, the transformation from martensite to austenite will occur when the difference between the above energies, with their signs reversed, is sufficiently large. Thus, a distinguishing characteristic of SMAs is **Hysteresis**, i.e. there is a difference between the forward and reverse transformation paths.

[1]This is called **Super-cooling** in materials science.

Another crucial characteristic of SMAs is the thermoelastic nature of these phase transformations, which means

- The transformations can be induced either by a temperature change, or by an applied stress both of which change the free energy of the material. The volume change associated with them is very small[2]. All deformation in transformations is recoverable.

- Once martensitic crystals have nucleated, they grow at a rate proportional to the cooling rate or the rate of increase of the applied stress (Funakubo 1987). Similarly, these crystals shrink upon heating and it has been found that in thermally induced transformations, the martensitic crystals that were formed first are the last to undergo the reverse transformation (Otsuka *et al.* 1971, Schroeder and Wayman 1977a, Christian 1982, Funakubo 1987).

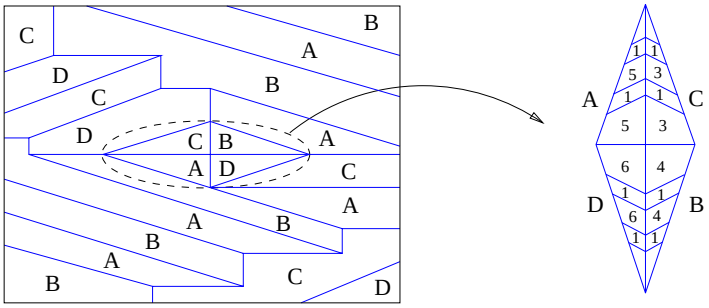

Figure 2.3: Schematic plot of a twinned martensite, where A, B, C, and D stands for different twinning groups, and 1, 3, 4, 5, and 6 are different martensite variants (from Saburi and Nenno 1982).

Since the austenite-martensite inter-phase is fully coherent[3], there is a definite relationship between the orientation of an austenite crystal and that of a neighbouring martensite crystal. Thus even in a single austenite grain, up to 24 **Martensite Variants** (only 12 in Nitinol) may be formed. The variants are crystallographically equivalent, but have different orientation, and different planes of shearing. Different martensite variants arrange themselves into twinning groups (refer Fig. 2.3 for an example), in order to minimise the internal stresses (Christian 1982). All transformations, free from external stress, tend to be self-accommodating since the shape deformation in any group will produce stress fields favouring the formation of some particular variants. Therefore, macroscopically there is no shape change[4].

[2]For example, Nitinol shrinks by 0.34% when it is transforms from austenite to martensite, see Appendix A.

[3]It is coherent inter-phase if the lattices of two phases matched perfectly on the inter-phase surface.

[4]Such martensite is often called **Twinned Martensite** (*TM*) (Wayman and Duerig 1988).

On the other hand, transformations induced by stress will tend to produce only these variants that have the most favourable orientation to the applied stress. which is the sum of the external stress plus the internal stress resulting from geometrical constraints of interphase and grain (for polycrystals only) boundaries etc. However, as shown by Patoor *et al.* (1996), in order to satisfy the grain boundary constraints in the case of polycrystals, even in a uniaxial tension test several martensite variant groups are found in a grain. These variant groups are different from the twinned martensite produced by external stress-free cooling. During the reverse transformation, the martensite goes back to austenite with the original orientation.

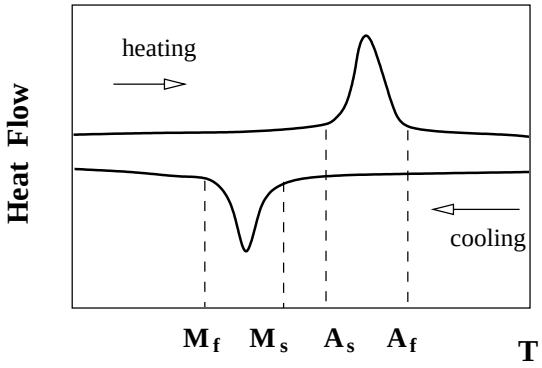

Figure 2.4: Schematic DSC plot.

The **Differential Scanning Calorimeter (DSC)** test measures the relationship between power input/output and temperature change for a small sample of material, and is the standard way of investigating temperature induced phase changes. Peaks and troughs in a plot of heat flow vs. temperature mark exothermic and endothermic transformations, respectively, and the temperatures at which these transformations begin and end can also be seen clearly, Fig. 2.4.

The phase transformations that occur by changing temperature without any external stress are shown in Fig. 2.5, where the martensite fraction as the vertical axis is the volume percentage of martensite (refer Eqn. 2.1). On cooling, pure austenite transforms into twinned martensite beginning at the temperature M_s (martensite start) and, on further cooling, the martensitic transformation is completed at the temperature M_f (martensite finish). Then, on heating, the reverse transformation begins at the temperature A_s (austenite start) and is completed at the temperature A_f (austenite finish).

Lattice defects in the crystals play an important role in the nucleation of martensite, reducing the free energy difference required for the transformation and the growth of martensite (Olson and Cohen 1982).

As shown in Figs. 2.4 and 2.5, austenite and martensite can co-exist in certain temperature ranges.

If the formation of martensite is induced by the application of external stress at low temperature, the deformation that remains after releasing the applied

stress can be recovered by heating, i.e. by inducing a transformation to austenite (SME, Fig. 2.1(a)). On the other hand, if martensite is induced at high temperature, all deformation can be recovered by unloading (superelasticity, Fig. 2.1(b)), since at high temperature only austenite is stable. However, there is a certain temperature, M_d, above which martensite cannot be stress-induced (Duerig and Pelton 1994).

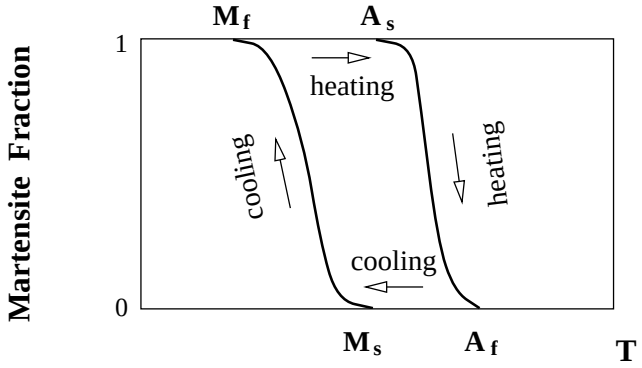

Figure 2.5: Martensitic fraction vs. temperature.

A special type of austenite $\Leftrightarrow$ martensite transformation, called **Two-way Shape Memory Effect (TWSME)**, is obtained by a special "*training*" process (Perkins and Hodgson 1988) normally consisting of a series of thermal cycles, during which high-temperature and low-temperature shapes are imposed on a SMA component.

Thus, one obtains a **Two-way Shape Memory Alloy (TWSMA)** which can remember both its low temperature shape (martensite) and high temperature shape (austenite). TWSMAs switch from their low temperature shape to their high temperature shape, but their recoverable strain is usually about half of the corresponding one-way recoverable strain for the same material. It is believed that the internal stress field produced in the material during the training process influences the growth of martensite (Schroeder and Wayman 1977b, Perkins and Hodgson 1988). Thus, during cooling, the induced martensite variants are in favour of both internal stress and external stress, plus boundary constraints.

An intermediate phase, called R-**phase**, with rhombohedral structure (Funakubo 1987), is sometimes found during the martensitic transformation. The formation of the R-phase has been linked to the existence of large energy barriers that oppose the completion of the normal martensitic transformation, but the fundamental reasons are still under investigation. The strain related to the R-phase is commonly less than 0.5% (Otsuka 1988), i.e. quite small in comparison with the main transformation strain.

2.1.2 Martensite Re-Orientation

Martensite re-orientation is a transformation between martensite variants, i.e. no phase change is involved. This transformation is always stress related and the

corresponding recoverable strain is associated with the conversion between variants. If a SMA specimen that consists only of twinned martensite is subjected to gradually increasing uniaxial stress, transformations will occur between variants within each twinning group, leading to the growth of a preferred variant. This process minimises the elastic energy in this group, as the change of internal stress partially counterparts the externally applied stress.

As the stress level increase, similar conversions will take place among martensite groups until the entire specimen consists of only one variant in single crystal, or in polycrystal, each crystal is dominated by certain variant or variant group[5], theoretically at last, and a large macroscopic strain is produced. This process is called **Detwinning**, and the resulting martensite is usually called **Detwinned Martensite** (DM).

If the maximum stress level is not high enough, the material will be only partially detwinned and there will still be several different variants/variant groups in each crystal. If the local stress field is changed, e.g. by unloading the specimen, the martensite variants may convert, according to the local stress, in order to minimise the total energy in the local area.

After deformation, the specimen can be heated to high temperature under zero external stress, so that only austenite remains, and it will go back to the shape that it had before twinning, i.e. it remembers its original shape (SME).

2.2 Thermomechanical Behaviour

Let us consider the simplest type of loading, one dimensional extension of a uniform SMA wire. In this case, the phase transformations may by described in terms of three external variables, σ (stress), ϵ (strain) and T (temperature), and three internal variables[6]: the austenite fraction ξ^A, the twinned martensite fraction ξ^{TM} and the detwinned martensite fraction ξ^{DM}, where

$$\begin{aligned} \xi^A &= \frac{V^A}{V} \\ \xi^{TM} &= \frac{V^{TM}}{V} \\ \xi^{DM} &= \frac{V^{DM}}{V} \end{aligned} \tag{2.1}$$

Here V^A is the volume of austenite, V^{TM} is the volume of twinned martensite, V^{DM} is the volume of detwinned martensite, and V is the total volume.

2.2.1 Tension Test and Thermal Cycling Test

- Loading/unloading at constant temperature

[5]The dominant variant or variant group varies from crystal to crystal.

[6]In fact, there are only two independent internal variables, since $\xi^A+\xi^{TM}+\xi^{DM}=1$.

Let us consider a SMA wire of uniform cross-section, containing a mixture of austenite and twinned martensite. The initial phase is (ξ^A, ξ^{TM}).

Put this wire into a standard tension testing machine and carry out a tension test. A plot from this test is shown in Fig. 2.6(a). During loading from a to b, the behaviour is mainly elastic although some transformation may happen, as indicated by a small amount of nonlinearity in the curve. If the stress goes over a certain critical stress, whose magnitude depends on the temperature of the specimen, suddenly a large transformation-induced strain occurs ($b \rightarrow c$). In this process, the transformations that occur are martensitic transformation and martensite re-orientation. After the martensitic transformation has almost been completed, from c to d, the martensite re-orientation (detwinning) dominates.

During unloading, after a period of pure elastic recovery, a small portion of the detwinned martensite may transform back to twinned martensite accompanied with some reverse martensitic transform ($d \rightarrow e$). If the temperature of the specimen is not too high, further unloading will lead to more reverse transformation ($e \rightarrow f$). The only way of fully recovering the original shape is by heating the wire above a certain temperature under zero stress (SME).

If the temperature is quite high, the stress vs. strain relation is that shown in Fig. 2.7(a) (superelasticity). Note that in Fig. 2.7 the critical stress, where transformation starts, does not always decrease as the temperature decreases, but goes up after a certain temperature, see also Fig. 2.8[7].

- Thermal Cycling at constant load

  In this test the SMA wire is loaded up to point d in Fig. 2.6(a), and then thermally cycled, Fig. 2.6(b). From d to g, a small part of the detwinned martensite goes back to austenite, due to the temperature increase, while some detwinned martensite transforms to twinned martensite, due to local changes in internal stress.

  From g through h to i, twinned and detwinned martensite transform to austenite, however some times very high temperature is required to get pure austenite. During cooling, the reverse series of transformations occurs. Finally, at d the wire returns to the same state that it was in before the thermal cycling.

Since both phase transformation and martensite re-orientation have the effect of changing the local stress distribution, all surrounding martensite variants will reorient themselves to achieve minimum local stress. This means that both transformations will cause surrounding martensite variants to reorient.

The deformation caused by the re-orientation of martensite, for example, in the transformation of twinned martensite $\Rightarrow$ detwinned martensite, normally cannot be totally recovered by releasing the external stress. Heating without any

[7]Similar result can be found in Saburi *et al.* (1984) for a single crystal of Nitinol.

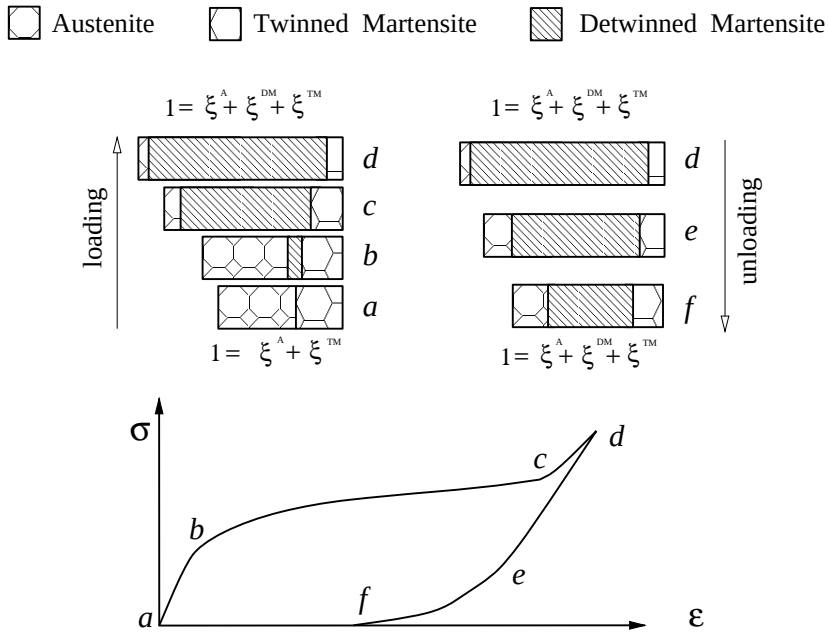

(a) Loading/unloading (constant temperature)

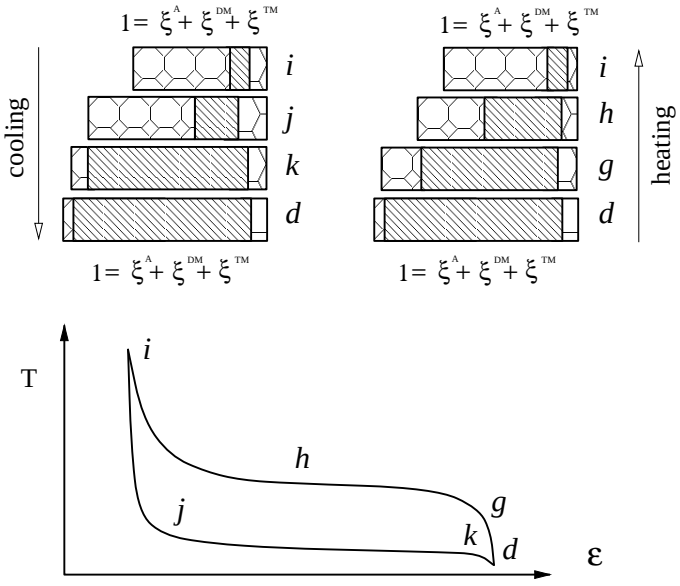

(b) Thermal Cycling (constant load)

Figure 2.6: Transformation-related phase changes. Bar length denotes the length of the specimen. (a) Loading/unloading (constant temperature); (b) thermal cycling (constant load).

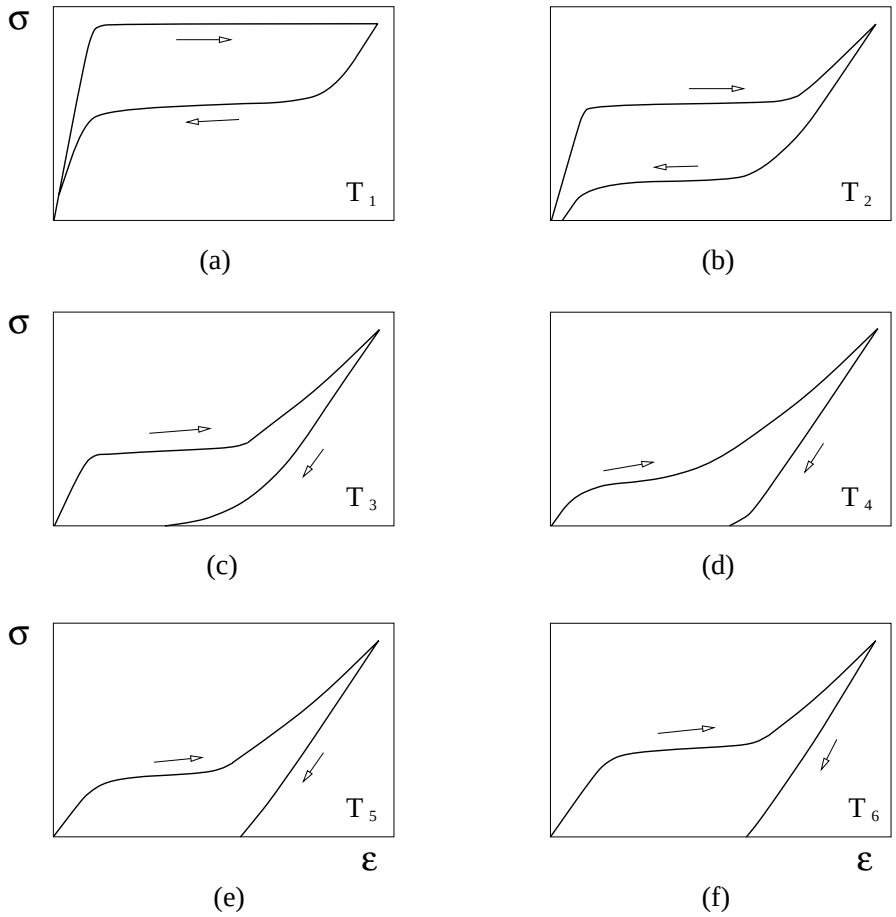

Figure 2.7: σ vs. ϵ relations at constant temperatures ($T_1 > ... > T_6$).

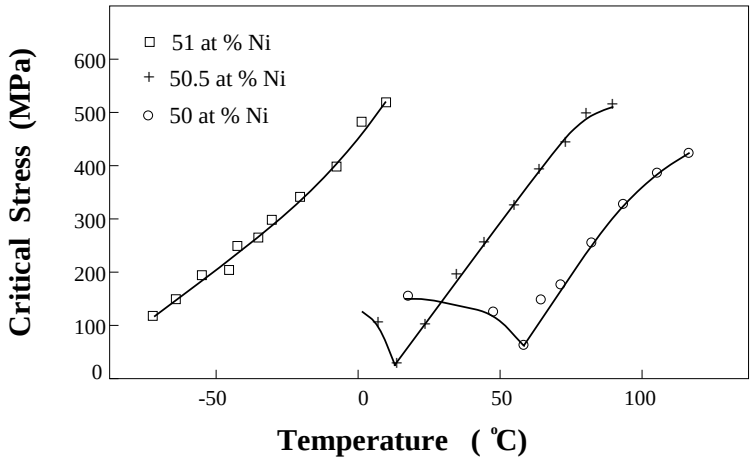

Figure 2.8: Critical stress vs. temperature for Nitinol (from Funakubo 1987).

geometric constraint and external stress is the usual way to recover the original shape. However, in some SMAs, such as, AuCd and CuZnAl, the original shape can be recovered simply by unloading. This phenomenon is called **Rubber-Like Behaviour (RLB)** (Cahn 1995). It is observed that RLB has a close relation with the stabilisation of martensite, and is believed to be driven by energy installed in the martensite variants by stressing.

2.2.2 Young's Modulus

The Young's Modulus of a single crystal is orientation dependent[8]. Also, the crystal structures of martensite and austenite are different, and therefore the Modulus of a SMA will vary with its phase composition and, therefore, temperature (Hasiguti and Iwasaki 1968). In a polycrystal SMA the measured Young's Modulus of the austenite phase can be several times higher than that of the martensite phase.

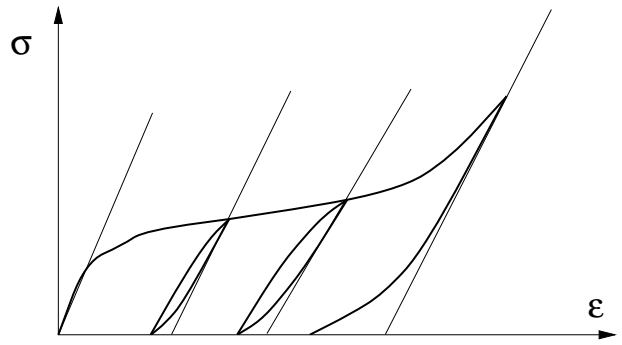

Figure 2.9: Young's Modulus.

Another effect that needs to be considered when examining the variation of the Modulus is the anisotropy of martensite during re-orientation. Hence, the Modulus of a SMA will depend not only on ξ^A, ξ^{DM} and ξ^{TM}, but also on the orientation and extent of each martensite variant.

Because of the interaction between the three effects described above, the Modulus of SMAs often varies as the applied stress increases. Because the strain measured at the early stages of a tension test is often partially due to internal transformations, the only accurate way of measuring the Modulus is at the very early stages of unloading, as shown in Fig. 2.9. However, note that further unloading will usually induce a strain recovery by reverse transformations.

2.2.3 Stress-Temperature Phase Map

The thermo-mechanical behaviour of SMAs may be represented schematically by the **Stress-Temperature Phase Map** shown in Fig. 2.10, although it must be

[8]See Chumljakov and Starenchenko (1995) and Shield (1995) for experimental results on single crystals of Nitinol and CuAlNi, respectively.

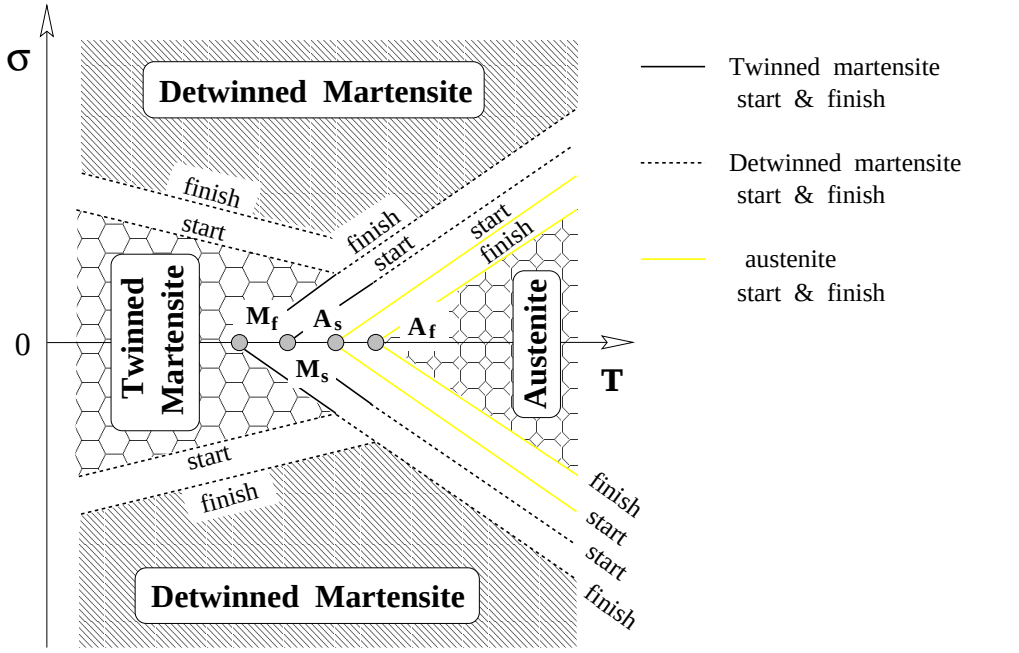

(a)

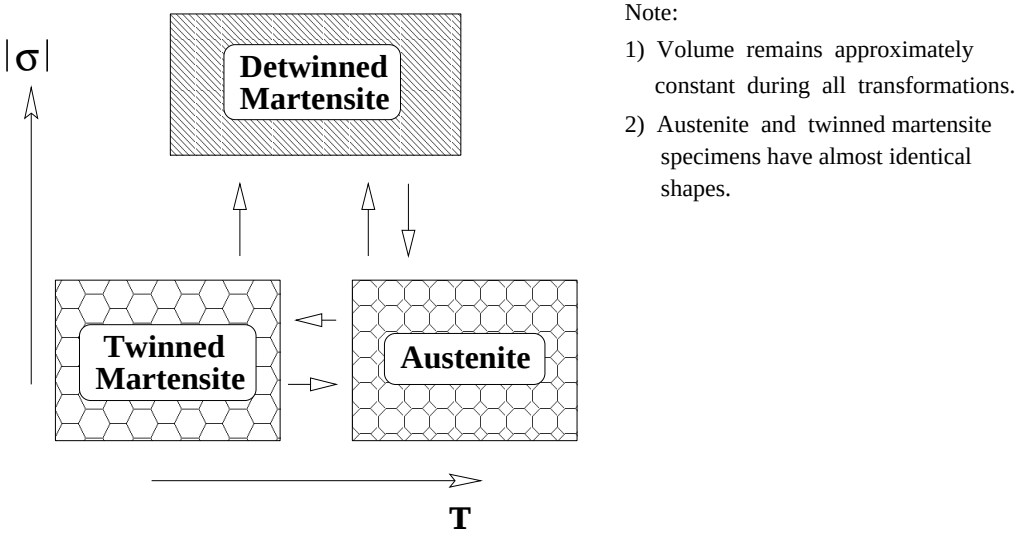

(b)

Figure 2.10: Stress-temperature phase map.

realised that the behaviour of real alloys is somewhat more complex than that shown in this map as explained in Section 2.2.1.

Points on the T-axis ($\sigma = 0$) mark the transformation temperature of 100% twinned martensite ($\xi^{TM} = 1$). Martensite starts to transform into austenite at A_s and finishes at A_f. For $T > A_f$, $\xi^A = 1$. On cooling, at M_s austenite starts to transform to twinned martensite and after M_f only twinned martensite exists ($\xi^{TM} = 1$).

Following a line parallel to the σ-axis shows that loading twinned martensite or austenite always produces detwinned martensite. The map shows that the austenite $\Rightarrow$ detwinned martensite transformation depends on the temperature, i.e.

1. The higher the temperature the bigger the stress needed to start the martensitic transformation;

2. At $T > A_f$, the reverse transformation happens just by reducing $|\sigma|$ (superelasticity, if there is no locked-in[9] behaviour).

2.3 Heat Treatment

In most cases, SMAs are supplied as raw materials, i.e. without shape memory. To memorise a certain shape, one forms the component into the required shape, clamps it to a rigid mould, and then heat treat the component while it is clamped.

The behaviour of SMAs is very sensitive to the temperature and duration of the heat treatment process, because their composition may change. Figure 2.11 shows that in general, TiNi $\rightarrow$ $Ti_{11}Ni_{14}$ $\rightarrow$ Ti_2Ni_3 $\rightarrow$ $TiNi_3$ as the heat treatment temperature is increased or as time at a constant temperature is increased.

Another reason for this sensitivity is that grain size and defect structure may be different after different heat treatments. Heat treatment is a kind of aging process and therefore, generally speaking, increasing the aging time can reduce the grain size and defect size. Grain boundaries act as a kind of constraint (Christian 1982, Saburi *et al.* 1984) and in larger austenite grains stacking faults can be formed in a relatively large number of planes. Where these planes intersect each other, there is an increase in the number of martensite nucleation sites (Durlu 1997). Hence increasing the grain size will increase M_s, see Fig. 2.12.

Figure 2.13 shows grain size effect on a Ti-50.5at.%Ni alloy under tension. A full recovery (superelasticity) is observed in polycrystal with fine grain size, 3% strain remains after unloading in a single crystal sample, and the recovery in polycrystal with grain size of 1 mm is between them. However, an investigation of the tensile behaviour of CuAlBe by Hautcoeur *et al.* (1995) showed superelasticity in single crystal, but SME in a polycrystal. In both cases, generally speaking, critical stress increases as grain size decreases.

[9] Refer Section 5.1.2.

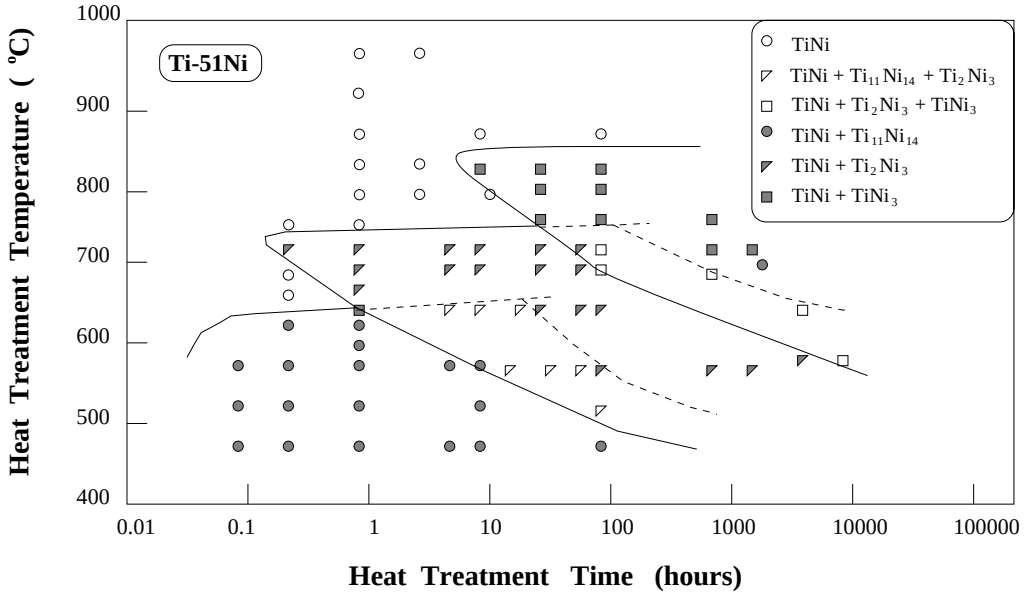

Figure 2.11: Temperature-time-transformation diagram (from Beyer 1995).

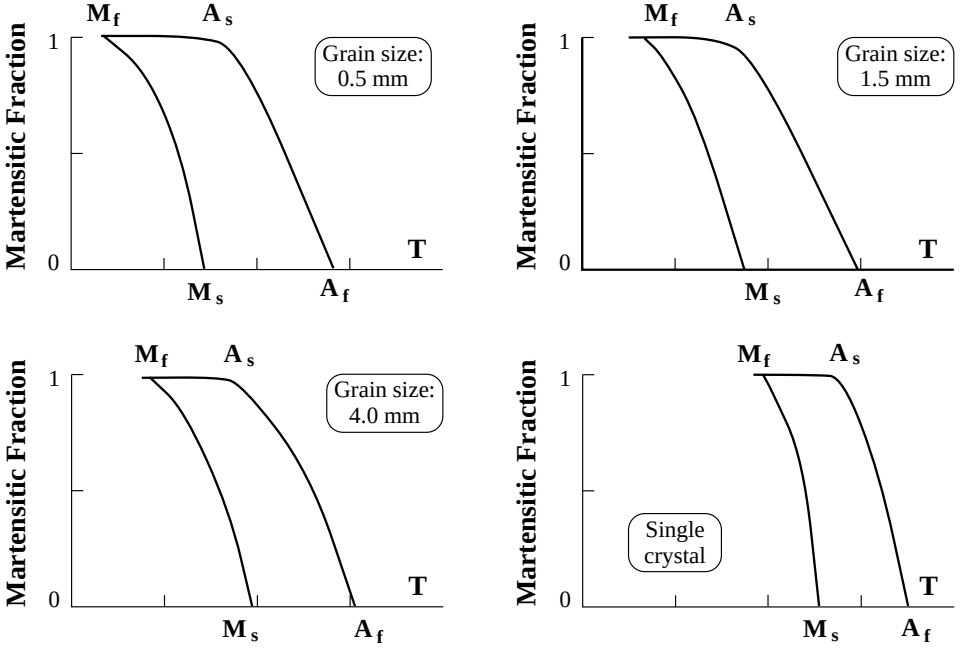

Figure 2.12: Transformation curves for polycrystalline Cu-14 Al-2.5 Ni (from Salzbrenner and Cohen 1979).

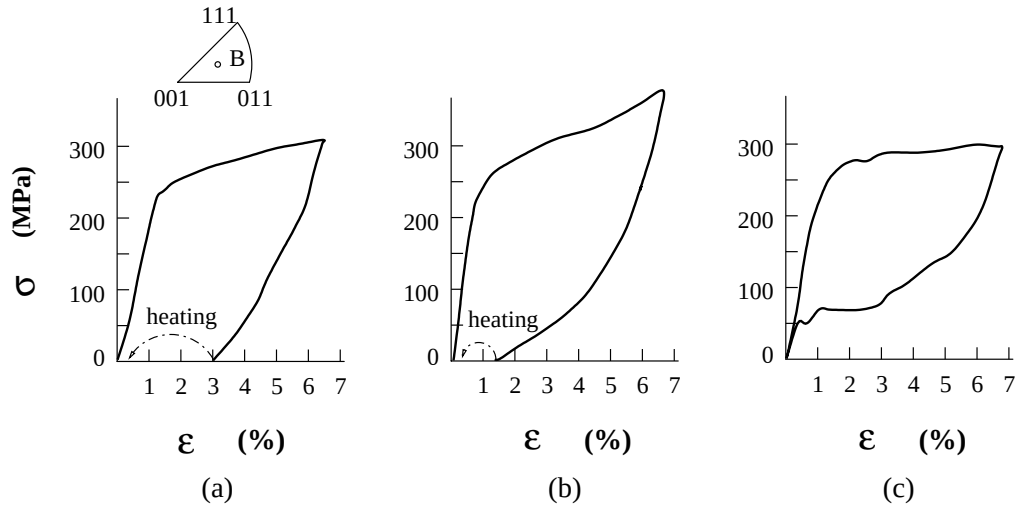

Figure 2.13: Grain size effect on a Ti-50.5at.%Ni alloy under tension (from Saburi *et al.* 1984). (a) Single crystal (tensile axis is orientation B); (b) grain size: 1 mm; (c) grain size: 50 μm.

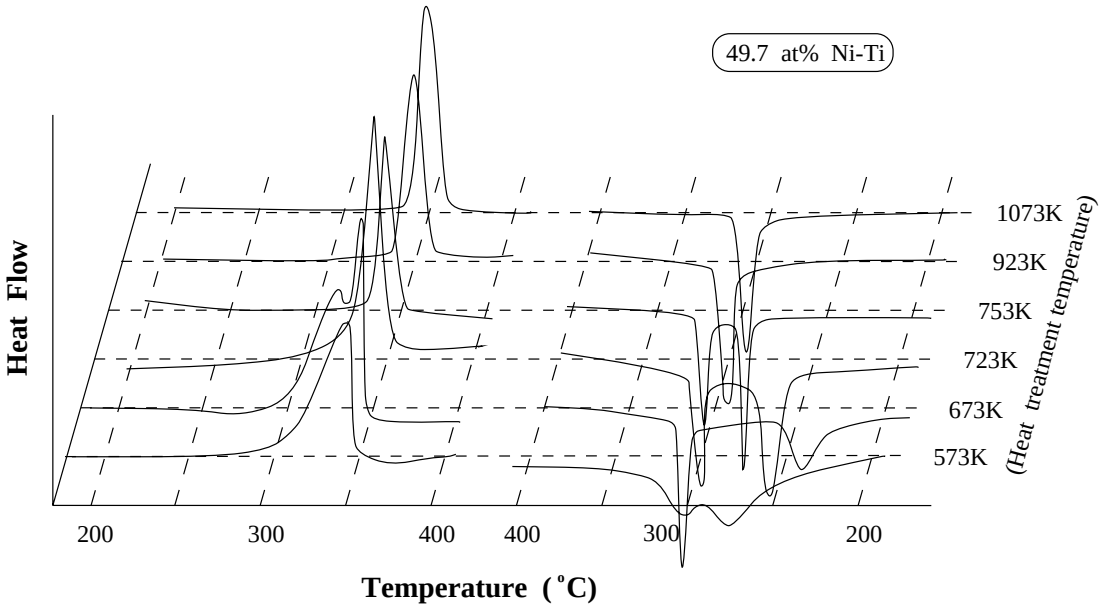

Figure 2.14: Effect of heat treatment temperature on DSC curve.

Figure 2.14 shows the results of DSC tests on Nitinol that has been subjected to different heat treatments[10]. In some cases, during cooling there are two valleys. The first valley indicates the formation of the R-phase, mentioned in Section 2.1.1.

[10] Author's name is unavailable.

Chapter 3

Experimental Characterisation of Nitinol

The first part of this chapter deals with the experimental characterisation of Nitinol wire by means of a purely thermal test, using a Differential Scanning Calorimeter. The second part of the chapter presents uniaxial thermomechanical tests, which include: tension test at constant temperature, tension test under constant strain rate, tension test under suddenly applied load, thermal cycling test at constant load, and thermal cycling test with fixed length, on two different Nitinol wires with diameters of 1 mm and 0.5 mm.

These wires were supplied by Thomas Bolton Ltd., Stoke on Trent in coiled shape and hard drawn condition, without shape memory. To memorise the straight, unstrained configuration, 150 mm lengths of wires were put in stainless steel "*hypodermic*" tubes with diameters of 1.5 mm and 1.0 mm, respectively and were heat treated by keeping them in a furnace at 500°C for one hour.

Preliminary tests showed that strains up to 9% could be fully recovered simply by heating the wire to over 180°C under zero stress. This means that no plastic deformation occurs at this strain level. So in all experiments described in this chapter the strain was always kept below 9%, in order to avoid plastic deformation.

Tests carried out on Nitinol bar will be presented in Chapter 8.

3.1 Thermal Tests

Differential Scanning Calorimeter (DSC) test is a standard tool in the study of phase transformation. By measuring the relationship between power input/output and temperature change, it determines the phase transformation/ temperature relation for a small specimen of the material.

Figure 3.1 shows thermo-graphs obtained from DSC tests on three different pieces of Nitinol which were cut from the same coil, but were heat-treated separately. Tests were carried out at 10°C/min, and the temperature varied between -70°C and 150°C. Only the temperature range in which phase transformations

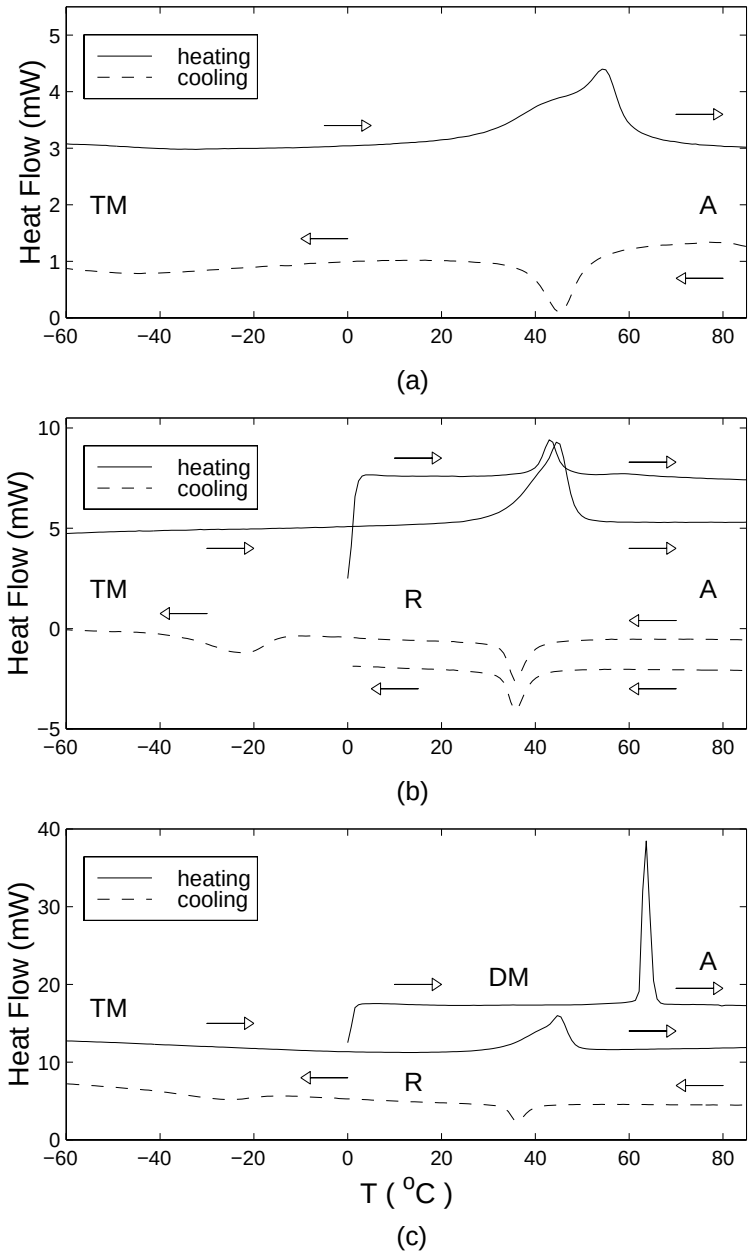

Figure 3.1: DSC results on 1 mm diameter Nitinol specimen. (a) Sample 1, starting from TM; (b) sample 2, starting from R; (c) sample 3, starting from DM.

were discussed has been shown in Fig. 3.1.

Fig. 3.1(a) refers to a specimen (sample 1) that was cut from the coil and heat-treated, without further processing. Note that there is only one trough in the cooling path and hence no R-phase in the sample, but this trough is much deeper than that for the other samples. The peak in the heating path is gradual at first and then quite sharp. The temperature range over which the $TM \Rightarrow A$ takes place is much greater than for the other samples.

Sample 2 was cut from a long wire which had been heat treated. Figure 3.1(b) shows the results of two thermal tests on this sample. One of the two cooling curves has two troughs, which indicates that the R-phase forms before TM. In another thermal cycle, subsequent heating from 0^oC after cooling to 0^oC produces a much smaller peak, since the transformation is $R \Rightarrow A$. Despite the fact that only one cycle is completed, the martensite start and finish temperature and the austenite start and finish temperature consistently estimated as $M_s \approx -15^o$C, $M_f \approx -33^o$C, $A_s \approx 25^o$C, and $A_f \approx 52^o$C.

Figure 3.1(c) shows the results from sample 3, which was cut from another long wire that had been stretched by applying a force of 350 N (corresponding to ≈ 0.45 GPa, see Fig. 3.6)[1] at an ambient temperature of about 24^oC after heat treatment. Thus, the initial phase is mainly DM. An extremely sharp peak at a much higher temperature than that for heating from TM or R to A and covering a very narrow temperature range, is observed upon heating this sample. It indicates that the transformation $DM \Rightarrow A$ is almost instantaneous. However, a further cooling and heating cycle shows almost the same results as for sample 2.

Hence, we may regard sample 2 as identical to sample 3, while different from sample 1. Therefore the thermomechanical behaviour of samples 2 and 3 will be almost the same, while those of samples 1 and 2 will be different.

It is believed that the difference is caused by the fact that they were cooled in different ways after heat treatment. Sample 2 and 3 were left on a hot block after being taken out of the furnace, thus prolonging their heat treatment, while sample 1 was cooled in air.

The difference between Fig. 3.1(b) and Fig. 3.1(c) can be explained as follows. The sample that has been stretched contains martensite or more precisely, partially detwinned martensite (for simplicity, we write it as DM), and a much higher internal stress field than that in the R-phase. As a result, a higher driving force, i.e. higher temperature, is required to trigger the transformation $DM \Rightarrow A$. Once this transformation starts, it will finish with little further temperature increase, since the material has already been overheated; and larger stored elastic energy, which is released as the transformation starts, helps to progress the transformation.

[1]Note that the strain that remains after unloading is recoverable by heating.

3.2 Apparatus and Experimental Setup

Unlike most experiments reported in the literature, in our experiments the wire was heated by passing an electrical current through it. No cooling system was used, and hence the lowest temperature that could be achieved was 19°C.

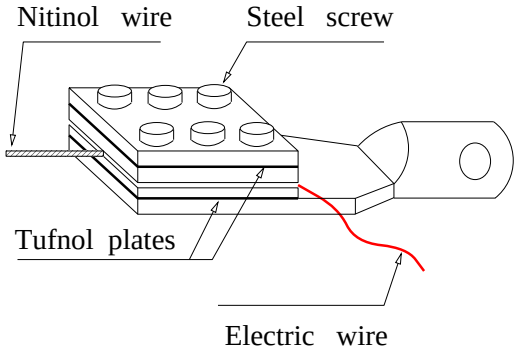

Figure 3.2: Clamp.

A Hounsfield Tensometer and an Instron 4483 testing machine were used for different tests. The Tensometer has a 1.2 kN loading beam, strain-gauged in the middle to accurately measure the force applied to the specimen. The specimen was loaded/unloaded by turning the handle of the Tensometer manually. The Instron has a 1.0 kN load cell, and can load/unload the specimen at a constant strain rate by moving one end at a constant speed.

In both cases, the Nitinol wire was gripped by two specially made steel clamps, as shown in Fig. 3.2. Note that the wire is clamped between two steel plates which are electrically and thermally insulated from the rest of the clamp by Tufnol plates. The strain in the wire was measured with a purpose-made, 32 mm long clip gauge. A small thermocouple was used to monitor the temperature in the wire.

The electrical resistance of a short length of Nitinol wire is quite low, and hence the specimen was connected through a rheostat to a small 9 V rechargeable battery. The voltage between the two ends of the wire was measured by a voltmeter. The current in the wire is directly measured by an ampere-meter. The resistance of the wire can be calculated from these measurement.

Figure 3.3 shows the layout of the experimental setup.

All measurements from tests with the Tensometer were taken by an analogue/digital conversion board connected to a personal computer, and were processed on-line using the package **Labview** from National Instruments. Thus, the experiment was monitored by displaying on the screen of the computer the stress vs. strain relationship, and the temperature vs. strain relationship in real time.

In the case of tests carried out with the Instron, all measurements were taken with a SI 3531D Data Acquisition System which displays the current readings and stores them on a disk.

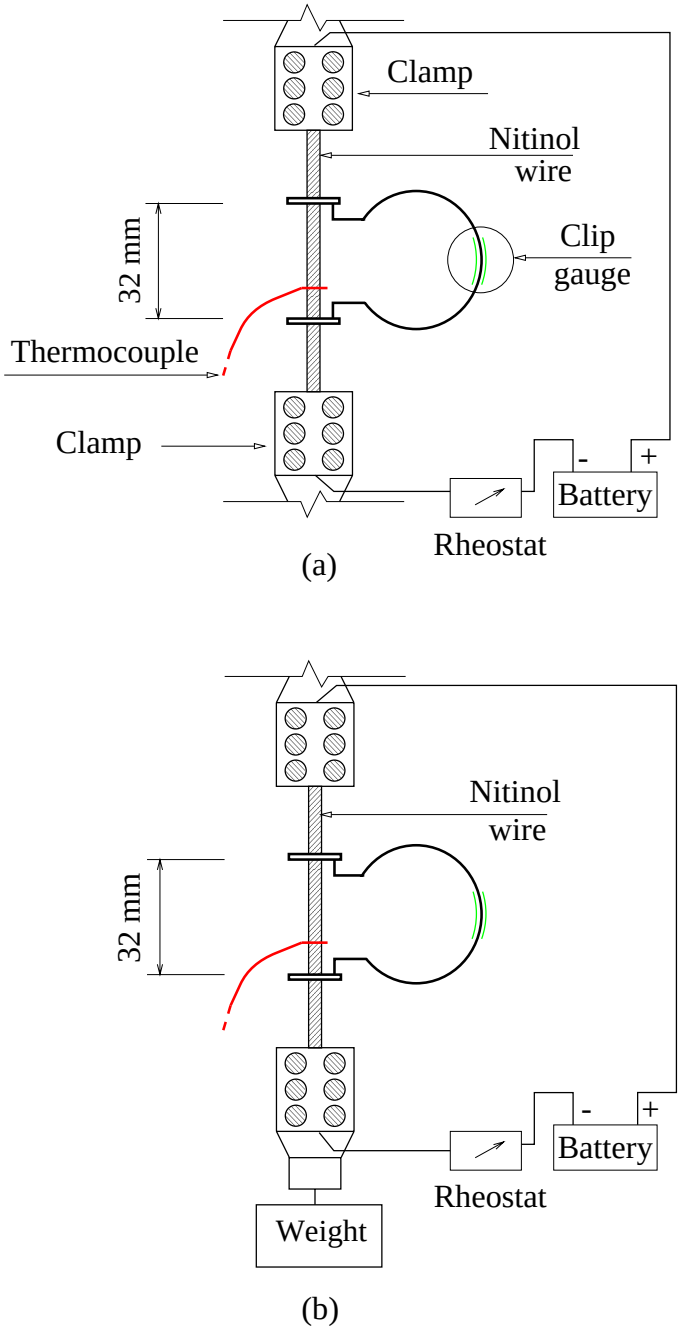

Figure 3.3: Layout of experiments. (a) Tension test and thermal cycling test (constant length); (b) thermal cycling test (constant load).

3.3 Tension Tests at Constant Temperature

1 mm diameter Nitinol wires were tested, using the Tensometer. Before each test, the wires were heated to over 180°C under zero stress, and then let cool to the required temperature. The full length of the specimen, i.e. the distance between two clamps was 101 mm.

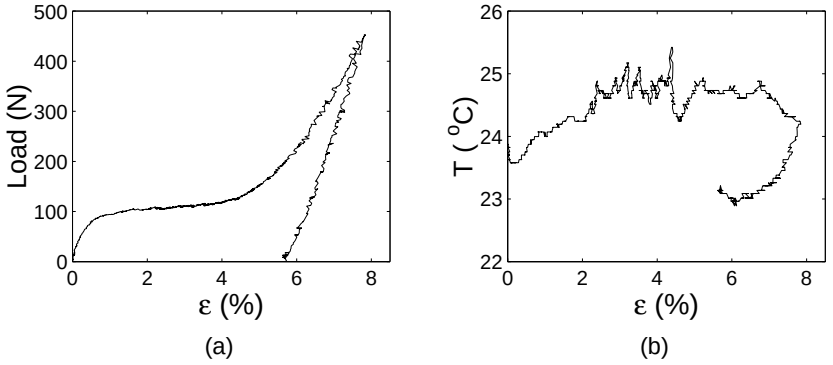

Figure 3.4: An attempt to keep the temperature constant during a tension test.

Temperature control in a test with a Tensometer is not an easy matter because the phase transformations are either exothermic or endothermic, which affects the temperature in the wire. Thus, the loading rate and the voltage between the ends of the wire had to be manually adjusted in order to maintain the temperature of the specimen reasonably constant. After some practice, it was found that it is possible to keep the temperature at the measuring point[2] within $\pm\ 2^o$C. Figure 3.4 shows an example where load was applied over 30 minutes.

Figures 3.5 and 3.6 show the stress vs. strain relationships measured from specimen 1 and 2, corresponding to sample 1 and 2 in Section 3.1, respectively, at different temperatures. These results have been re-plotted in Figs. 3.7 and 3.8 for ease of comparison. Note that the measured behaviour follows the general trends discussed in Section 2.2.1, but the details vary between the two specimens. Specimen2, which was left on a hot block after heat treatment, shows a much larger linear range at the beginning of the test.

From these results, it seems reasonable to divide the σ vs. ϵ relation of Nitinol in transformation range into two regimes. The first regime is dependent upon temperature: the higher the temperature, the higher the stress at the same strain. Beyond a certain point, which varies with the temperature, all the curves join together and the behaviour becomes temperature independent.

Most previous work has focussed mainly on the first regime, because the end of this regime is usually considered to mark the end of all transformations, beyond which there is a purely elastic range (e.g. Liang 1990). But it is clear from Figs. 3.5 and 3.6 that the unloading curve from a point which is within

[2]The temperature along the wire is in fact not uniform. More details are given in Appendix B.

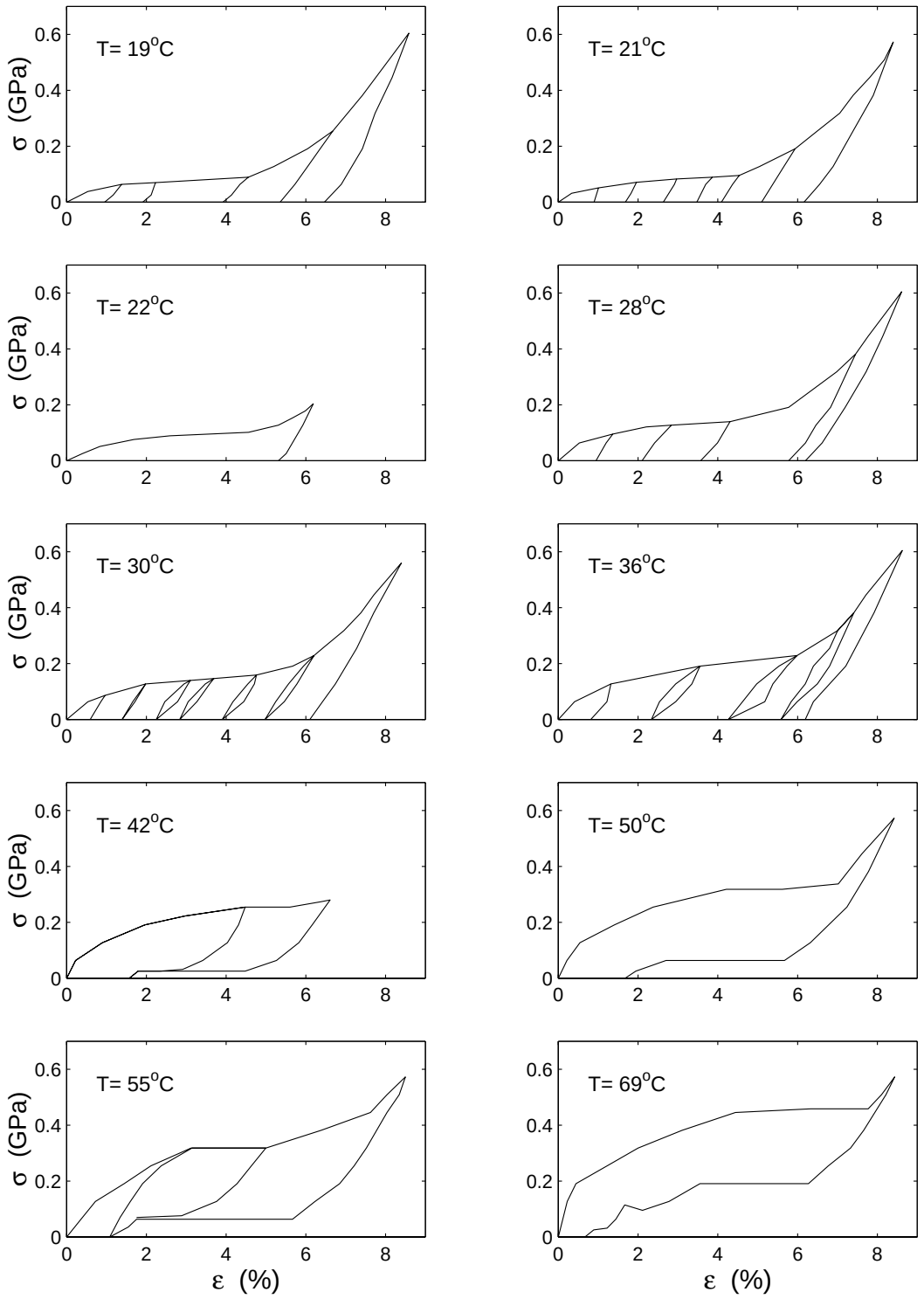

Figure 3.5: σ vs. ϵ relations for specimen 1 ($d = 1$ mm).

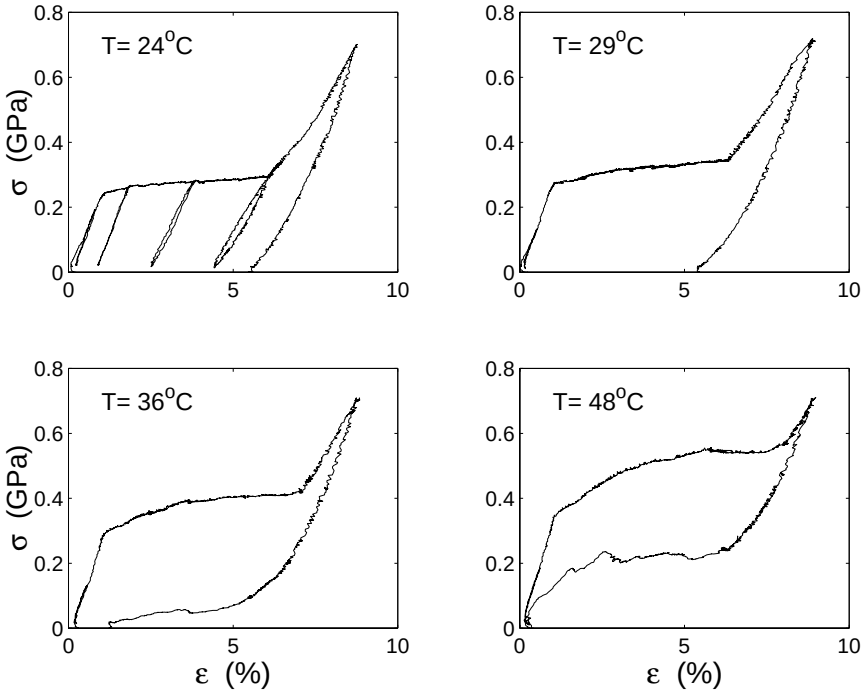

Figure 3.6: σ vs. ϵ relations for specimen 2 ($d = 1$ mm).

the second regime does not coincide with the loading curve. This shows that the transformations still continuing although at a much smaller rate than in the first regime[3]. This behaviour may be explained as follow:

- The first regime involves the transformation $R/A \Rightarrow M$. This is confirmed by Fig. 3.4: the temperature increases during loading, which indicates an exothermic transformation. In fact, if we stop loading by stopping turning the handle of the Tensometer at any point within this regime, the temperature as well as the measured force go down.

- The second regime corresponds mainly to the martensite reorientation, which is practically isothermal and hence the wire starts cooling towards room temperature. If we stop loading at any point within this regime, the measured force does not drop.

Figure 3.4 shows that during unloading the temperature decreases quite quickly, and even goes below the ambient temperature, which indicates an endothermic process, i.e. the transformation $M \Rightarrow A/R$.

Figure 3.9 shows the σ vs. ϵ behaviour in a series of loading/ unloading tests of gradually increasing amplitude.

[3]Recall that in our experiments all deformations are recoverable by heating after unloading.

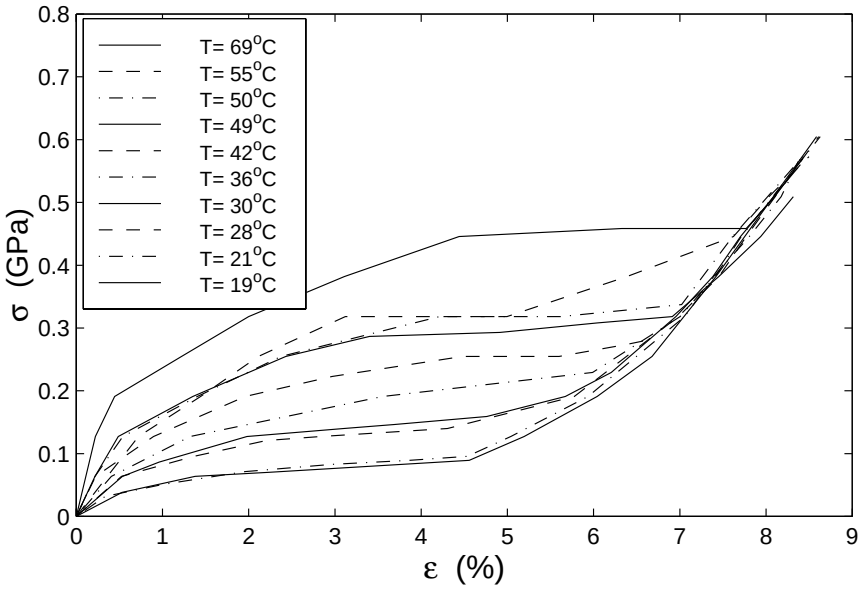

Figure 3.7: σ vs. ϵ relations for specimen 1 ($d = 1$ mm, Fig. 3.1(a)).

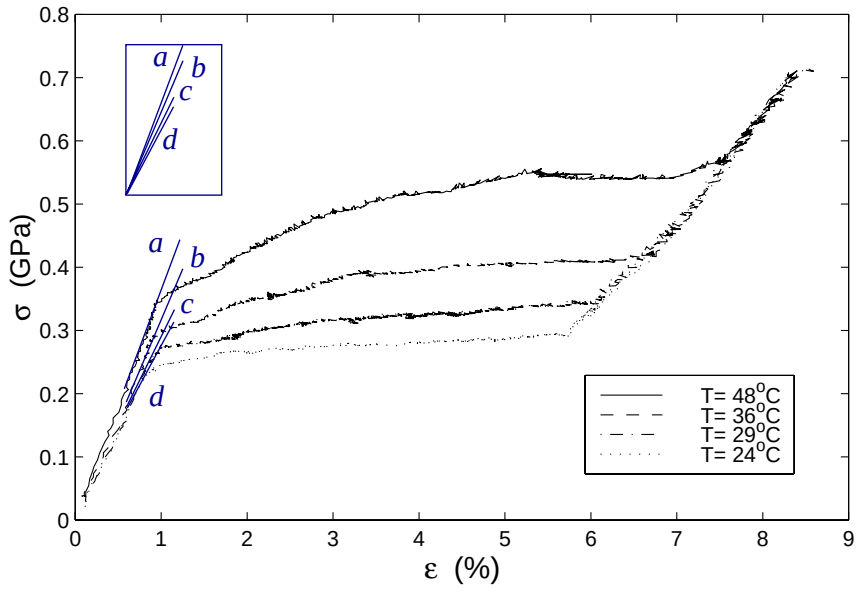

Figure 3.8: σ vs. ϵ relations for specimen 2 ($d = 1$ mm, Fig. 3.2(a)).

Following Section 2.2.2, the Young's Modulus, D, has been measured (averaged over the length of the clip gauge) at the beginning of the unloading path. Figure 3.8 shows that D increases, as the temperature and hence ξ^A, are increased at the start of the test. At 24°C, where $\xi^A \approx 0$ and $\xi^R \approx 1$ refer to Fig. 3.1(b), $D \approx 28$ GPa; whereas at 48°C, $\xi^A \approx 0.9$ and $\xi^R \approx 0.1$, and $D \approx 40$ GPa.

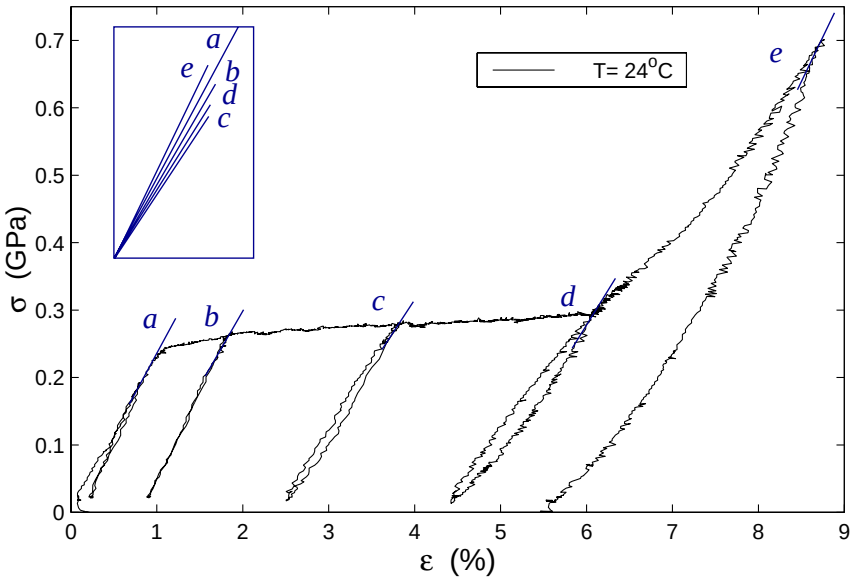

Figure 3.9: Loading/unloading test on specimen 2 ($d = 1$ mm).

In Fig. 3.9, D is no longer monotonic but decreases first and then increases during loading. As ξ^M increases from nearly zero[4], D first decreases from 28 GPa at point a ($\xi^R \approx 1$) to 22.5 GPa at point c. From point c to point e, D increases back to 30 GPa as the martensite aligns itself with the direction of the stress.

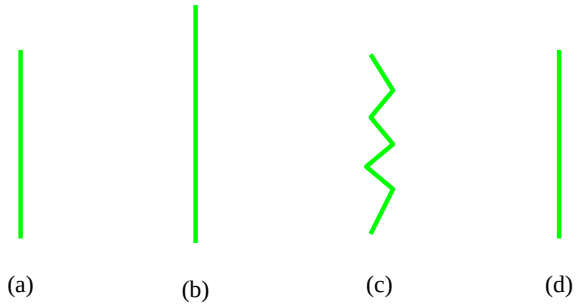

Figure 3.10: Zigzag intermediate shape in free recovery. (a) Initial shape; (b) after stretching; (c) zigzag; (d) final shape.

[4]It may not be exactly zero, since some stress induced martensite may be generated even in the "*elastic*" loading range, which causes slightly nonlinear behaviour.

It was observed that sometimes if a very high electrical current was passed through a stretched wire under zero load for a very short period, it showed a zigzag like intermediate shape before returned back to its initial straight shape after further heating (Fig. 3.10). This zigzag is quite likely the result of non-uniformity of phase transformation.

3.4 Tension Tests under Constant Strain Rate Effects

All tests reported in this section were done with the Instron, on a 0.5 mm diameter wire and a 1 mm diameter wire, similar to specimen 2 of Section 3.1.

Note, our tests are carried out in air. However, surrounding air condition is not still, since a fan, which is very close to the Instron machine, is in operation all the time.

3.4.1 0.5 mm Wire at $\dot{\epsilon} = 3.72 \times 10^{-5}$/s

The wire length between clamps was 112 mm. Two thermocouples were used to measure the temperature of the wire at two different positions within the clip gauge length, i.e. one is half-way between two attachment points, and another is 3 mm away from one attachment. Similar to those tests mentioned in Section 3.3, it showed that the temperature difference between the two thermocouples can be as much as 6^oC in a high temperature test, and the maximum temperature variation at a particular thermocouple location can be kept within $\pm\ 2^oC$ during a complete test. Figure 3.11, where the temperatures plotted are average values, shows that a two-regime transformation behaviour, similar to that described in Section 3.3, is observed.

3.4.2 1 mm wire at different $\dot{\epsilon}$

The length between two clamps was 64 mm, and tests were carried out at room temperature, i.e. no electrical current was used to heat the specimen. Unlike previous tests, the strain was estimated by means of measuring the displacement between the two clamps. Therefore, the measurement reflects the average behaviour of the whole length of wire between the two clamps instead of the "*local*" behaviour of the length between the attachments of the clip gauge. Three thermocouples were located at three different points, i.e. the top point (4.5 mm away from top clamp), the middle point (35 mm away from top clamp), and the bottom point of the specimen (3.0 mm away from bottom clamp). After the tests, it was observed that the behaviour of this specimen is similar, although not identical, to specimen 2 of Section 3.3.

In these tests the specimen was loaded to 350 N ($\approx$ 0.45 GPa) and then unloaded at four different strain rates, i.e. $\dot{\epsilon}$= 1.30×10^{-3}/s, 2.60×10^{-4}/s, 1.30×10^{-4}

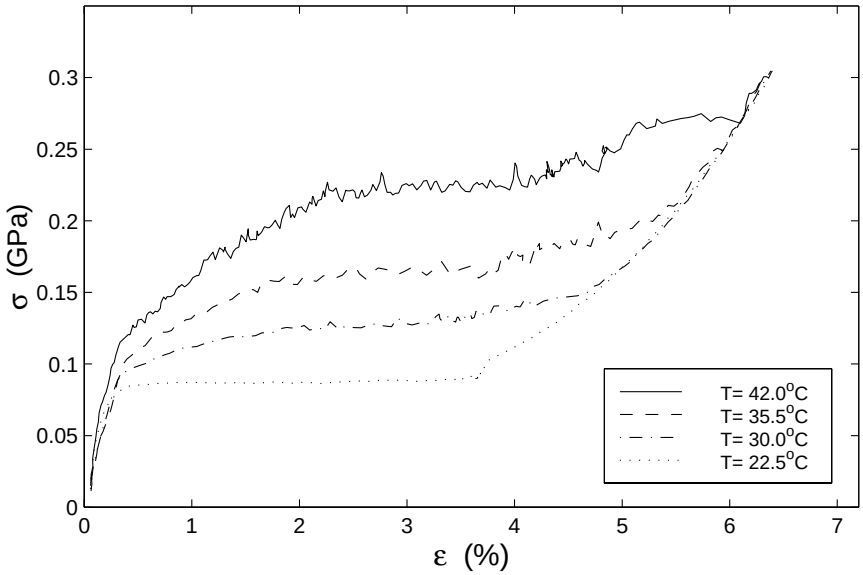

Figure 3.11: σ vs. ϵ relation for Nitinol wire with $d = 0.5$ mm Nitinol (loading only).

/s, and 2.60×10^{-5}/s[5].

The temperature vs. time (t) relations measured from these tests are plotted in Fig. 3.12, and σ vs. ϵ relations are plotted in Fig. 3.13.

- Figure 3.12 shows that at the highest $\dot{\epsilon}$ (1.30×10^{-3}/s), the temperature increases simultaneously at all three points, while at lowest $\dot{\epsilon}$ (2.60×10^{-5}/s), temperature peaks pass through one point after another.

- Although there are some differences between different $\dot{\epsilon}$, all T vs. t relations are quite similar. The top point shows a temperature peak first, followed by the middle point and finally by the bottom point. This suggests a kind of phase transformation front movement behaviour, since these temperature increases are due to the latent heat associated with the phase transformations. Therefore, temperature peaks mark the position of the transformation front, if there is only one such front in the specimen. However, as we will explain later, more than one temperature peaks may be observed in some cross sections, if there are more than two phase transformation fronts.

- Although the reverse transformation during unloading is quite small, note that in Fig. 3.13, the temperature drops below ambient temperature at the end of the test, which shows that the reverse transformation is endothermal.

- In Fig. 3.12 there are two temperature peaks for the top and middle point measurements, but there is only one peak in the bottom point measure-

[5]These strain rates correspond to the following speeds of the movement of the head of the Instron: 5.0 mm/min, 1.0 mm/min, 0.5 mm/min, and 0.1 mm/min, respectively.

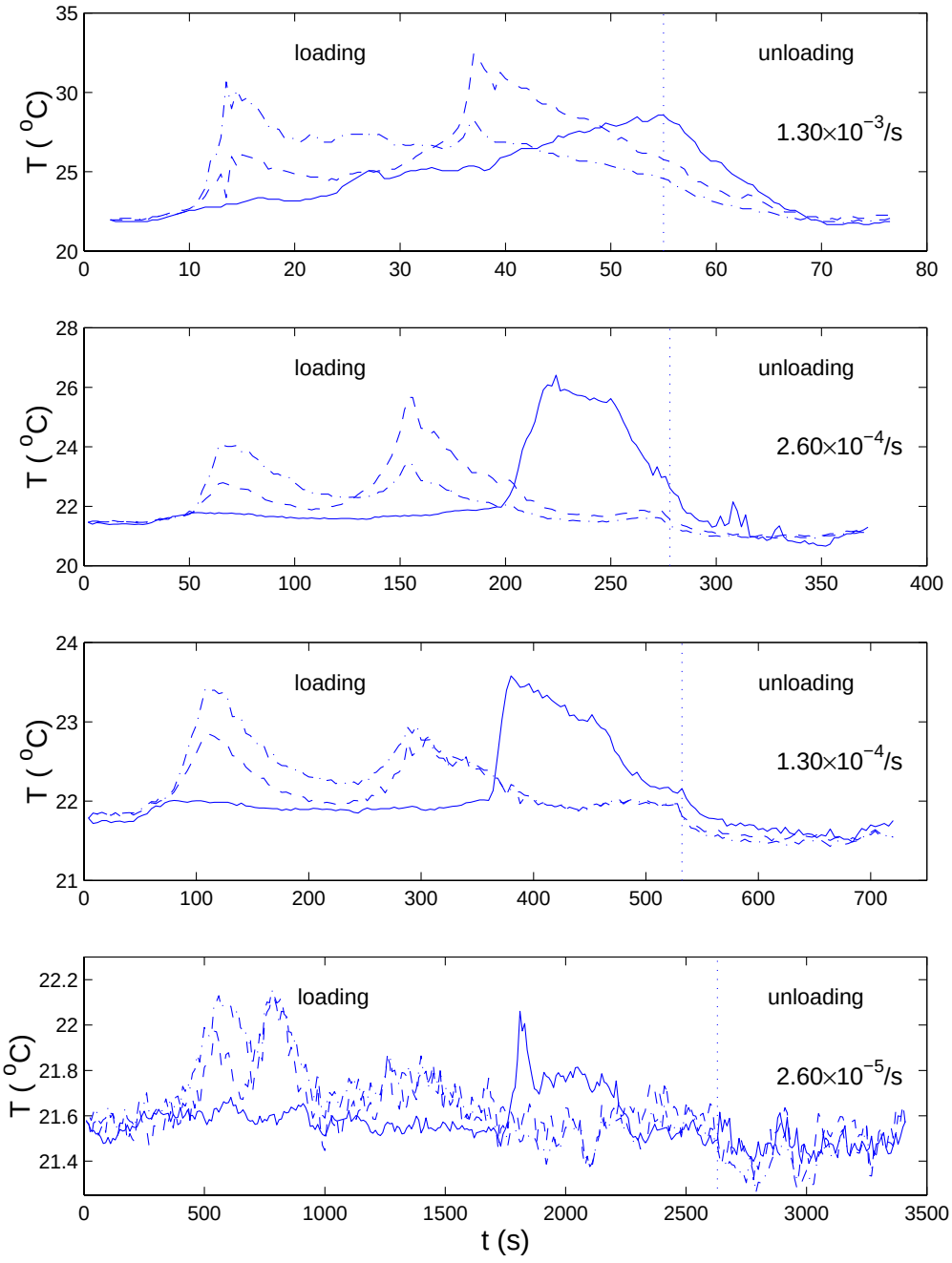

Figure 3.12: T vs. t relations for different $\dot{\epsilon}$ and at different points of the specimen (-·- top thermocouple; - - middle thermocouple; — bottom thermocouple).

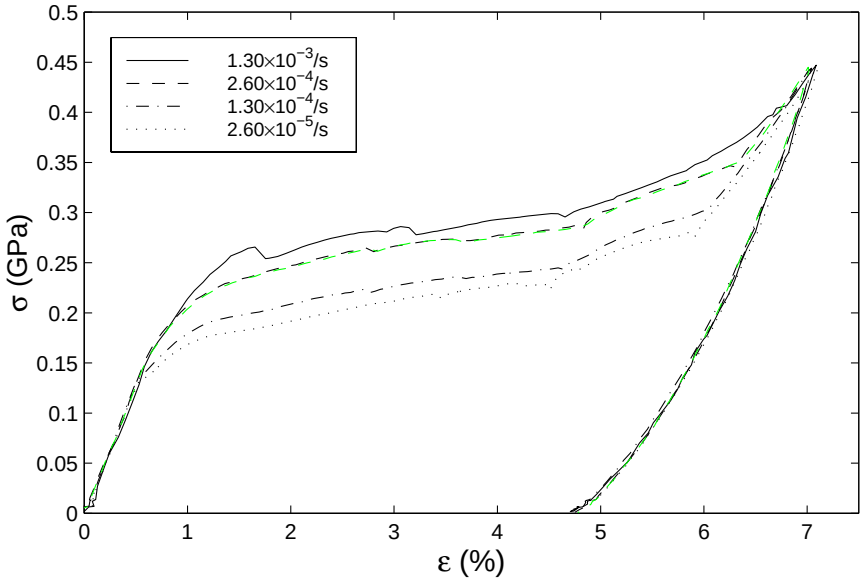

Figure 3.13: σ vs. ϵ relations at different $\dot{\epsilon}$.

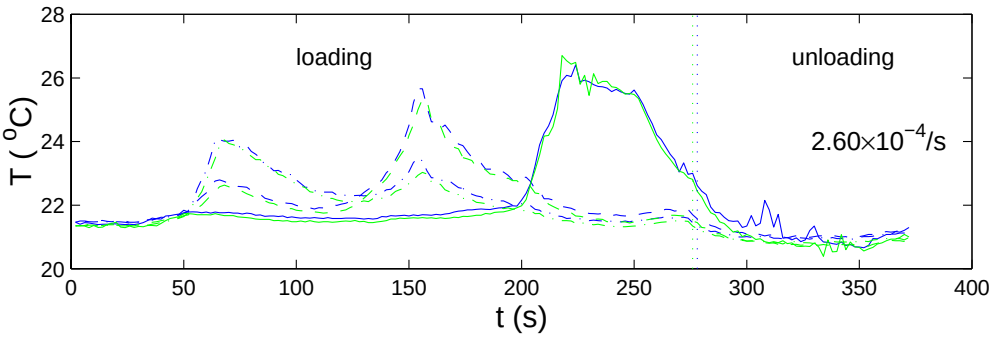

Figure 3.14: T vs. t relations at $\dot{\epsilon}$= 2.60×10^{-4}/s, and at different points of the specimen (-·- top thermocouple; - - middle thermocouple; — bottom thermocouple).

ment. The plots of the temperature distribution, shown in Fig. 3.15, means that the first peak at the top point may be caused by the passage of a transformation front. However, the second one may be caused by heat conducted from a lower point of the specimen when two phase transformation fronts merge together, causing a large temperature increase. A similar effect may explain the middle point measurement. However, this time the first peak may be due to heat conduction, while the second one may be caused by the passage of a phase transformation front. At the bottom point a transformation front is the only cause for a temperature peak.

- In the "*elastic*" loading range and during unloading, the σ vs. ϵ relations are almost the same in all tests. However, in the phase transformation range, the higher the $\dot{\epsilon}$, the higher the σ required to achieve the same strain level.

- The σ vs. ϵ relations in Fig. 3.13 show a kind of hardening behaviour during the whole loading process. This behaviour is different from that described by Leo *et al.* (1993) and Shaw and Kyriakides (1995), who found a plateau in the first transformation regime.

- Figure 3.13 shows small peaks and troughs in σ vs. ϵ relations. Further study, see also Fig. 3.15, suggests a link between these jumps and the start of a new phase transformation point. Hence, we may regard these jumps as the result of the "*super-cooling*" effect mentioned in Section 2.1.1. This effect is similar to the fluctuations associated with Lüders band behaviour (Hall 1970).

- As already reported by Shield (1995) for single crystals of CuAlNi, at the very beginning of the loading process some phase transformation occurs. The temperature increases in Fig. 3.12 and the nonlinearity of the σ vs. ϵ relation, Fig. 3.13, show that a small degree of phase transformation has already started.

- In both 1.30×10^{-3}/s and 2.60×10^{-4}/s cases, tests were carried out twice. Figure 3.14 shows that the T vs. t relations at strain rate of 2.60×10^{-4}/s in the two tests are almost identical. Very similar σ vs. ϵ relations can be found in Fig. 3.13. These similar plots suggest that every details of the transformation front movement behaviour is repeatable.

In order to get a further understanding of the phase transformation front movement behaviour, it is necessary to monitor the temperature distribution along the whole length of the wire in "*real time*" during loading. An experiment of this type was done by Shaw and Kyriakides (1997) with a thermal imaging camera. A simply way of carrying out this test is to stick a strip of temperature-sensitive liquid crystal film[6] to the wire. This film changes colour from initial dark brawn (at room temperature)→ orange → yellow → light blue → blue → dark

[6]Thermochromic Liquid Crystal Film, supplied by Merk Ltd., England.

blue as the temperature increases. Figure 3.15 shows sequences of photographs taken at three different $\dot{\epsilon}$.

The main features of each test are summarised as follows,

1. In the test of high $\dot{\epsilon}$, Fig. 3.15(a), the first blue colour area appears at the point near the top clamp. It gradually moves down as it becomes wider and longer.

   The second blue area (not shown in the photographs) starts at a position about 1/3 of the specimen length away from top clamp. It grows and moves along the specimen both up and down, and finally merges with the first zone. The resulting coloured strip extends further down with its top end gradually shrinking and changing colour to orange (indicating a temperature decrease).

   A third coloured area (mainly dominated by orange but with blue at the top end) starts near the bottom clamp. Then it extends upwards and becomes wider. Finally, all coloured areas join together covering almost the whole length of the specimen.

2. In the second test, at lower $\dot{\epsilon}$, Fig. 3.15(b), shows almost the same pattern of evolution of coloured zones, but the temperatures reached are a little lower, and hence the main colours are light blue with a significant orange skirt around it. Also, the motion of the coloured zones is much slower.

3. At the lowest $\dot{\epsilon}$, Fig. 3.15(c), the first coloured area, which is much smaller than that in the previous tests, appears at the point near the top clamp. Its full size is also much smaller (shorter and narrower). This coloured area moves downwards at a very slow speed.

   The next coloured area starts at the point near the bottom clamp. It moves upwards, meets and then merges with the first area which has travelled through almost 3/4 of the wire length from top.

   In this test, all coloured areas are dominated by orange with very little light blue in the middle.

Figure 3.15 shows that the temperature distribution along the wire is by no means uniform. The first coloured zone, which roughly indicates the temperature increase caused by the first phase transformation start point, is near the top clamp. The last new coloured zone starts at the point near the bottom clamp.

The reason why at low $\dot{\epsilon}$ there are only two coloured zones is that the sensitivity of the crystal film is less than 1^{o}C. As a matter of fact, if $\dot{\epsilon}$ is as low as 2.60×10^{-5}/s, almost no colour changes can be observed on the crystal film.

Other tests that were carried out on other specimens (cut from the same batch, and prepared in the same way) confirm the tendency for the phase transformation to begin near the clamps. This is linked to the stress localisation that occurs there. In a test on a much longer specimen (160 mm) the phase transformation started,

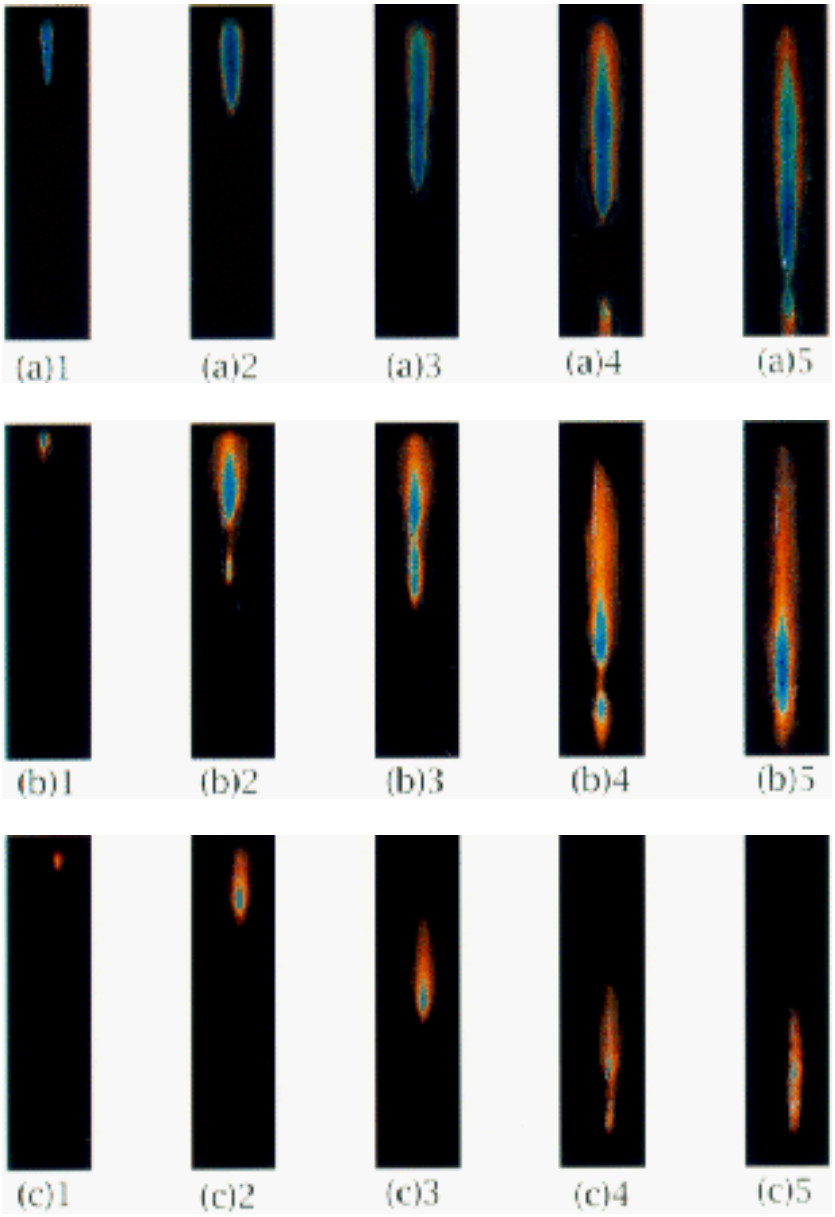

Figure 3.15: Phase transformation front movement at different strain rate. Photographs were taken at the moment when an important feature occured. (a) $\dot{\epsilon}$= 1.30×10^{-3}/s; (b) $\dot{\epsilon}$= 2.60×10^{-4}/s; (c) $\dot{\epsilon}$= 1.30×10^{-4}/s.

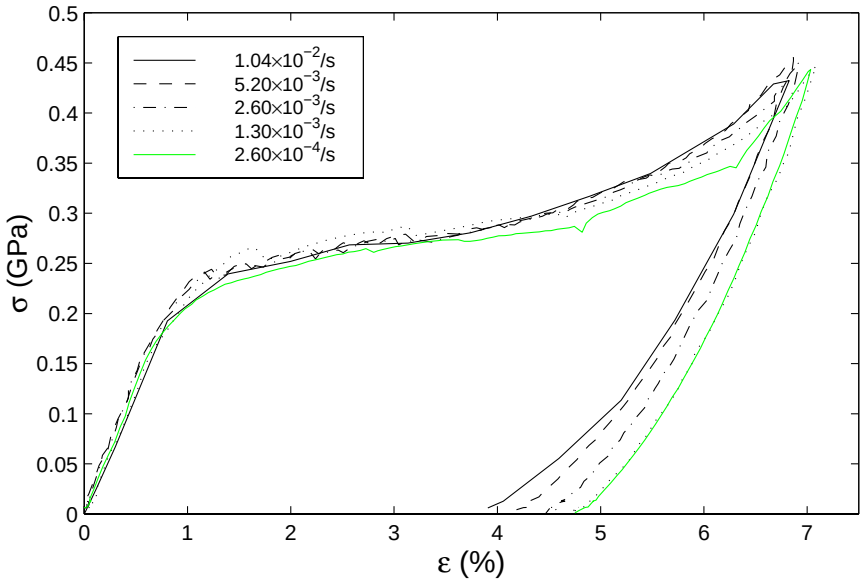

Figure 3.16: σ vs. ϵ relations at higher $\dot{\epsilon}$.

almost simultaneously, at several different points after the first front near the clamp.

Further tests were carried out at higher strain rate, and the results are shown in Figs. 3.16 and 3.17 for $\dot{\epsilon}$= 2.60 $\times$ 10^{-3}/s (10 mm/min), 5.20 $\times$ 10^{-3}/s (20 mm/min), and 1.04 $\times$ 10^{-2}/s (40 mm/min). Figure 3.16 shows also the results from two previous tests, $\dot{\epsilon}$= 2.60 $\times$ 10^{-4}/s and 1.30 $\times$ 10^{-3}/s.

A very interesting feature in these new tests is that, although the temperature reached continues to increase with $\dot{\epsilon}$, the kind of hardening behaviour described before is not confirmed in Fig. 3.16. In Fig. 3.16 all the new experimental curves fall between these described at lower $\dot{\epsilon}$. As to the unloading path of these plots, at higher $\dot{\epsilon}$, the residual strain is smaller.

The second observation can be explained in terms of the high temperature increase causing less phase transformation in the specimen. The extent of the phase transformation that occurs becomes smaller as the temperature increases, see Fig. 3.7, for a given stress level. However, we still cannot explain the behaviour drawn in first half of phase transformation, since the temperature does increase dramatically with $\dot{\epsilon}$.

Anyway, the higher $\dot{\epsilon}$, the smaller residual strain can be explained as the result of higher temperature due to higher strain rate. In loading, the higher the temperature, the less the transformation; in unloading, the higher the temperature, the more the transformation recovery.

Note that the temperature variation of the three measured points, Fig. 3.17, is similar to that described at lower $\dot{\epsilon}$, Fig. 3.12, but the peak variation gradually becomes less and less apparent as $\dot{\epsilon}$ increases.

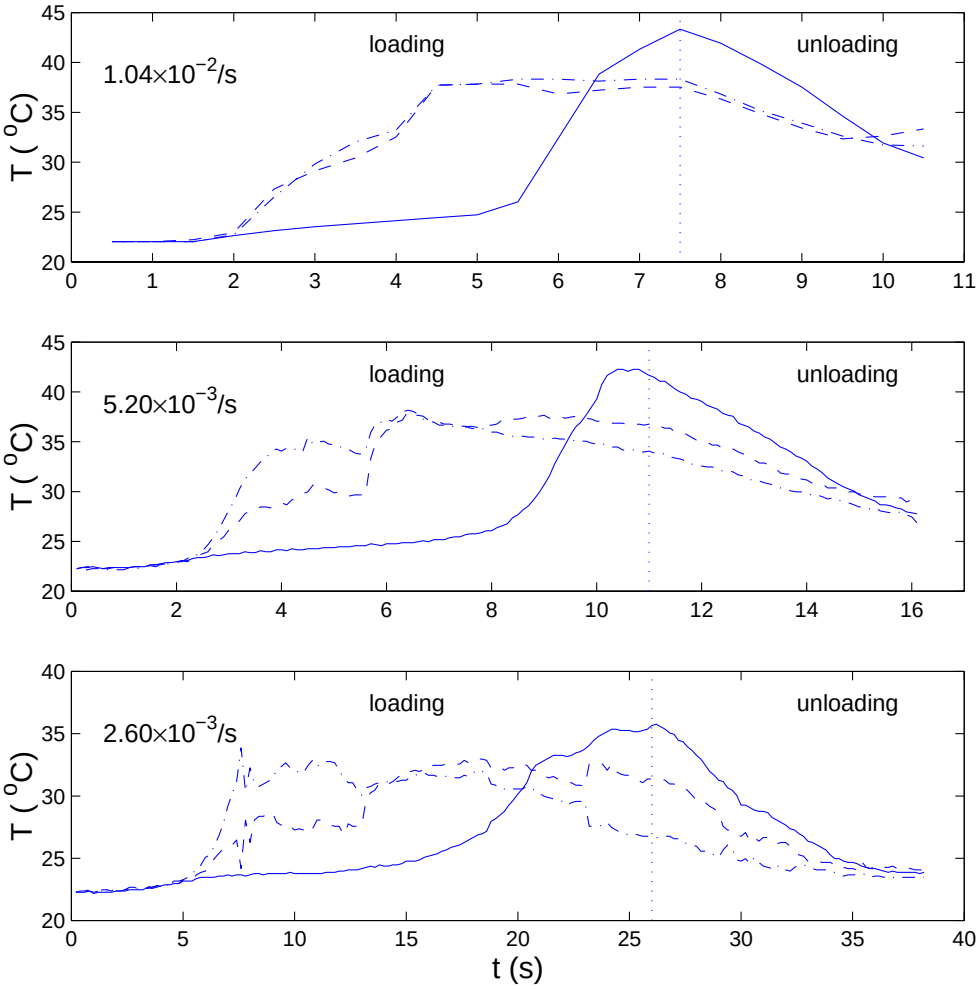

Figure 3.17: T vs. t relations at different $\dot{\epsilon}$ tests (at top point: dash/dot line; at middle point: dash line; and at bottom point: solid line).

3.5 Response to Suddenly Applied Loads

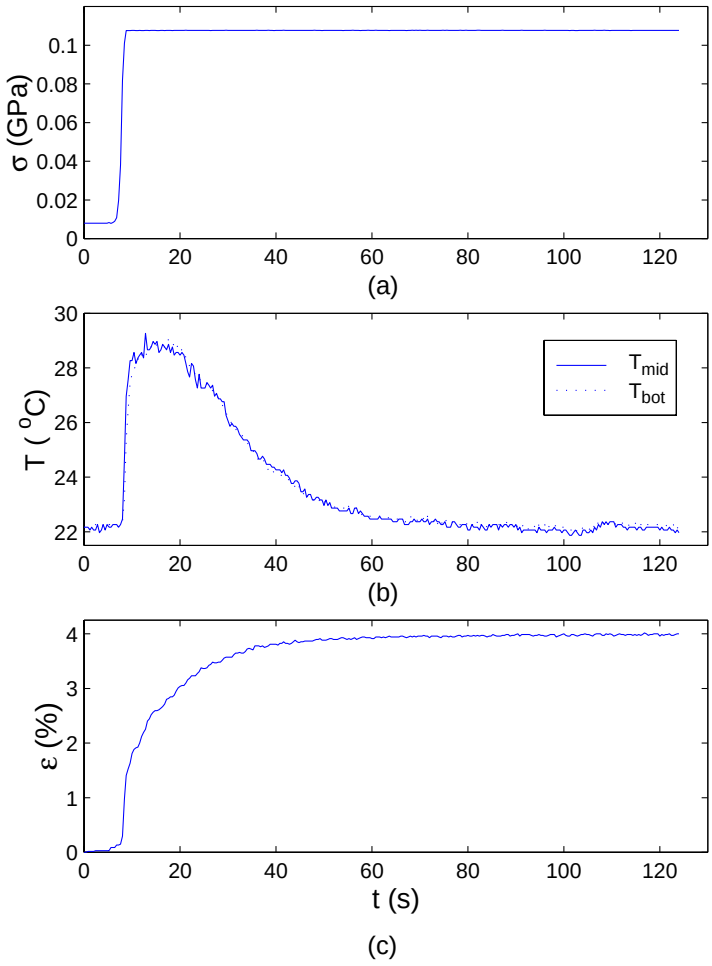

Figure 3.18: Suddenly-applied load tests ($d = 0.5$ mm), constant load is 21.1 N (≈ 0.11 GPa).

The aim of this test is to find the relationship between applied stress and the time when a wire reaches its "*full*" extension. Due to the heat generated during stretching, it usually takes some time to obtain its final extension. The engineering background of this study is that Nitinol wire is normally pre-stretched before installed into its operational position.

Figure 3.18 shows the response of a 112 mm long, 0.5 mm diameter wire which was suddenly subject to an applied stress of 0.11 GPa. This stress was supplied by releasing a dead weight without inducing any dynamic oscillation. The strain in the wire was measured with a clip gauge, as explained in Section 3.2, and the temperature measured at two different points.

Figure 3.18 also shows that the temperature increases instantaneously after the load is applied, but it takes a minute for the strain to reach its final value.

The maximum strain is reached after the temperature cools down to the ambient value, at which point the applied stress of 0.11 GPa is well into the martensite re-orientation regime, Fig. 3.11.

Note that by applying the stress of 0.11 GPa suddenly, we have achieved a strain of nearly 4%, which is more than should be obtained in an ordinary tension test (about 3.75%, see Fig. 3.11). The exact reason for this phenomenon is unclear, but it may be linked to some kind of time-related thermo-mechanism of stabilisation in phase transformation and martensite re-orientation.

We will not aim to model this effect, as we will study only the behaviour of SMAs in quasi-static situations.

In another test, in which the applied stress is 0.08 GPa, it takes more than six minutes to reach its final strain. The reason for this is that the applied stress of 0.08 GPa is just above the transformation start stress, Fig. 3.11. Hence transformation undergoes in a much gradual manner.

3.6 Thermal Cycling at Constant Load

In these tests the Nitinol wire was thermally cycled under different constant loads, while measuring temperature and strain. In a first set of tests, the wire was heated to 180^{o}C, unstressed, and then let cool to the required temperature. Afterwards, a dead weight was hung from the bottom of the wire, as shown in Fig. 3.3(b), thus imposing an initial strain whose magnitude depends on the imposed stress. Then, the wire was heated and then let cool back to the original temperature. In a second set of tests, a larger initial stress was applied to the wire, to obtain a larger initial strain, but the stress level was reduced before starting the thermal cycle. Results from these tests are shown in Figs. 3.19-3.21.

Note that each thermal cycle describes an anti-clockwise path in these plots. The behaviour is essentially the same for all tests. As the temperature increases, the strain starts decreasing rather slowly but, when a critical temperature is reached, a substantial strain recovery occurs while the temperature remains approximately constant. Then, the temperature starts increasing again as further strain is recovered, but at a slower rate, until finally the strain remains approximately constant.

On cooling a similar curve is traced, but the critical temperature is lower than during the heating cycle. At the end of the cycle, the strain level either returns back to the initial value, if the pre-stress is equal to the current stress level, or is less than that at the start of the cycle if the current stress is lower. It can be observed that the critical temperature (where very huge strain recovery starts) increases as the applied stress is increased.

We may conclude that the thermal cycling loops are approximately all identical, but shift up and down depending on the stress level. The larger the stress, the higher the temperature needed for the strain recovery. We also notice that the effect of pre-stress affects the critical temperature, but it is not as significant as seen in the DSC test, Fig. 3.1(c).

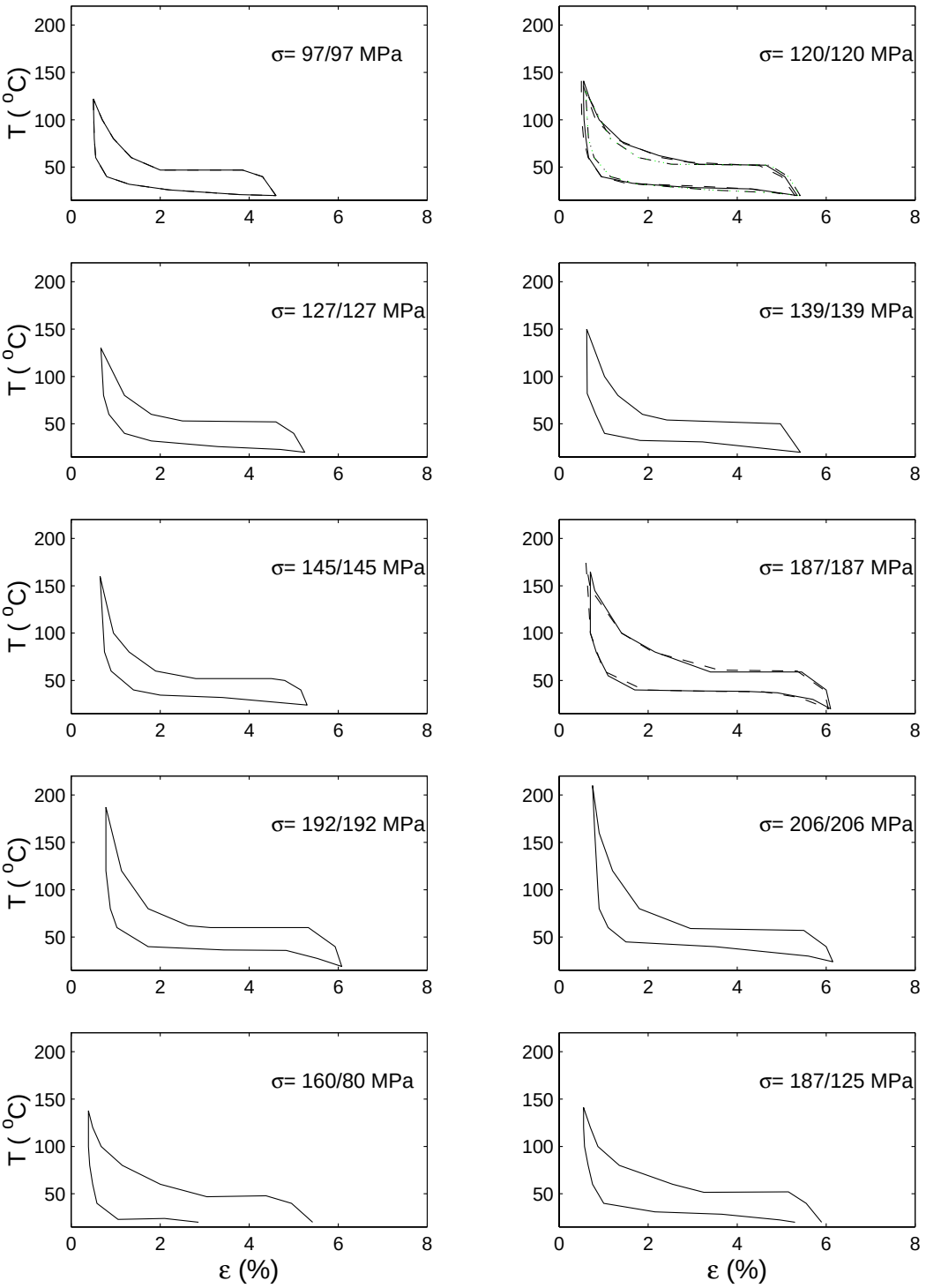

Figure 3.19: T vs. ϵ relations for specimen 1 ($d = 1$ mm). The two stress values in each legend are the initial pre-stress, and the stress applied during the thermal cycling, respectively.

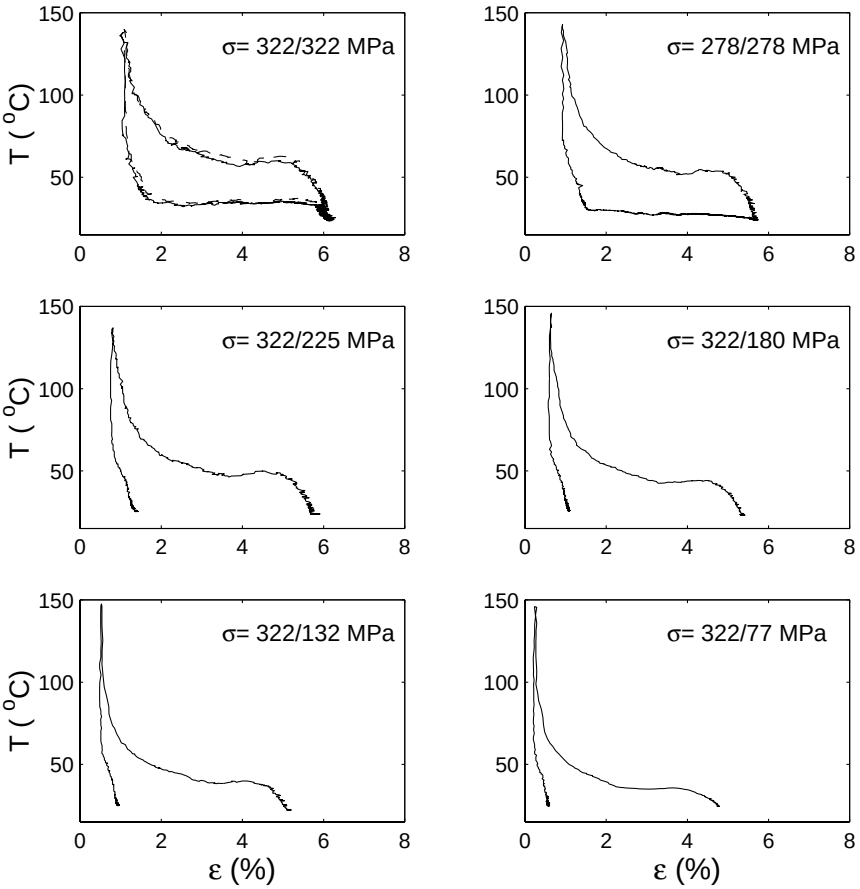

Figure 3.20: T vs. ϵ relations for specimen 2 ($d = 1$ mm). The two stress values in each legend are the initial pre-stress, and the stress applied during the thermal cycling, respectively.

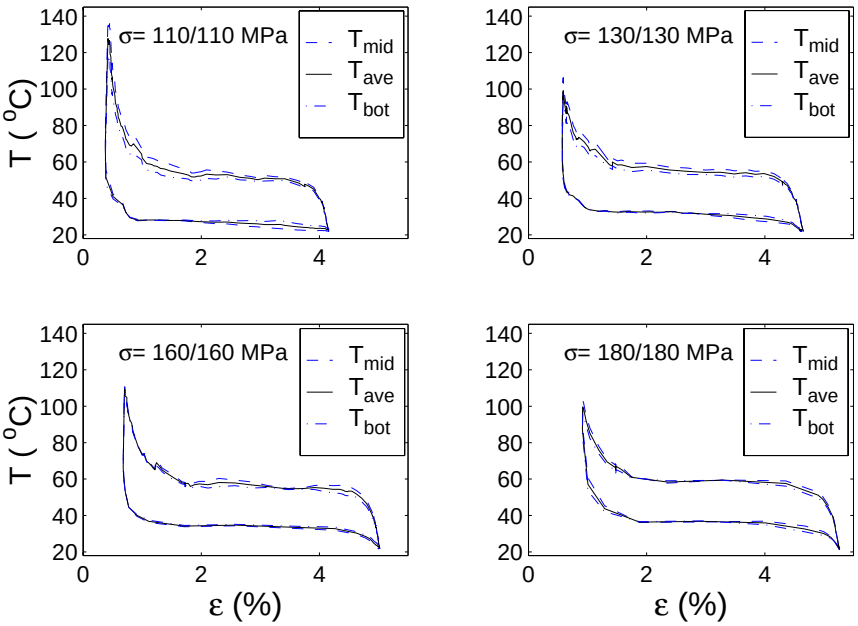

Figure 3.21: T vs. ϵ relations of 0.5 mm diameter wire. The two stress values in each legend are the initial pre-stress, and the stress applied during the thermal cycling, respectively.

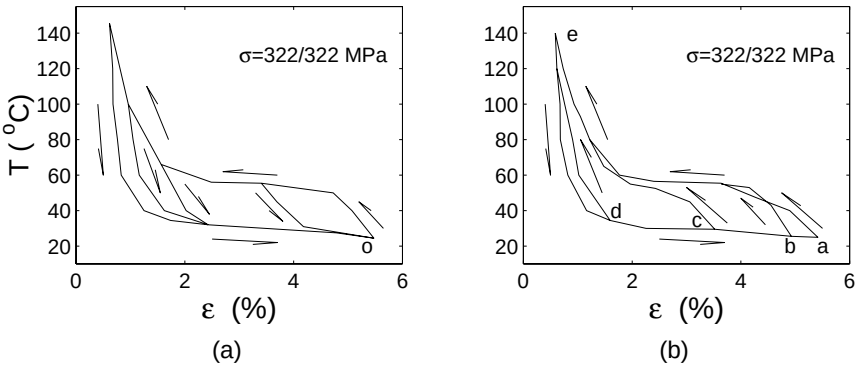

Figure 3.22: Partial thermal cycles on specimen 1 (d = 1 mm). The two stress values in each legend are the initial pre-stress, and the stress applied during the thermal cycling, respectively. (a) Heating from point o; (b) cooling from point e.

Two sets of "*incomplete*" or partial thermal cycles are shown in Fig. 3.22. In Fig. 3.22(a), each cycle started at point o, but cooling started at different temperatures. In Fig. 3.22(b), all cycles ended at same point e.

3.7 Thermal Cycling with Fixed Length

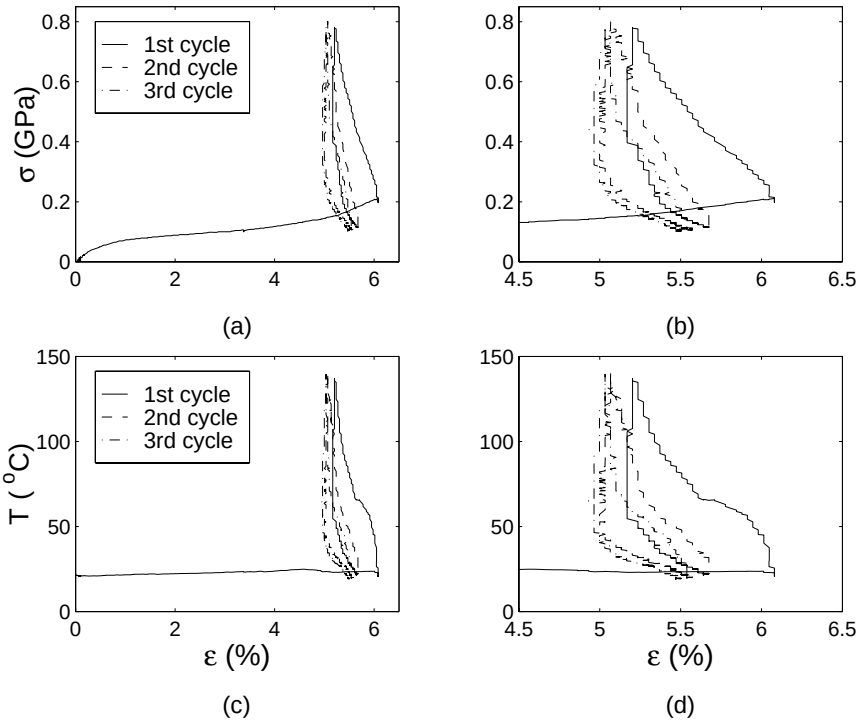

Figure 3.23: Behaviour of specimen 1 (d = 1mm) during thermal cycling with fixed length. (a) σ vs. ϵ relation; (b) detail of (a); (c) T vs. ϵ relation; (d) detail of (c).

To carry out these tests, the Tensometer was fitted with a stiff load beam, to minimise the elastic compliance of the testing machine. The maximum force in the wire during a thermal cycle goes up to 640 N and, because the stiffness of the Tensometer has been measured to be 7.5 kN/mm, the maximum deformation is 0.085 mm, which corresponds to a strain of 0.084% in the wire.

Extension of a 101 mm long wire was measured with the clip gauge described in Section 3.2 with the gauge length of 32 mm. The temperature was measured in the middle of the wire. Specimen 1 was loaded to about 157 N ($\approx$ 0.20 GPa) at about 24^{o}C and then held at a constant length as several thermal cycles were carried out.

Figure 3.23 shows the σ vs. ϵ and T vs. ϵ relationships that have been measured. The maximum stress goes up to about 0.8 GPa but, after the first

cycle, both the strain and stress are reduced. After subsequent cycles the strain and stress are further reduced, but by smaller amounts.

This is quite unexpected result, since we had thought that strain variation in the thermal cycle should be very small as a very stiff load beam was used in the Tensometer.

This is later explained as the result of the non-uniformity of the temperature distribution along the wire, see Appendix B.1 and, although the stress in the wire is constant, the phase distribution is not uniform.

In the middle of the wire the temperature is highest and therefore during heating the transformation DM $\Rightarrow$ A causes the wire to shorten in this region. This causes the stress to increase. In the meantime, the low temperature regions, near the clamps, undergo further detwinning, due to the stress increase, and hence the wire in these regions extends instead of shortening. A numerical simulation of this rather surprising behaviour is given in Section 4.4.

3.8 Discussion and Further Remarks

A series of tests on Nitinol wires have been reported in this chapter.

The first point to note is that since the wires are heated by passing a current through them, the temperature distribution along them is not uniform. As shown in Section 3.4, observed transformation front movement indicates the non-uniformity of phase along Nitinol wire. This is another cause of the non-uniformity of temperature distribution.

What has been measured in all tests is the deformation between two sections whose original distance is around 32 mm, and the temperature/temperatures at one, two or three points in the wire. As shown in Appendix B.1 and in our tests, Fig. 3.21, the temperature within the middle 32 mm region of a 64 mm long wire, in air, does not vary significantly.

However, when we carry out a constant length thermal cycle test, the non-uniformity of the temperature and the phase along the whole length of the wire between the clamps should be considered.

The second point is that our tension tests show two transformation regimes during loading. The first regime is temperature related: the higher the temperature, the higher the required stress to reach the same strain level. However, the second regime is temperature independent, and furthermore, all tests on the same specimen share almost the same σ vs. ϵ relationship regardless of the temperature.

The final point is that strain rate effects are quite complex. On the one hand, from low $\dot{\epsilon}$ to medium $\dot{\epsilon}$, they show that the higher the $\dot{\epsilon}$, the higher the temperature and the stress required to reach a given strain level. On the other hand, at high $\dot{\epsilon}$, the temperature still increases with $\dot{\epsilon}$, but the stress does not go up with it. The reason for this behaviour is unknown at present.

Chapter 4

Modelling the Behaviour of Nitinol

In this chapter we briefly review the main constitutive models for SMAs, and then present a phenomenological model suitable for the design of Nitinol-based structural actuators. This phenomenological model is then verified by comparing its predication to the experiments shown in Chapter 3.

Then , this model is used to simulate the behaviour of a Nitinol that is subject to thermal cycling with fixed length constraints, the effect of strain rate on stress-strain behaviour, and the phase transformation front phenomenon observed in Section 3.4.

4.1 Review of Constitutive Models

Many constitutive models have been developed to describe the thermomechanical behavior of SMAs. We can roughly summarise them into the following categories:

- Phenomenological models based on uniaxial stress-strain-temperature data (Tanaka 1985, 1986, Liang and Rogers 1990, Brinson 1993);
- A theory of non-equilibrium thermostatics that describes the thermodynamic paths of SMA (Cory and McNichol 1985);
- Models based on the interaction of the different sets of atoms in the alloy (Kafka 1994);
- Models derived from a special free energy formulation (Achenbach and Müller 1985, Leclercq and Lexcellent 1996);
- Models based on thermodynamic laws (Ortin and Planes 1991, Moumni and Nguyen 1996);
- Constitutive laws based on a model for hysteresis, *e.g.* Preisach model (Ortin 1992);

- Models based on nonlinear thermo-plasticity theory, generalised plasticity, or visco-plastic theory (Boyd and Lagoudas 1994, Lubliner and Auricchio 1996);
- Mathematical models for the dynamics of phase boundary motion (Abeyaratne and Knowles 1993, Bhattacharya and James 1996);
- Models derived from the deformation of crystal structure during phase transformation (Falk 1989, Fischer and Tanaka 1992);
- Constitutive laws that allows for micro-structural deformation during phase transformation and the free energy concept, using an energy dissipation or energy balance approach (Sun and Hwang 1993a, 1993b, Patoor *et al.* 1994, Huang and Brinson 1997).

Each of these models aims to describe the behaviour of SMAs from a certain aspect and on different scale. However, as stated by Humbeeck and Cederstrom (1994), "*... in spite of all these efforts and qualitatively very interesting results, no single model exists that is able to describe quantitatively the shape memory performance of a real material. The reason for this is related to the very strong influence of micro-structure and processing on the mechanical properties described in the (σ,ϵ, T)-space.*"

To fully understand the unique behaviour of SMAs from a theoretical point of view, we must start from the basics: the micro-structural changes that occurs during phase transformations. We will address these issues in Chapter 5.

On the other hand, from an engineering application point of view, the most practical and productive approach is based on phenomenological models, which fit the uniaxial experimental data, without attempting to capture the detailed underlying thermomechanical behaviour. Historically, the first such model was proposed by Tanaka (1985).

- **Tanaka's Model**

  Tanaka (1985) considered a one-dimensional element of SMA of length L, which is undergoing either the martensitic transformation or its reverse transformation. The general state variables are the strain ϵ, the temperature T and the martensite fraction ξ^M.

  The rate form of the thermomechanical constitutive equation is,

$$\dot{\sigma} = D\dot{\epsilon} + \Theta\dot{T} + \Omega\dot{\xi}^M \tag{4.1}$$

  where D is the Young's modulus, Θ the coefficient of thermal expansion, and Ω is a metallurgical quantity, known as the transformation coefficient.

  The martensite fraction is assumed to be an exponential function of stress and temperature, and hence is expressed as

$$\xi^{A\to M} = 1 - \exp[A_M(T - M_s^o) + B_M\sigma] \tag{4.2}$$
$$\xi^{M\to A} = \exp[A_A(T - A_s^o) + B_A\sigma] \tag{4.3}$$

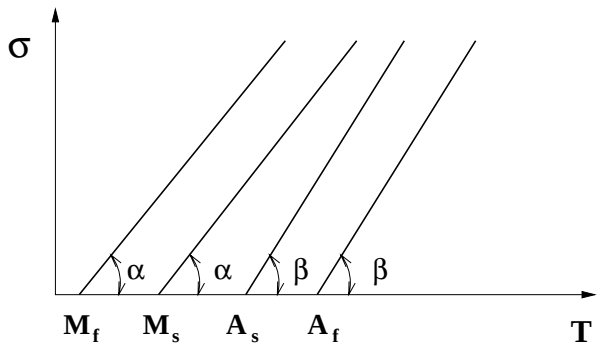

Figure 4.1: Transformation lines of SMAs.

Here A_A, A_M, B_A and B_M are material constants related to the transition temperatures A_s^o, A_f^o, M_s^o and M_f^o. The superscript "o" stands for zero stress condition.

As is usual in metallurgy, a transformation is regarded as complete when ξ^M or ξ^A are 0.99. Substituting this value and its corresponding temperature into Eqns. 4.2 and 4.3, the constants A_A and A_M can be expressed as

$$A_M = -2\ln 10/(M_s^o - M_f^o) \quad (4.4)$$

$$A_A = -2\ln 10/(A_f^o - A_s^o) \quad (4.5)$$

The constants B_A and B_M can be expressed as

$$B_A = \frac{A_A}{C_A} \quad (4.6)$$

$$B_M = \frac{A_M}{C_M} \quad (4.7)$$

where C_A and C_M represent the slopes defined in Fig. 4.1, i.e.

$$C_M = \tan\alpha$$

$$C_A = \tan\beta$$

Tanaka's model is simple and based on material parameters that can be measured easily. It has been used in a variety of studies (Tanaka *et al.* 1995).

- **Liang's Model**

  Liang (1990) assumed D, Θ and Ω to be constants. Hence Eqn. 4.1 can be integrated to give

$$\sigma - \sigma_o = D(\epsilon - \epsilon_o) + \Theta(T - T_o) + \Omega(\xi^M - \xi_o^M) \quad (4.8)$$

  where (σ_o, ϵ_o, T_o , ξ_o) represent the initial states of the material.

Liang assumed ξ^M to be a cosine function, and hence the transformation from austenite to martensite could be described by

$$\xi^{A\rightarrow M} = \frac{1-\xi_o}{2}\cos[a_M(T - M_f^o - \frac{\sigma}{C_M})] + \frac{1+\xi_o}{2} \tag{4.9}$$

where

$$C_M(T - M_s^o) < \sigma < C_M(T - M_f^o) \tag{4.10}$$

While the reverse transformation is described by

$$\xi^{M\rightarrow A} = \frac{\xi_o}{2}\cos[a_A(T - A_s^o - \frac{\sigma}{C_A})] + \frac{\xi_o}{2} \tag{4.11}$$

where

$$C_A(T - A_f^o) < \sigma < C_A(T - A_s^o) \tag{4.12}$$

where a_M and a_A are given by

$$a_M = \frac{\pi}{(M_s^o - M_f^o)} \tag{4.13}$$

$$a_A = \frac{\pi}{(A_f^o - A_s^o)} \tag{4.14}$$

and C_M and C_A are the same as in Tanaka's model.

- **Brinson's Model**

  Both models described above can be used only at temperatures higher than M_s, because they assume that there is no twinned martensite. In Brinson's model (Brinson 1993) the martensitic fraction ξ^M is divided into two parts

$$\xi^M = \xi^{TM} + \xi^{DM} \tag{4.15}$$

  where ξ^{TM} is fraction of twinned martensite, and ξ^{DM} is fraction of de-twinned martensite.

  Hence, Eqn. 4.1 is re-written as

$$\sigma = D\,\epsilon + \Theta\,T + \Omega_{DM}\,\xi^{DM} + \Omega_{TM}\,\xi^{TM} \tag{4.16}$$

  Another change in Brinson's model is that D and Ω are assumed to vary linearly with the martensite fraction, instead of being constant.

Both the exponential function assumed by Tanaka and the cosine function assumed by Liang do not describe the behaviour of SMAs accurately. This is not surprising, as these functions are not based on the material itself, i.e. they are not directly obtained from experiments. Since SMAs are very sensitive to composition, heat treatment, grain size, etc., it is reasonable to expect that ξ will vary with these parameters. In Brinson's model separate martensite fractions are used, but often one has to deal with cases where initially there is a mixture of twinned martensite and austenite, and hence the actual value of ξ is not known. In such cases, this model is hard to use.

Another problem in applying these models is that the transformation temperatures are often ambiguous, and sometimes not in the sequence $M_f < M_s < A_s < A_f$, which is implicitly assumed in the above models. For such materials the above expressions for ξ can hardly be applied.

Finally, Fig. 4.1 does not take any internal variables, such as the internal stress and initial phase condition, into consideration when setting up a relation between transformation temperature and applied stress. If no unloading occurs Fig. 4.1 may be roughly correct. However, if unloading ever occurs, which is quite likely in a real application, the assumed simple behaviour as shown in Fig. 4.1 may be unrealistic.

4.2 Phenomenological Model

Previous attempts to improve the accuracy of Tanaka's and Liang's models have introduced additional state variables that attempt to model more accurately the phase composition of the material. During the period of this study, it has been found that such an approach leads to practical difficulties, and hence a new model was developed which uses the same state variables as Tanaka's model, but does not assume a particular form for the function ξ. Thus, ξ is chosen such that it fits the measured behaviour of the particular SMA that is used.

The model presented in this section is based on the experimental results obtained from the tests described in Sections 3.3 and 3.6 for a 1 mm diameter Nitinol. But in the same way we could set up a model for any other wire. It is assumed that there is no unrecoverable (plastic) strain in the material.

4.2.1 Thermal Expansion

The thermal expansion coefficient of Nitinol is in the region 6.6 $\sim$11 $\times$ 10^{-6} /^{o}C, see Table A.2. If the temperature varies, approximately by 200^{o}C, the corresponding thermal strain is 0.2%. Compared with strains of nearly 7% which are recovered through shape memory, thermal effects can be neglected. Thus, Eqn. 4.1 can be simplified as

$$\dot{\sigma} = D\dot{\epsilon} + \Omega\dot{\xi} \tag{4.17}$$

4.2.2 Strain Components

We consider the total strain

$$\epsilon = \epsilon^e + \epsilon^t \tag{4.18}$$

where ϵ^e is the elastic strain and ϵ^t is the strain due to transformation. We assume that the Young's Modulus is a constant, hence

$$\epsilon^e = \frac{\sigma}{D} \tag{4.19}$$

Also

$$\epsilon^t = \epsilon^t_{max} \times \xi \tag{4.20}$$

where ϵ^t_{max} is the maximum transformation strain.

4.2.3 Constitutive Equation

By integration of Eqn. 4.17, we obtain

$$\sigma - \sigma_o = D(\epsilon - \epsilon_o) + \Omega(\xi - \xi_o) \tag{4.21}$$

where σ_o, ϵ_o and ξ_o are any set of initial conditions. To calculate the value of Ω, we carry out a tension test on a SMA wire which had been heated to high temperature and then cooled under zero stress. Hence, $\sigma_o = \epsilon_o = \xi_o = 0$ and Eqn. 4.21 becomes

$$\sigma = D\epsilon + \Omega\xi \tag{4.22}$$

During the test, σ is increased until the wire consists of $\approx 100\%$ detwinned martensite. At this point the wire is unloaded without any reverse transformation and the transformation strain ϵ^t_{max} is measured. Substituting ϵ^t_{max} and $\xi = 1$ into Eqn. 4.22 we obtain

$$\Omega = -D\epsilon^t_{max} \tag{4.23}$$

For $\epsilon^t_{max} = 6.7\%$ and $D = 28.26$ GPa, Eqn. 4.23 gives $\Omega = -1.893$ GPa.

4.2.4 $\xi(T, \sigma)$ Function

We consider two separate functions, one for the transformation from A/TM to DM, and one for the reverse transformation. The effect of R-phase, if there is any, is ignored.

A. $A/TM \Rightarrow DM$

Let us consider the three σ vs. ϵ curves shown in Fig 4.2(a) (Refer to the Section 3.3 where these curves were obtained) . Subtraction of the elastic strain ϵ^e gives the σ vs. ϵ^t relations shown in Fig. 4.2(b). Clearly, the maximum transformation strain is almost constant:

$$\epsilon^t_{max} \approx 6.7\% \tag{4.24}$$

This maximum transformation strain, 6.7%, is the same value as reported in Liang's experiment (Liang 1990), and is very near the value, 6.8%, which was reported by Leo *et al.* (1993).

We can calculate

$$\xi = \frac{\epsilon^t}{\epsilon^t_{max}} \tag{4.25}$$

and, to find a simpler relation, we take the logarithm of ξ, Fig. 4.2(d).

The σ vs. $\ln(\xi)$ relation can be divided into two parts. The first part is almost linear, and is temperature dependent. It corresponds to the transformation $A/TM \Rightarrow DM$. The second part is almost temperature independent, and corresponds mainly to martensite re-orientation.

We can express the σ vs. $\ln(\xi)$ relationship by means of two separate functions, a straight line and a second-order polynomial. For this particular specimen, the equation of the straight line is

$$\sigma = (0.0019T - 0.0191)\ln\xi + (0.0083T - 0.0672) \tag{4.26}$$

Solving for ξ, we obtain

$$\xi_1 = \exp\left(\frac{\sigma - 0.0083T + 0.672}{0.0019T - 0.0191}\right) \tag{4.27}$$

The equation of the polynomial is

$$\sigma = 4.0349(\ln\xi)^2 + 3.0457\ln\xi + 0.6584 \tag{4.28}$$

and, solving this equation, we obtain

$$\ln(\xi) = \frac{-3.0457 \pm \sqrt{3.0457^2 - 4 \times 4.0349 \times (0.6584 - \sigma)}}{2 \times 4.0349} \tag{4.29}$$

From these two solutions, we choose the larger one because the polynomial function is a parabola with a vertical axis, and we need only the right-hand side part. Hence, we take

$$\xi_2 = \exp\left(\frac{-3.0457 + \sqrt{3.0457^2 - 4 \times 4.0349 \times (0.6584 - \sigma)}}{2 \times 4.0349}\right) \tag{4.30}$$

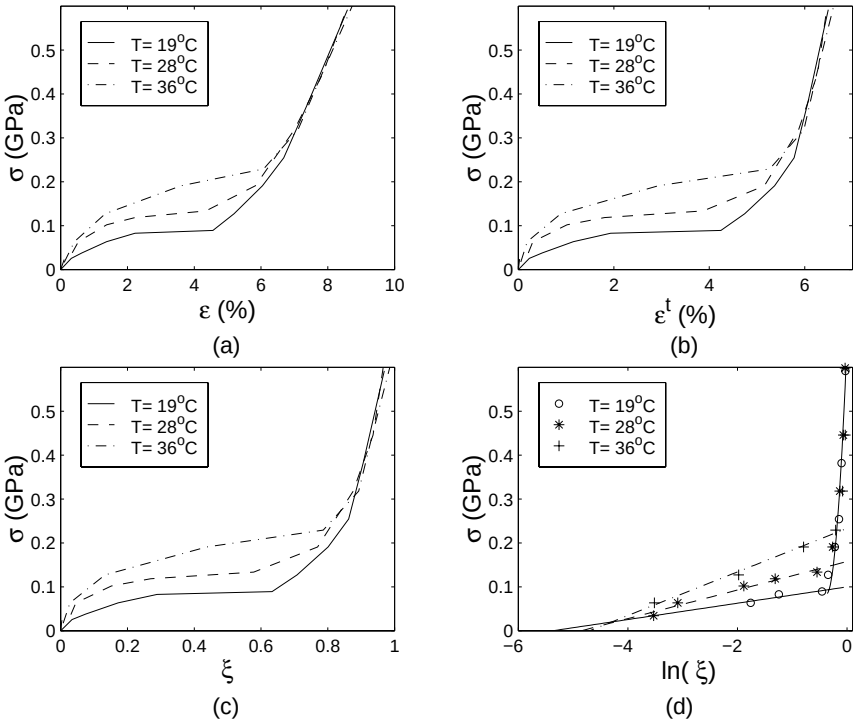

Figure 4.2: Function $\xi(T, \sigma)$ for $A/TM \Rightarrow DM$.

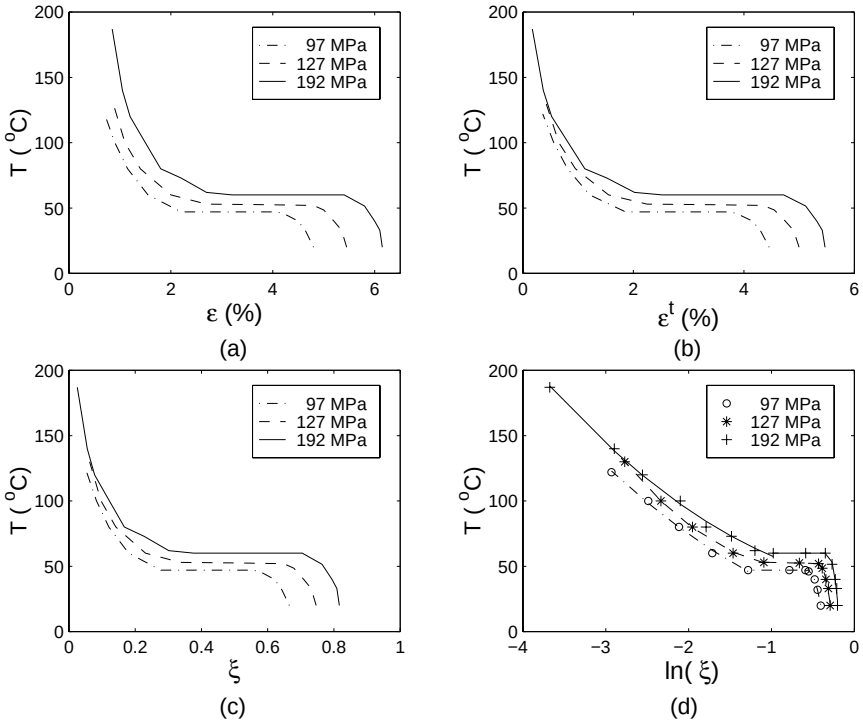

Figure 4.3: Function $\xi(T, \sigma)$ for $DM \Rightarrow A/TM$.

Given σ and T we calculate the corresponding values of ξ_1 and ξ_2 from Eqns. 4.27 and 4.30, and then

$$\xi = min(\xi_1, \xi_2) \tag{4.31}$$

B. $DM \Rightarrow A/TM$

In principle, it should be possible to calculate the second function $\xi(T, \sigma)$ from the data obtained during the unloading part of the tension test. However, a much more reliable way of obtaining this function is from the thermal test.

Let us consider the three T vs. ϵ curves shown in Fig. 4.3(a) and, as above, let us re-plot these curves in term of T vs. $\log(\xi)$, Fig. 4.3(d). Each curve can be divided into three lines. For specimen 1 the first line has the expression

$$T - T_o = -200 \times (\ln\xi - \ln\xi_o) \tag{4.32}$$

from which

$$\xi_1 = \exp(\ln\xi_o + \frac{T_o - T}{200}) \tag{4.33}$$

The second line has the equation

$$T = 130.3 \times \sigma + 38.1 \tag{4.34}$$

Here 130.3 is in the unit of ^{o}C/GPa. This value corresponds to 7.6 MPa/^{o}C, which is exactly the same value as reported by Leo *et al.* 1993.

To consider the pre-stress effect on transformation temperature (see Section 3.1), in Eqn. 4.34 σ is replaced by $\sigma + a \times (\sigma_{max} - \sigma)$, where σ_{max} is the pre-stress. In this particular specimen, $a = 0$, if $\sigma_{max} \leq \sigma$; and $a = 0.12$, for $\sigma_{max} > \sigma$.

The third line has the expression

$$T = (10.7 \times \sigma - 48.3) \times \ln\xi + 189.9 \times \sigma - 32 \tag{4.35}$$

from which

$$\xi_3 = \exp\left(\frac{T + 32 - 189.9 \times \sigma}{10.7 \times \sigma - 48.3}\right) \tag{4.36}$$

Note that in the middle part of the transformation $DM \Rightarrow A/TM$ a large strain change occurs under almost constant temperature, but there is no such behaviour in the transformation $A/TM \Rightarrow DM$ during cooling under constant stress. This confirms that the $\xi(T, \sigma)$ relations for these two transformations are different.

Also note that a variable Young's Modulus could be introduced into this model by using various of methods, such as a Voigt approximation (Mura, 1987), but this would make it more complex from the modelling point of view.

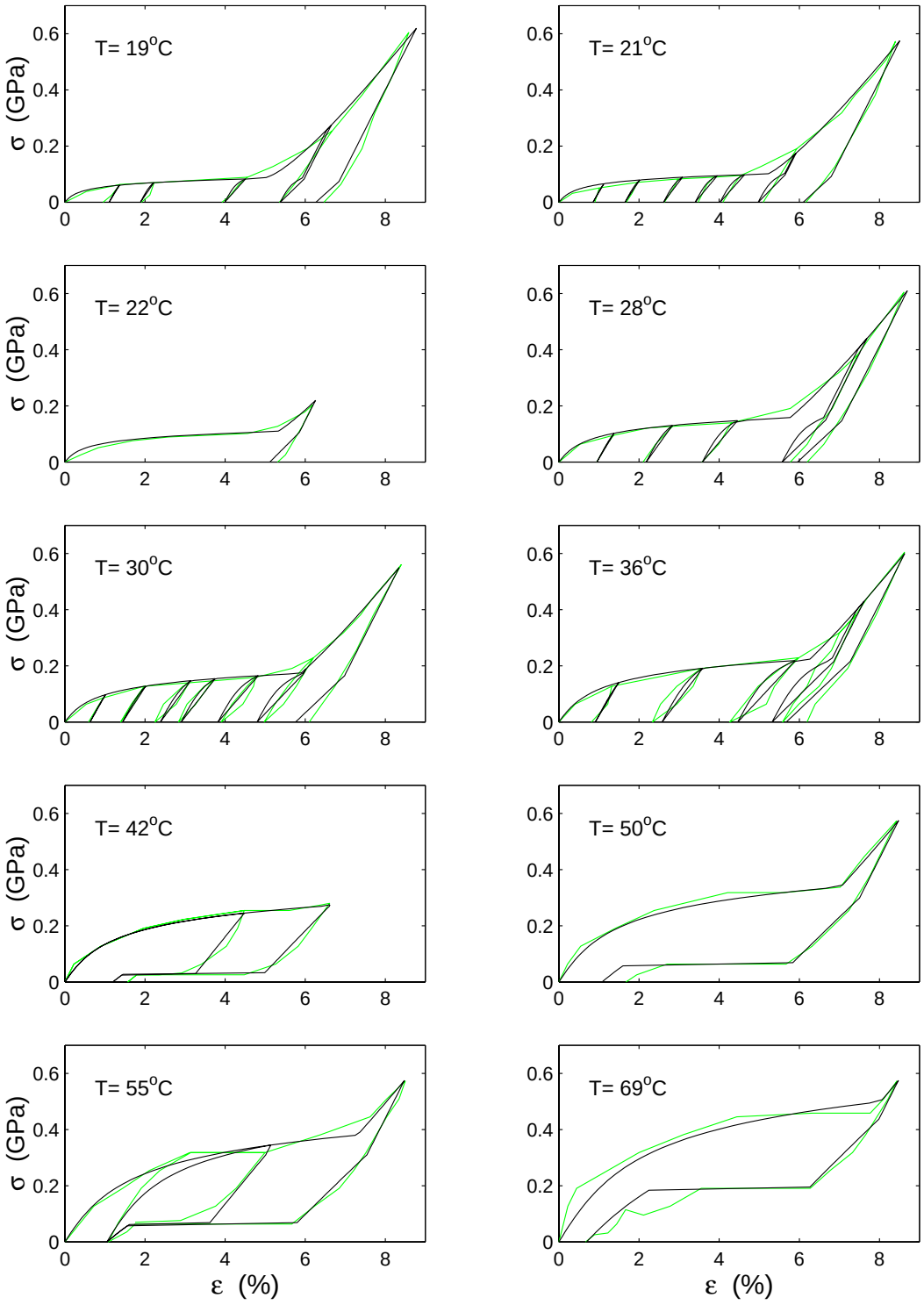

Figure 4.4: σ vs. ϵ relations for specimen 1 (d = 1 mm). Black lines denote prediction from this model; grey lines denote measurement.

4.2.5 Incomplete Transformation

There are a number of cases where the transformations are incomplete, for examples, many loading/unloading cycles in Fig. 3.9; and secondly Fig. 3.22, where different initial values of ξ_o in thermal cycling. In such cases, the value of ϵ^t_{max} should be appropriately adjusted.

4.3 Validation of Phenomenological Model

In this section we compare the predictions from the constitutive model presented in the previous section with a series of experimental results (for the Nitinol wires $d = 1$ mm).

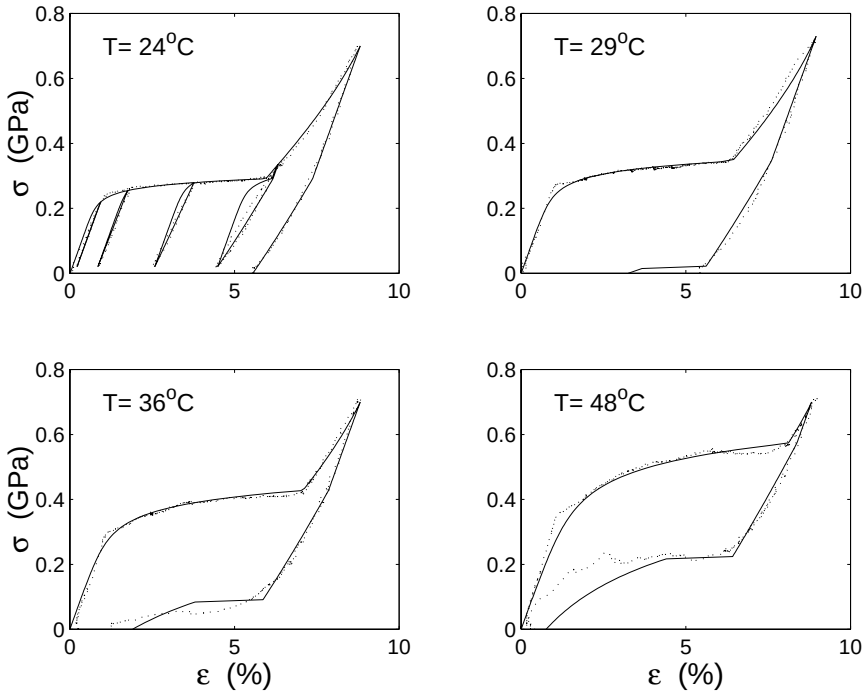

Figure 4.5: σ vs. ϵ relations for specimen 2 ($d = 1$ mm). Black lines denote prediction from this model; dotted lines denote measurement.

- σ vs. ϵ relation (Figs. 4.4 and 4.5)
  - The loading curve, which corresponds to the transformation $A/TM \Rightarrow DM$, is obtained from Eqn. 4.31.
  - The unloading curve, which corresponds to the transformation $DM \Rightarrow A/TM$, is obtained from Eqns. 4.33, 4.34 and 4.36.
- T vs. ϵ relation (Figs. 4.6, 4.7 and 4.8)

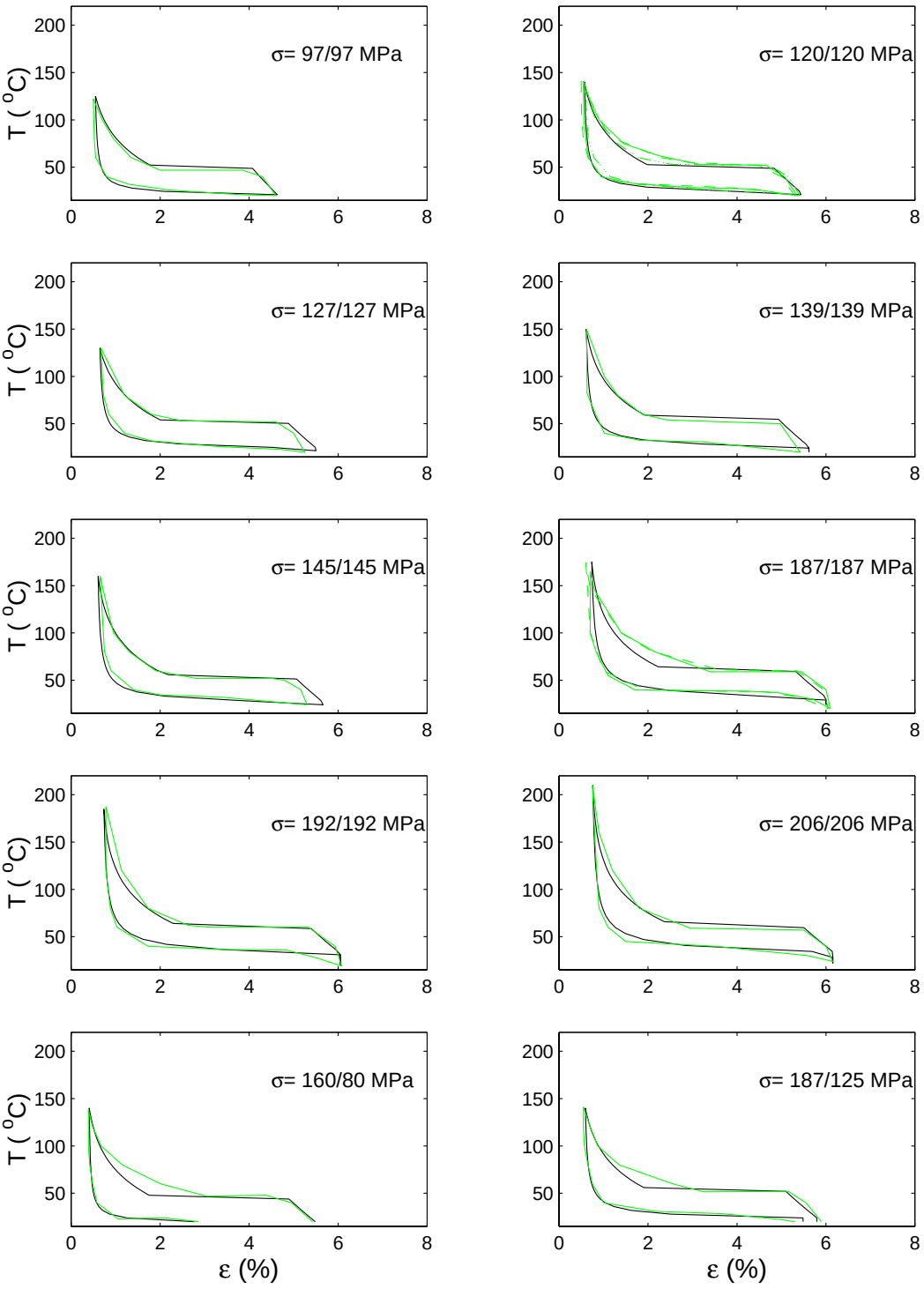

Figure 4.6: T vs. ϵ relations for specimen 1 (d = 1mm). Black lines denote prediction from this model; grey lines denote measurement.

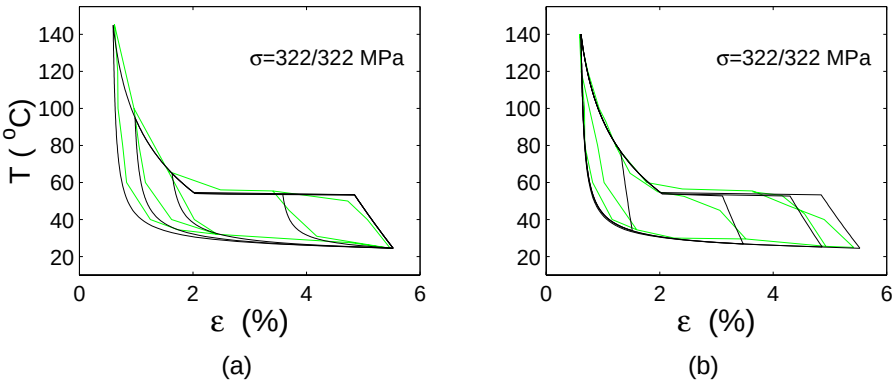

Figure 4.7: T vs. ϵ relations for specimen 1 (d= 1mm). Black lines denote prediction from this model; grey lines denote measurement.

- During heating, if the wire is initially on the polynomial part of the curve defining the $A/TM \Rightarrow DM$ transformation, no $DM \Rightarrow A/TM$ transformation occurs until the temperature is higher than the temperature at which the functions of ξ_1 and ξ_2 begin to intersect (Eqn. 4.31). After that, the heating process is described by Eqns. 4.33, 4.34 and 4.36.
- During cooling, we have the same behaviour as during heating but this time the temperature needs to be below the temperature of intersection of the two functions. Equation 4.31 is used for this process.

Generally speaking, this model can provide quantitative prediction to the behaviour of Nitinol in tension at constant temperature and thermal cycling at constant load. The predictions agree well with experimental measurements.

However, as we can see, there are several situations where it does not work very well.

- The "*elastic*" range of tension at high temperature. In this range, our prediction is usually lower than experimental result. The consideration of a changing Young's Modulus instead of a constant value may improve our prediction, but it will make the model much more complex.
- In some cases, e.g. T= 48°C in Fig 4.5, our prediction of unloading behaviour is far away from measurement. The main reason is due to the difficulty of controlling the temperature of specimen in unloading by turning the handle of the Tensometer properly and, in the meaning time, adjusting the rheostat.
- In several heating cases, Fig. 4.6, the earlier third line towards high temperature does not fit well with experimental data. The possible reason is that we have heated the wire too fast. Thus, the measured temperature is higher than our prediction. This has been improved in the later tests.

- This model can not predict the thermal cycling behaviour correctly, if the transformation strain is very small (see Fig. 4.7(b)). The reason is that we have not done enough tests in this transformation strain range, thus we make a linear assumption (since the involved transformation strain is comparatively small) to simplify it.

- Specimen 2 has R-phase in its transformation as described in Section 3.1. Since the effect of R-phase is ignored, we do not consider any transformation caused by it. Hence, we can not predict well the small elongation in cooling of specimen 2 when the applied stress is small, e.g. in Fig. 4.8, when the applied stress during cooling is smaller than 225 MPa.

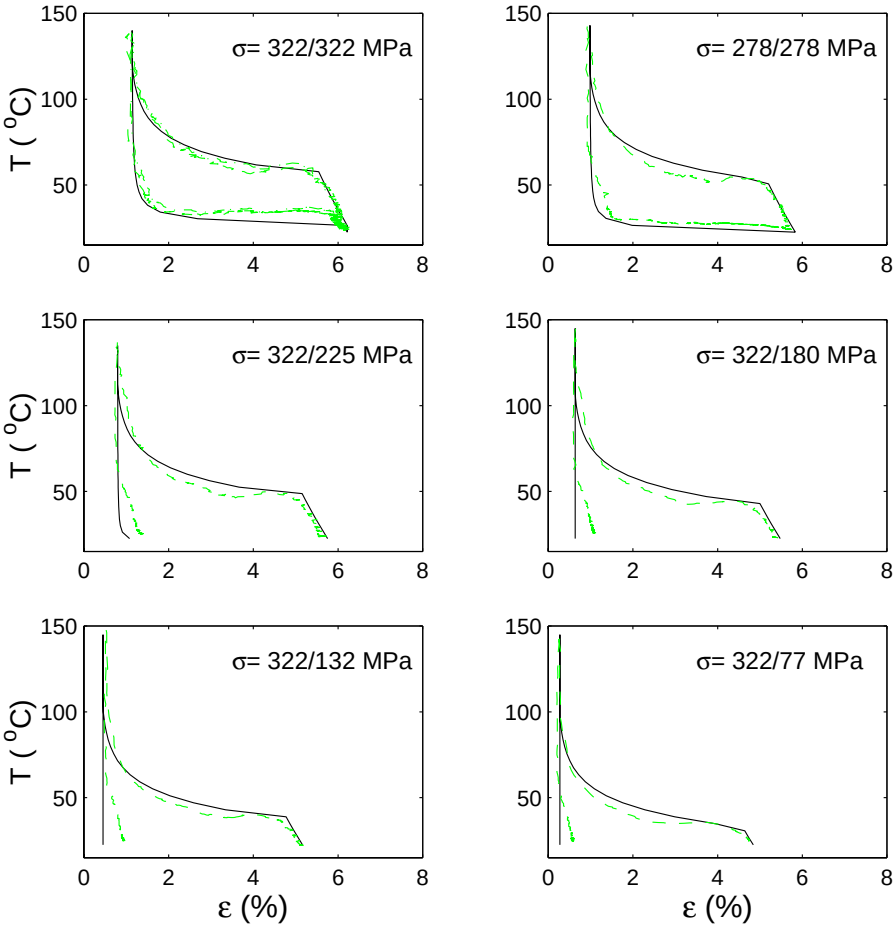

Figure 4.8: T vs. ϵ relations for specimen 2 (d= 1mm). Black lines denote prediction from this model; grey lines denote measurement.

4.4 Simulation of Thermal Cycling with Fixed Length

In this section and the next two we simulate three phenomena, thermal cycling with fixed length, effects of strain rate on hysteresis, and phase transformation front, using the material model derived in the previous section.

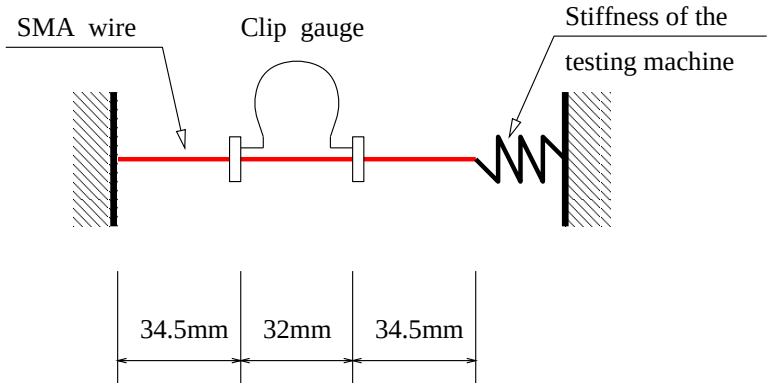

Figure 4.9: Schematic diagram of thermal cycling test at constant length.

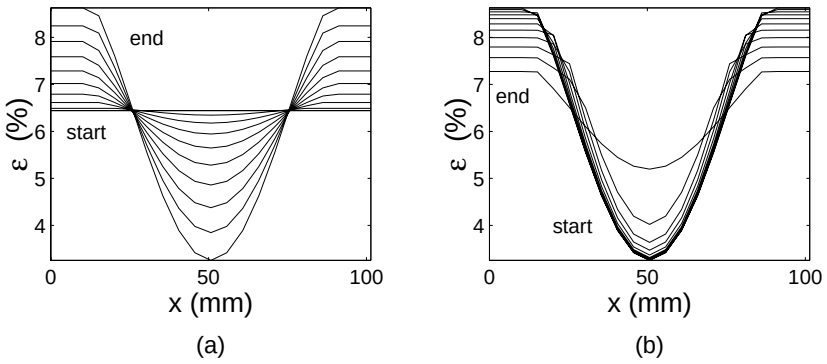

Figure 4.10: Strain distribution during a thermal cycle. (a) During heating; (b) during cooling.

The wire-Tensometer system is modelled by the wire-spring system shown in Fig. 4.9. The measured stiffness of the spring is 7500 N/mm. First, we load the wire to 300 N and hold the two ends. Next, we heat the wire by passing a current through it so that the temperature at the mid-point increases from 20°C to 120°C. Then, we cool it back to 20°C. It is assumed that the temperature at the ends of the wire remains equal to 20°C. This assumption roughly takes the steel clamps used in the test into consideration and ignores any possible temperature increase of them.

This thermal cycle was analysed using the constitutive model for specimen 2 and the steady-state temperature distribution derived in Appendix B.1. The

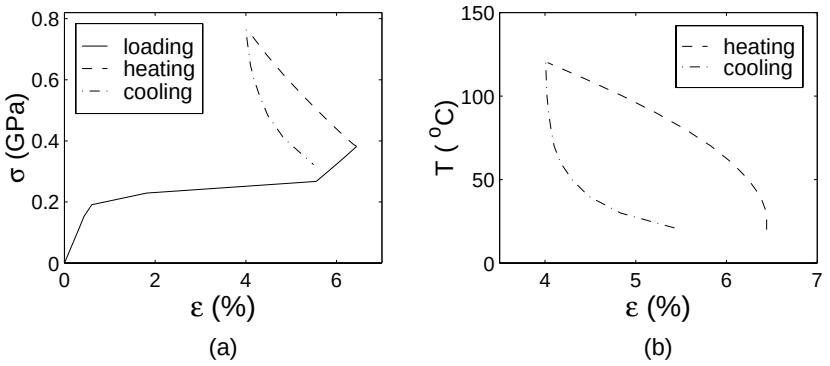

Figure 4.11: Behaviour during a thermal cycle. (a) Stress vs. average strain (including loading); (b) Temperature vs. average strain.

half length of the wire is divided into 20 elements. In each step, the temperature distribution along the wire is calculated, and then the strain and stress in each element is analysed using the temperature in this element. The boundary condition in each step is such that the total length of the wire is a constant.

Figure 4.10 shows that during heating the strain along the wire is not constant. When the temperature in the middle of the wire is 120^{o}C, the strain at the same point is reduced to less than 3.5% while at the ends it has increased to around 8.5%. Hence, the wire contracts in the middle while at the two ends it stretches due to the increased stress level. During cooling, the force goes down and the strain along the wire is re-distributed. When the temperature is back to 20^{o}C, the strain in the middle is about 5.25% while at the two ends it goes back to around 7.25%.

Figure 4.11 shows the stress vs. the average strain in the middle length of 32 mm and the temperature vs. the average strain in the same range relationships. After one cycle, the strain along the wire is no longer uniform, the stress is lower and the strain measured by the clip gauge is also 1% less than at the start.

Note that the σ vs. ϵ relation of Fig. 4.11(a) is similar to the measured behaviour in Fig. 3.23.

4.5 Simulation of Strain Rate Effects

Strain rate effects on the stress-strain behaviour of SMAs has been reported in many papers (Schroeder and Wayman 1979, Leo *et al.* 1993, Shaw and Kyriakides 1995). We have carried out tension tests under different strain rates in Section 3.4.

It has been found that, in SMAs with superelasticity, Fig. 2.1(b), high strain rate enlarge the hysteresis loop, and this is explained by the delay introduced by the need to evacuate or absorb the transformation latent heat (Ortin 1992). We give a numerical analysis of such behaviour.

Assume we have a unit length of austenite SMA wire in which temperature

is a constant everywhere. The standard one-dimensional heat transfer equation including a heat source term (ρdq) and a convection term ($\frac{hl}{A}(T - T_o)$) at time t_i to t_{i+1} may be written as (Carslaw and Jaeger 1959)

$$\rho c \frac{dT}{dt} = \rho dq - \frac{hl}{A}(T - T_o) \tag{4.37}$$

with the initial condition

$$T(0) = T_i \tag{4.38}$$

Here T_i is the temperature at time t_i and T_o the initial temperature of the specimen, A the cross-sectional area, l perimeter of the section of the wire, ρ the density of the wire, c its specific heat, h is convection heat-transfer coefficient, and dq is the heat source during the time dt.

$$dq = q \times \frac{d\xi}{dt} \tag{4.39}$$

where q is the latent heat of the material. For properties of Nitinol and h of water, see Appendix B.1.

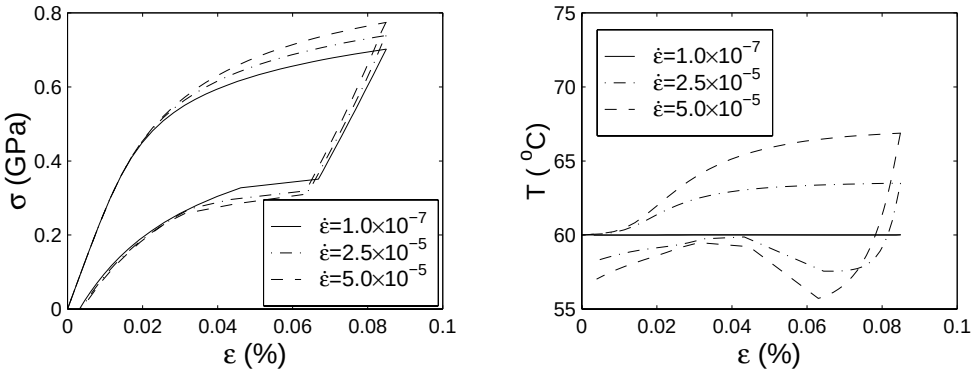

Figure 4.12: Effects of strain rate on hysteresis loop.

We assume that $d\xi/dt$ is constant during the time interval dt. Let

$$a = \frac{dq}{c} \tag{4.40}$$

$$b = \frac{hl}{A\rho c} \tag{4.41}$$

Thus

$$T = T_o + \frac{a}{b} + e^{-bdt}C \tag{4.42}$$

where

$$C = T(0) - T_o - \frac{a}{b} \tag{4.43}$$

and

$$d\xi = \frac{d\epsilon^t}{\epsilon^t_{max}} \tag{4.44}$$

Here ϵ^t is the transformation strain which is decided by the applied stress and the temperature of the specimen, and ϵ^t_{max} is the maximum transformation strain.

The applied constitutive model is for specimen 2 ($d = 1$mm). The analysis is basically the same as the simulation of loading/unloading behaviour but with a changing temperature.

Let T_o= 60^{o}C, where Nitinol is almost pure austenite as shown in Fig. 3.1(b). Results at three different strain rates $\dot{\epsilon}$= 1.0×10^{-7}/s, 2.5×10^{-5}/s, and 5.0×10^{-5}/s, are shown in Fig. 4.12.

We can see that thermal effects associated with strain rates change the hysteresis loop of a wire. The higher is the strain rate, the larger is the loop. However, recall that our experimental results in Section 3.4 showed that further increase of strain rate did not show the same tendency. Although h may not be a constant due to the instability of experimental condition, the thermal effects analysed in this section cannot fully explain our experimental results. Therefore further investigation is needed.

4.6 Simulation of Phase Transformation Front

The **Phase Transformation Front Movement Phenomenon** has been reported in several papers (Leo *et al.* 1993, Shaw and Kyriakides 1995, Shaw and Kyriakides 1997), and was demonstrated in Section. 3.4.

There are some similarities between this behaviour and the onset of plasticity, in particular the formation of **Lüders bands** (Hall, 1970), during the yielding of polycrystalline metals, such as aged low-carbon steel in a tension test. Yielding begins at a point where there is an initial defect (such as a stress concentration due to a dislocation, or a geometrical imperfection) and then propagates along the specimen. It is usually argued that the region near a Lüders band is softer than the rest of the material and hence further plastic deformation occurs at the boundary between the initial band and the un-yielded material (McClintock and Argon, 1966).

Instead of yielding, here we are interested in exothermal phase transformations. Also we know from Section 3.4 that if the temperature becomes too high the propagation of the transformation front will stop because a higher stress is required for propagation. Thus, a new transformation front will have to be formed at another point of the specimen.

Lüders bands are normally accompanied by an almost constant pulling force, with small fluctuations only, while we have seen that the load may increase quite a lot during phase transformation front movement. This is the main difference between Lüders bands and the phase transformation front movement.

We will try to simulate the phase transformation front phenomenon in an approximate manner, making several simplifying assumptions.

4.6.1 Internal Stress

Our preliminary study shows that the stress increase due to the reduction in cross-section of a "neck" area is not enough to generate any transformation front movement. Hence, we have to look for a different mechanism to cause it.

The crystal structures of austenite and martensite are different. Hence, an internal stress is required to maintain full coherency of the austenite-martensite inter-phase, see Section 2.1.1. Also, the transformation $A \Rightarrow M$ is also accompanied by a small volume change. This is another cause for the existence of an internal stress.

This internal stress can be minimised by the formation of martensite variants (Mura *et al.* 1976). The lowest stress field occurs in twinned martensite that is generated by cooling austenite under zero applied stress. If the applied stress is increased gradually, the internal stress will have to increase, in order to maintain coherency at all inter-phase.

So what is the level of this internal stress? It is very difficult to calculate precisely. Especially, because it depends on the shape and size of the martensite. We can estimate the level of the internal stress by an analysis based purely on volume changes.

Before starting, we define the equivalent internal stress $\bar{\sigma}^*$ and the equivalent transformation strain $\bar{\epsilon}^*$ which have the same form as equivalent stress and equivalent strain used in plastic theory

$$\bar{\sigma}^* = \sqrt{\frac{1}{2}\left[(\sigma^*_{11}-\sigma^*_{22})^2+(\sigma^*_{22}-\sigma^*_{33})^2+(\sigma^*_{33}-\sigma^*_{11})^2+6\times(\sigma^{*2}_{12}+\sigma^{*2}_{23}+\sigma^{*2}_{31})\right]} \tag{4.45}$$

and

$$\bar{\epsilon}^* = \sqrt{\frac{2}{9}\left[(\epsilon^*_{11}-\epsilon^*_{22})^2+(\epsilon^*_{22}-\epsilon^*_{33})^2+(\epsilon^*_{33}-\epsilon^*_{11})^2+\frac{3}{2}(\epsilon^{*2}_{12}+\epsilon^{*2}_{23}+\epsilon^{*2}_{31})\right]} \tag{4.46}$$

where σ^*_{ij} $(i,j=1,2,3)$ is the internal stress tensor, and ϵ^*_{ij} $(i,j=1,2,3)$ the transformation strain tensor. We will assume that the level of internal stress is related to $\bar{\sigma}^*$.

In this approach, we consider different Young's Moduli for martensite and austenite. Two kinds of martensite shapes are studied: sphere and disk. For each case, we want to know the stress at the inter-phase surface and the equivalent internal stress $\bar{\sigma}^*$.

Consider a infinite region of austenite. Within that region a sphere (or disk) of radius r_A transforms into a sphere (or disk) of martensite of radius r_M. We define

$$\alpha = \frac{r_A - r_M}{r_A}$$

The volume change for Nitinol is -0.34% $(A \Rightarrow M)$. The Young's Modulus of martensite (D_M) and austenite (D_A) are taken as 34.5 GPa and 79 GPa by

averaging the values shown in Table A.3. The Poisson's ratio is $\nu=$ 0.33, as shown in Table A.3.

We seek the stress that are set up in this system as a result of this phase change. Solving problem (refer Qian and Ye 1980), we have:

For martensite of spherical shape with a radius of r

$$\sigma_r = \begin{cases} Ax^3/r^3 & (x \geq r) \\ A & (x \leq r) \end{cases}$$

and $\sigma_\theta = \sigma_\varphi = -\sigma_r/2$ $(x \geq r)$, $\sigma_\theta = \sigma_\varphi = \sigma_r$ $(x \leq r)$. Here

$$A = \frac{4\mu_A(3\lambda_M + 2\mu_M)\alpha}{3\lambda_M + 2\mu_M + 4\mu_A}$$

where λ_M is Lame's elastic constant for martensite ($\lambda_M = D_M\nu/(1+\nu)/(1-2\nu)$), and

$$\mu_M = \frac{D_M}{2(1+\nu)}$$
$$\mu_A = \frac{D_A}{2(1+\nu)}$$

For martensite of disk shape with a radius of r

$$\sigma_r = \begin{cases} Bx^2/r^2 & (x \geq r) \\ B & (x \leq r) \end{cases}$$

and $\sigma_\theta = -\sigma_r$ $(x \geq r)$, $\sigma_\theta = \sigma_r$ $(x \leq r)$. Here

$$B = \frac{\alpha}{\frac{1+\nu}{D_A} + \frac{1-\nu}{D_M}}$$

Figure 4.13(a) shows the stress in the radial direction vs. x/r, where r is the radius of the martensite, and x is the distance from the centre of the martensite. Figure 4.13(b) shows the equivalent internal stress $\bar{\sigma}^*$ vs. x/r.

Since the stress at the inter-phase equals the stress in the radial direction at position $x = r$, we have inter-phase stress about 0.08 GPa for martensite of spherical shape and about 0.047 GPa for martensite of disk shape. The maximum equivalent internal stress, on the austenite side of the inter-phase, is 0.12 GPa for spheres and 0.08 GPa for disks, and the corresponding equivalent stresses in martensite are $\bar{\sigma}^*= 0$, and $\bar{\sigma}^*= 0.47$ GPa, respectively.

From the above study, it seems reasonable to assume that the maximum equivalent internal stress $\bar{\sigma}^*_{max}$ in Nitinol is around 0.08 GPa. Then, we may assume that $\bar{\sigma}^*$ proportionally to the transformation $A \Rightarrow M$. Therefore, we may write the following relation to link ξ^M and the current equivalent internal stress $\check{\sigma}^*$

$$\check{\sigma}^* = \bar{\sigma}^*_{max}\xi^M \tag{4.47}$$

Note that if two adjacent sections in a Nitinol wire have different $\check{\sigma}^*$, the real value used in analysis should be the larger one.

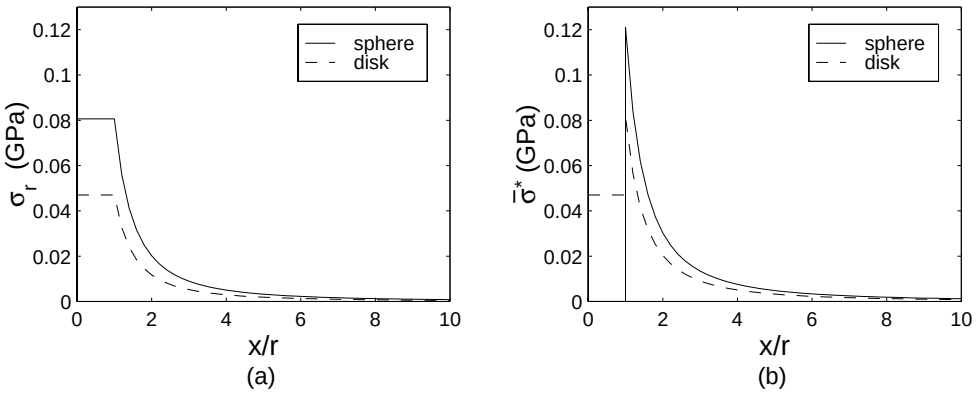

Figure 4.13: (a) Radial stress and (b) equivalent stress due to volume change (r is the radius of the martensite, x the distance from the centre of martensite).

4.6.2 Initial Defects

Initial defects come from geometrical and mechanical imperfections. Geometrical non-uniformity is the most common geometrical imperfection. Mechanical imperfections may be due to internal stress or stress concentration, etc. For example, in a tension test, the specimen is normally held by clamps, and therefore, the two ends of the specimen are likely to be pre-stressed before testing.

In our simulation only geometrical imperfections will be considered, assuming a reduction in the diameter of the wire.

4.6.3 Quasi-Static Thermodynamic Model

In the thermal analysis, the temperature at each section is assumed to be constant, but it may vary from section to section along the wire, Fig. 4.14. The standard one-dimensional heat transfer equation, including a heat source term $\tilde{Q}$ (generated by the phase transformation), can be written as (Carslaw and Jaeger 1959)

$$\rho c \frac{\partial T}{\partial t} - k \frac{\partial^2 T}{\partial x^2} = \tilde{Q}(x) - \frac{hl}{A}(T - T_o) \tag{4.48}$$

with boundary conditions

$$T(t, 0) = T_1(t)$$
$$T(t, L) = T_2(t)$$

and initial condition

$$T(0, x) = f(x)$$

The only difference between Eqn. 4.48 and Eqn. 4.37 is the new term $(k\frac{\partial^2 T}{\partial x^2})$, which represents the non-uniform temperature along the wire.

The heat source term is calculated by

$$\tilde{Q}(x) = \rho q \xi_o^A \frac{d\xi(x)}{dt} \tag{4.49}$$

in each time interval dt. Here ξ_o^A is the initial austenite fraction of the wire.

The solution of Eqn. 4.48 is presented in Appendix B.2.

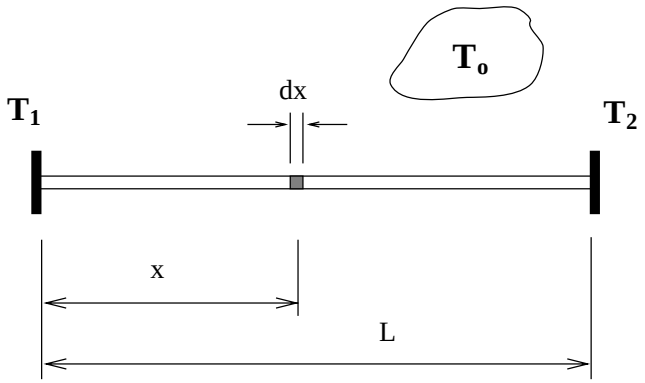

Figure 4.14: Schematic diagram for the analysis of transformation front movement.

Our thermomechanical analysis is carried out by using Eqn. 4.22. However, in order to include the internal stress described in Section 4.6.1, we redefine

$$\sigma = \sigma_{ext} + \check{\sigma}^* \tag{4.50}$$

Here σ_{ext} is the applied external stress. Another modification is that we define the transformation strain by the approximate expression

$$\epsilon^t = \epsilon^t_{max} \frac{\sigma_{ext}}{\sigma} \xi(T, \sigma) \tag{4.51}$$

since the direction of the internal stress is normally not the same as that of the applied external stress.

The whole length of the wire is divided into n elements, with $n+1$ nodes. In each step, i.e. time interval dt, first a thermomechanical analysis is carried out to calculate the strain and stress at each node by using the temperature distribution calculated in the previous step. Then, $\tilde{Q}(x)$ is obtained from Eqn. 4.49. Then, a new temperature is calculated at each node by solving Eqn. 4.48.

A new thermomechanical analysis is then carried out using the average between the two temperature distribution. This thermomechanical analysis is then followed by a new thermal analysis, and the whole sequence is repeated three times before we move to the next dt.

4.6.4 Transformation Front

We use the constitutive model for specimen 1 in our simulation, assuming that the initial temperature of the specimen is 70^oC, where Nitinol is initially austenite.

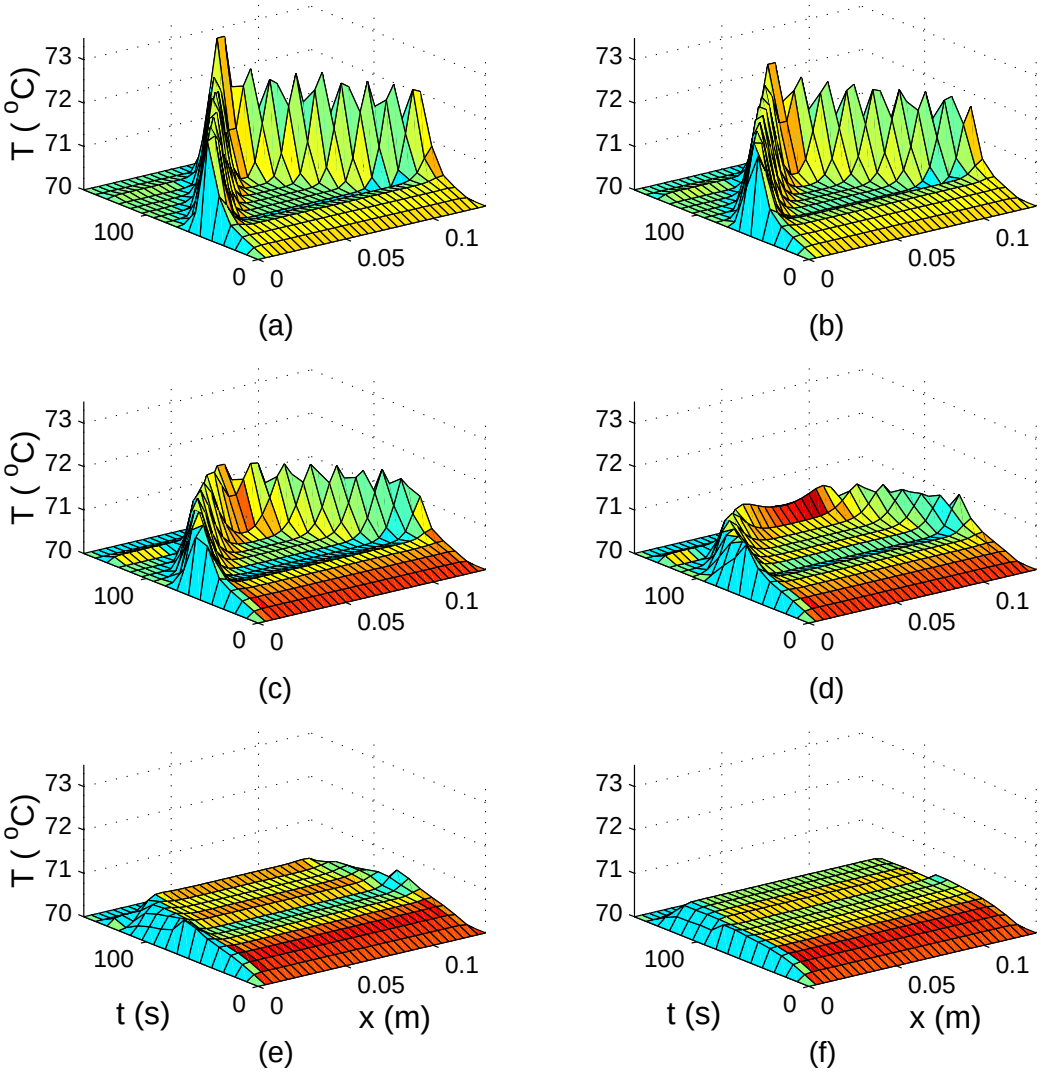

Figure 4.15: Temperature distributions in wires with initial imperfections at the ends, strained at $\dot{\epsilon} = 6.4\times10^{-4}$/s. The equivalent internal stresses have a maximum values of (a) 0.125 GPa; (b) 0.1 GPa; (c) 0.075 GPa; (d) 0.05 GPa; (e) 0.025 GPa; (f) 0 GPa.

If we can successfully simulate transformation front movement phenomenon in this material, there will be no difficulty to get similar result in other hardening materials.

We simulate the behaviour of a Nitinol wire with diameter of $d = 0.65$ mm, as tested by Leo *et al.* (1993). Its parameters are $L = 130$ mm, $\dot{\epsilon}= 6.4\times10^{-4}$/s, $h = 890$ W/m^{2o}C. The latent heat for austenite is 28,000 J/Kg.

Since the number of transformation fronts is not reported in Leo *et al.* (1993), we assume that there are two fronts starting from the two ends of the wire. Hence, the initial defect is assumed to consist in the two end-sections having diameters of $0.95d$.

Figure 4.15 shows the temperature distribution along the wire as a function of time for different maximum equivalent internal stresses $\bar{\sigma}^*$. The maximum strain has been set at 10%, and the computation has been carried out according to the scheme described in Section 4.6.3.

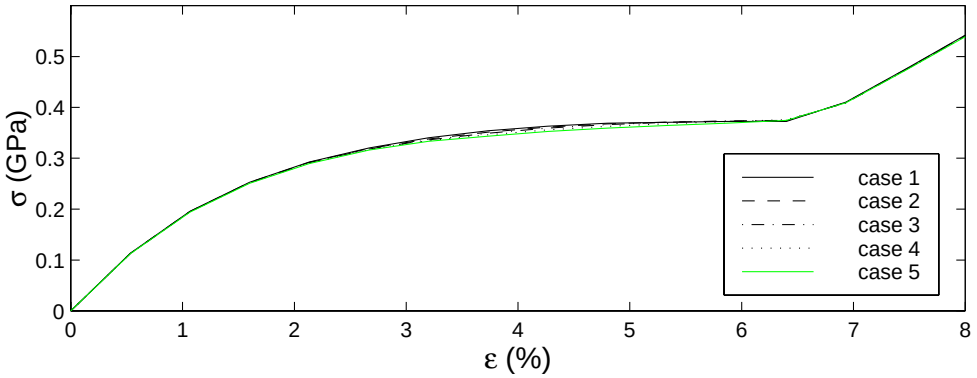

Figure 4.16: σ vs. ϵ relationships.

case	number of defects	position (node number)
1	0	
2	1	1
3	2	1, 64
4	3	1, 32, 64
5	4	1, 22, 43, 64

Table 4.1: Initial defects.

In Fig. 4.15(e), where $\bar{\sigma}^*_{max}$ is 0, there is no transformation front. Except the areas near the ends, the temperature distribution is roughly uniform. With the increase of $\bar{\sigma}^*_{max}$, the transformation front behaviour becomes apparent. The maximum temperature increase in Fig. 4.15(c), where $\bar{\sigma}^*_{max}= 0.075$ GPa, is very close to the value of 2.0^oC reported by Leo *et al.* (1993).

It is useful to examine the effects of the transformation fronts on the σ vs. ϵ relationship. A 100 mm long, 1 mm diameter wire has been analysed. In order

to get a significant transformation front behaviour, the equivalent internal stress is set to 0.125 GPa. All the other parameters are the same as in the earlier simulation.

We divided the wire into 63 elements, and hence there are 64 nodes. The initial defects ($0.95d$) for each case studied are shown in Table. 4.1.

As shown in Fig. 4.16, the σ vs. ϵ relationships are not much different. Hence, from a practical point of the view, we may ignore the effects of the transformation front behaviour when we simulate the behaviour of Nitinol wire that is part of an actuator system.

Chapter 5

Thermo-Micromechanical Model

Although the thermomechanical behaviour of SMAs has been investigated both experimentally and theoretically for more than 40 years, there are still many contradictions in the literature.

In this section a thermo-micromechanical model based on complementary free energy and micromechanical transformation system is developed, to explain the shape memory related behaviour (V-shape of critical stress as shown in Fig. 2.8, non-symmetrical behaviour in tension and compression, transformation front behaviour, and multi-phase transformation materials).

The chapter will start with the foundations for this model and then discuss the simplest case, single crystal Nitinol in tension, compression and cycling. Finally, polycrystaline Nitinol is discussed.

5.1 Foundations

This thermo-micromechanical model involves two theories: a thermomechanical formulation based on complementary energy and a micromechanical theory of phase transformations.

5.1.1 Thermomechanical Formulation

For simplicity, we will assume the material to be homogeneous. The complementary free energy (Ψ) of a unit volume has the expression (Sun and Hwang 1993a, Patoor *et al.* 1994, Huang and Brinson, 1997)

$$\Psi(\Sigma_{ij}, T, \xi) = -[\Phi(\Sigma_{ij}, T, \xi) - \Sigma_{ij} E_{ij}] \tag{5.1}$$

where, Σ_{ij} is the macroscopic stress tensor and E_{ij} is the macroscopic strain tensor, which can be divided into elastic strain E^e_{ij}, and transformation strain E^t_{ij}, i.e. $E_{ij} = E^e_{ij} + E^t_{ij}$. T is the temperature and ξ is the fraction of phase transformation. In this expression Helmoltz free energy Φ is defined as (Sun and Hwang 1993a, Patoor *et al.* 1994, Huang and Brinson, 1997)

$$\Phi(\Sigma_{ij}, T, \xi) = \triangle G_{ch}(T) + W_{mech} + W_{surf} \tag{5.2}$$

where $\triangle G_{ch}$ is the change of chemical free energy due to phase transformations, W_{surf} is the surface energy at the inter-phase, i.e. between austenite and martensite, and at the interface (between martensite variants). This term is small and can be ignored. W_{mech} is the mechanical energy.

According to the second law of thermodynamics, we have

$$d\Psi = dE_{fric} \geq 0 \tag{5.3}$$

for any transformation process. Here E_{fric} is the energy dissipation, which is mainly caused by friction during movement of the inter-phase and interface mentioned above.

In a material that is uniform and homogeneous the chemical free energy is a function of temperature only. Its change of chemical energy due to the martensitic phase transformation ($A \Rightarrow M$) at temperature T may be written as

$$\triangle G_{ch}(T) = [G_{ch}^{M}(T) - G_{ch}^{A}(T)]\xi^{A\to M} = \triangle G_{ch}^{A\to M}(T)\xi^{A\to M} \tag{5.4}$$

It may be reasonably accurate to use a linear approximation for $\triangle G_{ch}(T)$ around the equilibrium temperature T_{equ} (where the free energies of the two phases are equal). In this case, we can write

$$\triangle G_{ch}(T) = \triangle \bar{G}_{ch}(T - T_{equ})\xi^{A\to M} \tag{5.5}$$

The mechanical energy, i.e. elastic strain energy, is defined as (Mura, 1987)

$$W_{mech} = \frac{1}{2}\Sigma_{ij}C_{ijkl}\Sigma_{kl} + W_{int} \tag{5.6}$$

where C_{ijkl} are elastic moduli and W_{int} is the internal energy. This last term plays an key role in SMAs. Many methods have been presented to derive approximate expressions for W_{int} (Eshelby 1957, Mura *et al.* 1976). However, due to the complexity of the present problem, none of these methods would be exact. Hence, we will adopt a simple linear function in our discussion for simplicity.

5.1.2 Micromechanics of Transformation

There are two kinds of transformations. The first sort involves a phase change, either from austenite to martensite ($A \Rightarrow M$) or from martensite to austenite ($M \Rightarrow A$). Thus chemical free energy will change in this transformation. Phase transformation can be induced by stress or thermal, i.e. stress induced phase transformation and thermal induced phase transformation. The second sort of transformation is transformation between martensite variants (re-orientation), which are crystallographically equivalent, but have different orientation and different planes of shearing. In both transformations, different martensite variants try to arrange themselves into groups which minimise the internal stress and therefore result in a minimum free energy in a local area.

Hence, in a thermally induced martensite transformation, the martensite that is found is TM, which requires almost no macroscopic shape change from austenite. Stress induced martensite is also in a kind of "*twinned*" structure, but it is different from thermally induced martensite, since the boundary conditions are different. During further loading, one variant which has the most favourable orientation, will expand at the cost of other variants. And finally, a single martensite variant DM may be reached.

We can calculate the favourite transformation system in an approximate manner by **Schmid Law**, which has been used in micromechanical plastic theory for many years.

For yielding, the Schmid Law, as described by Kocks (1970), is stated in a form that is applicable to any stress state: *A single crystal yields on any particular slip system if the shear stress resolved on that slip plane and slip direction reaches a critical value, the "yielding strength" on the that slip system.* If the stress state is specified by the tensor σ_{ij}, and the yield strength on system s as τ^s, this law may be expressed as

$$m_{ij}^s \sigma_{ij} \leq \tau^s \quad (i,j = 1,2,3) \tag{5.7}$$

where m_{ij}^s is the tensor transformation matrix. The left-hand side of Eqn. 5.7 is the properly resolved applied stress, while the right-hand side depends on material property.

For the case of single slip system $s = 1$ in a single crystal under pure tension in the z direction, m_{ij}^s is the **Schmid Factor** Ω

$$\Omega = m_{ij}^s = \cos\chi \cos\lambda \tag{5.8}$$

where χ and λ are the angles between the slip plane normal and the slip direction on the one hand and the tensile axis on the other, see Fig. 5.1.

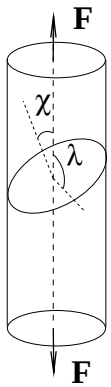

Figure 5.1: χ and λ in uniaxial tension test (from Gilman 1969).

In SMA, instead of yielding, it is phase transformation or martensite reorientation. Therefore, slip system is replaced by transformation system which results to different martensite variants.

Schroeder and Wayman (1977a, 1978, 1979) applied this concept in their study of CuZn single crystal and more recently, Shield (1995) used it to predict the crystal orientation of the minimum transformation stress in a single crystal of CuAlNi, with some success. We should notice that

1. There may be several transformation systems which are possible under the same applied stress. As Shield (1995) observed, these transformation systems may or may not interact. As a result of this interaction, the micro-structure may become **Locked in**, and hardening behaviour can be observed.

2. In thermally induced martensite, nucleation may occurs at many points (therefore many martensite groups are generated simultaneously), as temperature decreases. In fact martensite is much more likely to nucleate in areas of high dislocation density. However, by applying a thermal gradient, it is also possible to generate only one phase transformation front. This is the experimental principle of **Crystallographic Phenomenological Theory (CPT)** suggested by Lieberman *et al.* (1955) to measure the micro-structure of martensite (Nishiyama 1978).

5.2 Thermally Induced Transformation

In this section, SMA is thermally cycled, without any external load. Thus

$$W_{mech} = W_{int}^{A \to M^{tim}}$$

If a SMA material is cooled from high temperature (where only austenite exists) to low temperature, at M_s the martensitic transformation starts and at M_f all austenite is transformed into martensite (TM). If SMA is then heated to high temperature, at A_s reverse transformation starts and it will finish at A_f. Although the proportion of martensite variants present in thermally induced martensite may change with the martensite fraction, for simplicity, we write it as one symbol as M^{tim}. Thus, during cooling, the transformation is $A \Rightarrow M^{tim}$ and it is $M^{tim} \Rightarrow A$ during heating.

In a cooling process, for a small $d\xi^{A \to M^{tim}}$, we may write

$$d\Psi = -\triangle \bar{G}_{ch}(T - T_{equ}) d\xi^{A \to M^{tim}} - \bar{W}_{int}^{A \to M^{tim}}(\xi^{M^{tim}}) d\xi^{A \to M^{tim}} = dE_{fric} = \bar{E}_{fric}^{A \to M^{tim}} d\xi^{A \to M^{tim}}$$

for each small transformation step. Solving for T

$$T = T_{equ} - \frac{\bar{E}_{fric}^{A \to M^{tim}} + \bar{W}_{int}^{A \to M^{tim}}(\xi^{M^{tim}})}{\triangle \bar{G}_{ch}} \tag{5.9}$$

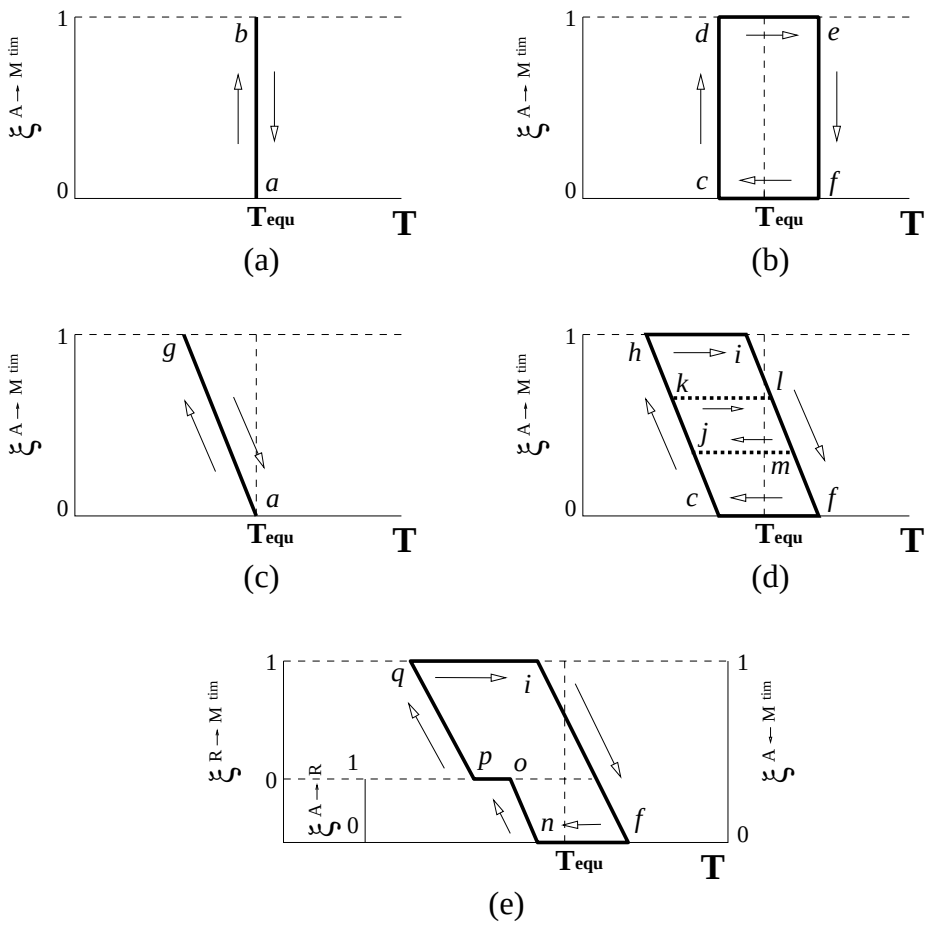

Figure 5.2: Thermally induced phase transformation. (a) $\bar{E}_{fric} = 0, \bar{W}_{int} = 0$; (b) $\bar{E}_{fric} \neq 0, \bar{W}_{int} = 0$; (c) $\bar{E}_{fric} = 0, \bar{W}_{int} \neq 0$; (d) $\bar{E}_{fric} \neq 0, \bar{W}_{int} \neq 0$; (e) $\bar{E}_{fric} \neq 0, \bar{W}_{int} \neq 0$ (with R-phase).

Substituting the two extreme temperature M_s and M_f, and the corresponding value of $\xi^{M^{tim}} = 1$, as well as $\bar{W}_{int}^{A\rightarrow M^{tim}}(0) = 0$

$$M_s = T_{equ} - \frac{\bar{E}_{fric}^{A\rightarrow M^{tim}}}{\triangle \bar{G}_{ch}} \tag{5.10}$$

$$M_f = T_{equ} - \frac{\bar{E}_{fric}^{A\rightarrow M^{tim}} + \bar{W}_{int}^{A\rightarrow M^{tim}}(1)}{\triangle \bar{G}_{ch}} \tag{5.11}$$

In a similar way, we obtain

$$T = T_{equ} + \frac{\bar{E}_{fric}^{A\leftarrow M^{tim}} - \bar{W}_{int}^{A\rightarrow M^{tim}}(\xi^{M^{tim}})}{\triangle \bar{G}_{ch}} \tag{5.12}$$

for $d\xi^{A\leftarrow M^{tim}}$. Thus

$$A_f = T_{equ} + \frac{\bar{E}_{fric}^{A\leftarrow M^{tim}}}{\triangle \bar{G}_{ch}} \tag{5.13}$$

$$A_s = T_{equ} + \frac{\bar{E}_{fric}^{A\leftarrow M^{tim}} - \bar{W}_{int}^{A\rightarrow M^{tim}}(1)}{\triangle \bar{G}_{ch}} \tag{5.14}$$

Figure 5.2 shows the behaviour in four different situations.

- Figure 5.2(a) Energy dissipation $\bar{E}_{fric} = 0$, internal energy $\bar{W}_{int} = 0$. $M_s = M_f = A_s = A_f = T_{equ}$.
- Figure 5.2(b) Energy dissipation $\bar{E}_{fric} \neq 0$, internal energy $\bar{W}_{int} = 0$. $M_s = M_f < T_{equ} < A_s = A_f$.
- Figure 5.2(c) Energy dissipation $\bar{E}_{fric} = 0$, internal energy $\bar{W}_{int} \neq 0$. $M_s = A_f < A_s = M_f = T_{equ}$.
- Figure 5.2(d) Energy dissipation $\bar{E}_{fric} \neq 0$, internal energy $\bar{W}_{int} \neq 0$. Whether $M_f < M_s < A_s < A_f$ or $M_f < A_s < M_s < A_f$ depends on $\bar{W}_{int}^{A\rightarrow M^{tim}}$.

Both Figs. 5.2(a) and (b) show an instantaneous transformation due to lack of internal energy. Figure 5.2(b) represents the case where a thermal gradient is applied, as mentioned in connection with CPT in Section 5.1. Figures 5.2(c) and (d) show a gradual transformation behaviour, due to the existence of internal energy. In Fig. 5.2(d), $j \rightarrow k \rightarrow l \rightarrow m \rightarrow j$ indicates an incomplete thermal cycle.

The total energy dissipation E_{fric}^{total} in a full thermal cycle equals the sum of the total heat measured in this cycle, i.e. in a DSC test. Hence, it is given by the difference between the area under the peak minus the area under the trough, Fig. 2.4. Suppose that T_{equ} is known and the energy dissipations in both forward and reverse transformations are the same, i.e. $E_{fric}^{A\rightarrow M^{tim}} \approx E_{fric}^{A\leftarrow M^{tim}} \approx E_{fric}^{total}/2$,

we will be able to calculate $\bar{W}_{int}(1)$ numerically from a DSC test (Ortin and Planes 1988).

Tong and Wayman (1975) have suggested a way to estimate T_{equ} of the hypothetical AB type binary alloy (free from any kind of defects) based on the enthalpies associated with AA, BB, and AB bonds. A simpler and more practical approach used by many researchers, such as Ortin and Planes (1988, 1989), Funakubo (1987) etc., is the approach proposed by Salizbrenner and Cohen (1979). In this approach, T_{equ} is estimated as the average temperature

$$T_{equ} = (M_s + A_f)/2 \tag{5.15}$$

However, we can see in Fig. 5.2(b) and (d) that if $\bar{E}_{fric}^{A \rightarrow M^{tim}}$ differs a lot from $\bar{E}_{fric}^{A \leftarrow M^{tim}}$, this approximation will be far from accurate.

Different energy dissipations in the forward and reverse transformations can be partially explained by the existence of R-**Phase**. Instead of the martensitic transformation ($A \Rightarrow TM$) as the temperature goes down, austenite may go through an R-phase transition before reaching twinned martensite (Otsuka 1988). However, there is no R-phase transformation during the heating process. The result is a higher energy barrier in the transformation $A \Rightarrow TM$, Fig. 5.2(e).

5.3 Stress Induced Transformation

If deformation is carried out at an extremely slow speed, the temperature of the material will remain equal to the ambient temperature during the whole process. Depending on the ambient temperature and the thermal pre-history of the material, its initial state may be austenite ($\xi_{init}^A = 1$), austenite + twinned martensite ($1 > \xi_{init}^A > 0$), or twinned martensite ($\xi_{init}^A = 0$). We will discuss these three different cases separately.

5.3.1 Case $\xi_{init}^A = 1$

A. Micro-mechanism

As the material temperature is lower than M_d, which is the highest temperature where a stress induced martensitic transformation can occur (Adler *et al.* 1990), but is still higher than M_s, $\xi_{init}^A = 1$. When the applied load F is over a certain value, the stress induced martensitic transformation starts.

To understand what happens in this process, a description of the associated micro-deformation is required. The martensitic transformation includes a *lattice deformation*, a *lattice invariant strain*, and a *rigid-body rotation* (see Nishiyama 1978, Funakubo 1987 for details).

Thus, in general, the deformation $m_i \boldsymbol{d}_i$ can be written as, see Fig. 5.3

$$m_i \boldsymbol{d}_i = m_i^p \boldsymbol{d}_i^p + m_i^n \boldsymbol{p}_i^n \tag{5.16}$$

where $m_i^p \boldsymbol{d}_i^p$ and $m_i^n \boldsymbol{p}_i^n$ are the pure shearing component and the expansion (or contraction) component, respectively (Christian 1982). Here, $\boldsymbol{d}_i$, $\boldsymbol{d}_i^p$, and $\boldsymbol{p}_i^n$ are unit vectors.

m_i^n is caused by the difference in volume between austenite and martensite, and can be calculated as

$$m_i^n = \frac{V^M - V^A}{V}$$

However, in most SMAs this volume change is small (e.g. Nitinol shrinks by 0.34% after the martensitic transformation). Compared with the contribution from the shearing component, this term can be ignored.

If the martensite plate shown in Fig. 5.4(a), is loaded by the tensile force F, the transformation strain along the direction of F is (Funakubo 1987)

$$\begin{aligned} \epsilon^{t^{A\to M^i}} &= \sqrt{(m_i^p \cos\chi)^2 + 2m_i^p \cos\chi\cos\lambda + 1} - 1 + m_i^n \cos^2\chi \\ &\approx m_i^p \cos\chi\cos\lambda = \Omega m_i^p \end{aligned} \tag{5.17}$$

Note that λ is also the angle between the tensile axis and the $\boldsymbol{d}_i^p$ direction.

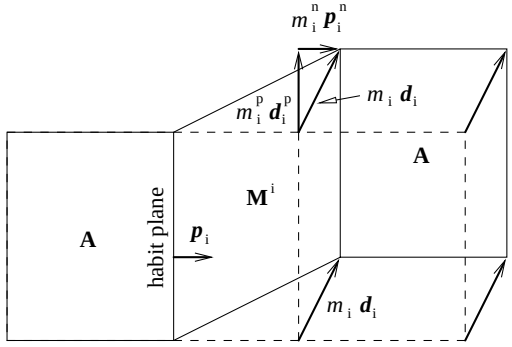

Figure 5.3: Shape deformation accompanying the formation of a single martensite plate (from Funakubo 1987).

In Fig. 5.4(a), it is assumed that a tiny defect in the volume dV has triggered the transformation there. From Eqns. 5.1 and 5.2

$$d\Psi = -[\triangle \bar{G}_{ch}(T - T_{equ}) + W_{mech} - \Sigma_{ij} E_{ij}]dV = \bar{E}_{fric}^{A\to M^i} dV$$

Since $W_{int} = 0$, if there is only one martensite variant, substituting Eqn. 5.6 for W_{mech}

$$-\frac{1}{2}\Sigma_{ij}(C_{ijkl}^A - C_{ijkl}^{M^i})\Sigma_{kl} + \Sigma_{ij} E_{ij}^t = \bar{E}_{fric}^{A\to M^i} + \triangle \bar{G}_{ch}(T - T_{equ})$$

Rewriting this equation in terms of σ, $\epsilon^{t^{A\to M^i}}$, D^A, and D^{M^i} (where D^A and D^M are the Young's Moduli[1] of austenite and of martensite variant i, respec-

[1]Obviously, the Young's Modulus is orientation dependent.

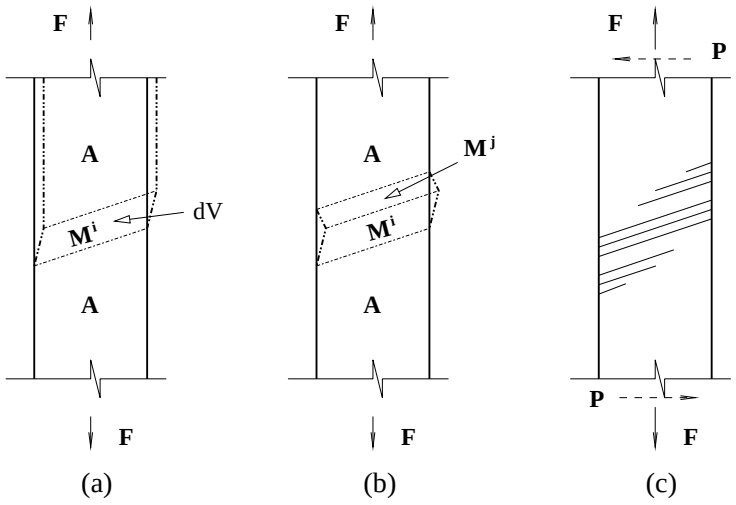

Figure 5.4: Tension test. (a) Without constraint; (b) with constraint (*twinned martensite*); (c) with constraint (tension-shearing effect, macroscopic view).

tively), we can solve to find the stress to generate the phase transformation

$$\sigma^{A\to M^i} = \frac{\epsilon^{t^{A\to M^i}} - \sqrt{(\epsilon^{t^{A\to M^i}})^2 + 2(\frac{D^A - D^{M^i}}{D^A D^{M^i}})[\bar{E}^{A\to M^i}_{fric} + \triangle\bar{G}_{ch}(T - T_{equ})]}}{\frac{D^{M^i} - D^A}{D^A D^{M^i}}} \tag{5.18}$$

For simplicity, we may assume $D^A \approx D^{M^n} = D, (n = i, j, k, ...)$,

$$\bar{E}^{A\to M^i}_{fric} + \triangle\bar{G}_{ch}(T - T_{equ}) = \sigma^{A\to M^i}\epsilon^{t^{A\to M^i}} = \Omega m_i^p \sigma^{A\to M^i} \tag{5.19}$$

Since m_i^p is a constant,

$$\Omega\sigma^{A\to M^i} = \frac{\bar{E}^{A\to M^i}_{fric} + \triangle\bar{G}_{ch}(T - T_{equ})}{m_i^p} \tag{5.20}$$

Thus, provided that $\bar{E}^{A\to M^n}_{fric}(n = j, j, k, ...)$ is also a constant, Eqn. 5.20 has the form of Schmid Law (Eqn. 5.7).

We can use Eqn. 5.20 to investigate the non-symmetrical behaviour in tension and compression of Nitinol reported by Chumljakov and Starenchenko (1995).

Figure 5.5 plots the maximum $\epsilon^{t^{A\to M}}$ along the direction of pulling for Nitinol grains with different orientation, for both tension and compression. In order to consider grains in any orientation, we have introduced three Eulerian angles ϕ, θ, and ψ — see Fig. 5.6 — which vary in the range (Falk 1989)

$$-\pi \le \phi \le \pi, \quad -\pi/2 \le \theta \le \pi/2, \quad -\pi/2 \le \psi \le \pi/2$$

In the coordinate system of Fig. 5.6 ϕ has no effect on $\epsilon^{t^{A\to M}}_{max}$ and, because of symmetry, we only need to calculate within the range of $0 \le \theta \le \pi/2, 0 \le$

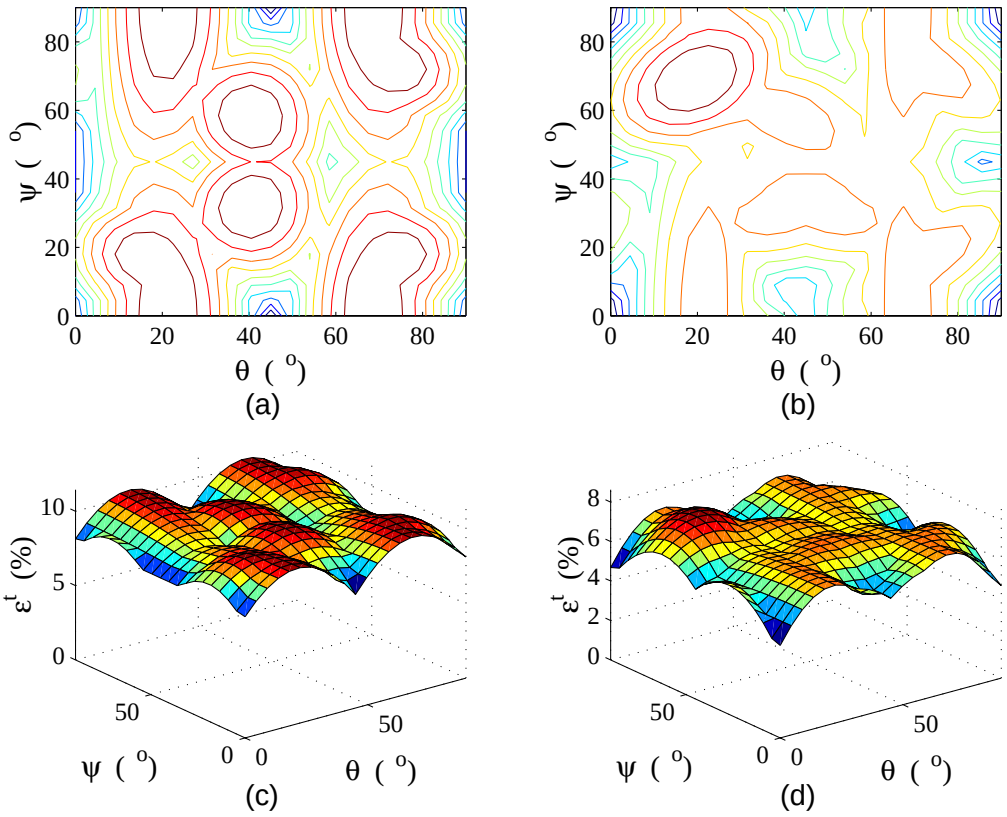

Figure 5.5: $\epsilon_{max}^{t^{A\rightarrow M}}$ of unconstrained Nitinol grains with different orientation. (a) Contour of $\epsilon_{max}^{t^{A\rightarrow M}}$ in tension; (b) contour of $\epsilon_{max}^{t^{A\rightarrow M}}$ in compression; (c) $\epsilon_{max}^{t^{A\rightarrow M}}$ in tension; (d) $\epsilon_{max}^{t^{A\rightarrow M}}$ in compression.

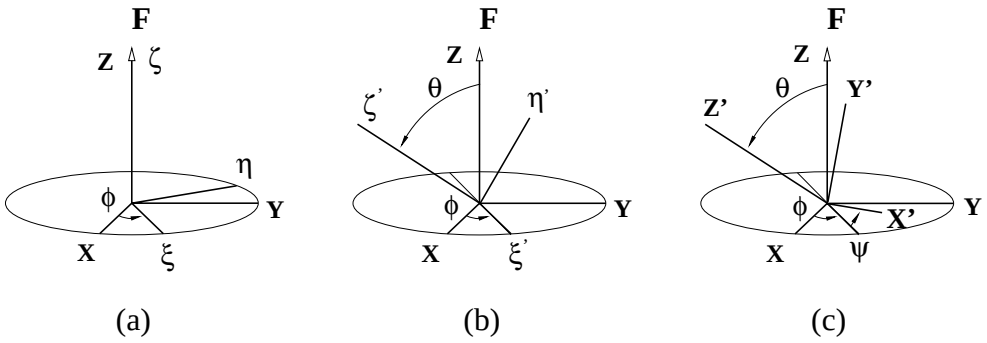

Figure 5.6: Definition of Euler angles ϕ, θ, and ψ (from Goldstein 1950).

$\psi \leq \pi/2$. See Knowles and Smith (1981), Saburi and Nenno (1982) for details of the associated micro-structure, correspondence variants and how to calculate the transformation strain in a global coordinate system.

Figure 5.5 shows that the $\epsilon_{max}^{t^{A\to M}}$ in tension differs a lot from that in compression. The maximum $\epsilon_{max}^{t^{A\to M}}$ and average $\epsilon_{max}^{t^{A\to M}}$ in tension case are 10.45% and 9.63%, respectively, while in compression they are 7.63% and 6.55%, respectively. Therefore, the transformation stress in tension is normally lower than that in compression.

B. Behaviour in Tension

As shown in Fig. 5.7(a) and (b), during loading from $a \to b$ the deformation is purely elastic

$$\epsilon = \epsilon^e = \frac{\sigma}{D} \tag{5.21}$$

When σ reaches $\sigma^{A\to M^i}$, where

$$\sigma^{A\to M^i} = \frac{\bar{E}_{fric}^{A\to M^i} + \triangle \bar{G}_{ch}(T - T_{equ})}{\epsilon^{t^{A\to M^i}}} \tag{5.22}$$

austenite transforms to martensite (M^i). At point c the total strain is

$$\epsilon = \frac{\sigma^{A\to M^i}}{D} + \epsilon^{t^{A\to M^i}} \tag{5.23}$$

The unloading $c \to d$ is purely elastic, until σ reaches another critical value, $\sigma^{A\leftarrow M^i}$, where

$$\sigma^{A\leftarrow M^i} = \frac{-\bar{E}_{fric}^{A\leftarrow M^i} + \triangle \bar{G}_{ch}(T - T_{equ})}{\epsilon^{t^{A\leftarrow M^i}}} \tag{5.24}$$

Obviously, $\epsilon^{t^{A\to M^i}} = \epsilon^{t^{A\leftarrow M^i}}$. Note that practically cd should not be parallel to ab, since $D^A \neq D^M$.

If the temperature is high, as shown in Fig. 5.7(a), all strain is recovered after the external load is released (**Superelasticity**). However, if the temperature is not very high, as we see in Fig. 5.7(b), $\sigma^{A\leftarrow M^i}$ may be negative. In that case, we can either heat SMA to a higher temperature ($f \to a$ in Fig. 5.7(b)) or, if T is still higher than T_{equ}, we can apply a compressive stress and then release it ($d \to e \to a$ in Fig. 5.7(b)), to get full recovery.

It is also possible that instead of transforming back to A, M^i may transform to another variant ($M^{i'}$) by re-orientation under compression, if $\sigma^{A\leftarrow M^i} > \sigma^{M^i\to M^{i'}}$. $a \to b \to c \to f \to a$ is shape memory effect (SME). σ^{A-M^i} is known as **Maxwell Stress** (Leo *et al.* 1993), where the two phases are in equilibrium.

In some SMAs, further loading may trigger another phase transformation as shown in Fig. 5.7(c). We use X to denote this phase. During unloading, the

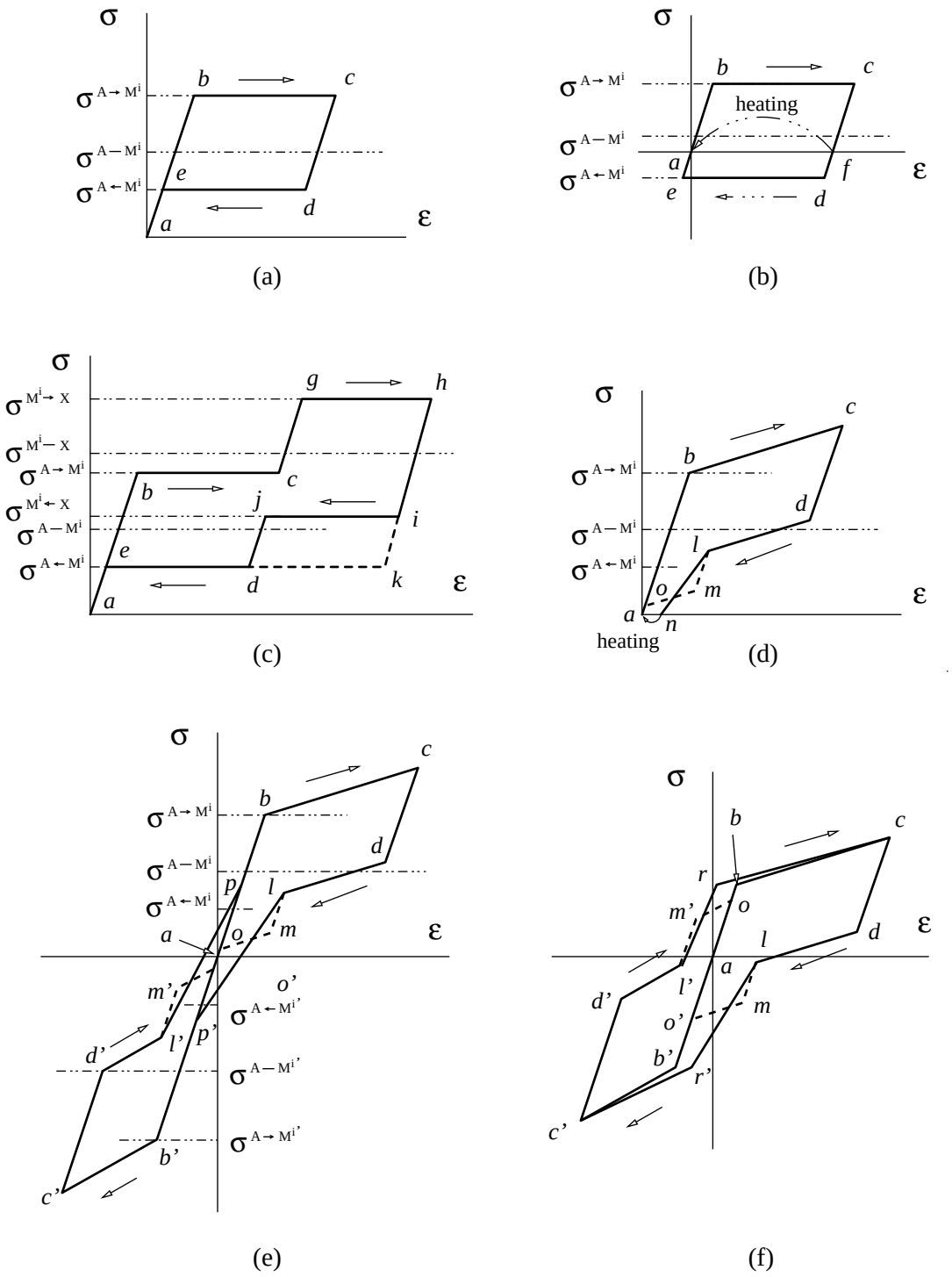

Figure 5.7: Loading/unloading $\xi^A_{init} = 1$. (a) High temperature (superelasticity); (b) low temperature (SME); (c) three-phase material at high temperature; (d) SMA with hardening and locking-in; (e) tension-compression at high temperature; (f) tension-compression at low temperature.

material may go back one phase after another along the path $h \rightarrow i \rightarrow j \rightarrow d \rightarrow e$, or it may go from $X \Rightarrow A$ directly ($h \rightarrow i \rightarrow k \rightarrow d \rightarrow e$), if $\bar{\sigma}^{A \leftarrow X} < \bar{\sigma}^{M^i \leftarrow X}$. The experimental result which shows the latter situation can be seen in Fig. 10 of Schroeder and Wayman (1979).

It should be pointed out that in a real tensile test the specimen is normally constrained by clamps at both ends. Thus, deformation, such as that shown by a dashed line in Fig. 5.4(a), may not be produced everywhere. Instead, the shape shown in Fig. 5.4(b) or Fig. 5.4(c) may be observed (see Fig. 2 in Schroeder and Wayman 1979).

Since the heat is generated in the martensitic transformation, it becomes harder for further movement of the inter-phase due to the temperature increase around the transformation area. If there is lack of the interactive force, such as W_{int} in the inter-phase, the phase transformation front may stop and a new front may start at somewhere else. This explains why there is no phase transformation front movement behaviour in the test carried out by Schroeder and Wayman (1979).

It is quite possible that several martensite variants have the same maximum Schmid factor. Thus, several transformation systems (martensite variants) may be triggered under the same tensile stress (Shield 1995). If these transformation systems do not interact at all, the transformation stress is the same as that in a single transformation system case, but its transformation strain is $\sum \epsilon^{t^{A \rightarrow M^n}}$.

However, sometimes a strong interaction develops and even locking-in of the micro-structure. Therefore, we will expect hardening behaviour during loading. We can include the hardening effect as a W_{int} term into the analysis. A locked-in structure has the feature that it is easy to form, but is much harder to eliminate. Therefore, we only need to pay attention to the effects of the locking-in structure during the reverse transformation.

Due to the effect of locked-in structure, the last-formed, first-reversed behaviour often found in the literature (Christian 1982), may not hold.

C. Tension/Compression Cycle

We have explained that the transformation stress in compression is normally higher than that in tension, we will not expect symmetry between tension and compression.

Figure 5.7(e) and (f) show two examples at high and medium temperatures, respectively. The point we should notice in Fig. 5.7(e) is that $l \rightarrow p'$ and $l' \rightarrow p$ are $M \Rightarrow A$ transformations, which means at p and p' the material is pure austenite. If temperature is lower, not all transformation $M^{i,j\cdots} \Rightarrow A$ can be finished before the reverse transformation $A \Rightarrow M^{i',j'\cdots}$ starts during reverse loading. Thus some of the remaining martensite ($M^{i,j\cdots}$) will transform to another martensite variant ($M^{i',j'\cdots}$) directly. This is the case shown in Fig. 5.7(f). If the ambient temperature is even lower, for example $M_s < T < A_s$, there will be no austenite after the first loading (either in tension or compression), and all later transformations involves

only martensite re-orientation.

5.3.2 Case $\xi^A_{init} = 0$

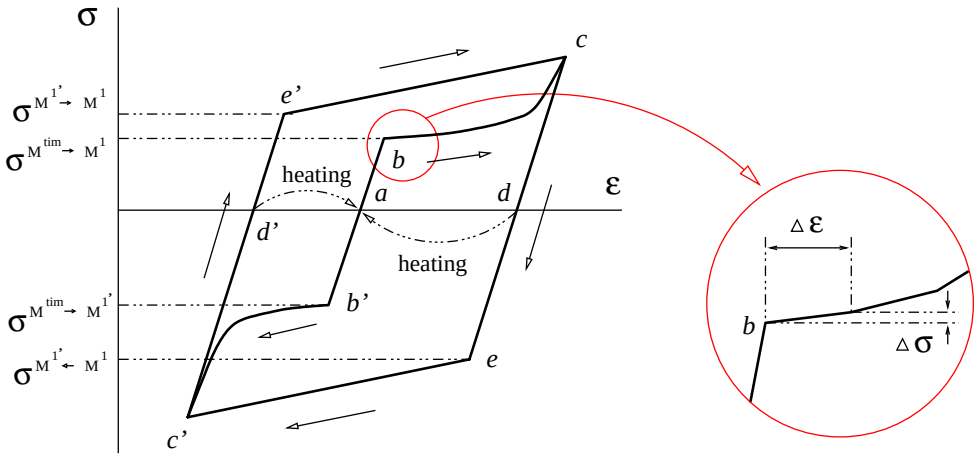

Figure 5.8: Tension/compression cycle at $\xi^A_{init} = 0$.

If $\xi^A_{init} = 0$, we start with twinned martensite (M^{tim}) at point a, see Fig. 5.8. During loading, M^{tim} goes through a re-orientation process, i.e. growth of certain martensite variants (M^1) which have the most favoured orientation, at the expense of other variants. This re-orientation process (detwinning process) can be performed in a more gradual manner, as the transformation strain can be very small in each re-orientation step. As shown in the detail of Fig. 5.8, when the load increases, both ϵ^t and ϵ^e increase in a small steps after re-orientation starts ($b \rightarrow c$).

The stress at which the re-orientation starts ($\sigma^{M^{tim} \rightarrow \triangle M^1}$) can be calculated in a similar way to Eqn. (5.22) but with $\bar{W}^{A \rightarrow M^{tim}}_{int}(1)$ instead of the term $\triangle \bar{G}_{ch}$. Hence, we have

$$\sigma^{M^{tim} \rightarrow \triangle M^1} = \frac{\bar{E}^{M^{tim} \rightarrow \triangle M^1}_{fric} - \bar{W}^{A \rightarrow M^{tim}}_{int}(1)}{\epsilon^{t^{M^{tim} \rightarrow \triangle M^1}}} \tag{5.25}$$

This tiny step is completed at

$$\sigma^{M^{tim} \rightarrow \triangle M^1} = \frac{\bar{E}^{M^{tim} \rightarrow \triangle M^1}_{fric} - \bar{W}^{A \rightarrow M^{tim}}_{int}(1) + \bar{W}^{M^{tim} \rightarrow \triangle M^1}_{int}(1)}{\epsilon^{t^{M^{tim} \rightarrow \triangle M^1}}} \tag{5.26}$$

Further loading can be analysed in the same manner. However, as the re-orientation goes further, the associated transformation strain decreases and, therefore, the slope of the curve increases. The martensite re-orientation is completed at point c where martensite variant group is symbolised as M^1 (Note that this

M^1 can be the same as M^i in Fig. 5.7). In that case, the stress at c may be written approximately as

$$\sigma_c \approx \frac{\bar{E}_{fric}^{M^{tim}\to M^1} + \bar{W}_{int}^{M^{tim}\to M^1}(1)}{\epsilon^{t^{M^{tim}\to M^1}}} \tag{5.27}$$

The unloading $c \to d$ is almost elastic. The application of a compressive force will lead to further elastic deformation ($d \to e$). At point e, the stress reaches another critical value, which leads the transformation of M^1 to $M^{1'}$. This transformation starts at

$$\sigma^{M^1\to\triangle M^{1'}} = \frac{-\bar{E}_{fric}^{M^1\to\triangle M^{1'}} + \bar{W}_{int}^{M^{tim}\to M^1}(1)}{\epsilon^{t^{M^1\to\triangle M^{1'}}}} \tag{5.28}$$

and finishes at c', where

$$\sigma_{c'} \approx \frac{-\bar{E}_{fric}^{M^1\to M^{1'}} + \bar{W}_{int}^{M^1\to M^{1'}}(1)}{\epsilon^{t^{M^1\to M^{1'}}}} \tag{5.29}$$

Here, $\bar{W}_{int}^{M^1\to M^{1'}}(1) \approx \bar{W}_{int}^{M^{tim}\to M^{1'}}(1)$.

5.3.3 Case $1 > \xi_{init}^A > 0$

In this circumstance, both martensitic transformation and martensite re-orientation occur during loading. The real situation is quite complex due to the coupling of both processes. We will only discuss the V-**Shape of the Critical Stress** shown in Fig. 2.8. This phenomenon has been reported for many SMAs, for example in CuZn (Wayman and Duerig 1988) and NiTi (Adler *et al.* 1990).

Sun and Hwang (1993b) regarded this phenomenon as the result of the anomalous decrease of the elastic moduli in the vicinity of the transformation temperature, i.e. lattice softening. Their evidence was the elastic modulus vs. temperature relation measured by Hasiguti and Iwasaki (1968). However, the elastic modulus is hard to measure without the triggering a transformation.

Here we try to explain this behaviour from a thermo-micromechanical point of view. We first analyse a SMA which is cooled from high temperature, where initially $\xi^A = 1$, and then study a material which is heated from low temperature, where initially $\xi^{M^{tim}} = 1$. To simplify the situation, we assume that

- $\epsilon^{t^{A\to M^{i,j\cdots}}} = \epsilon^{t^{M^{tim}\to\triangle M^1}}$;
- $\bar{E}_{fric}^{A\to M^{i,j\cdots}} = \bar{E}_{fric}^{M^{tim}\to\triangle M^1}$.

The cooling process is illustrated in Fig. 5.9(a). For stress induced martensite, we have the transformation start stress

$$\sigma^{A\to M^{i,j\cdots}} \approx \frac{\bar{E}_{fric}^{A\to M^{i,j\cdots}} + \triangle\bar{G}_{ch}(T - T_{equ})}{\epsilon^{t^{A\to M^{i,j\cdots}}}} \tag{5.30}$$

for $T > M_s$ (line: $a - b$), and

$$\sigma^{A \to M^{i,j\cdots}} \approx \frac{\bar{E}_{fric}^{A \to M^{i,j\cdots}} + \triangle \bar{G}_{ch}(T - T_{equ}) - \bar{W}_{int}^{A \to M^{tim}}(\xi_{init}^{M^{tim}})}{\epsilon^{t^{A \to M^{i,j\cdots}}}} \tag{5.31}$$

for $M_s > T > M_f$ (line: $b - c$). For martensite re-orientation, we have the re-orientation start stress

$$\sigma^{M^{tim} \to \triangle M^1} \approx \frac{\bar{E}_{fric}^{M^{tim} \to \triangle M^1} - \bar{W}_{int}^{A \to M^{tim}}(\xi_{init}^{M^{tim}})}{\epsilon^{t^{M^{tim} \to \triangle M^1}}} \tag{5.32}$$

for $M_s > T > M_f$ (line: $e - f$), and

$$\sigma^{M^{tim} \to \triangle M^1} \approx \frac{\bar{E}_{fric}^{M^{tim} \to \triangle M^1} - \bar{W}_{int}^{A \to M^{tim}}(1)}{\epsilon^{t^{M^{tim} \to \triangle M^1}}} \tag{5.33}$$

for $T < M_f$ (line: $f - g$).

Thus the real critical stress is expected to vary following the path $a - b - h - f - g$, which has a characteristic V-shape.

The heating process is illustrated in Fig. 5.9(b). For stress induced martensite, we have the transformation start stress

$$\sigma^{A \to M^{i,j\cdots}} \approx \frac{\bar{E}_{fric}^{A \to M^{i,j\cdots}} + \triangle \bar{G}_{ch}(T - T_{equ})}{\epsilon^{t^{A \to M^{i,j\cdots}}}} \tag{5.34}$$

for $T > A_f$ (line: $a - b$), and

$$\sigma^{A \to M^{i,j\cdots}} \approx \frac{\bar{E}_{fric}^{A \to M^{i,j\cdots}} + \triangle \bar{G}_{ch}(T - T_{equ}) - \bar{W}_{int}^{A \to M^{tim}}(\xi_{init}^{M^{tim}})}{\epsilon^{t^{A \to M^{i,j\cdots}}}} \tag{5.35}$$

for $A_f > T > A_s$ (line: $b - c$). For martensite re-orientation, we have the re-orientation start stress

$$\sigma^{M^{tim} \to \triangle M^1} \approx \frac{\bar{E}_{fric}^{M^{tim} \to \triangle M^1} - \bar{W}_{int}^{A \to M^{tim}}(\xi_{init}^{M^{tim}})}{\epsilon^{t^{M^{tim} \to \triangle M^1}}} \tag{5.36}$$

for $A_f > T > A_s$ (line: $e - f$), and

$$\sigma^{M^{tim} \to \triangle M^1} \approx \frac{\bar{E}_{fric}^{M^{tim} \to \triangle M^1} - \bar{W}_{int}^{A \to M^{tim}}(1)}{\epsilon^{t^{M^{tim} \to \triangle M^1}}} \tag{5.37}$$

for $T < A_s$ (line: $f - g$). Thus, the critical stress is expected to vary following the path $a - b - j - i - h - f - g$, which also describes a V-shape, but much smaller than that obtained for cooling.

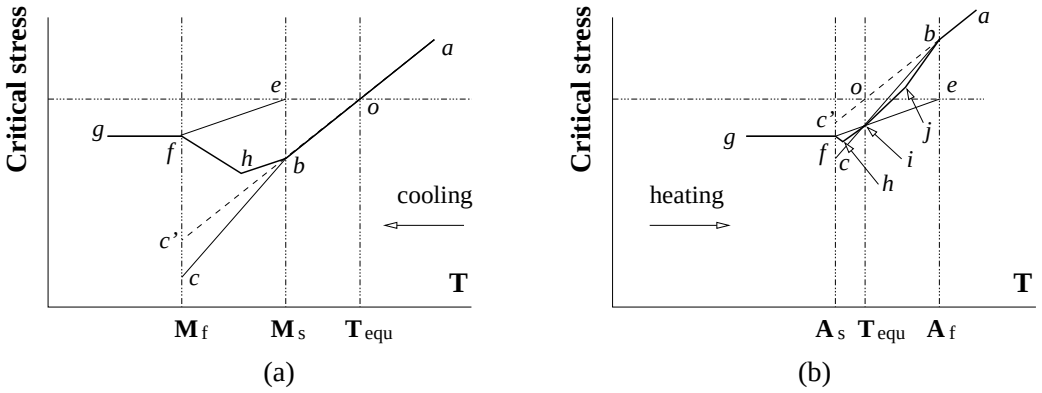

Figure 5.9: V-shape of critical stress. (a) During cooling; (b) during heating.

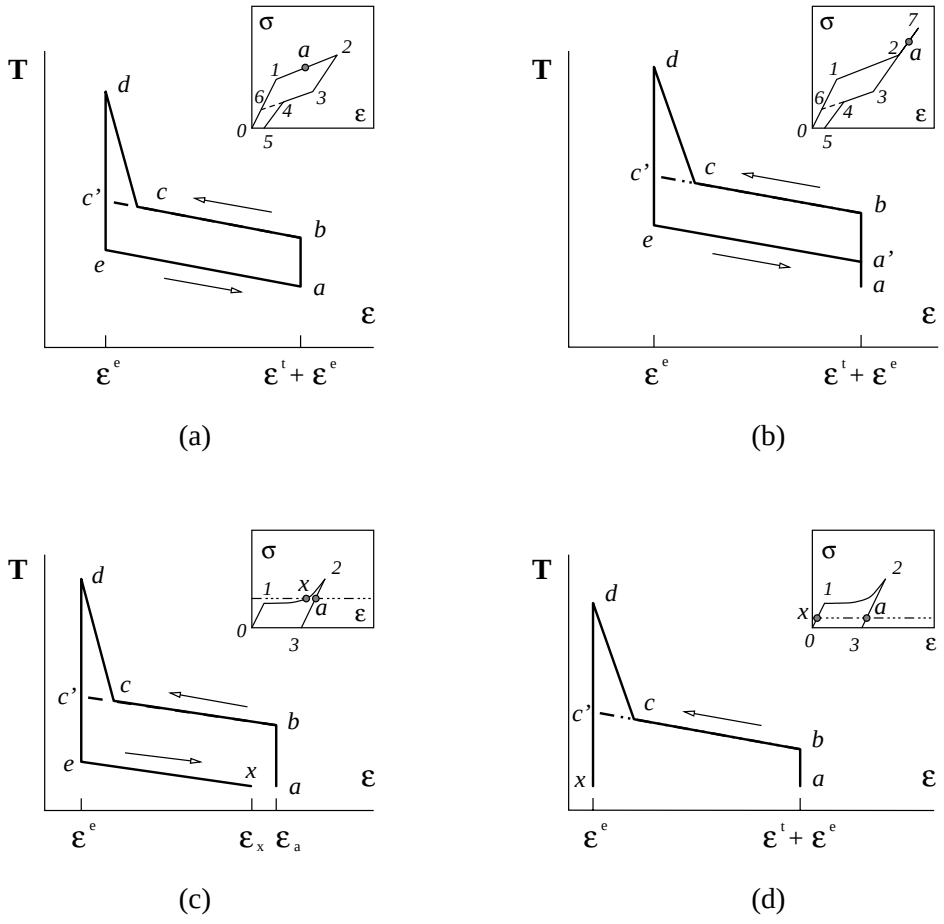

Figure 5.10: Thermal cycling. (a) $\xi^M < 1$, loading; (b) $\xi^M = 1$, loading; (c) loading followed by a small unloading; (d) loading followed by a large unloading.

5.4 Thermal Cycling under Load

There are many initial conditions that thermal cycling may start from. SMA can be loaded from austenite, twinned martensite, or a mixture of austenite and twinned martensite. Alternatively, before thermal cycling, SMA can be loaded, or loaded and then unloaded. We only discuss four situations, whose numerical analysis can be performed in a similar way to the previous section.

1. Figure 5.10(a). Before thermal cycling, SMA (initially austenite) has been loaded to a, within its phase transformation regime, i.e. $\xi^M < 1$. Thus, upon heating a complete thermal cycling will produce only elastic straining to point d, and upon cooling a full recovery back to the start point a. Due to the locking-in effect, $M \Rightarrow A$ does not finish at c', instead a much higher temperature is required to reach pure austenite.

2. Figure 5.10(b). If SMA (initially austenite) has been loaded to its regime where $\xi^M = 1$, we will observe $a' - a$ during cooling. The reason is that the transformation is completed at point a'.

3. Figure 5.10(c). First, twinned martensite is loaded to the transformation finish point (point 2), and then unloaded to a. After one thermal cycle, the total strain moves back from a to x, since a full detwinning cannot be completed at this reduced load.

4. Figure 5.10(d). If loading force is further reduced, thermal cycling may result in only elastic strain.

Generally, the higher the applied load, the higher the temperature required for the transformation $M \Rightarrow A$. However, if thermal cycling is started after unloading, the transformation temperature for heating will be affected by the previous loading as well.

5.5 Polycrystals

The main difference between a single crystal and a polycrystal is that in a polycrystal, neighbouring grains apply a constraint on the each other's deformation.

In SMAs, grain size effects on transformation temperatures have been recognised (e.g. Section. 2.3). Durlu (1997) recently reported a nearly linear relationship between grain size and M_s with FeMnMo in thermal induced martensite. But this kind of relationship has not been found in other SMAs.

In stress induced transformation, different transformation system will be induced in different grain, and as reported by Patoor *et al.* (1996), due to the effects of grain boundary, many different martensite variant groups are formed in one grain even in uniaxial tension case. Therefore, the transformation start stress and the stress vs. strain relationship are also affected by the grain size as shown in Fig. 2.13.

It is also extremely difficult to consider the effects of heat treatment, and slight variation of composition (Duerig and Pelton 1994) or small proportion of additional other element[2] etc. in a theoretical model for real engineering applications.

The thermo-micromechanical model presented in this chapter was not used in actuator design.

[2]For examples, in Nitinol, Cu element shifts transformation towards low temperature (Goubaa *et al.* 1988), while Pt and Pd tend to decrease M_s and then increase it, eventually achieving as high as 350°C (Duerig and Pelton 1994).

Chapter 6

Development of Wire Actuators: First Step

In this Chapter, we present the design, testing and simulation of two actuators based on two different concepts. This is the first step of our design. Our aims were to build a prototype of Nitinol wire-based actuator for each concept to gain experience in practical design, and to apply the model we have developed in the simulation. After exploring different concepts, we chose one concept from them for our next step: to design a two-way Nitinol wire-based actuator.

6.1 First Concept

The basic idea for a simple wire actuator is shown in Fig. 6.1. Two rigid disks are mounted on a shaft at a distance H. Disk 1 is fixed to the shaft, while disk 2 is free to rotate. A Nitinol wire of unstrained length L_o is attached to disk 1 at point o, and to disk 2 at point a. Both points are at a distance R from the centre of the shaft. Disk 2 is rotated by an amount of θ_o while the wire becomes taut ($\theta_o = 0$ if $L_o = H$). Then, a torque M is applied to disk 2, whose magnitude is sufficiently large to induce a transformation in the Nitinol wire. Thus, the length of the wire increases to

$$L = L_o\ (1 + \epsilon) \tag{6.1}$$

while the rotation θ of disk 2 increases to

$$\theta = 2\ \sin^{-1}(\frac{x}{2\ R}) \tag{6.2}$$

where

$$x = \sqrt{L^2 - H^2} \tag{6.3}$$

If the wire is heated above the temperature A_f, it contracts back, thus rotating disk 2 by $(\theta - \theta_o)$.

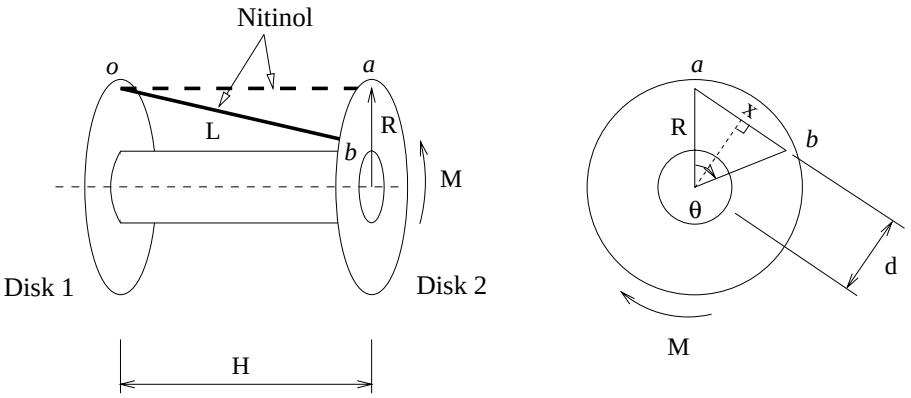

Figure 6.1: Concept of first actuator ($\theta_o = 0$).

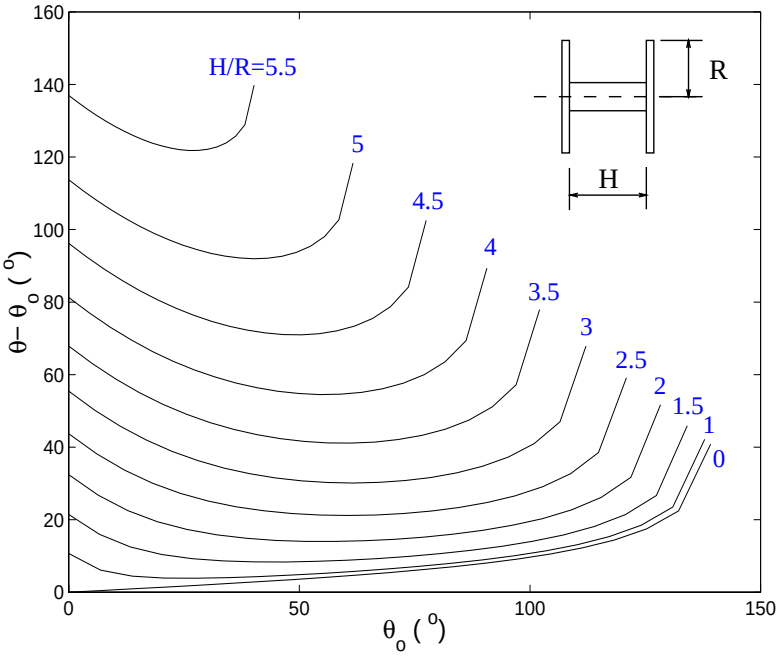

Figure 6.2: Geometric relation for first actuator concept ($\epsilon^t = 6.7\%$).

The performance of this simple actuator depends on the values of θ_o and H/R. Figure 6.2 shows plots of the rotation $(\theta - \theta_o)$ vs. the initial rotation θ_o for different values of H/R. In Eqn. 6.1, $\epsilon = \epsilon^e + \epsilon^t$. The elastic strain ϵ^e varies with the stress in the wire during actuation, but we can ignore its contribution for simplicity. The transformation strain ϵ^t is 6.7%, which is the maximum strain measured in our tests (Section 4.2.3).

It is observed that larger rotation angles are obtained for $\theta_o \approx 0^o$ and also for larger θ_o, but the problem with large initial angles is that the wire would touch the shaft. Hence, in Fig. 6.2 a cut-off point for each curve has been derived from the condition $\theta = 180^o$ which is still in fact impossible to achieve. Hence, the value $\theta_o \approx 0^o$ is the best solution.

It is also observed that the rotation angle increases with H/R and, subject to any overall size constraints, it is desirable to choose H/R as large as possible.

6.2 Design and Simulation

A schematic diagram of an actuator based on this concept is shown in Fig. 6.3. A central disk — mounted on a ball bearing — is connected by a single Nitinol wire to two fixed shoulders. In this configuration, $H = 52$ mm. In another configuration simulated, where three disks were used, $H = 26$ mm.

The disk consists of a 7 mm thick steel annulus shrunk fit onto a SKF deep-groove ball bearing (o.d. 24 mm, i.d. 9 mm). In order to insulate both electrically and thermally the Nitinol wire from the steel disk, a series of Macor[1] cylinders with 1.1 mm diameter holes in the centre are inserted into 5 mm diameter holes in the disk.

Two specially designed clamps are used to fix the ends of the wire, Fig. 6.3(b). A small preload can be applied on the wire by turning the square head of the clamp. A thin Tufnol plate is inserted between the shoulder of the actuator and the wire clamp, for electrical insulation. The shaft is not made as a single piece, but consists of four segments with a threaded head at one end and a threaded hole at the other end. Thus, both the one-disk and the three-disk configurations can be tested on the same hardware. The disks have an outer diameter of 48 mm with holes for the Nitinol wire at $R = 18.5$ mm from the centre of the shaft.

We simulate the behaviour of the actuator in the two different configurations, one-disk and three-disks, under a constant torque M. Our simulation is based on the constitutive model of Section 4.2 (specimen 1), and includes the effects of the actual force in the Nitinol wire, which varies as the disks rotate. The temperature distribution is assumed to be uniform at this stage.

Figure 6.4 shows the predicted behaviour of the single-disk actuator with an initial rotation angle $\theta_o = 0$ and $H/R = 2.8$. First, the external torque is increased from 0 to 2 Nm. The disk turns by about 60^o, Fig. 6.4(a), while the stress in the wire increases to about 230 MPa, Fig. 6.4(b), and a total strain of about 6.5% builds up. Then, under a constant torque of 2 Nm the wire is heated from

[1]Macor is a machinable ceramic with the required insulating properties.

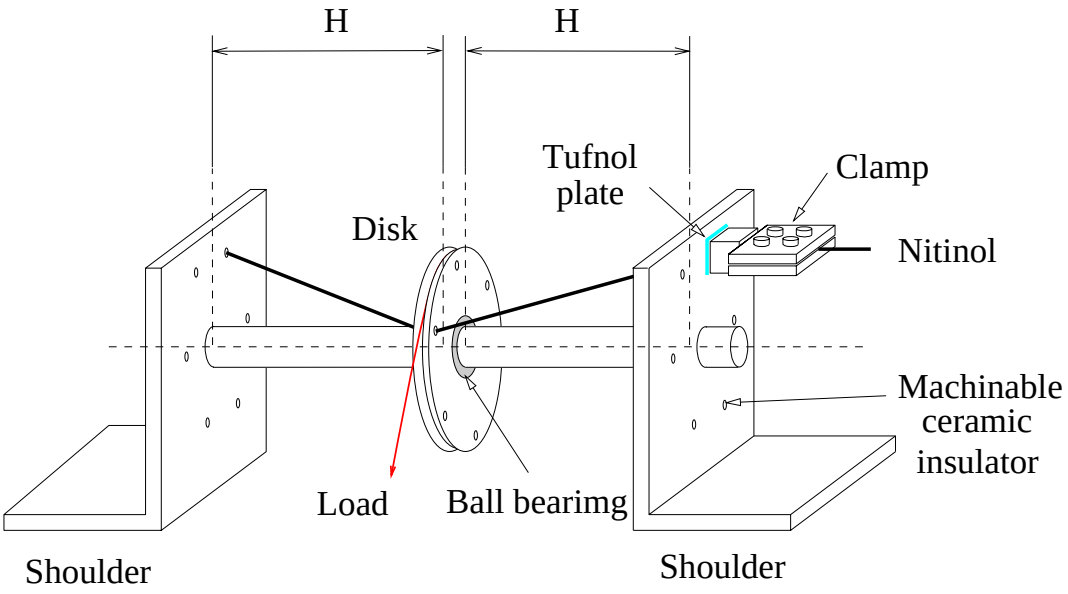

(a)

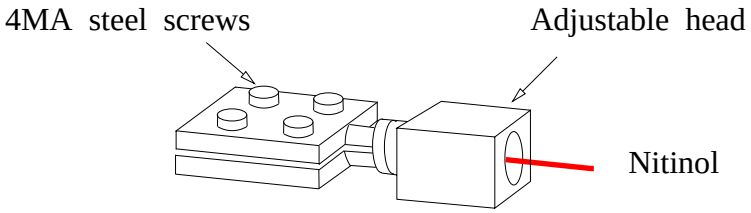

(b)

Figure 6.3: Schematic diagram of first concept (configuration with one disk). (a) Actuator; (b) details of clamp.

20^oC to 160^oC, and the disk turns back by about 30^o while the stress increases to 400 MPa. Finally, the wire is cooled back to the ambient temperature and the disk returns to its position before the start of the thermal cycle. The main result, shown in Fig. 6.4(d), is the relationship between T and rotation angle.

Figure 6.5 shows the predicted behaviour of the three-disk actuator with θ_o= 0 and H/R = 1.4. The plots show that the maximum rotation of the three-disk actuator is approximately identical to the one-disk actuator. This was expected because as shown in Fig. 6.2, the rotation angle for θ_o= 0 is roughly proportional to H/R.

So far, it has been assumed that the temperature along the wire is constant. To take the actual temperature distribution into consideration, we assume that the temperature at the two ends of the wire remains equal to the ambient temperature and, because the wire is heated/cooled slowly, we use the steady-state solution given in the Appendix B.1 for the temperature distribution.

Figure 6.6 shows that when we consider the non-uniformity of the temperature distribution, the rotation angle decreases in both cases, in the one disk actuator by about 7.5^o while in the three-disk case by 6^o.

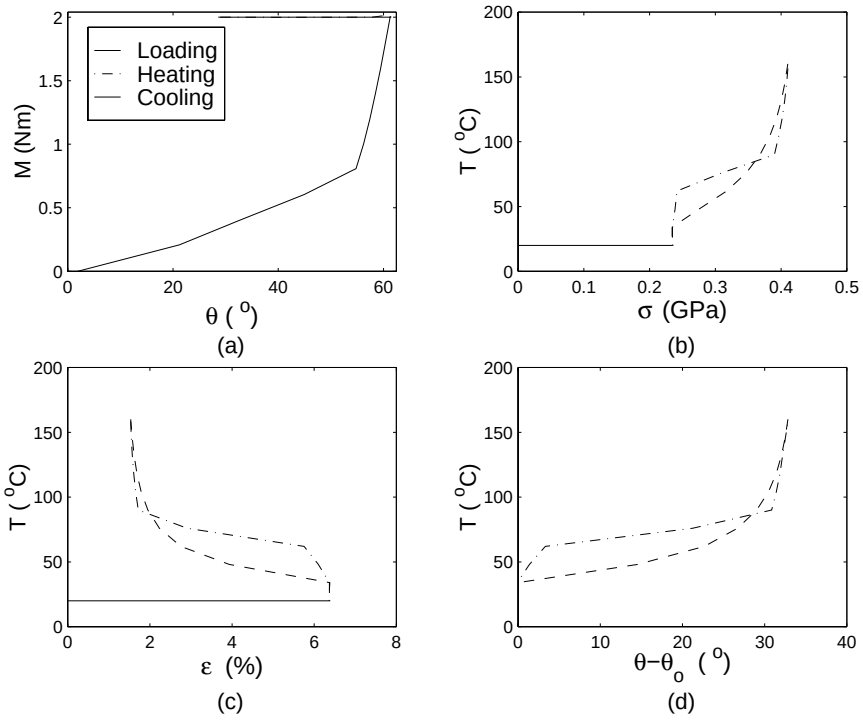

Figure 6.4: Predicted behaviour of first actuator (One disk).

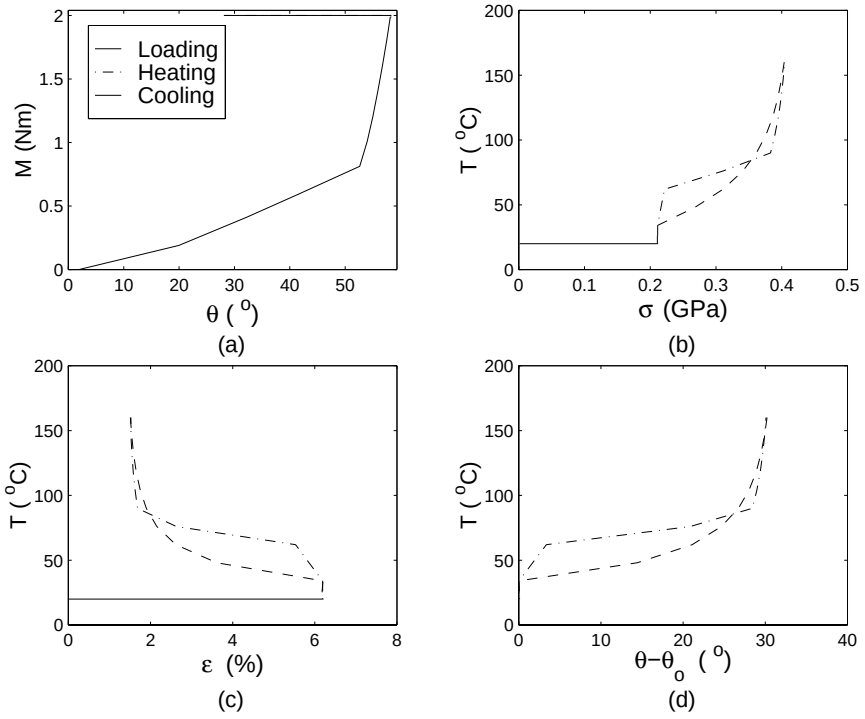

Figure 6.5: Predicted behaviour of first actuator (Three disks).

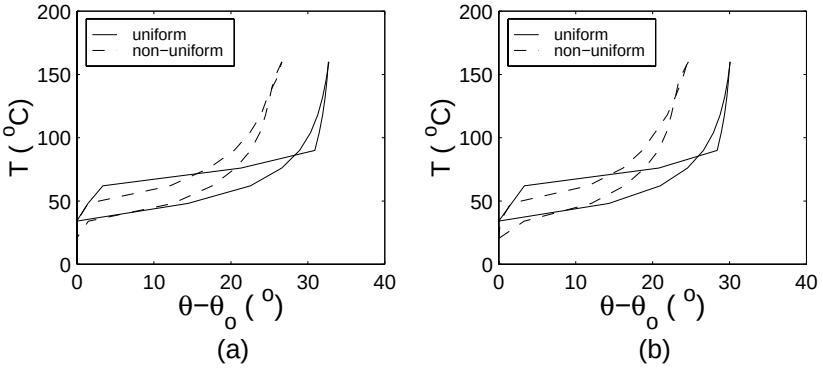

Figure 6.6: Effect of temperature distribution on first actuator. The temperature is at the point which is half-way between the centeral disk and the shoulder. (a) One-disk case; (b) Three-disk case.

6.3 Testing of a Prototype

A prototype was made, see Fig. 6.7, and tested. Figure 6.8 is a sketch of the loading system, which applies a constant torque of $W \times r$, where r= 22.75 mm. The rotation angle of the disk is measured by a potentiometer.

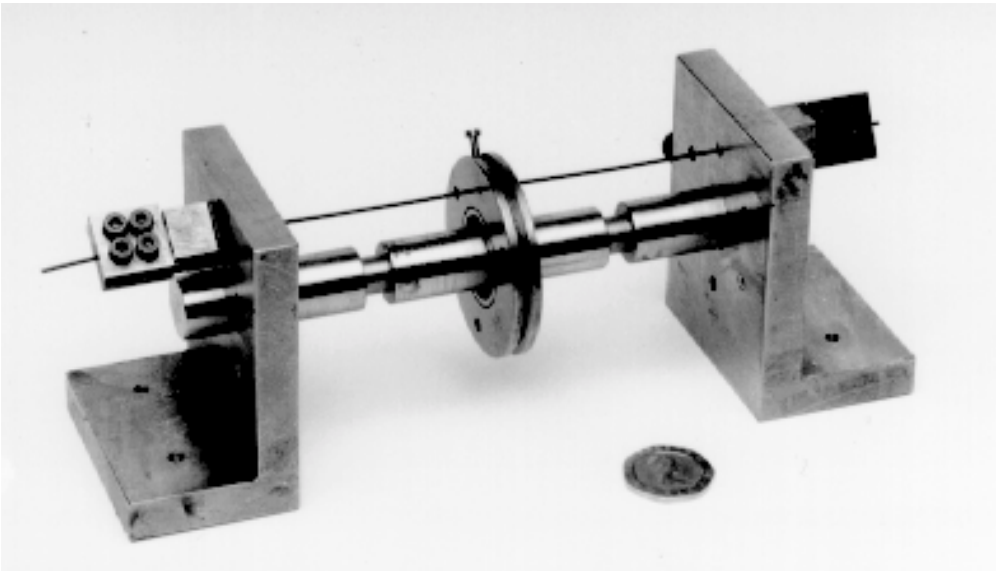

Figure 6.7: Photograph of first actuator.

Several tests were carried out, both in the one-disk and three-disk configurations. The applied torques were 2.3 Nm and 3.2 Nm. In the one-disk case, H was measured to be 53 mm ($H/R = 2.86$). In the three-disks case, H was 23 mm ($H/R = 1.24$).

The experimental and analytical results are compared in Fig. 6.9.

- In the one-disk case, the measured rotation angle is 27^o under a torque of 2.3 Nm and it is 29^o under a torque of 3.2 Nm.
- In the three-disks case, the measured rotation angle is 22^o under a torque of 2.3 Nm, and it is 22.5^o under a torque of 3.2 Nm.

In all cases, the temperature at the control point, which was located half-way between the central disk and the shoulders, increased from room temperature ($\approx 20^o$C) to 145^oC.

A simple control system was set up to control the rotation angle, see Fig. 6.10. The reading of the current rotation angle θ is passed to a personal computer (PC), which runs *Labview* version 4.0 through an interface box (National Instruments Signal Conditioning eXtension for Instrumentation, *SCXI*), and then compared with the required rotation angle, which is input by typing on the key board of the computer. If the current angle is bigger than the required value (θ_r), the

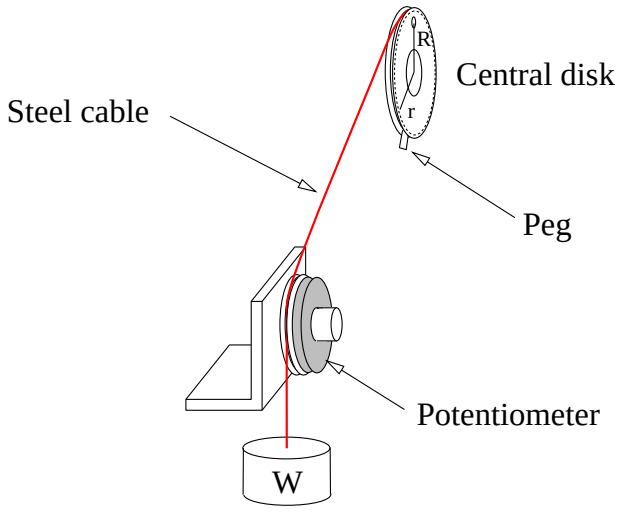

Figure 6.8: Loading and displacement measurement system.

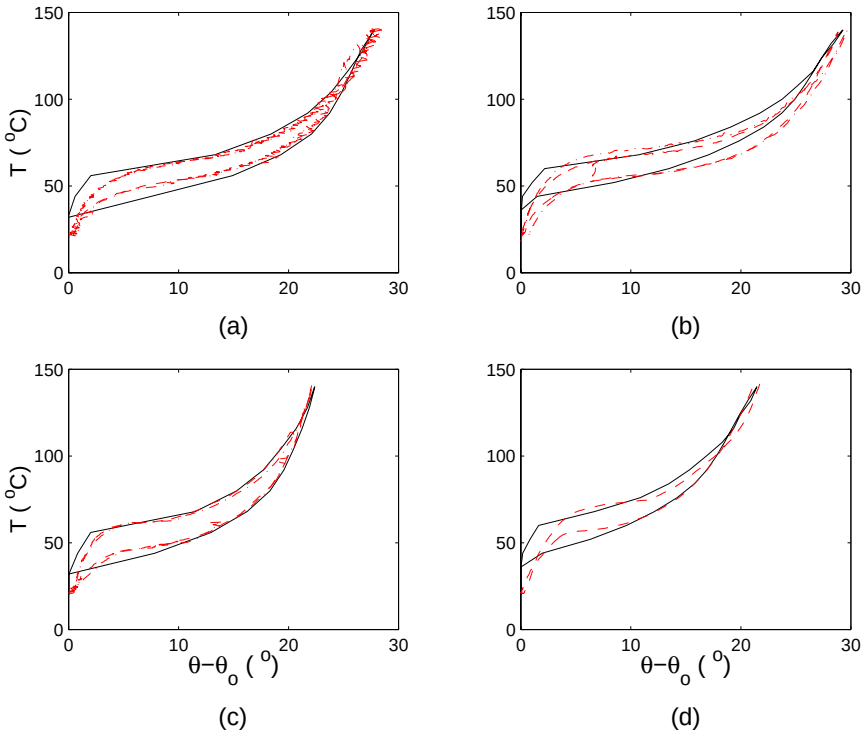

Figure 6.9: Behaviour of first actuator. Black lines denote prediction; grey lines denote measurment. (a) One-disk, M= 2.3 Nm; (b) one-disk, M= 3.2 Nm; (c) three-disk, M= 2.3 Nm; (d) three-disk, M= 3.2 Nm.

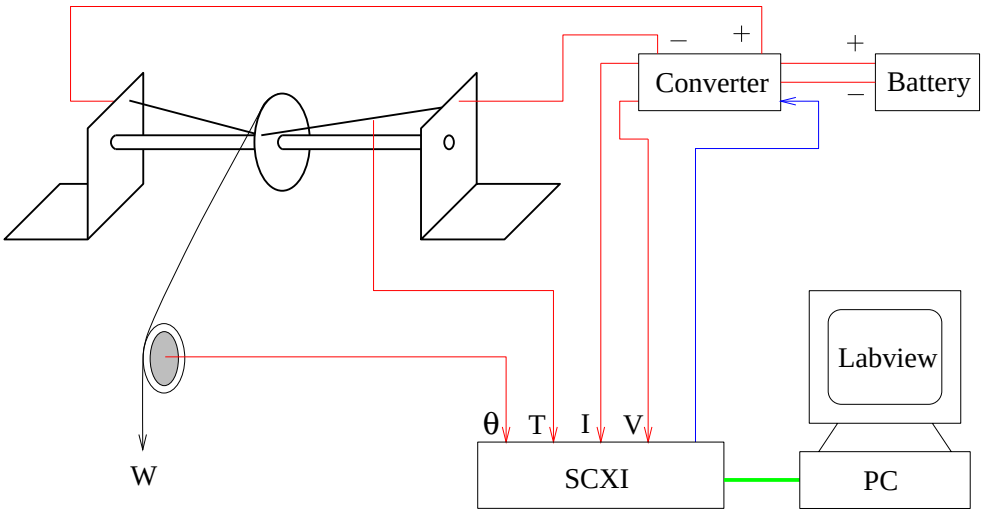

Figure 6.10: Layout of control system.

current passed to the Nitinol wire is reduced by a factor of $(\theta - \theta_r)/50$, and *vice versa*. This procedure is repeated every 0.25 second. The output voltage for the $SCXI$ box is input into a voltage-to-current converter, made by the Electronic Development Section of the Engineering Department.

Figure 6.11 shows the results with the one-disk configuration, for applied constant torque of 1.1Nm. At $t = 26.5$ s, a rotation of 18.5^o was prescribed. This angle was reached in 34 s. Next prescribed rotation angle was set to be 11.25^o, which was achieved 33 s after this requirement was keyed-in. The third prescribed angle of 21.25^o was reached in 23 s. The last required angle of 6.25^o was achieved in 77s.

As we can see, it takes a much longer time to reach the required angle by reducing the current angle than by increasing the current value. This is due to the lack of a cooling system.

The accuracy with which this control system can achieve a prescribed angle is $\pm 0.5^o$. Note that the resolution of this system is about $\pm 0.5^o$.

6.4 Second Concept

In the first actuator concept the rotation angle was limited by the physical size of the actuator, this is a general problem when using straight wires.

To reduce the size of the actuator while increasing the angle through which it is able to turn, we consider a much longer wire which has been stretched to a transformation strain ϵ^t. Imagine coiling this wire around a rigid shaft of diameter D whose surface is frictionless, and let the pitch be H, Fig. 6.12. If the wire is clamped to the shaft at one end, and is then heated above the temperature where

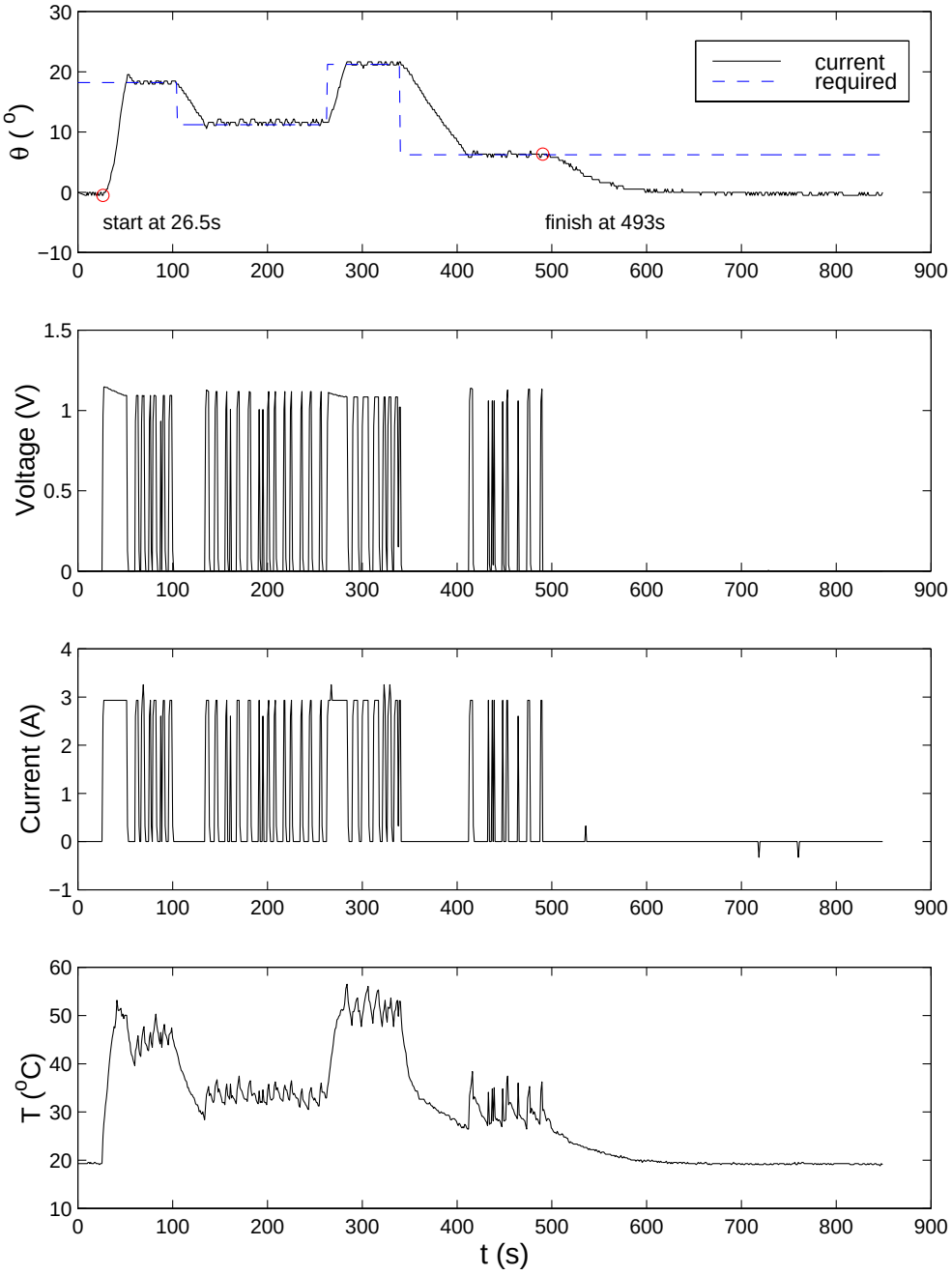

Figure 6.11: Simple control (one-disk, $M = 1.1\text{Nm}$).

the strain recovery takes place, its free end will move. If $D \gg H$, the rotation of the free end will be

$$\theta = 2\pi n \epsilon^t \tag{6.4}$$

where n is the number of turns. The length L of this actuator is

$$L = nH \tag{6.5}$$

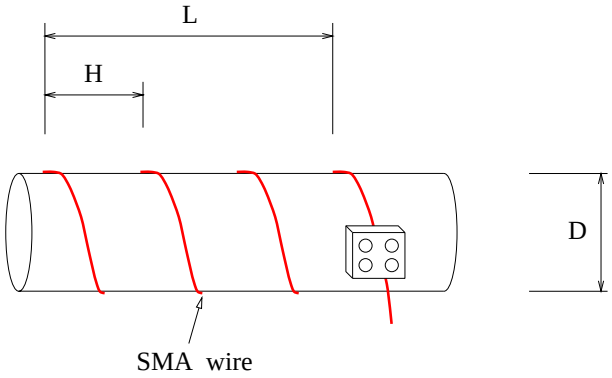

Figure 6.12: Concept of second actuator.

Figure 6.13 shows the relationship between rotation angle θ and actuator length L for different values of ϵ^t and for H= 5 mm. H must be bigger than the diameter of the wire, to avoid a short circuit when the wire is heated by passing a current through it. The figure shows that the wire at the end of a 50 mm long shaft ($n = 10$) would turn through over 180^o if $\epsilon^t > 5\%$. Hence, this concept can potentially be used to make very compact actuators, but in practice it is difficult to find a suitable material for the shaft. This material needs to be both a good electrical and thermal insulator, and to have a low friction coefficient with Nitinol. Also, it needs to be stiff, even at high temperature, otherwise the wire will sink into the shaft when it softens.

6.4.1 Frictional Effect

Let F_1 and F_2 be the forces at the two ends of a wire which is wrapped on a continuous drum; let α be the total angle subtended by the wire, expressed in radians ($\alpha = 2n\pi$ if there are n complete turns of wire); and let μ be the static friction coefficient between the wire and the drum. The force build up that can occur is given by

$$\frac{F_2}{F_1} = \mathrm{e}^{-\mu\alpha} \tag{6.6}$$

This relationship has been plotted in Fig. 6.14 for α up to 180^o. It is obvious that friction effects in a long wire wound over a continuous shaft would totally invalidate our earlier, purely geometric analysis.

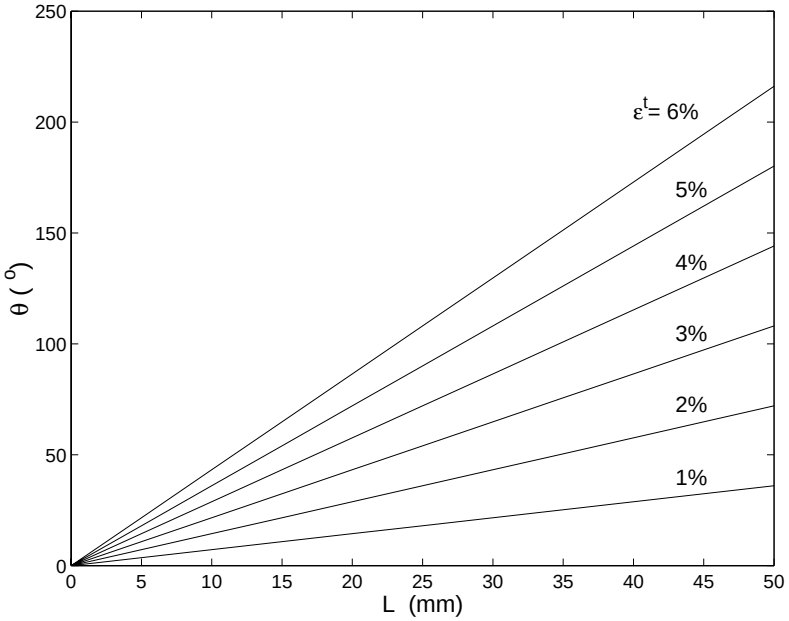

Figure 6.13: Angle of turning for actuator of length L.

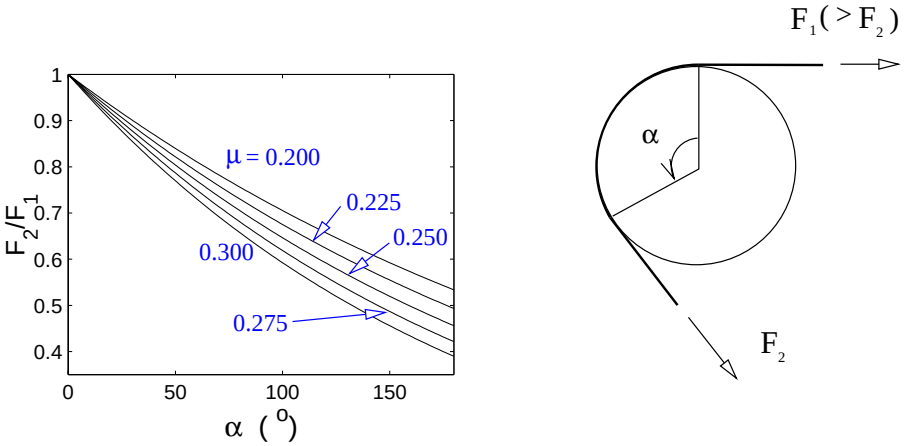

Figure 6.14: Force build up.

This shortcoming may be avoided by replacing the continuous shaft with many separate Macor disks, mounted on a common solid shaft through ball-bearings.

If each turn of the wire lies across one disk only, and we pull on both ends of the loop, the maximum value of α in Eqn. 6.6 is π and hence the minimum force build-up is around 44%, Fig. 6.14. The static friction coefficient between Nitinol and Macor that we measured is about 0.259.

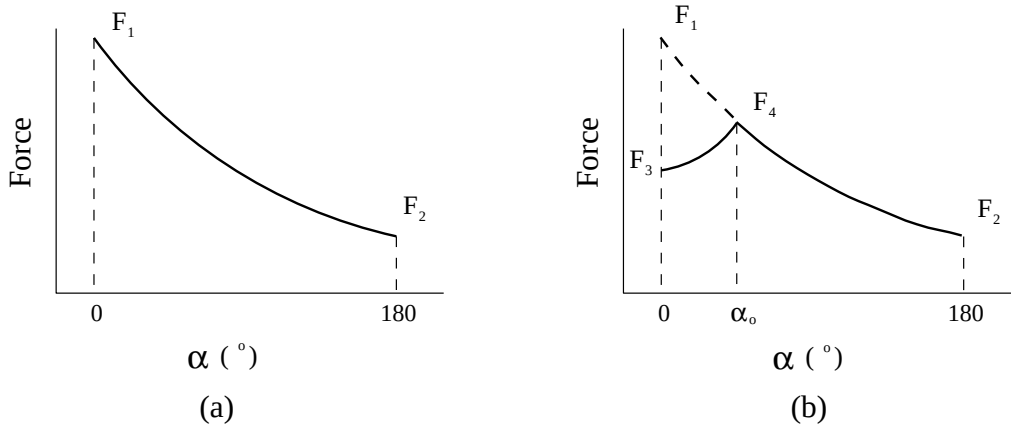

Figure 6.15: Force distribution. (a) Loading; (b) unloading.

Assume a wire is wrapped on a disk by one complete turn. We pull both ends of the wire. Thus, when the pulling force is F_1, we have the force distribution in half a turn as shown in Fig. 6.15(a). The distribution in another half, i.e. $\alpha = 180^o \sim 360^o$, is symmetric to this half. Figure 6.15(b) shows the force distribution that is obtained by gradually decreasing the value of F_1 down to F_3. The maximum force will be F_4

$$\frac{F_1}{F_4} = \mathrm{e}^{\mu\alpha_o} \tag{6.7}$$

Since

$$\frac{F_4}{F_3} = \mathrm{e}^{\mu\alpha_o} \tag{6.8}$$

So we have

$$\alpha_o = \frac{\ln(\frac{F_1}{F_3})}{2\mu} \tag{6.9}$$

Hence, the force distribution along the wire can be determined by Eqns. 6.7, 6.8 and 6.9. Examples are shown in Fig. 6.16 for F_3/F_1= 0.75, 0.5, and 0.25, respectively.

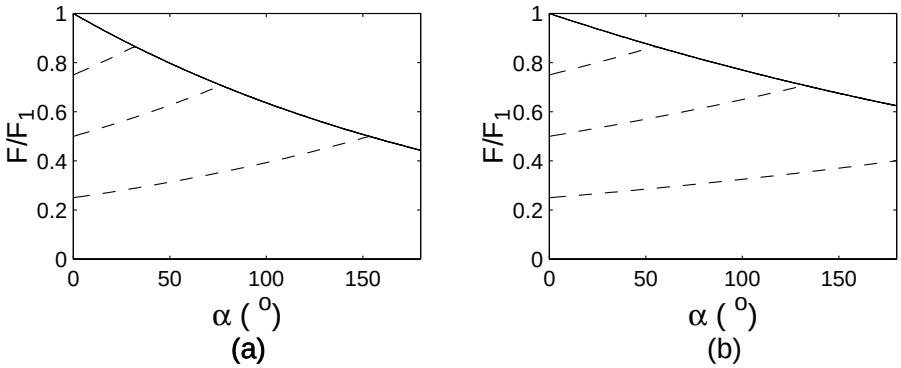

Figure 6.16: Force distribution in the wire. (a) μ= 0.259; (b) μ= 0.150.

6.5 Design and Simulation

A schematic diagram of the model actuator is shown in Fig. 6.17. Up to 7 disks, with a thickness of 5 mm and outer diameter of 39 mm, can be mounted on SKF deep groove ball bearings. The diameter of the inner steel shaft is 8 mm. This shaft is rigidly connected to the left-hand block. On the right-hand side, a free-turning steel block, mounted on two ball-bearings like those used for the Macor disks, provides a clamping point for the Nitinol wire. The loading system is attached to this block in a way similar to Fig. 6.8.

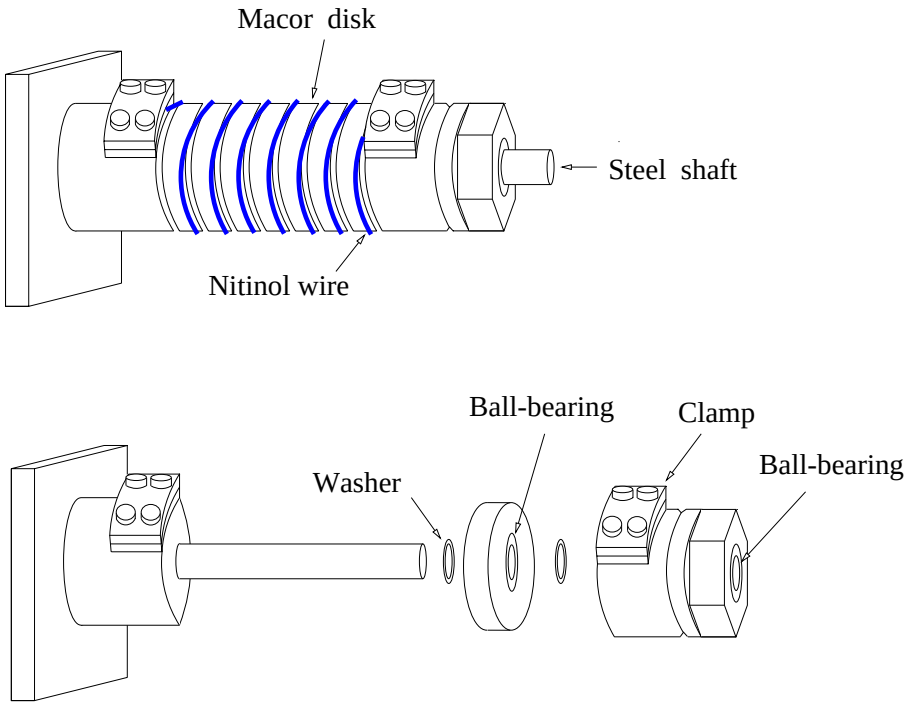

Figure 6.17: Schematic diagram of second actuator.

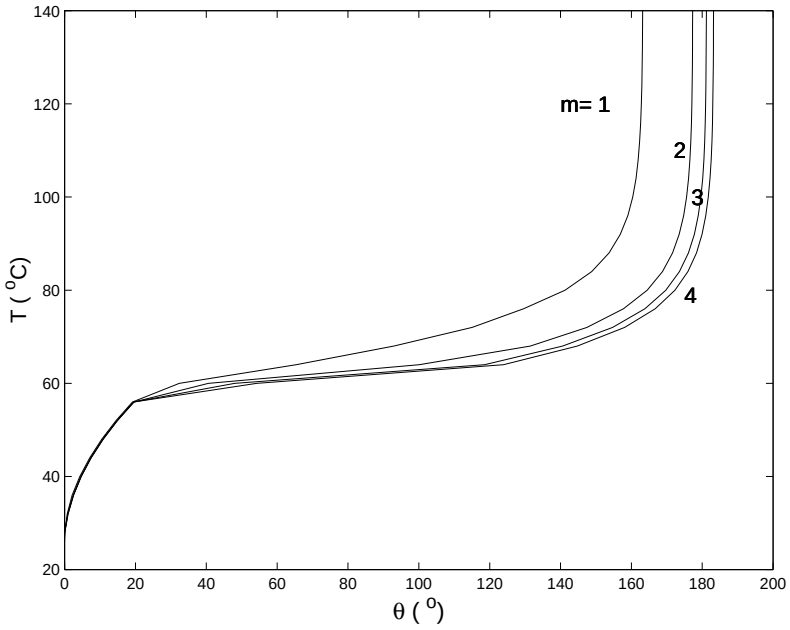

Figure 6.18: Simulation of second actuator, with 10 turns of initially unstrained Nitinol wire, m is number of disks per turn of wire (M_o= 8 Nm, M= 2 Nm).

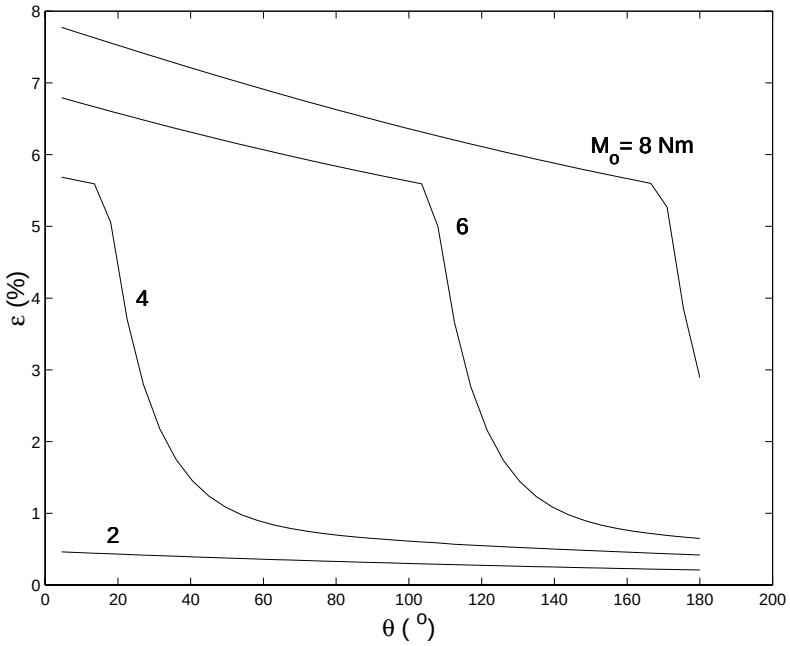

Figure 6.19: Variation of strain in the wire ($m = 1$).

A simulation of the behaviour of the second actuator was made, using the constitutive model for specimen 2. The total number of turns of Nitinol wire is $n = 10$, but the total number of disks varies between 10 and 40, with the number of disks per turn of wire, m, varying between 1 and 4.

In this simulation, it was assumed that the wire is clamped to the actuator initially unstrained, then a torque M_o= 8 Nm is applied to the end block, which is then reduced to $M = 2$ Nm. The temperature of the wire is uniformly increased from 20°C to 140°C. The relationships between rotation angle and temperature that have been computed are plotted in Fig. 6.18.

Figure 6.19 plots the strain in the wire for different values of M_o, for m= 1. Due to friction effects the strain is not proportional to M_o. A large M_o is required to impose a large ϵ^t, which in turn results to achieve a large rotation angle.

6.6 Testing of a Prototype

Figure 6.20 shows a photograph of the prototype actuator. The Nitinol wire used in these tests is more than 500 mm long (diameter= 1 mm) and hence the temperature distribution can be assumed to be reasonably constant.

Four different tests are reported, see Table 6.1 and Fig. 6.21. The largest rotation, about 120°, was obtained with the largest number of disks, 7, and the largest number of turns of wire, 7. It is interesting to compare Fig. 6.21(c) and Fig. 6.21(d), the only difference is that in Fig. 6.21(c) the wire was pre-stretched, whereas in Fig. 6.21(d) an equivalent torque was applied after the wire had been coiled on the disks. The experiments show that pre-stretching produces a rotation angle 15° larger.

Test	Disks	Turns of Wire	Stretch Load	Torque
(a)	4	4	294 N	2.0 Nm
(b)	7	7	316 N	2.1 Nm
(c)	7	4	412 N	2.8 Nm
(d)	7	4	8.4 Nm	2.0 Nm

Table 6.1: Test conditions.

6.7 Modification and Re-Testing

Two problems become apparent during the tests described above,

1. Friction between the Nitinol wire and Macor is quite high. It is not convenient to have to pre-strain the wire and then mount it onto the actuator before each test. Pre-stretching by means of an applied torque is much more practical, but very large torque is required to induce a reasonable amount of transformation strain into the wire since friction is too high.

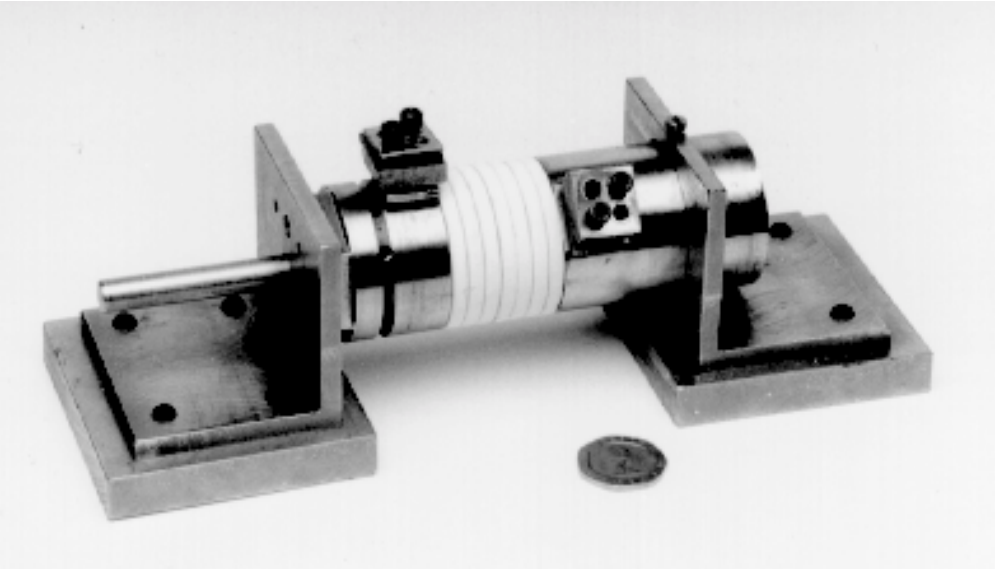

Figure 6.20: Photograph of second actuator.

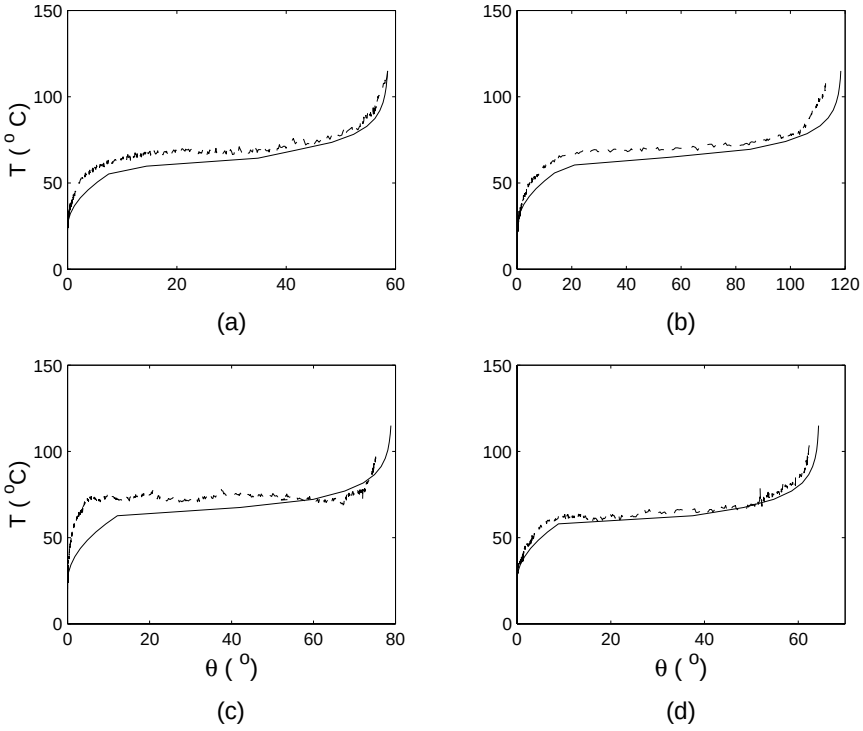

Figure 6.21: Comparison of measured and predicted behaviour of second actuator, see Table 6.1 for details.

2. The Nitinol wire slides on the Macor surface, both during actuation and during the initial pre-loading. Although we have tried many times to mount the wire carefully, from time to time it falls into the gap between disks causing damage.

It was found that a way of avoiding these problems was to put the Nitinol wire inside PTFE sleeve. The PTFE sleeve is low friction, semi-hard, non-conductive, also no significant melting at about 250°C. The sleeve (od≈ 3.14 mm) was cut into segments about 115 mm long. Each segment is a little shorter than the perimeter of the Macor disk, so that the Nitinol wire comes out of the sleeve as it goes across the gap between adjacent disks. The average static friction coefficient between Nitinol and PTFE is 0.150, which is much smaller than that of Nitinol and Macor.

A new simulation of the behaviour of the modified actuator was made using 0.150 as the new friction coefficient.

Fig. 6.22 shows the result of several simulation for a single disk with one turn of wire.

In Fig. 6.22(a), the wire is initially stretched by torques of 2 Nm, 3 Nm, and 4 Nm, respectively, at 20°C. Then, it is heated to 120°C against a 2 Nm torque. The larger the initial torque, the greater the rotation during heating.

In Fig. 6.22(b) the wire is stretched by a torque of 4 Nm and is then heated to 120° under torques of 4 Nm, 2 Nm, and 1 Nm. The bigger the applied torque during heating, the higher the temperature needed to get the same rotation, but the maximum rotation angle is the same since the initial torque is unchanged.

These plots show that by applying a 4 Nm torque, we can get a rotation of over 15° per disk. Which means that a 12-disk actuator would rotate by more than 180°; the working part of such an actuator, excluding clamps, would be 60 mm long. The resistance of the Nitinol wire in this 12-disk actuator would be about 1.5 Ω, and hence the phase transformation could be triggered by a 12 V battery, providing a current of up to 8 A.

As described in Section 3.5, it takes some time for the strain to reach its final value in air when a load is suddenly applied. In this actuator, since Nitinol wire was covered by PTFE sleeves, the load was held for at least half an hour before thermal cycling started.

The modified actuator with 7 disks was re-tested. Figure 6.23 shows that after applying an initial torque of 3.4 Nm, it rotates by almost 100° against a torque of up to 2.4 Nm. Smaller initial torques of 2.4 Nm or 1.7 Nm were also applied, but the rotation angle was smaller.

Our predictions agree well with the measured behaviour, which means that our analytical method can be used as a reliable tool for actuator design.

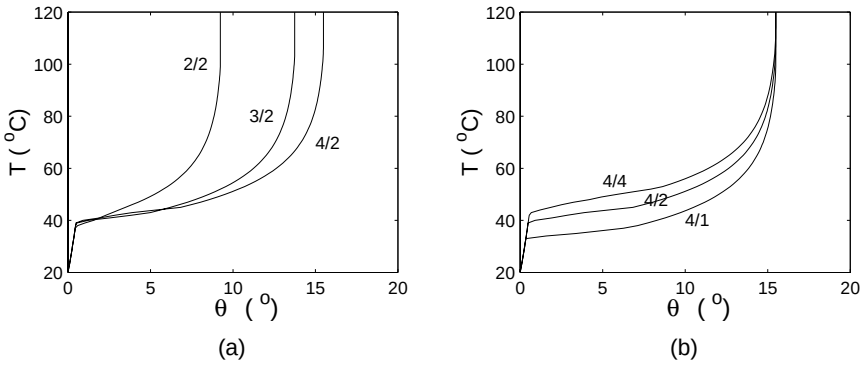

Figure 6.22: Simulation of modified second actuator with one disk only. The two numerical values that are given for each curve denote the initial torque and the working torque, in Nm.

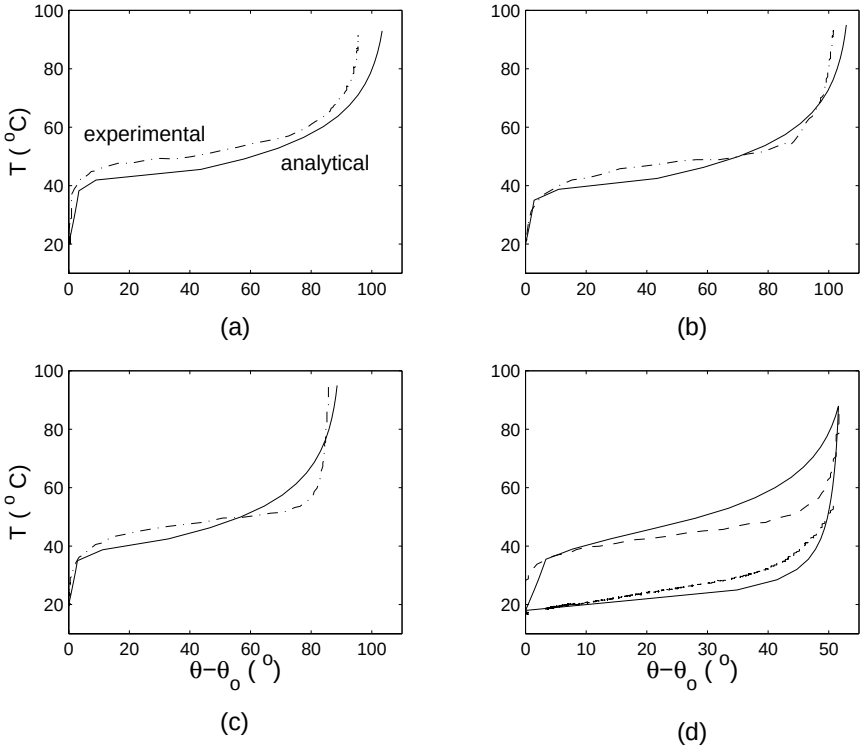

Figure 6.23: Comparison of measured and predicated behaviour of modified second actuator. (a) M_o= 3.4 Nm, M= 2.4 Nm; (b) M_o= 3.4 Nm, M= 1.7 Nm; (c) M_o= 2.4 Nm, M= 1.7 Nm; (d) M_o= 1.7 Nm, M= 1.7 Nm.

Chapter 7

Two-Way Wire Actuator

In this chapter, the design, testing and simulation of a two-way actuator based on Nitinol wire is presented. This actuator is based on the same concept as the second actuator studied in Section 6.4, but it is designed much more carefully, to avoid the practical difficulties that had been encountered when testing the prototype described in Section 6.6. Also, two actuators are put together, one against the another, in order to obtain a two-way actuator which rotates back and forth when different wires are heated.

7.1 Simple Two-Way Actuator

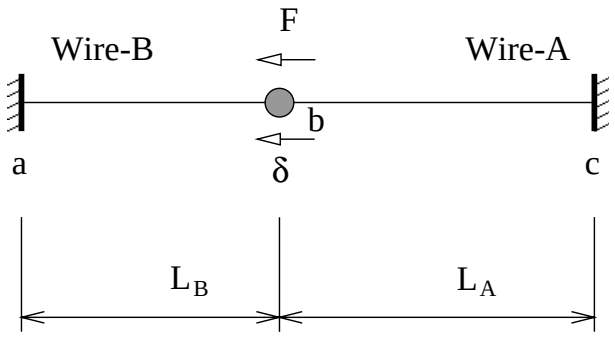

Figure 7.1: A simple two-way actuator.

We consider a simple two-way system, as shown in Fig. 7.1, which includes two 1 m long Nitinol wires. Assume that each wire has 0.5 mm diameter, and has the same thermomechanical behaviour as the 0.5 mm wire that we have tested in Chapter 3. Wire-A is pre-strained by loading it to 45 N (0.23 GPa) and then unloading it to F= 25 N (0.13 GPa), at a temperature of 22.5^{o}C. Then wire-A and wire-B are connected together, and the force F = 25 N is applied at the connection point. So, the total length of this "*actuator*" is

$$L = L_A + L_B \tag{7.1}$$

L_A can be calculated by using the model presented in Chapter 4. L_B= 1 m.

It is assumed that the temperature in each wire is uniform, and there is no temperature change due to phase transformation, i.e. the speed of thermal cycling is very slow. Hence, when one wire is undergoing thermal cycling, the temperature of the other wire is 22.5^{o}C.

We can use the model presented in Chapter 4 to simulate the behaviour of this simple actuator. There are two things that should be pointed out. First, the forces in wire-A (F_A) and wire-B (F_B) are related to the external force F by the relation

$$F_A = F + F_B \tag{7.2}$$

Second, the total length of wire-A plus wire-B is a constant as stated in Eqn. 7.1, provided that slackening does not occur.

We monitor the displacement of point b during operation, see Fig. 7.1, and the stress and temperature in each wire. The initial position of b, before thermal cycling starts, is set as the zero.

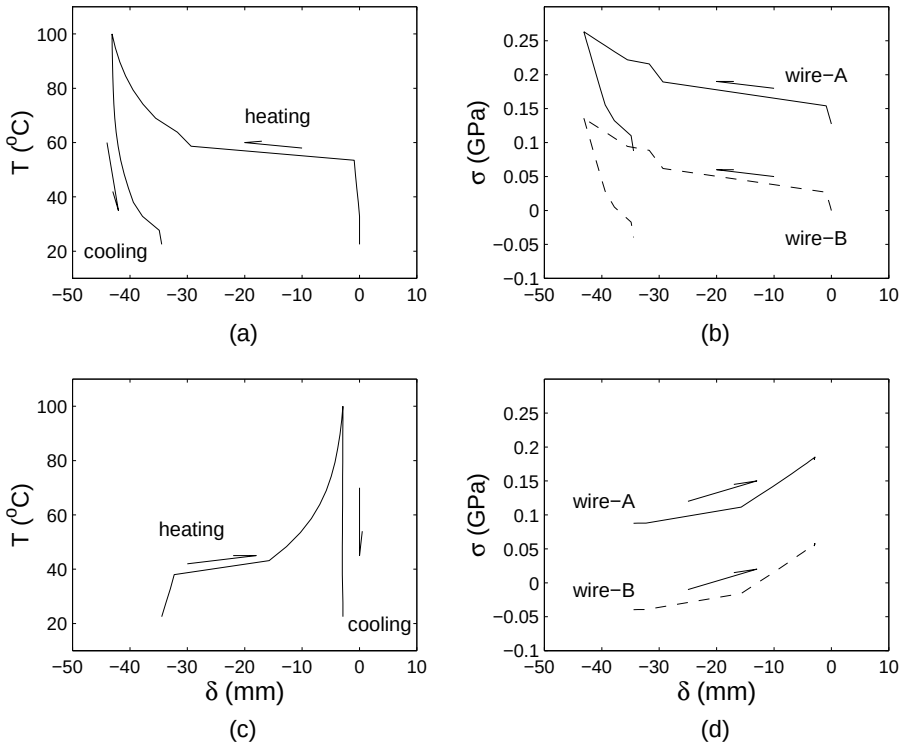

Figure 7.2: Behaviour of simple two-way actuator. (a-b) During heating/cooling of wire-A; (c-d) during heating/cooling of wire-B.

A full two-way operation cycle includes two stages.

In the first stage, Fig. 7.2(a-b), we heat wire-A to 100^{o}C and then cool it to 22.5^{o}C. Point b moves to the right, as wire-A undergoes the transformation

$DM \Rightarrow A$. Thus, wire-B is pulled to the right and undergoes the low-temperature transformation $A/TM \Rightarrow DM$. The stresses in both wires increases. When wire-A is cooled, point b moves to left and the stress in both wires decrease. Wire-A undergoes the transformation $A \Rightarrow M$, and the transformation in wire-B is $DM \Rightarrow A/TM$ (unloading).

In the second stage, Fig. 7.2(c-d), wire-B is heated to 100^oC and then cooled to 22.5^oC. This time during heating, b moves to the left. Wire-B undergoes the transformation $M \Rightarrow A$, while wire-A is loaded at low temperature and undergoes the transformation $A/TM \Rightarrow DM$. The stresses in both wires go up, but lower than in the first stage. At the end of the cycle, b has returned very near to its initial position, but the stresses in both wires are higher.

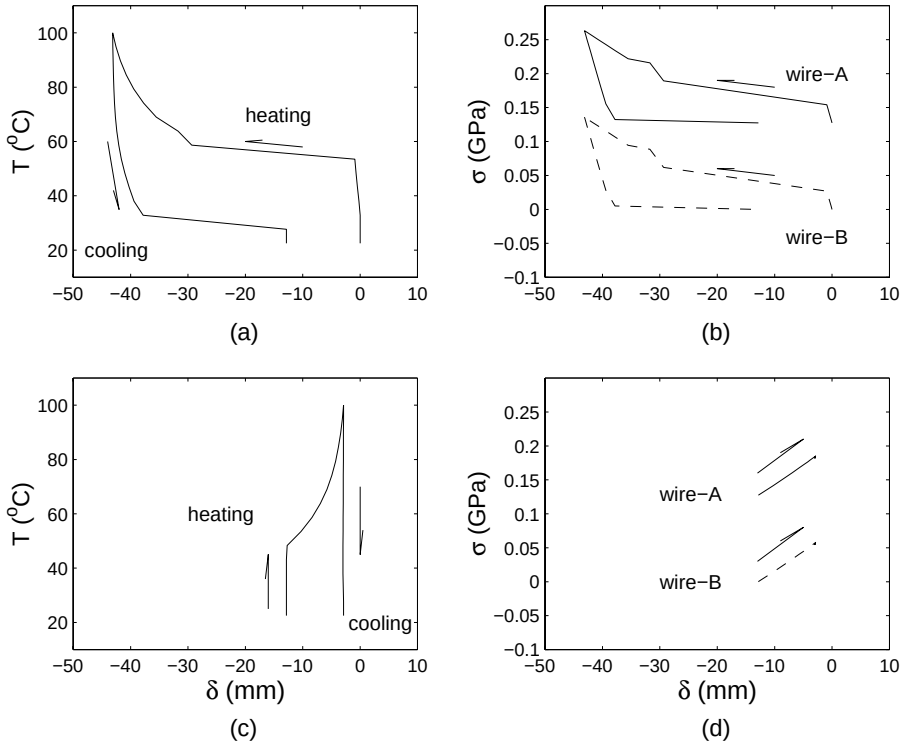

Figure 7.3: Behaviour of simple two-way actuator (no compression). (a-b) Heating/cooling wire-A; (c-d) heating/cooling wire-B.

Note that the stress in wire-B is negative, i.e. the wire is in compression, during a part of the process described above. Actually, this is impossible, since a long wire cannot take any compression force. When the stress in wire-B reaches zero, the whole of the applied force F will be carried by wire-A. We can take this effect into account by letting $F_A = F$ and $F_B = 0$ while wire-B is slack. In this case, $L \leq L_A + L_B$. Therefore, in the later heating of wire-B, b will not move until $L = L_A + L_B$. Figure 7.3 shows the behaviour of the actuator, if no compressive stress in wire-B.

7.2 Actuator Design

The actuator described in this section is based on the concept of Section 6.4.

The key aims in the design presented in this section were (i) to better control the position of the Nitinol wire, in order to eliminate the need for time-consuming adjustment before each test, and (ii) to produce a more robust design which is not easily damaged. These aims were achieved, first, by replacing the brittle Macor disks with steel disks that have a deep groove, like a pulley, and by pre-loading the disks one against the other with a stiff spring. Thus, it is much more difficult for the Nitinol wire (contained inside a PTFE sleeve) to move laterally and, if it does move, the gap between adjacent disks is too small for the wire to sink into it. Also, the end attachments for the Nitinol wire were positioned in-line with the last disk, to avoid that the wire having to twist sharply.

A photograph of the actuator model, with a Nitinol wire mounted on side-A, is shown in Fig. 7.4. The overall layout of the actuator is shown in Fig. 7.5, and an exploded view of side-B only is shown in Fig. 7.6. Details of the standard steel disk and PTFE washer are shown in Fig. 7.7.

The complete actuator consists of 40 standard steel disks, with thickness of 5 mm and outer diameter of 46 mm, with a 3 mm deep and 3.2 mm wide groove, mounted on SKF deep groove ball bearings.

The diameter of the central steel shaft is 10 mm. Eight hardened steel balls with a diameter of 2 mm are used to separate adjacent steel disks; these balls are held in position by 1.8 mm thick PTFE washers in which eight 2.2 mm diameter holes have been punched. The ball bearings are separated by 0.1 mm thick steel washers, so that each steel disk can rotate freely.

Disk-A cannot rotate, while disk-B can be fixed by three M2 screws, or allowed to rotate.

Thermal and electrical insulation for the Nitinol wire are provided by the same PTFE sleeve used in Section 6.7. There is no stop to prevent the middle disk from rotating back during cooling. This means that slackening, as described in Section 7.1, can happen in this actuator. Since each PTFE sleeve is pushed into the disk groove, a little slackening is not a very serious problem when the applied torque is not very high.

Part of the shoulder of each steel disk is cut to allow the Nitinol wire to go across disks. The angle 2β subtended by this cut, see Fig. 7.7, is chosen such as to avoid that the wire, which is not covered by the insulating sleeve as it goes from one disk to the next, touches the shoulder. According to our analysis, this is the only important issue we should consider. The magnitude of 2β was calculated as follows.

Consider two adjacent disks whose cutting angles $\angle aoc = \angle a'oc' = 2\beta$ are set to match in the initial configuration of the actuator, as shown in Fig. 7.8(a). The Nitinol wire will go across the disks between points a and c'. If one disk gradually rotates, ac' will touch the inner circle, which has a diameter of r (Fig. 7.7), when the rotation angle reaches α as shown in Fig. 7.8(b). Our design is to ensure that when we have a given rotation angle, the wire will not touch the inner circle.

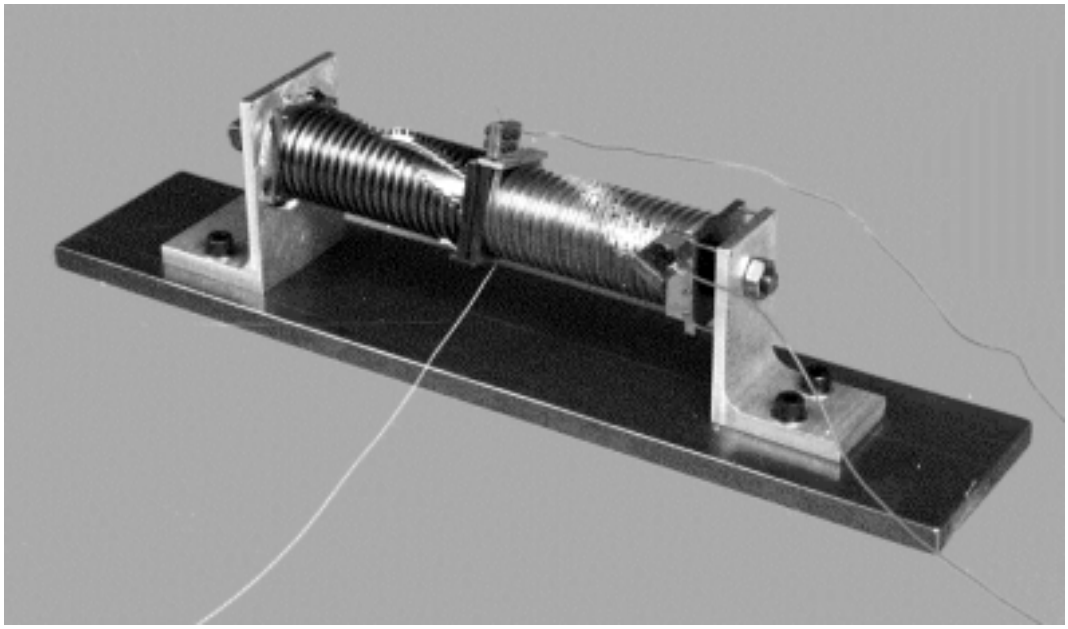

Figure 7.4: Photograph of two-way wire actuator, with Nitinol wire (covered by PTFE sleeves) mounted on side-A.

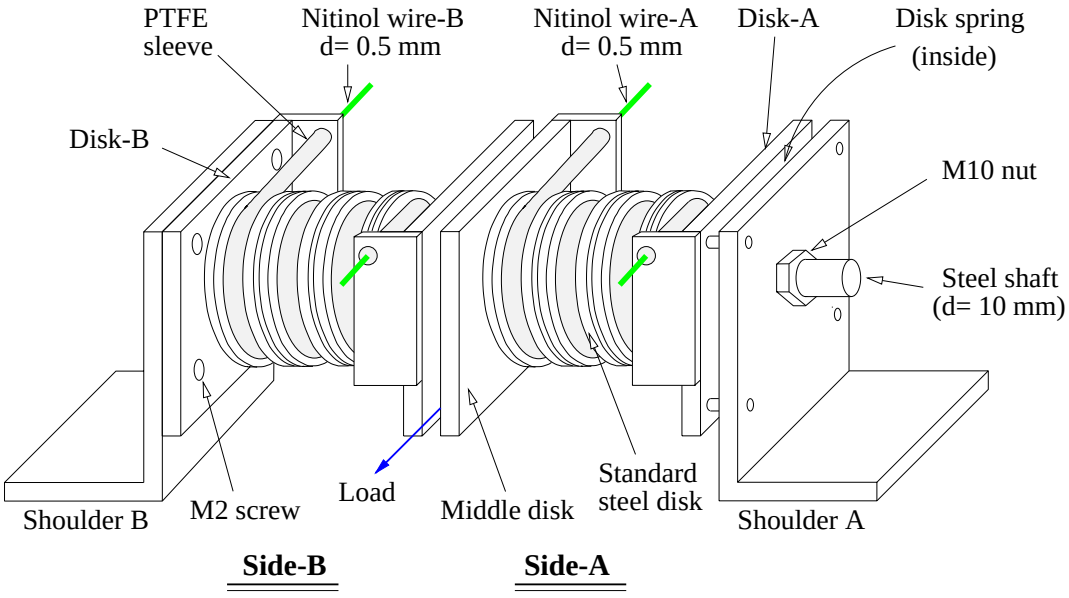

Figure 7.5: Schematic diagram of two-way wire actuator.

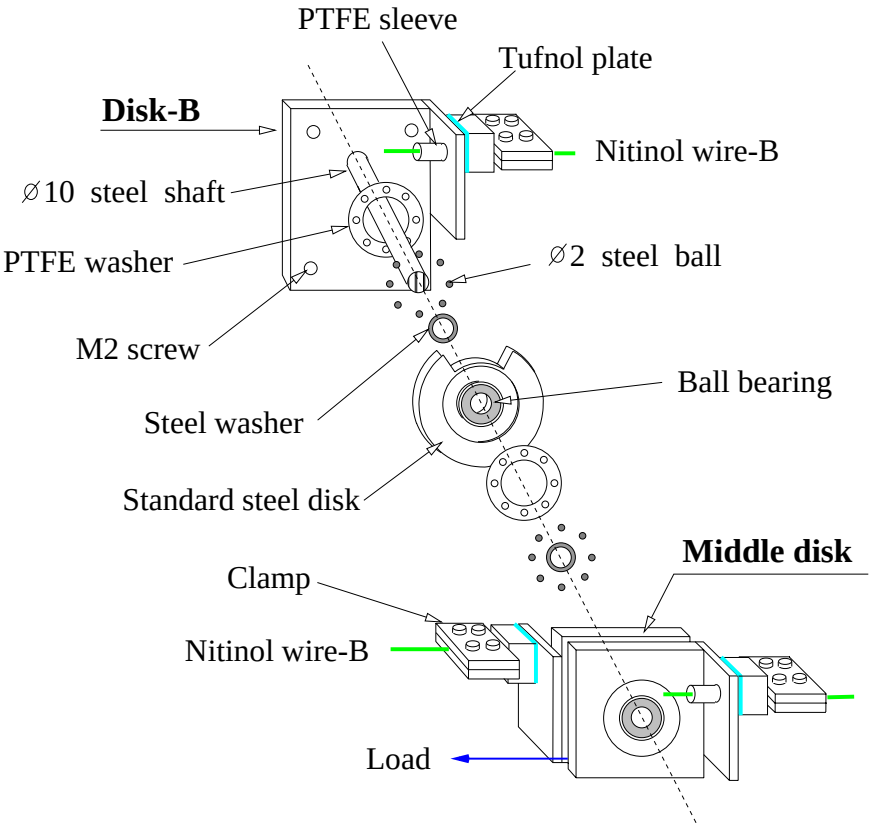

Figure 7.6: Exploded view of side-B of two-way wire actuator.

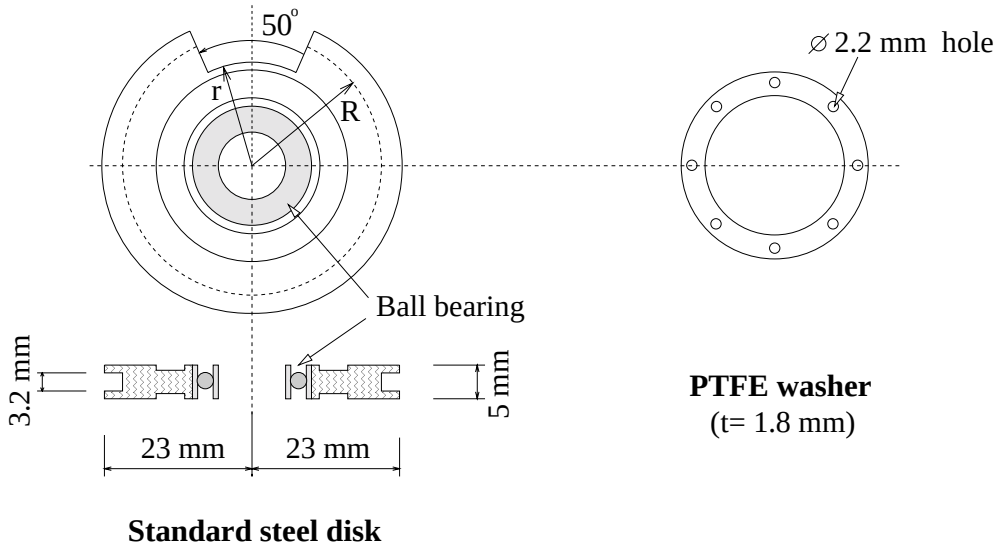

Figure 7.7: Details of standard disk and PTFE washer.

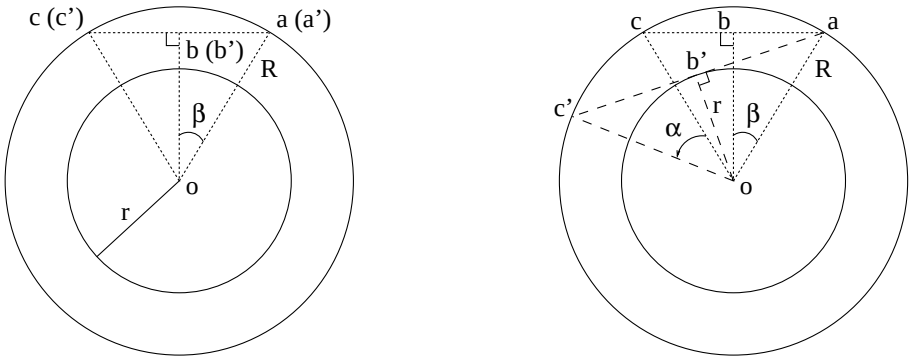

(a) Before rotation (b) After rotation

Figure 7.8: Geometrical relation. (a) Before rotation; (b) after rotation.

Here R and r are decided by geometrical conditions.

In the extreme case, i.e. ac' just touches the inner circle, we have

$$\frac{r}{R} = \cos(\beta + \alpha/2)$$

Thus,

$$\beta = \text{acos}(\frac{r}{R}) - \alpha/2 \tag{7.3}$$

Put r = 17 mm, R= 20 mm, and α= 10^o into Eqn. 7.3. We have $\beta = 26.8^o$.

In our design, the cutting angle $2\beta = 50^o$. Since the real r = 15 mm, we have at least 2 mm gap for safety.

If α= 10^o, the maximum rotation angle of this two-way actuator in the configuration with 20 disks in each side is about 200^o.

7.3 Simulation

Instead of using 1 mm Nitinol wire, it was decided to use two 0.5 mm diameter wires, since at the time of these experiments we had run out of 1 mm wire, but had plenty of 0.5 mm wire. The thermomechanical behaviour of this type wire has been investigated in Chapter 3.

Note that if 1 mm wire is used in this actuator, it will be able to carry three times more load then 0.5 mm wire.

In our simulation, we assume that the temperature is uniform in each Nitinol wire. And, if one wire is thermally cycled, the temperature of the other wire does not change. The friction coefficient between wire and PTFE is the same as used in the second actuator concept in Section 6.7 (μ = 0.150).

7.3.1 Pre-Strain

As we have done with the second actuator in Section 6.7 we apply a torque in the middle disk while letting disk-B rotate freely, to pre-strain wire-A. This torque may be reduced before disk-B is fixed to shoulder B. This induces an initial rotation of the middle disk.

By following the same analytical method used for the second actuator concept, in Section 6.7, we can calculate the strain and stress in wire-A, and therefore the initial rotation angle.

Instead of pre-straining wire-A, we could also pre-strain wire-B, or both wires. But our simulations have shown that these changes would not affect the behaviour of the actuator.

7.3.2 Behaviour of Actuator

As mentioned for the second actuator concept in Section 6.5, due to friction, the stress and strain distribution in a Nitinol wire are not uniform. On the other hand, since the wires are very long ($\approx$ 2800 mm), we ignore the effects of temperature non-uniformity in the simulation.

Three multi-thermal cycling cases are simulated in Fig. 7.9, for the pre-loading conditions listed in Table 7.1. Here θ is the rotation of the middle disk. A solid line corresponds to the first thermal cycling, while a dashed line corresponds to subsequent thermal cycles. In each simulation four complete thermal cycles have been carried out, where a full thermal cycle includes heating/cooling wire-A and then heating/cooling wire-B. We assume that the pre-loading is carried out at 25^{o}C, and during each thermal cycle the temperature varies between 125^{o}C and 30^{o}C.

As we can see, in the first thermal cycle, heating/cooling wire-A generates a slightly larger rotation than the subsequent heating/cooling of wire-B in all cases. However, after one thermal cycle, the behaviour of the actuator reaches a steady state. This actuator, after pre-loading wire-A by a 0.68 Nm torque, can rotate back and forth in a range from 160^o to 193^o under torques in the range from 0 Nm to 0.62 Nm. The greater the applied torque, the larger the rotation angle. However, the larger applied torques tend to cause slackening of wire-B.

Note that, in case (a), after one cycle the behaviour becomes symmetric.

The stress and strain distribution in the wire wrapped over half of a disk (α= 0^o $\sim$ 180^o) is shown in Fig. 7.10, for case (a) during the heating and cooling cycling of wire-A. The distribution over the other half disk, i.e. from 180^o to 360^o, is symmetric.

7.4 Experimental Behaviour

Both the one-way behaviour and two-way behaviour of this actuator were tested, and the measured response was compared to simulations.

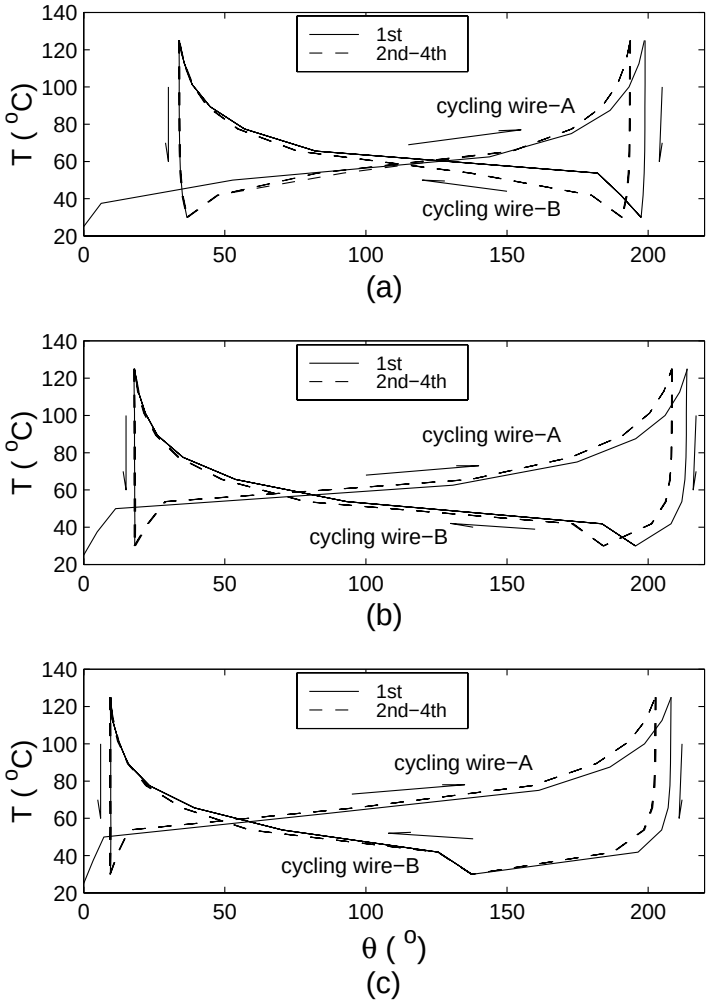

Figure 7.9: Simulation of two-way wire actuator (refer to Table 7.1 for pre-loading conditions).

	Wire-A		
Case	Max. load	Final load	Working torque
(a)	0.68 Nm	0.00 Nm	0.00 Nm
(b)	0.68 Nm	0.42 Nm	0.42 Nm
(c)	0.68 Nm	0.62 Nm	0.62 Nm

Table 7.1: Pre-loading conditions.

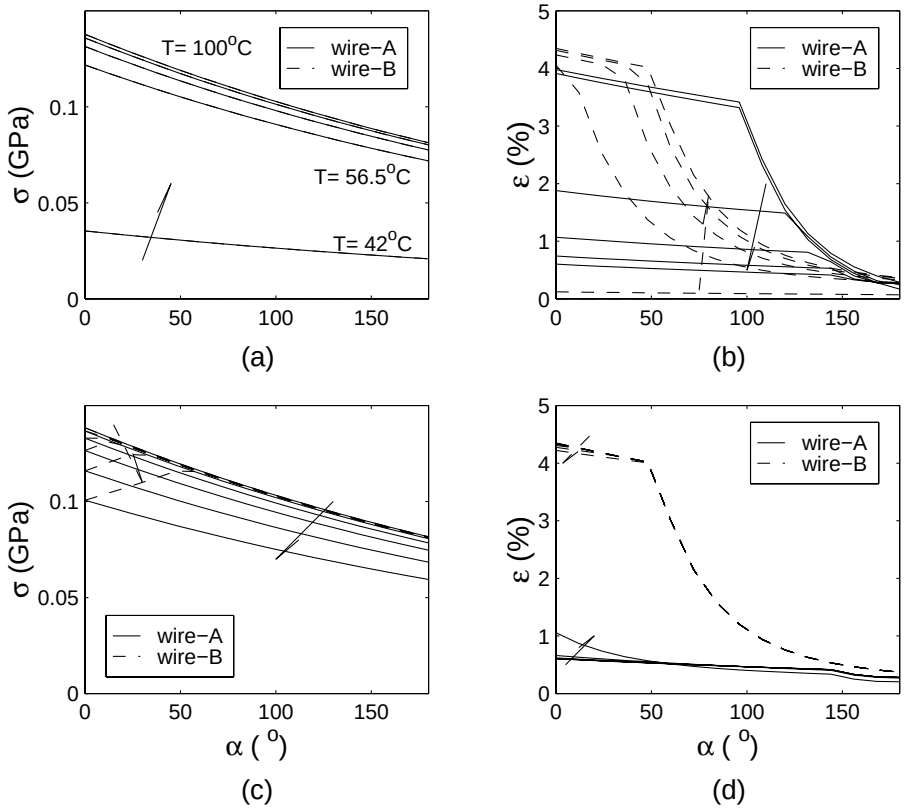

Figure 7.10: σ and ϵ distributions in segments of wire-A and wire-B. (a-b) Wire-A is heated; (c-d) wire-A is cooled.

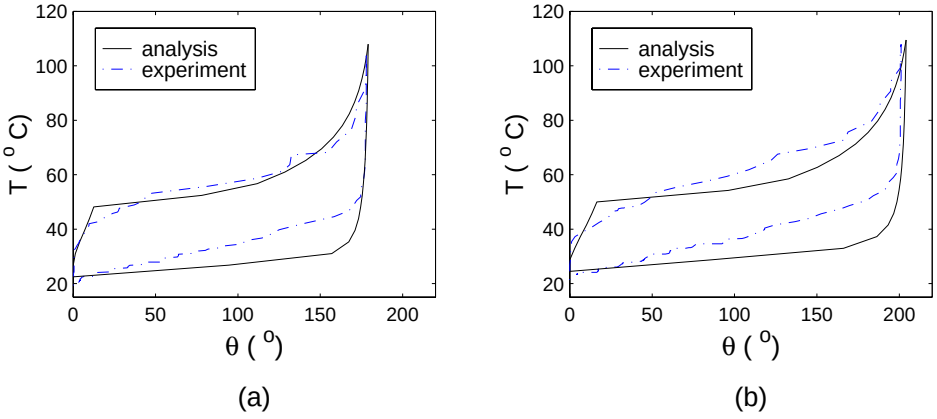

Figure 7.11: One-way behaviour of prototype actuator. (a) 0.52 Nm; (b) 0.62 Nm.

7.4.1 One-Way Behaviour

The reason for carrying out a one-way test was to check the testing system, and to see if our model can catch the one-way behaviour of this actuator, before it is used in a more complex simulation, i.e. two-way behaviour.

A constant torque was applied to the middle disk connected to a 0.5 mm diameter Nitinol wire at side-A, while wire-B was removed.

As shown in Fig. 7.11, our simulation agrees with the experimental results. A rotation of nearly 200^o was obtained against a 0.62 Nm torque. The most significant difference is in the cooling path, where our simulation gives the temperature a little lower than the experimental result in the middle of the path. The reason may be that the temperature in the Nitinol wire is less uniform during cooling. In the middle of the PTFE sleeve, the temperature of the wire is high, while in the regions near the end of the sleeve, or without sleeve, the temperature is low. The measured temperature depends on the position of the thermocouple.

7.4.2 Two-Way Behaviour

The two-way performance of this actuator was tested and also simulated with working torques in the range from -0.22 Nm to 0.62 Nm. The pre-loading conditions and working torque values in each tests are listed in Table 7.2. Note that by applying a torque of 0.22 Nm, there is very little rotation. Hence, in case (a) we applied a negative torque of -0.22 Nm, after disk-B had been fixed to shoulder B.

Pre-loading was carried out at room temperature ($\approx 22.5^o$C). It was done by applying a constant load to the middle disk. As described in Section 6.7, the load was held for at least half an hour before thermal cycling started.

The measured behaviour heavily depends on the speed of thermal cycling. If one wire is heated very fast, the other wire will not be able to reach its maximum strain due to the temperature increase in it. Since the PTFE sleeve is heated together with the Nitinol wire, if the heating speed is slow, the temperature of the sleeve will be as high as the wire. Then during cooling it takes a long time to cool the sleeves and the wire inside.

Both experimental and simulation results are shown in Fig. 7.12, the plots show the relation between the rotation of the middle disk and the temperature of the particular wire which is undergoing thermal cycling. θ is the measured rotation angle of the middle disk. The starting angle is set to be 0^o. In the first thermal cycle, wire-A is heated and then cooled in air. In the second cycle, wire-B is thermally cycled.

Note that the results shown in Fig. 7.12 were obtained after several thermal cycles, i.e. after the behaviour of the actuator had reached a steady state.

During these tests, slackening of the wire was observed. The larger the applied torque, the more significant the slackening. In case (a), there was no noticeable slackening. However, in some cases, the Nitinol wire (covered by the PTFE sleeve) got out of the grooves in the steel disks and did not automatically return into the

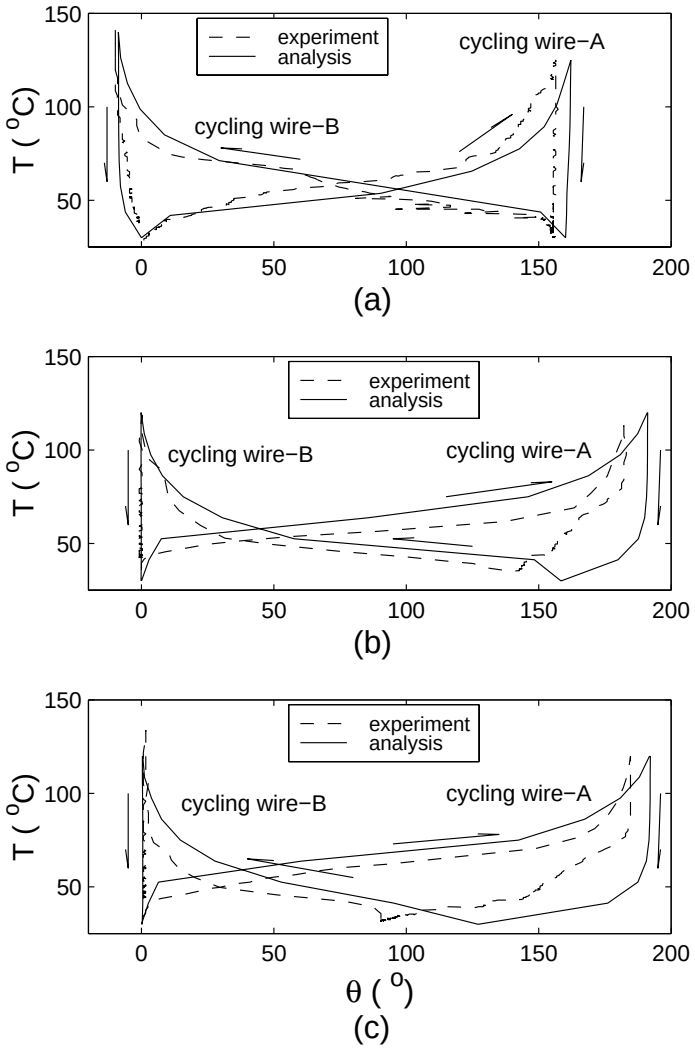

Figure 7.12: Two-way behaviour of prototype actuator (see Table 7.2 for pre-loading conditions).

	Wire-A		
Case	Max. load	Final load	Working torque
(a)	0.68 Nm	0.00 Nm	-0.22 Nm
(b)	0.68 Nm	0.52 Nm	0.52 Nm
(c)	0.68 Nm	0.62 Nm	0.62 Nm

Table 7.2: Pre-loading conditions.

grooves when the other wire was heated, which caused malfunctioning.

Generally speaking, our simulations agree with the experimental results, but the measured rotation angle is always smaller than the simulation. This may be due to three reasons. First, friction between disks, which we have not taken into consideration. Second, after many cycles the friction coefficient between the PTFE sleeve and Nitinol wire tends to increase. Third, after many thermal cycles, the PTFE sleeve tends to soften. As the diameter of the Nitinol wire is 0.5 mm, it is likely that it sank into the PTFE sleeves at high temperature deeper than that the 1 mm wire in which the original friction measurements, obtained in Section 6.4.1, had been carried out.

7.5 Power Requirements

In this section, we investigate the power requirements in all three actuators that we have tested.

7.5.1 Predications

We are interested in estimating the power requirements during the heating part of a thermal cycle, since no power is needed during cooling. A simple estimate of the total power required can be obtained by adding the energy required to raise the temperature of the wire (assuming that its specific heat remains constant), the energy required for the phase transformation, and the mechanical energy required to turn the actuator against the resisting torque.

Assuming that energy is required at a constant rate, we can divide the total energy by the actuation time t and thus obtain the following relationship

$$P_1 = (cV \triangle T\rho + qV\rho + M\ \theta)/t \tag{7.4}$$

where $c, q,\ \rho,\ M,\ \theta$ and V are the specific heat, the latent heat of the phase transformation, the density, the applied torque, the rotation angle and the volume of the material, respectively. $\triangle T$ is the uniform temperature change between the end and the beginning of the actuation cycle.

An improved analysis can be carried out, if the resistance R can be assumed to remain constant, using the following expression for the total energy required

$$E_2 = \int_0^t I^2 R dt + qV\rho + M\ \theta \tag{7.5}$$

where I is the electrical current. Hence, the mean power requirement is

$$P_2 = (\int_0^t I^2 R dt + qV\rho + M\ \theta)/t \tag{7.6}$$

The estimated energy and power required of the first actuator are give in Table 7.3 for different constant values of the electric current I. R and V were

I (A)	Time (sec)	$I^2\ R\ t$ (J)	$q\ V\ \rho$ (J)	$M\ \triangle\theta$ (Nm)	E_2 (J)	P_2 (W)
2	360	152.5	14.75	0.87	168.2	0.47
3	49.5	47.2	14.75	0.87	62.8	1.27
4	24.0	40.7	14.75	0.87	56.3	2.35
5	14.4	38.1	14.75	0.87	53.8	3.73
6	9.8	37.4	14.75	0.87	53.0	5.41
7	7.1	36.9	14.75	0.87	52.5	7.39
8	5.4	36.6	14.75	0.87	52.2	9.67

Table 7.3: Estimated energy and power requirements for different values of I in the first actuator.

calculated for a Nitinol wire that is 104 mm long and 1 mm in diameter. Other parameters were M= 2 Nm, θ= 25°, q= 28,000 J/Kg, ρ= 6450 Kg/m^3, and the electrical resistivity 0.80×10^{-6} Ωm. The time t was taken to be the time required to increase the temperature half-way between the central disk and the shoulder from 20°C to 145°C. It was calculated by using the unsteady-state temperature distribution solution in Appendix B.1.

As shown in Table 7.3, the dominant part of E_2 goes towards heating of the material. The second largest contribution is towards the latent heat required for the phase transformation. The work part is very small. Thus the input energy is mainly decided by the thermal term. If we apply a high current, the total energy required decreases because the heat loss is reduced.

7.5.2 Measured Power Requirements

The measured power requirements may be calculated as

$$P = \frac{1}{t}\int_0^t I\ U dt \tag{7.7}$$

where I and U are the measured electrical current and voltage, respectively.

7.5.3 Further Comparisons

Figure 7.13 shows the average power consumption to turn the disk in the one-disk tests of the first actuator, and our estimates by using the same parameters as for Table 7.3.

The average power consumption of the second actuator without PTFE sleeve, against a torque of 2 Nm, is plotted in Fig. 7.14. The estimates are based on a 474 mm long, 1 mm diameter wire, and $M\theta$= 2.5 Nm, the temperature is increased from 20°C to 110°C, and the I is a constant.

The average power consumption of the two-way actuator is plotted in Fig. 7.15. In using Eqns. 7.4 and 7.6 we assumed that the Nitinol wire is 2800 mm long, and the Nitinol wire (0.5 mm diameter) is heated from 25°C to 120°C. In Eqn. 7.4, M is 0; while in Eqn. 7.6, M = 0.62 Nm and θ is 180°, and again the I is a constant.

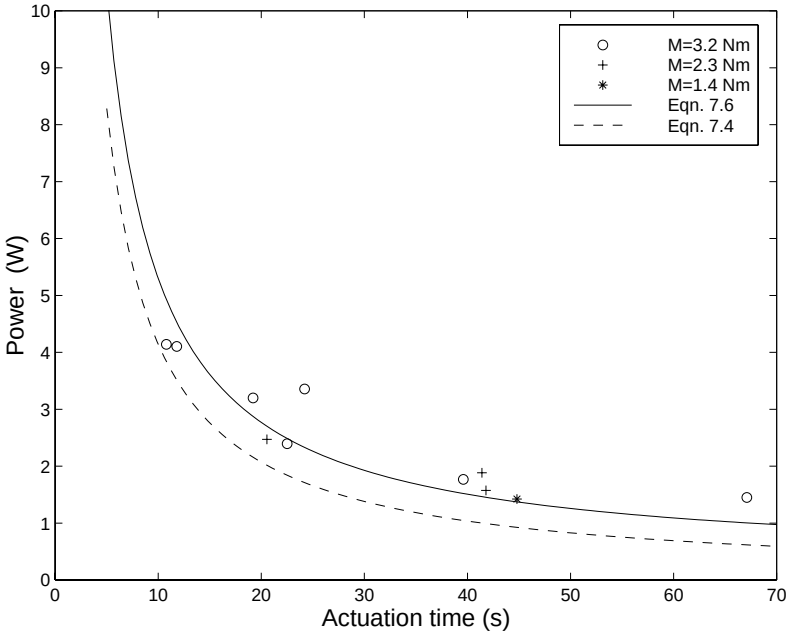

Figure 7.13: Average power consumption of the first actuator (one-disk).

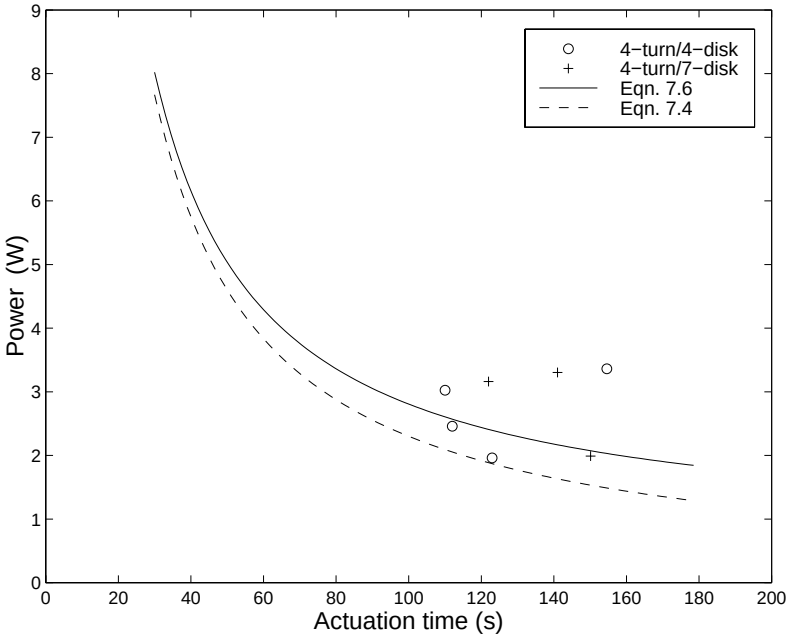

Figure 7.14: Average power consumption of the second actuator.

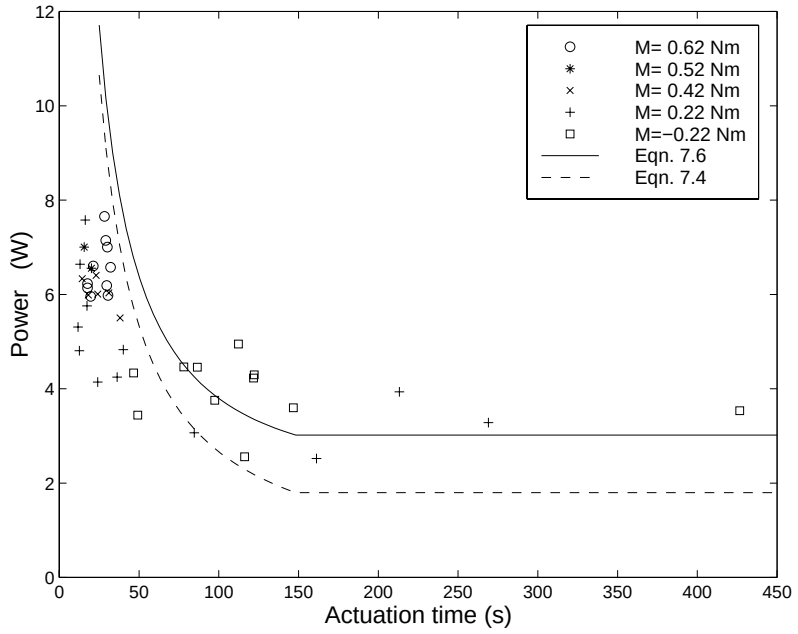

Figure 7.15: Average power consumption of the two-way actuator.

There is a minimum current requirement, i.e. I_{min}, in this actuator. If the supplied current is smaller than this value, the temperature of the wire cannot reach the temperature required. Hence, the two curves obtained from Eqns. 7.4 and 7.6 become straight lines parallel to the x-axis, indicating this minimum required power consumption.

As we can see, the estimates of the second actuator and the two-way actuator are not as good as those for the first actuator. The reason is that our calculations assumed that the Nitinol wires are in air, which is correct only for the first actuator.

7.6 Remarks

In this chapter, we have presented a Nitinol-wire based actuator which can function both as a one-way actuator and a two-way actuator. Supplied by an average power of less than 8 W, this actuator can rotate over 180^o against a constant torque of 0.62 Nm.

If we replace the 0.5 mm diameter Nitinol wire by 1 mm diameter wire, the same actuator would be able to operate against a constant torque of 2 Nm, with the same rotation capability.

We also have discussed the power requirements for all three actuators which we have tested. A method to calculate the power requirements of each actuator has been presented.

Chapter 8

Nitinol Bar

This chapter presents an experimental study of a Nitinol bar with nominal diameter of 6.5 mm. First, some torsional experiments, including torsional cycling at constant temperature and thermal cycling under constant torque, were carried out. The main aim of these tests was to investigate the behaviour of a Nitinol bar as a hinge actuator. In these tests, a kind of two-way memory behaviour was observed and hence, a series of uniaxial tension tests was performed in order to understand the phenomena seen in the torsion test.

After presenting this experimental work, we discuss the reasons for the behaviour of this Nitinol bar.

8.1 Material Preparation

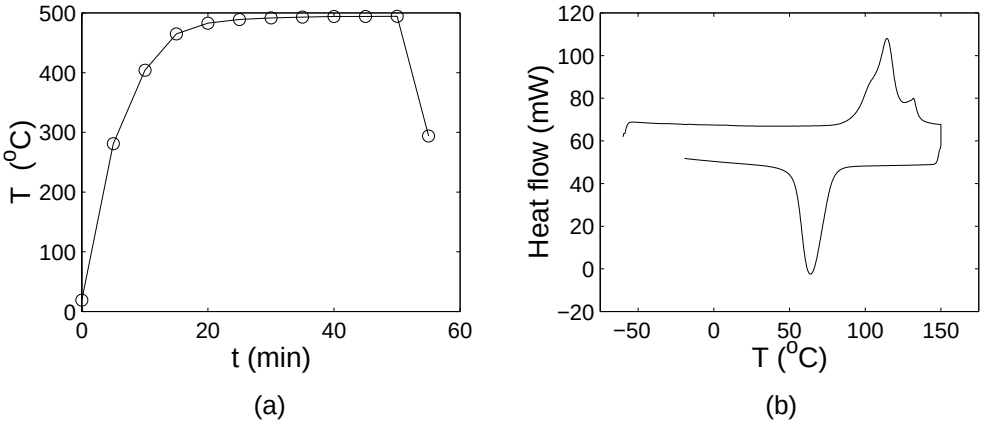

Figure 8.1: Heat treatment and DSC test. (a) T vs. t relationship in a typical heat treatment; (b) DSC test.

Several 150 mm long specimens were cut from a 1 m long Nitinol bar supplied by Advanced Materials and Technologies (AMT), Belgium. Since the bar was

supplied far from straight, a small jig was made up to hold it straight and then heat treat it at about 500°C for about 40 minutes, see Fig. 8.1(a). A small variation of the diameter at different cross-sections was measured.

A DSC test, see Section 3.1, was carried out on a small piece of Nitinol cut from one of these 150 mm long specimens after heat treatment. As shown in Fig. 8.1(b), the transformation temperatures are $M_f \approx 44^o$, $M_s \approx 88^o$C, $A_s \approx 80^o$C, and $A_f \approx 144^o$C. Therefore, at room temperature, the stable phase is martensite. And the transformation that occurs if one loads the bar at room temperature is martensite re-orientation (or detwinning).

8.2 Torsion Tests

The idea behind the use of a Nitinol bar in torsion to drive a hinge is based on the following principle. If the bar is subject to a transformation shear strain γ^t on the outer surface, the total rotation θ of one end with respect to the other end is

$$\theta = \frac{\gamma^t \times L}{d/2} \tag{8.1}$$

where L is the total length of the bar, and d the diameter. Converting this shear strain into an equivalent linear strain by assuming that Poisson's ratio is 0.5, refer Eqn. 4.46, we have

$$\gamma^t \approx \sqrt{3}\epsilon^t \tag{8.2}$$

for a very rough estimation. Hence,

$$\theta = \sqrt{3}\epsilon^t \frac{L}{d/2} \tag{8.3}$$

If d is 6.5 mm, we have the θ vs. L relationship shown in Fig. 8.2. That is to say, one end of a 130 mm long Nitinol bar is able to rotate by about 180° with respect to the other end, if $\epsilon^t = 4.5\%$.

8.2.1 Experimental Setup

Figure 8.3 shows the layout of the rig for the torsion tests and a photograph of the experimental set-up is shown in Fig. 8.4.

A constant torque can be applied by means of dead weights hanging from the pulley on the left hand side. Alternatively the pulley can be locked, and a rotation of one end relative to the other can be imposed by turning the wheel of the worm drive gear box on the right-hand side. The applied torque is measured by two strain gauges glued on the turned-down section of the shaft connected directly to the specimen. Rotation of either end of the specimen is measured by converting it with a flexible bond to a potentiometer, which measures to an

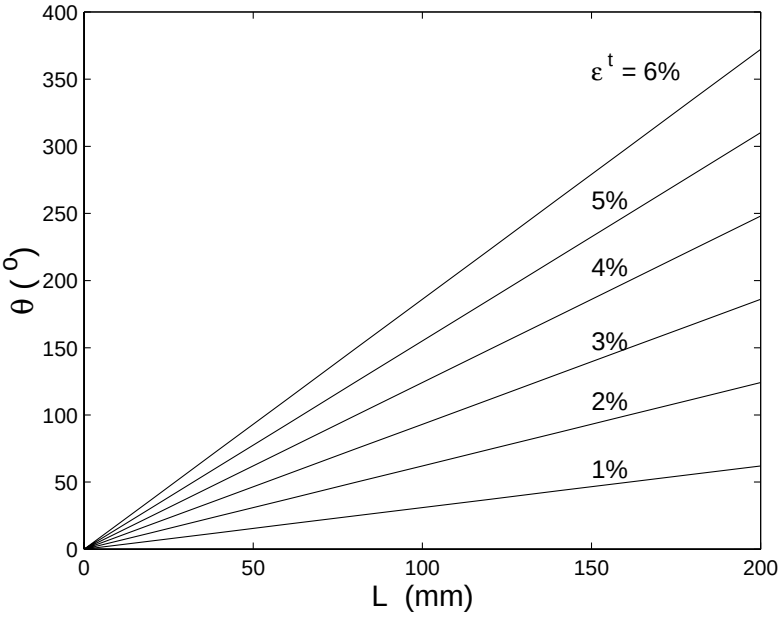

Figure 8.2: Geometric relation for a torsion bar.

accuracy of $\pm 0.3^o$. The free length of the specimen between the two end clamps is 130 mm. The Nitinol bar had square mild steel blocks silver soldered onto the ends, these were pinned through as an extra precaution.

Nichrome wire, which was first wrapped by polyimide electrical adhesive tape, was used to heat the bar by passing a current through it. Two thermocouples, one at the middle of the bar and another at one end of the bar, were used to measure the surface temperature of the bar. In order to keep the temperature distribution as even as possible the ends of the bars were insulated from the test rig by means of a high temperature, low thermal conductivity epoxy. The maximum temperature difference was found to be about 15^oC. We use the temperature measured at the middle of the bar in all the plots in this section.

The entire experiment was monitored and controlled (except for the application of loads) from a personal computer with an analogue/digital/analogue conversion board, running the **Labview** package from National Instruments. Plots of torque (M) vs. rotation (θ), torque (M) vs. temperature (T), and rotation (θ) vs. temperature (T) relationships, were available on the screen in real time.

The particular Nitinol bar that was tested had already been tested during the course of a previous, final-year undergraduate project. The previous tests included: torsion tests at constant temperature, thermal cycling under a constant torque, and thermal cycling with fixed ends. All torques applied were in the same direction, and up to 8.3 Nm in magnitude. We define this direction of application of the previous load as positive.

The experimental results presented in the next section are laid out in the order in which they were obtained. However, the results shown in Fig. 8.5(d) are

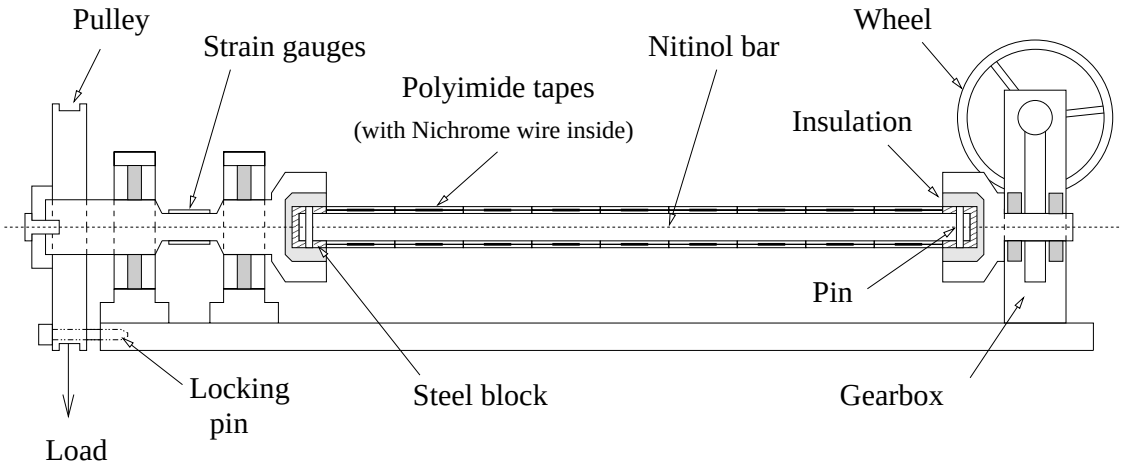

Figure 8.3: Layout of torsion bar test.

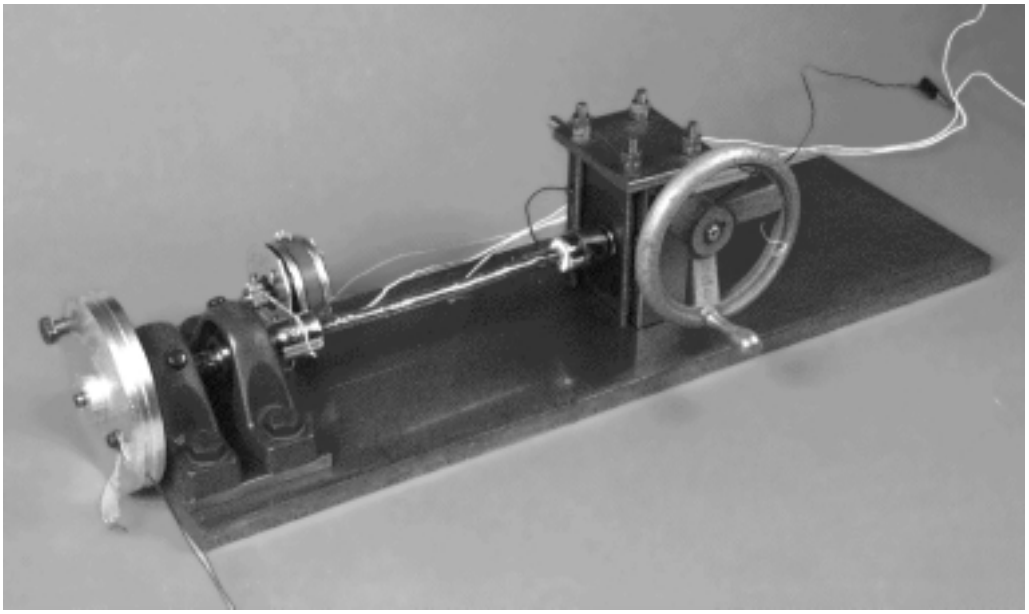

Figure 8.4: Photograph of experimental set-up.

taken from the previous set of tests.

8.2.2 Torsional Cycling

Torsion cycling was carried out by turning the wheel of the worm drive gear box forward and backward, with the pulley locked.

The load was cycled between 8.1 Nm and -8.0 Nm at room temperature ($\approx 22^o$C). Figure 8.5(a) shows the applied torque (M) vs. rotation angle (θ) relationship that was measured.

As we can see, after loading to 8.1 Nm, a rotation of about 35^o is observed. After unloading to 0 Nm, a residual rotation of about 11^o is left. Under the reverse loading we get a rotation of -21^o under a torque of -8.0 Nm. Releasing the torque, the bar goes almost back to its initial position, i.e. $\theta \approx 0^o$. The following two cycles show almost identical results.

These three cycles were carried out quite quickly. Other tests carried out at extremely slow speed showed the same behaviour but with a slightly larger rotation ($\approx 38^o$ under an a applied torque of 8.1 Nm).

It seems that torques of up to ± 8 Nm induce very little residual deformation. By using Eqn. 8.3, we have $\epsilon \approx 0.96\%$ on the surface of the bar when the rotation angle is 38^o.

Since the M vs. θ relationship shown in Fig. 8.5(a) is roughly linear, it is reasonable to assume that the shear stress distribution varies linearly and, using the standard formula from Timoshenko (1956)

$$\tau = \frac{Ma}{\pi d^4/32} \tag{8.4}$$

where d is the diameter of the bar, and a the distance from the point of interest to the central axis. Equation 8.4 gives τ^{max}= 0.150 GPa, for M = 8.1 Nm, which corresponds to a tension stress σ = 0.260 GPa (refer Eqn. 4.45). Thus the Young's Modulus of this bar can be estimated roughly as

$$D \approx \frac{\sigma}{\epsilon} \approx 27.1 \text{ GPa} \tag{8.5}$$

This value is very close to the Young's Modulus of martensite as shown in Table A.3. Thus, if there are no initial stresses in the bar, we would expect it to remain in the elastic range during the torsional cycling test.

8.2.3 Thermal Cycling

Before starting the thermal cycling test, the Nitinol bar was thermally cycled up to 190^oC several times without any applied load in order to eliminate the effects of the previous tests.

Two kinds of thermal cycling tests were carried out, cycling under a positive torque, Fig. 8.5(b-d), and under a negative torque, Fig. 8.7.

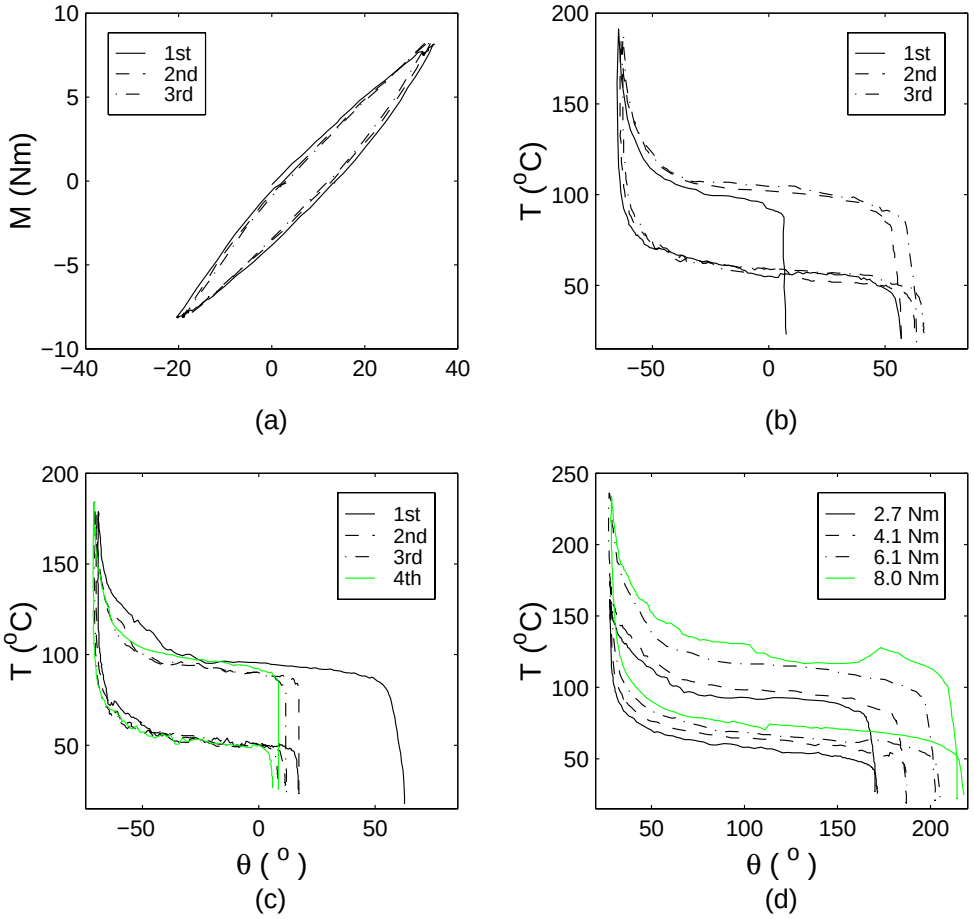

Figure 8.5: Experimental results. (a) Torsional cycling at room temperature; (b) thermal cycling under a constant torque of 2.0 Nm; (c) free thermal cycling; (d) thermal cycling under constant torques of different magnitudes.

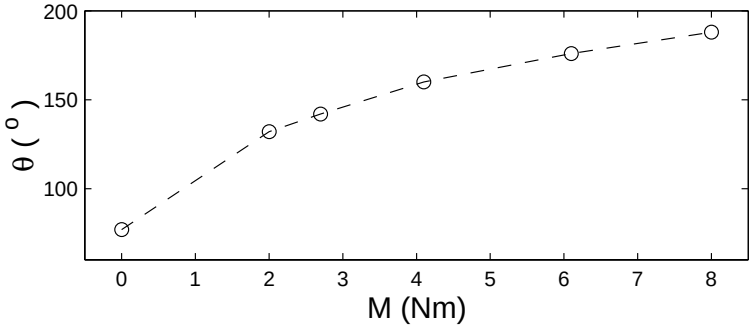

Figure 8.6: Relationship between applied torque (M) and rotation (θ) achieved in thermal cycles.

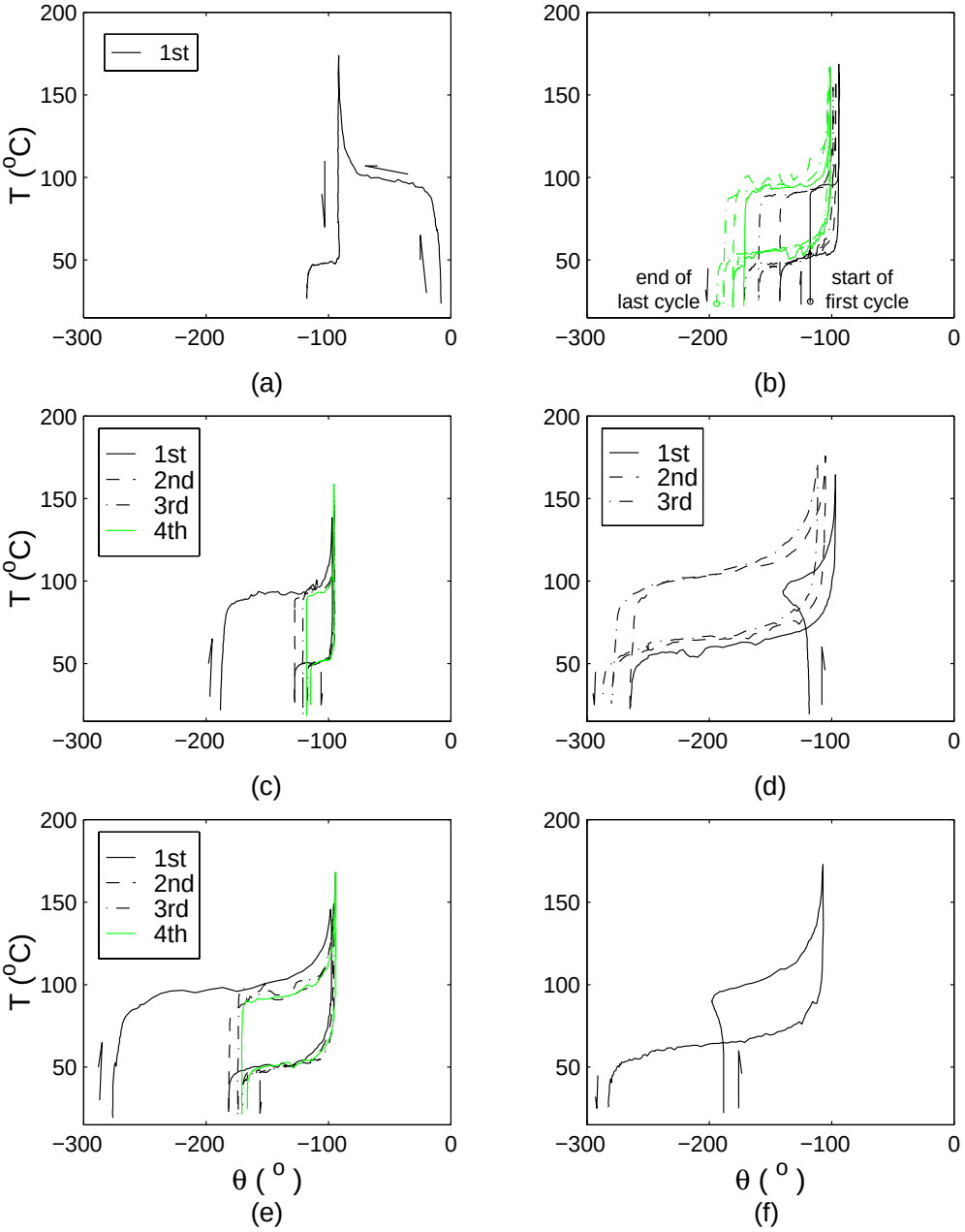

Figure 8.7: Experimental results. (a) 1st thermal cycle under -2.0 Nm; (b) further cycles under -2.0 Nm; (c) free thermal cycles ; (d) thermal cycles under -5.9 Nm; (e) free thermal cycles; (f) thermal cycle under -5.9 Nm.

We started our experiment by applying a constant torque of 2.0 Nm. Figure 8.5(b) shows the result of three successive thermal cycles under this torque. In the first cycle, a backward rotation of 70^o was measured at the temperature of 190^oC. Upon cooling, the Nitinol bar went past its initial position, rotating forward by 49^o. In the following two cycles, the rotation angle after cooling increased further, moves forward more and gradually converging to around 67^o.

The next test consisted of four free thermal cycles, Fig. 8.5(c). The first cycle produced a backward rotation by 132^o, upon heating, and then a forward rotation by 87^o. The following three cycles, produced approximately the same negative rotation reached in the first cycle, but the forward rotation upon heating gradually decreased and finally became stable. The finish angle converged to 5^o which gives a rotation of near 76^o in the last cycle.

There are several features in the above tests that we have not seen in the tests on Nitinol wires represented in Chapter 3.

- During torsional cycling between 8.1 to -8.0 GPa, the behaviour of the bar is essentially linear elastic, as the residual rotations after unloading are small. However, in thermal cycling under a constant torque of only 2 Nm, a large rotation was observed.

- During free thermal cycling, the bar rotates backwards upon heating, and forward upon cooling. This phenomenon looks just like two-way shape memory effect, see Section 2.1.1.

- All thermal cycling tests, with or without an applied torque, always show an evolutionary behaviour that gradually reaches a stable state, after several cycles.

Before moving to the thermal cycling tests under a negative torque, we note the thermal cycling test results under positive torque of different magnitudes, Fig. 8.5(d), showing that the larger the applied load, the higher the temperature needed for the transformation. Figure 8.6 plots the rotation range θ vs. the applied torque. All results are from previous tests and are taken after reaching a steady state after several cycles. By increasing the applied torque, we can increase the rotation that can be achieved in a thermal cycle: a rotation of more than 180^o was achieved in the test where the applied torque was 8 Nm.

Four more free thermal cycles were performed after the test shown in Fig. 8.5(c). In all the following tests, the applied torques were negative or zero.

First, a constant torque of -2.0 Nm was applied. The T vs. θ relation for the first cycle is plotted in Fig. 8.7(a). For the first part of the cycle, corresponding to the behaviour during heating phase there is not much difference from the previous test under positive torques. However, the cooling curve shows a very different behaviour, i.e. instead of rotating forward as in the previous tests, it twists backwards by 25^o more.

During the following six cycles the second part of this curve gradually grows into a cycle with a rotation amplitude of 92^o, Fig. 8.7(b). Note that the rotation angle gradually increases, the T vs. θ curve shifts forward slightly.

Figure 8.7(c) shows the behaviour observed during four free thermal cycles, after the tests under a torque of -2.0 Nm. Similar two-way shape memory behaviour as shown in Fig. 8.5(c) is observed, but the rotation is now in the opposite direction and of a much smaller amplitude.

The next cycling tests were under an applied torque of -5.9 Nm, Fig. 8.7(d). A significant kink in the first heating process is shown. The bar rotates backward and then forward, as the temperature is increased from 60°C to 90°C. In the following cycles there is no kink. Compared with the test under -2.0 Nm, the rotation angle is much larger. Still its T vs. θ curve shifts backward slightly in every cycle. However, the gap between the starting angle and finishing angle in each cycle converges much faster.

Four free thermal cycles carried out after this test showed similar behaviour to Fig. 8.7(c), but on a much larger scale, Fig. 8.7(e).

The kink described in the first thermal cycle under -5.9 Nm, Fig. 8.7(d), is found again, but a little smaller, when the same torque of -5.9 Nm is re-applied after the thermal cycles under zero load, Fig. 8.7(f). If we keep repeating this procedure, i.e free thermal cycling followed by a thermal cycling under a torque of -5.9 Nm, we find that the kink becomes smaller and smaller.

Generally speaking, all the results shown by the negative torque test are similar to the results for a positive torque, except the kink. It seems that this kink might be the result of the many previous tests under a positive torque, since its size gradually decreases as more and more tests are carried out.

At this stage it is difficult to explain these observations for Nitinol bars, as they appear to be in conflict with many aspects of the behaviour observed in Nitinol wires. Especially, how can a torque as low as -2 Nm change the direction of the rotation during thermal cycling?

In order to try to get a clearer picture, we need to get rid of the effects of the non-uniformity of the stress and strain field associated with a torsion test, a tension test was carried out.

8.3 Tension Test

A new, 150 mm long, bar was heat treated in the same way as described in Section 8.1 and was used in the tension tests.

8.3.1 Experimental Setup

The layout of the experiment is shown in Fig 8.8. An Instron testing machine was used for the test, the applied load being measured directly by the machine load cell. Two star washers mounted on the Nitinol bar were used to fixed a clip gauge, which could be mounted at different positions around the specimen. The position of the clip gauge is defined by the angle β. The strain measured by the clip gauge is the average over an initial gauge length of about 34.5 mm. The specimen was wrapped by a polyimide electrical adhesive tape covering a Nichrome wire,

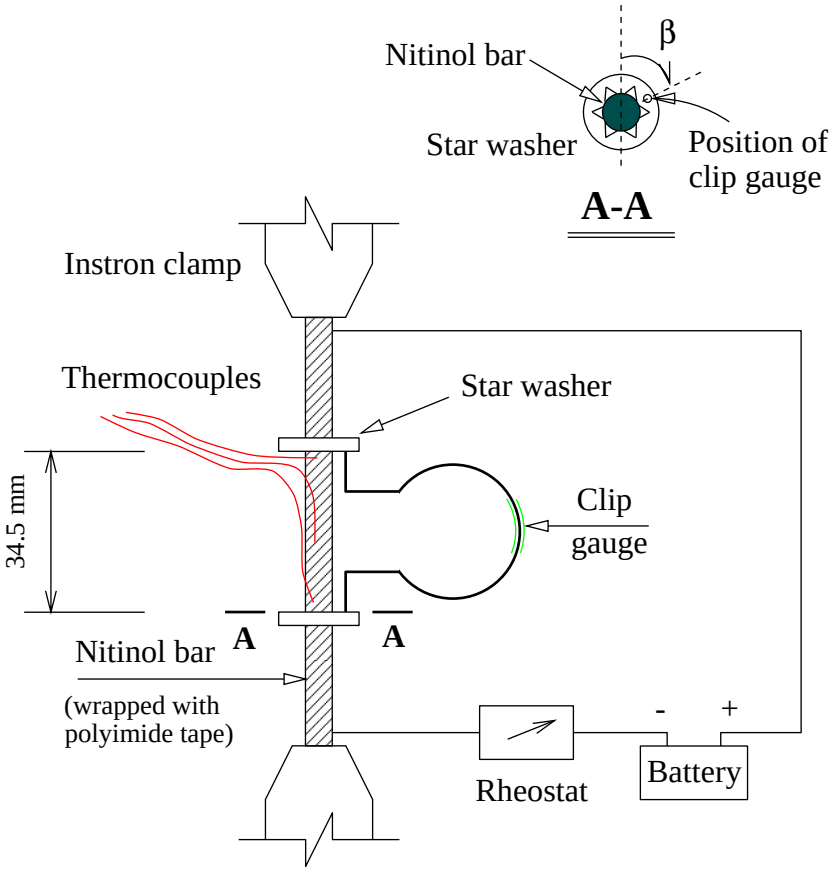

Figure 8.8: Layout of experimental setup for tension test.

as described in Section 8.2.1. Thus, the specimen can be heated by passing an electrical current through the Nichrome wire. The surface temperature of the bar was measured at three positions, as shown in Fig 8.8.

The measured temperature at three different positions was not the same. Up to 30°C of difference was measured. Since there was no thermal insulator at the end of the bar, the temperature near the two Instron clamps was lower. Hence, these temperature measurements were averaged and it is this average value that is used for all plots.

For the tension test and the thermal cycling test with fixed length, the distance between the two Instron clamps was set at about 100 mm, but in the free thermal cycling test, the top clamp was loosened before starting the test. The rest of the setup was the same as in Section 3.2.

8.3.2 Testing Cycle

A typical cycle consists of a tension test followed by a free thermal cycle test. In the first three tension tests, the maximum applied stress was gradually increased to 0.56 GPa; from then on the maximum applied stress was 0.56 GPa. All tension

tests, except test No. 9, which was carried out at a temperature of 47°C in the middle of the bar, were conducted at room temperature (22°C).

Figure 8.9 shows the relationship between σ and ϵ obtained from tension tests No. 3, 9, 10, and 11. The strain at the start of test No. 3 is set as zero point. As more and more tests were carried out, the σ vs. ϵ curve gradually shifts to the right, but the residual strain after each loading/unloading cycle becomes smaller and smaller. After about eleven cycles, no further permanent strain is accumulated. This suggests that a significant amount of non-recoverable (plastic) deformation builds up during the initial tension tests.

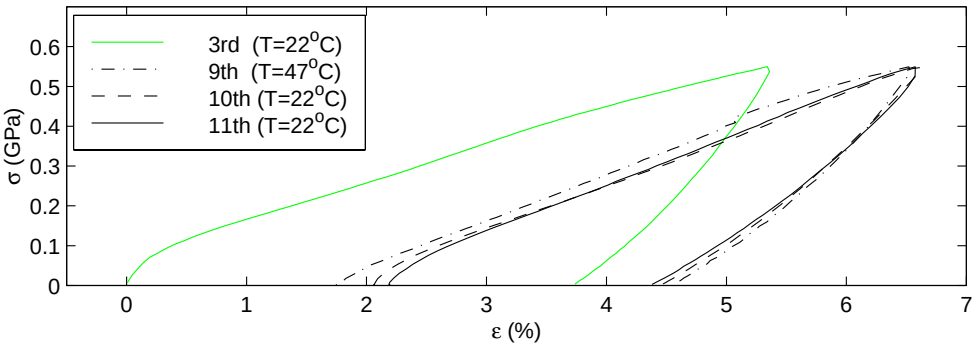

Figure 8.9: σ vs. ϵ relationships for tension test.

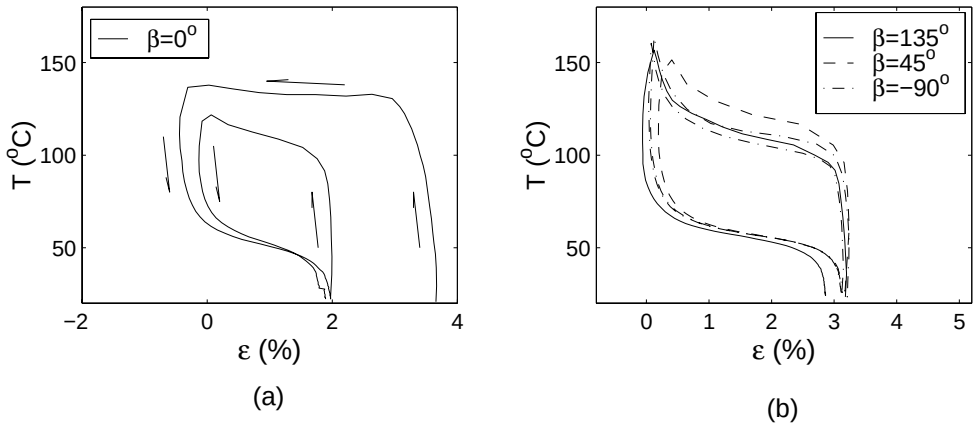

Figure 8.10: T vs. ϵ relationships in free thermal cycling. β denotes the position of the clip gauge. (a) Two free thermal cycles after tension test No. 3; (b) free thermal cycling after tension test No. 11.

Measurements from the thermal cycling tests carried out after tension test No. 3 are plotted in Fig. 8.10(a). In the first cycle, a strain of -0.5% is observed upon heating, but after cooling, a +2% strain is left over. The next cycle shows typical a two-way shape memory behaviour: at high temperature, the strain is

about 0%, while at low temperature, it is 2%. A nearly closed loop is described by the thermal cycle.

Since no external stress was applied, this two-way behaviour can only be driven by an internal mechanism, which is triggered thermally.

In order to check that there is no significant bending of the specimen or deflection of the star washer as the diameter of the specimen varies during testing, we measured the strain at three different positions (β= 135^o, 45^o, and -90^o) around the specimen. Figure 8.10(b) shows that the three T vs. ϵ relationships are not much different. Therefore, the bending of the specimen is very small, if there is any.

8.4 Discussion

The initial torsion tests, in Section 8.2, have shown some unexpected phenomena, which have been partly classified by the tension tests. Thus, we can now attempt to explain our experimental observations, as follows.

The two-way behaviour shown in both tension and torsion tests is due to the **Two-Way Shape Memory Effect**. This effect was defined by Wasilewski, R. J. as: *Under suitable prior deformation conditions in either the martensitic or parent*[1] *structures a "recoverable" expansion/contraction may be developed to accompany the forward transformation; and a change of equal magnitude but opposite in sense will then be present in the reverse transformation* (Schroeder and Wayman 1977b).

As mentioned in Section 2.1.1, two-way shape memory alloys can be obtained by training from one-way SMA. After training, a non-uniform residual stress field is introduced into the material, which is the result of non-recoverable deformation, such as motion of dislocations, at microscopic level. The growth of a particular martensite variant is associated with this non-uniform residual stress field.

Several training methods have been used (Schroeder and Wayman 1977b, Perkins and Hodgson 1988). To obtain stable two-way shape memory generally required many training cycles.

One training method is to deform the specimen severely below M_s. Using this method Schroeder and Wayman (1977b) were able to obtain two-way shape memory after just one tension test on a single crystal of CuZn.

At room temperature, the Nitinol used in our test is martensite, see Fig. 8.1(b). The two-way behaviour observed in the Nitinol is the result of two-way shape memory, while the build-up of permanent strain, seen in the tension tests, Fig. 8.9, is the result of training cycles. After 11 cycles the behaviour of the bar becomes stable, i.e the training is completed.

The general requirement of this training method is "*severe*" deformation, but the stress level applied during training does not seem very "*severe*". One possible explanation is that this Nitinol is much softer than the wires tested previously, possibly because a significant amount of strain hardening was produced by the

[1]This is another name for austenite.

wire-drawing process. Therefore, a non-uniform non-recoverable micro-strain field can be easily introduced into the material.

On the other hand, in cooling from austenite under a very small torque, this Nitinol can easily adapt itself to its loading and constraint conditions by the "*growth*" of particular martensite variant. This is a feature that I have not seen in my literature survey.

Therefore, by applying a small torsion load in the opposite direction (-2 Nm), the torsion bar starts to change its shape memory initially, by twisting into the opposite direction, Fig. 8.7(a). A shape memory is gradually built up by more cycling, or by cycling under a larger load. In the Nitinol bars that have been investigated, the application of a bigger load is a more efficient training method then a larger number of cycles, Fig. 8.7.

The reason for the lack of residual deformation in the torsional cycle at room temperature is that the applied torque is not large enough to produce widespread transformation. Therefore, only the area around the outer surface undergoes transformation.

The kink phenomena shown in Fig. 8.7 are the result of the shape memory built up during the previous test under a positive applied torque. We may roughly explain them as follows.

In the first thermal cycling under a torque of -2 Nm, Fig. 8.7(a), the bar rotates backward as before upon heating since the internal stress field is initially unchanged. However, upon cooling, it continues to rotate backward since the negative torque starts to control the growth of the martensite variant. As a result of this, a new internal stress field is formed in the outer part of the bar, where the applied stress is larger.

In the following cycles, the internal stress field in the outer area of the bar gradually extends towards the inside. Since the amount of training is not enough, i.e. the applied torque is small and the number of training cycles is not enough (in Fig. 8.7(b) the T vs. θ curve has yet to stabilise), the inner area is still dominated by the internal stress field generated by the previous tests at positive torque.

After more training in the negative side, the kink gradually disappears. It seems that free thermal cycling after cycling under a negative torque plays a role in the formation of a kink in the next cycling under a negative torque.

Chapter 9

Conclusions

The aims of this dissertation were twofold. The first was to further investigate and model the thermomechanical behaviour of shape memory alloys (Nitinol). The second, was to design, test and simulate Nitinol based actuators for deployable structures.

The main achievements are summarised as follows.

9.1 Behaviour of Nitinol

We have investigated the behaviour of Nitinol both experimentally and analytically. A thermo-micromechanical model was developed to explain the shape memory related behaviour. A phenomenological model was presented for the design of Nitinol wire-based actuators.

9.1.1 Experimental Characterisation

In order to get a complete picture of the thermomechanical behaviour of Nitinol, two kinds of experiment, purely thermal tests and thermomechanical tests, were carried out on Nitinol wire and bar.

In the purely thermal tests, a Different Scanning Calorimeter was used to determine the phase transformation/temperature relation of Nitinol wire with diameter of 1 mm and Nitinol bar. For the Nitinol wire it was found that different ways of cooling after heat treatment result different phase transformations. In particular, R-phase could be produced by leaving the Nitinol sample on a hot block after it was taken out of the furnace. We also found that the transformation temperature of detwinned martensite is higher than twinned martensite.

The thermomechanical tests, including tension tests at different temperatures, tension tests under different strain rates, response to suddenly applied loads, thermal cycling under different loads and thermal cycling with fixed length were carried out on Nitinol wire.

Generally speaking, the stress vs. strain relation of the Nitinol wire that we have tested in tension can be divided into three regimes. The first regime is mainly

elastic deformation. The second regime involves a phase transformation which is dependent upon the temperature of the specimen. The higher the temperature, the higher the stress at the same strain. Beyond a certain point, which varies with temperature, all the stress vs. strain curves join together and the behaviour becomes temperature independent. This is the third regime which corresponds mainly to the martensite re-orientation, a practically isothermal transformation. Note that in some cases, there is practically no elastic range.

The variation of the Young's Modulus during loading was observed.

In the tension tests under different strain rates, we found that at low strain rate, the higher the applied strain rate, the higher the temperature increase of the wire, and the higher the stress required to reach the same strain level. However, in the tests carried out at high strain rate, although the temperature increased with the increase of strain rate, the stress did not go up.

We found that in the case where the Nitinol wires are heated by passing a current through them, the temperature distribution along them is not uniform, due to the fact that the clamping blocks at the end of the wire behave as heat sinks.

We have observed the phase transformation front movement in Nitinol wires under tension. A strip of temperature-sensitive liquid crystal film was used to monitor the temperature distribution in the wire in real time during loading.

The response to suddenly applied loads of 0.5 mm diameter wire was tested. Due to the temperature increase, which was caused by the heat generated in the phase transformation during loading, it took approximately one minute for the wire to reach its full extension.

Torsional tests, thermal cycling under different torques, and normal tension and thermal cycling tests were carried out on Nitinol bars with diameter of 6.5 mm. This bar showed very different behaviour from the wires, as it can be easily trained to acquire two-way shape memory by training it in tension or by subjecting it to thermal cycles under a constant torque. Only a few training cycles are required to get stable shape memory behaviour. Under torsion, a large rotation can be obtained by thermal cycling under a very small torque.

9.1.2 Thermo-Micromechanical Model

We have developed a thermo-micromechanical model based on complementary free energy and micromechanical transformation system to investigate the behaviour of shape memory under uniaxial load cycling and thermal cycling.

Experimentally observed phenomena, such as V-shape of critical stress, non-symmetrical behaviour in tension and compression, transformation front behaviour, and multi-phase transformation, were explained by this model.

9.1.3 Phenomenological Model for Nitinol Wire

This phenomenological model is based on tension test, carried out at different constant temperatures, and thermal cycling test under different constant loads.

We have shown that our model can reproduce accurately the stress-strain-temperature relationship for all the quasi-static tests we have carried out on Nitinol wires. This model has no difficulty in dealing with incomplete loading or thermal cycling.

This model has been used to simulate thermal cycling behaviour with fixed length, strain rate effects, and phase transformation front behaviour.

9.2 Nitinol-Based Actuators

Three Nitinol wire-based rotatory actuators have been designed and tested. The behaviour of these actuators has been simulated by using the phenomenological model that we have developed.

The first actuator is a biased actuator which is 190 mm long, with diameter of 48 mm. Its maximum rotation was about 30^o. It has been tested against a resisting torque up to 3.2 Nm. Since the Nitinol wire in this actuator is very short, temperature non-uniformity has to be taken into consideration in the simulation. A simple control system has been set up to control the rotation angle of this actuator.

The second actuator is a one-way actuator, length$\approx$ 185 mm and diameter $\approx$ 40 mm, and has produced a maximum rotation of 110^o against a torque of 2.1 Nm. A key difficulty in the design of this actuator is friction. The solution that has been adopted is based on a series of 5 mm thick ceramic disks that are mounted on ball bearings. This solution has worked well, but a good alignment between the wire and the disks was found to be essential for the correct operation of this concept. An improvement has been made by covering the Nitinol wire with PTFE sleeves, to reduce the friction and prevent the wire falling into the gaps between disks.

In these two actuators, Nitinol wires with diameter of 1 mm were used.

The third actuator is a two-way actuator based on the same concept as the second actuator, but it was designed more carefully, to avoid the practical difficulties that had been encountered when testing the prototype of the previous actuator. Also, two actuators were put together, one against another, in order to obtain a two-way actuator, which can rotate forward and backward by heating different wires. This actuator is about 250 mm long and 46 mm in diameter. It can rotate over 180^o against a torque of 0.62 Nm. An average power of less than 8 W is required for its actuation. If we replace the 0.5 mm wire that we used for the tests by 1 mm wire, the same actuator will be able to operate against a constant torque of 2 Nm and with the same rotation capability.

The behaviour predicted by our analytical model agrees remarkably well with the measured behaviour of all actuators. The general design procedure for Nitinol wire-based actuators that emerged from this work is summarised in the next section.

The power consumption to operate all actuators was measured. Two simple approaches were proposed to estimate the average power requirements.

Finally, a preliminary study of a torsional actuator has been made. The actuator consists of a Nitinol bar with diameter of 6.5 mm and a length of 130 mm. It can easily rotate by over 180^o against a torque of 8 Nm. This particular type of Nitinol bar may be used as an actuator after enough training. But the applied load should be smaller than the training load, and it must be in the same direction as the training load.

9.3 Design Procedure for Wire-Based Actuators

The design procedure for SMA based actuators is different from ordinary design in many aspects. The main stages of the design procedure for actuators that are based on Nitinol wire are summarised as follows.

(i) Preliminary Design

Investigation of the relationship between the stroke of any chosen actuator configuration vs. actuator parameters such as length and diameter. Typical properties of commercially available Nitinol may be used at this stage, see Appendix A. At the end of this phase, a particular actuator design is chosen, and key properties of the required Nitinol wire are determined, e.g. the length of the wire and its cross-section.

(ii) Material Characterisation

Once the particular type of Nitinol wire selected in (i) has been obtained, it is heat-treated, see Sections 2.3 and 3.1. Then, the two types of thermo-mechanical tests described in Sections 3.3 and 3.6 are carried out in order to determine the parameters of the constitutive model introduced in Section 4.2.

(iii) Preliminary Simulation

A simulation of the actuator response is made by assuming that the temperature in the Nitinol wire(s) is uniform throughout. Thus, it is possible to estimate the relationship between stress in the wire, displacement/rotation of the actuator, and temperature. Note that a key parameter, time, is missing from this simulation. A more accurate simulation requires that the total energy required for the actuation cycle be estimated, see Section 7.5. Then, for any chosen actuation time the mean power required can be calculated, from which the required electrical current is obtained.

(iv) Detailed Design

Key details of the actuator design that have to be decided include:

- Insulation

  Electrical insulation is required if the Nitinol wire is heated by passing a current through it. A Nitinol wire can be insulated from other

metal components of the actuator either by covering it with insulating elements, or by covering the other metal components with insulating layers. In the former case, the insulator should be hard but flexible. In the latter case, only the contact points between the Nitinol wire and other components need to be insulated. Thin Tufnol plate is a good choice.

In some cases, thermal insulation is also required, to reduce energy consumption.

Both electrical insulator and thermal insulator must be able to stand high temperatures without softening or melting. Particularly, to avoid that the Nitinol wire digs into the insulator at high temperature. The exact temperature depends on the transformation temperature of the Nitinol used. For the Nitinol wire that we used, this temperature is about 250°C. The PTFE sleeve we used is good for a limited number of operation cycles, but not for a large number of cycles.

- Friction

  Friction is an important issue if the Nitinol wire is going to be in contact with the surface of other components, such as pulleys or shafts. In order to improve the performance of an actuator, one may use some kind of low friction layer between the wire and the other components. Again, such a layer must be able to survive at high temperature. If this layer is required to act as insulator as well, then its insulation properties have to be considered.

- Connections

  Welding or mechanical clamps are possible. The final choice should be made considering also the insulation method, strategy for pre-stretching the wire, etc.

- Pre-stretching

  The initial conditions of Nitinol wires, i.e. their pre-strain and pre-stress are issues that should be considered.

- Effects of slackening

  It is relatively common for the Nitinol wires in a two-way actuator to become slack in some configurations. This may cause the wires to move away from their correct position, which may result in malfunctioning of the actuator. The amount of slackening can be reduced by reducing the applied load, but it may be necessary to prevent the slackened wire from moving too much by using some kind of holders.

(v) Accurate Simulation

Once all details of an actuator have been decided, we re-simulate the behavior of the actuator by taking friction, temperature distribution, pre-stretching, etc. into consideration. One may have to go back, even to the

very beginning, i.e. stage (i), to re-consider the design, if the final result is not satisfactory.

9.4 Future Work

In terms of future work, there are many paths to follow.

- The Nitinol we have tested was in wire and bar shape and in one-dimensional loading conditions, i.e. uniaxial tension or torsion. Further work may be carried out on multi-dimensional situations to get further knowledge of the thermomechanical behaviour of SMAs.
- It may be possible to discover the relationship between tension behaviour and behaviour under other load conditions, e.g. compression, torsion, and even multi-axial loading, by using the thermo-micromechanical model we developed. This relationship will be very useful in order to develop realistic finite element models for structures including SMA components.
- Our phenomenological model could be extended from Nitinol wire to Nitinol in other shapes/loading conditions and to other shape memory alloys. How to model the two-way shape memory behaviour is also a topic for study.
- The PTFE sleeve used in the two-way actuator is not good for long-life operation. A different material should be found which is strong and can stand many high temperature cycles.
- In this dissertation, the design was based on wire and bar. Design, manufacture and testing of SMA-based actuators using different concepts is surely necessary.
- Actuator performance can be optimised and by using closed-loop temperature control to improve timing accuracy.

Bibliography

Abeyaratne, R. and Knowles, J. K.(1993), A Continuum Model of a Thermoelastic Solid Capable of Undergoing Phase Transformations, Journal of the Mechanics and Physics of Solids, Vol. 41, No. 3, pp 541-571

Achenbach, M. and Müller, I.(1985), Shape Memory as a Thermally Activated Process, Plasticity Today Modelling, Methods and Applications, Elsevier Applied Science Publishers

Adler, P. H., Yu, W., Pelton, A. R., Zadno, R., Duerig, T. W. and Barresi, R.(1990), On the Tensile and Torsional Properties of Pseudoelastic NiTi, Scripta Metallurgica et Materialia, Vol. 24, pp 943-947

Aiken, I. D., Nims, D. K., Whittaker, A. S. and Kelly, J. M.(1993), Testing of Passive Energy Dissipation Systems, Earthquake Spectra, Vol. 9, No. 3

Anders, W. S. and Rogers, C. A.(1991), Design of a Shape Memory Alloy Deployment Hinge for Reflector Facets, AIAA-91-1162-CP, pp 148-158

Baz, A., Ro, J., Mutua, M. and Gilheany, J.(1992), Active Buckling Control of Nitinol-Reinforced Composite Beams, ADPA/AIAA/ASME/SPIE Conference on Active Materials and Adaptive Structures-Session 10, pp 167-176

Bergamasco, M., Salsedo, F. and Dario, P.(1989), A Linear SMA Motor as Direct-Drive Robotic Actuator, 1989 IEEE International Conference on Robotics and Automation, pp 618-623

Beyer, J.(1995), Recent Advances in the Martensitic Transformations of Ti-Ni Alloys, Journal de Physique IV, Vol. 5, No. C2, pp 433-442

Bhattacharyya, A., Lagoudas, D. C., Wang, Y. and Kinra, V. K.(1995), On the Role of Thermoelectric Heat Transfer in the Design of SMA Actuators: Theoretical Modeling and Experiment, Smart Materials and Structures, Vol. 4, pp 252-263

Bhattacharya, K. and James, R. D.(1996), A Theory of Shape-Memory Thin

Films with Applications, submitted to MRS Proceedings on Advances in Materials for Smart Systems

Boyd, J. G. and Lagoudas, D. C.(1994), A Constitutive Model for Simultaneous Transformation and Reorientation in Shape Memory Materials, AMD-Vol. 189/PVP-Vol. 292, Mechanics of Phase Transformations and Shape Memory Alloys, ASME 1994, pp 159-178

Brinson, L. C.(1993), One-Dimensional Constitutive Behavior of Shape Memory Alloys: Thermomechanical Derivation with Non-Constant material Functions and Redefined Martensite Internal Variable, Journal of Intelligent Material Systems and Structures, Vol. 4, pp 229-242

Cahn, R. W.(1995), Metallic Rubber Bounces Back, Nature, Vol. 374, pp 120-121

Carpenter, B. F., Head, R. J. and Gehling, R.(1995), Shape Memory Actuated Gimbal, SPIE, Vol. 2447, pp 91-100

Carslaw, H. S. and Jaeger, J. C.(1959), Conduction of Heat in Solid, Oxford

Choi, S. J., Lu, C. and Feland, J.(1996), A Nitinol-Based Solar Array Deployment Mechanism, Presented on the NASA/Lockheed Martin 30th Aerospace Mechanisms Symposia Proceedings

Christian, J. W.(1982), Deformation by Moving Interface, Metallurgical Transactions A, Vol. 13A, pp 509-538

Chumljakov, J. I. and Starenchenko, S. V.(1995), Stress Induced Martensitic Transformation in Aged Titanium Nickel Single Crystals, Journal de Physique, Vol. 5, No. C8, pp 803-808

Cory, J. S. and McNichol, J. L.(1985), Nonequilibrium Thermostatics, Journal of Applied Physics, Vol. 58, No. 9(1), pp 3284-3294

Ditman, J. B., Bergman, L. A. and Tsao, T. C.(1994), The Design of Extended Bandwidth Shape Memory Alloy Actuators, AIAA-94-1757-CP, pp 210-220

Duerig, T. W., Melton, K. N. and Wayman, C. M.(1990), Engineering Aspects of Shape Memory Alloys, Butterworth-Heinemann

Duerig, T. W. and Pelton, A. R.(1994), Ti-Ni Shape Memory Alloys, Material Properties Handbook, Titanium Alloys, ASM International 1994

Durlu, T. N.(1997), Effect of Austenite Grain Size on ϵ Martensite Formation in an Fe-Mn-Mo Alloy, Journal of Materials Science Letters, Vol. 16, No. 4, pp 320-321

Dye, T. E.,(1990), An Experimental Investigation of the Behavior of Nitinol, Master's Thesis, Department of Mechanical Engineering, Virginia Polytechnic Institute and State University

Eshelby, J. D.(1957), The Determination of the Elastic Field of an Ellipsoidal Inclusion and Related Problems, Proceedings of Royal Society, Vol. A241, pp 376-574

Falk, F.(1989), Pseudoelastic Stress-Strain Curves of Polycrystalline Shape Memory Alloys Calculated from Single Crystal Data, International Journal of Engineering Science, Vol. 27, No. 3, pp 277-284

Fischer, F. D. and Tanaka, K.(1992), A Micromechanical Model for the Kinetics of Martensitic Transformation, International Journal of Solids and Structures, Vol. 29, No. 14/15, pp 1723-1728

Funakubo, H.(1987), Shape Memory Alloys, Gordon and Breach Science Publishers

Gabriel, K. J., Trimmer, W. S. N. and Walker, J. A.(1988), A Micro Rotary Actuator Using Shape Memory Alloys, Sensors and Actuators, Vol. 15, pp 95-102

Gandhi, M. V. and Thompson, B. S.(1992), Smart Materials and Structures, Chapman & Hall

Gilman, J. J.(1969), Micromechanics of Flow in Solids, McGraw-Hill Book Company

Goldstein, H.(1950), Classical Mechanics, Addison-Wesley Publishing Company, Inc.

Gorbet, R. B. and Russell, R. A.(1995), A Novel Differential Shape Memory Alloy Actuator for Position Control, Robotica, Vol. 13, pp 423-430

Goubaa, K., Orlionnet, V., Masse, M. and Bouquet, G.(1988), NiTiCu Shape Memory Alloy Tested on a "Soft" Torsion Machine, Scripta Metallurgica, Vol. 22, pp 1023-1028

Graesser, E. J. and Cozzarelli, F. A.(1992), Shape-Memory Alloys as New Materials for Aseimic Isolation, Journal of Engineering Mechanics, Vol. 117, No. 11, pp 2590-2608

Grant, D. and Hayward, V.(1995), Variable Structure Control of Shape Memory Alloy Actuators, unpublished paper

Hall, E. O.(1970), Yield Point Phenomena in Metals and Alloys, Macmillan

Hasiguti, R. R. and Iwasaki, K.(1968), Internal Friction and Related Properties of the TiNi Intermetallic Compound, Journal of Applied Physics, Vol. 39, No. 5, pp 2182-2186

Hautcoeur, A., Eberhardt, A., Patoor, E. and Berveiller, M.(1995), Thermomechanical Behaviour of Monocrystalline Cu-Al-Be shape Memory Alloys and Determination of the Metastable Phase Diagram, Journal de Physique, Vol. 5, No. C2, pp459-464

Hirose, S., Ikuta, K. and Umetani, Y.(1989), Development of a Shape Memory Alloy Actuator: Performance Assessment and Introduction of a New Composing Approach, Advanced Robotics, Vol. 3, No. 1, pp 3-16

Hostenkamp, R. G.(1985), Features of the Solar Array Driver Mechanism for the Space Telescope, Aerospace Mechanisms Symposium 1985, NASA CP2371, pp 315-327

Huang, M. and Brinson, L. C.(1997), A Multivariant Model for Shape Memory Alloys, submitted to Journal of the Mechanics and Physics of Solids

Humbeeck, J. V. and Cederstrom, J.(1994), The Present State of Shape Memory Materials and Barriers Still to be Overcome, Proceedings of the First International Conference on Shape Memory and Superelastic Technologies, California, USA, pp 1-6

Jabs, H. and Moignier, P.(1996), Shape Memory Alloy Application, Proceedings of Conference on Spacecraft Structures, Materials & Mechanical Testing (ESA SP-386), The Netherlands, pp 1423-1425

Jia, J. and Rogers, C. A.(1990), Formulation of a Laminated Shell Theory Incorporating Embedded Distributed Actuators, Journal of Mechanical Design, Vol. 112, pp 596-604

Jenkins, P. P. and Landis, G. A.(1995), A Rotating Arm Using Shape-Memory Alloy, 29th Aerospace Mechanisms Symposium, NASA conference Publication 3293, pp 167-171

Kafka, V.(1994), Shape Memory: A New Concept of Explanation and of Mathematical Modelling. Part I: Micromechanical Explanation of the Causal-

ity in the SM Processes, Journal of Intelligent Material Systems and Structures, Vol. 5, pp 809-814

Kakizawa, T., and Ohno, S.(1996), Utilization of Shape Memory Alloy as a Sensing Material for Smart Structures, in Advanced Composite Materials in Bridges and Structures, pp 67-74

Kim, S.(1995), Passive Control Techniques in Earthquake Engineering, SPIE, Vol. 2445, pp 214-224

Knowles, K. M. and Smith, D. A.(1981), The Crystallography of the Martensitic Transformation in Equiatomic Nickel-Titanium, Acta Metallurgica, Vol. 29, pp 101-110

Kocks, U. F.(1970), The Relation Between Polycrystal Deformation and Single-Crystal Deformation, Metallurgical Transactions, Vol. 1, pp 1121-1143

Labview(1996), Labview User Manual, National Instruments

Leclercq, S. and Lexcellent, C.(1996), A General Macroscopic Description of the Thermomechanical Behaviour of Shape Memory Alloys, Journal of the Mechanics and Physics of Solids, Vol. 44, No. 6, pp 953-980

Leo, P. H., Shield, T. W. and Bruno, O. P.(1993), Transient Heat Transfer Effects on the Pseudoelastic Behavior of Shape-Memory Wires, Acta Metallurgica et Materialia, Vol. 41, pp 2477-2485

Liang, C.(1990), The Constitutive Modelling of Shape Memory Alloys, PhD Dissertation, Department of Mechanical Engineering, Virginia Polytechnic Institute and State University

Liang, C. and Rogers, C. A.(1990), One Dimensional Thermomechanical Constitutive Relations for Shape Memory Materials, Journal of Intelligent Materials System and Structures, Vol. 1, pp 207-234

Lieberman, D. S., Wechsler, M. S. and Read, T. A.(1955), Cubic to Orthorhombic Diffusionless Phase Change — Experimental and Theoretical Studies of AuCd, Journal of Applied Physics, Vol. 26, No. 4, pp 473-484

Likhachev, V. A., Razov, A. I., Cherniavsky, A. G., Kravchenko, Y. and Trusov, S. N.(1994), Truss Mounting in Space by Shape Memory Alloys, Proceedings of the First International Conference on Shape Memory and Superelastic Technologies, California, USA, pp 245-248

Lipscomb, I. P. and Nokes, L. D. M.(1996), The Application of Shape Memory

Alloys in Medicine, Antony Rowe Ltd.

Lubliner, J. and Auricchio, F.(1996), Generalized Plasticity and Shape-Memory Alloys, International Journal of Solids and Structures, Vol. 33, No. 7, pp 991-1003

Maclean, B. J., Draper, J. L. and Misra, M. S.(1990), Development of a Shape Memory Material Actuator for Adaptive Truss Applications, First Joint U.S./Japan Conference on Adaptive Structures, Technomic Publishing Co., pp 1038-1055

McCarty, L. M.(1990), Shape Memory Alloy Derives Rotatory Actuator, Design News (Boston), Vol. 46, No. 3, pp 180-181

McClintock, F. A. and Argon, A. S.(1966), Mechanical Behaviour of Materials, Addison-Wesley Publishing Company

Moorleghem, W. V.(1993), The Use of Shape Memory Alloys in Space Structures, Either as an Actuator or as a Passive Damping Element, Space Structures 4, Thomas Telford, London, pp 833-842

Moumni, Z. and Nguyen, Q. S.(1996), A Model for Material with Phase Change and Applications, Journal de Physique IV, Vol. 6, No. C1, pp 335-345

Mura, T., Mori, T. and Kato, M.(1976), The Elastic Field Caused by a General Ellipsoidal Inclusion and the Application to the Martensite Formation, Journal of the Mechanics and Physics of Solids, Vol. 24, pp 305-318

Mura, T.(1987), Micromechanics of Defects in Solids, Martinus Nijhoff Publishess, Dordrecht

Nagaya, K. and Hirata, Y.(1992), Analysis of a Coupling Made of Shape Memory Alloy and Its Dynamic Response due to Impacts, Journal of Vibration and Acoustics, Vol. 114, pp 297-304

Nishiyama, Z.(1978), Martensitic Transformation, Academic Press

Olson, G. B. and Cohen, M.(1982), Theory of Martensitic Nucleation: A Current Assessment, Proceeding International Conference on Solid-Solid Phase Transformations, The Metallurgical Society of AIME, pp 1145-1163

Ortin, J. and Planes, A.(1988), Thermodynamic Analysis of Thermal Measurements in Thermoelastic Martensitic Transformations, Acta Metallurgica, Vol. 36, No. 8, pp 1873-1889

Ortin, J. and Planes, A.(1989), Thermodynamics of Thermoelastic Martensitic Transformations, Acta Metallurgica, Vol. 37, No. 5, pp 1433-1441

Ortin, J. and Planes, A.(1991), Thermodynamics and Hysteresis Behaviour of Thermoelastic Martensitic Transformations, Journal de Physique IV, Vol. 1, No. C4, pp 13-23

Ortin, J.(1992), Preisach Modeling of Hysteresis for a Pseudoelastic Cu-Zn-Al Single Crystal, Journal of Apply Physics, Vol. 71, No. 3, pp 1454-1461

Otsuka, K., Sawamura, T., Shimizu, K. and Wayman, C. M.(1971), Characteristics of the Martensitic Transformation in TiNi and the Memory Effect, Metallurgical Transactions, Vol. 2, pp 2583-2588

Otsuka, K.(1988), Introduction to the R-Phase Transition, Engineering Aspects of Shape Memory Alloys, Edited by: Duerig, T. W. *et al.*, Butterworth-Heinemann, pp 36-45

Patoor, E., Eberhardt, A. and Berveiller, M.(1994), Micromechanical Modelling of the Shape Memory Behaviour, AMD-Vol. 189/PVP-Vol. 292, Mechanics of Phase Transformations and Shape Memory Alloys, ASME 1994, pp 23-38

Patoor, E., Eberhardt, A. and Berveiller, M.(1996), Micromechanical Modelling of Superelasticity in Shape Memory Alloys, Journal de Physique, Vol. 6, No. C1, pp 277-292

Pelton, A. R., Hodgson, D. and Durig, T.(1994), Proceedings of SMST-94, The first International Conference on Shape Memory and Superelastic Technologies, Pacific Grove, California, USA

Pelton, A. R., Hodgson, D., Russell, S. and Durig, T.(1997), Proceedings of SMST-97, The Second International Conference on Shape Memory and Superelastic Technologies, Pacific Grove, California, USA

Perkins, J. and Hodgson, D.(1988), The Two-Way Shape Memory Effect, Engineering Aspects of Shape Memory alloys, Edited by: Duerig, T. W. *et al.*, Butterworth-Heinemann, pp 195-206

Qian, W. C. and Ye, K. Y.(1980), Elasticity, Science Publication (in Chinese)

Rogers, C. A. (1992), Mechanics Issues of Induced Strain Actuation, SPIE, Vol. 1777, pp 163-175

Saburi, T. and Nenno, S.(1982), The Shape Memory Effect and Related Phenomena, in Proceedings of an International Conference on Solid-Solid Phase

Transformations, The Metallurgical Society of AIME, pp 1455-1479

Saburi, T., Yoshida, M. and Nenno, S.(1984), Deformation Behaviour of Shape Memory Ti-Ni Alloy Crystals, Scripta Metallurgica, Vol. 18, pp 363-366

Salizbrenner, R. J. and Cohen, M.(1979), On the Thermodynamics of Thermoelastic Martensitic Transformations, Acta Metallurgica, Vol. 27, pp 739-748

Schetky, L. M.(1991), Shape Memory Alloy Applications in Space Systems, Materials & Design, Vol. 12, No. 1, pp 29-32

Schmidt-Mende, P. and Reiss, H.-G.(1991), Design of Actuating Elements Made of Shape Memory Alloys, Journal de Physique IV, Vol. 1, No. C4, pp 175-180

Schlobmacher, P., Haas, T. and Schubler, A.(1994), Laser Welding of Ni-Ti Shape Memory Alloys, Proceedings of the First International Conference on Shape Memory and Superelastic Technologies, California, USA, pp 85-90

Schroeder, T. A. and Wayman, C. M.(1977a), The Formation of Martensite and the Mechanism of the Shape Memory Effect in Single Crystals of Cu-Zn Alloys, Acta Metallurgica, Vol. 25, pp. 1375-1391

Schroeder, T. A. and Wayman, C. M.(1977b), The Two-Way Shape Memory Effect and Other "Training" Phenomena in Cu-Zn Single Crystals, Scripta Metallurgica, Vol. 11, pp 225-230

Schroeder, T. A. and Wayman, C. M.(1978), Martensite-to-Martensite Transformations in Cu-Zn Alloys, Acta Metallurgica, Vol. 26, pp. 1745-1757

Schroeder, T. A. and Wayman, C. M.(1979), Pseudoelastic Effects in Cu-Zn Single Crystals, Acta Metallurgica, Vol. 27, pp. 405-417

Shaw, J.A. and Kyriakides, S.(1995), Thermomechanical Aspects of NiTi, Journal of the Mechanics and Physics of Solids, Vol. 43, No. 8, pp 1243-1281

Shaw, J.A. and Kyriakides, S.(1997), On the Nucleation and Propagation of Phase Transformation Fronts in a NiTi Alloy, Acta Materials, Vol. 45, No. 2, pp 683-700

Shield, T. W.(1995), Orientation Dependence of the Pseudoelastic Behavior of Single Crystals of Cu-Al-Ni in Tension, Journal of the Mechanics and Physics of Solids, Vol. 43, No. 6, pp 869-895

Skrobanek, K. D., Kohl, M. and Miyazaki, S.(1997), Stress-Optimised Shape

Memory Microvalves, Proceedings of the Tenth Annual International Workshop on Micro Electro Mechanical Systems, Nagoya, Japan, pp 256-261

Smith, S. H., Purdy, B. and Nygren, B.(1997), Development of a New, No-Shock Separation Mechanism for Spacecraft Release Applications, 31th Aerospace Mechanisms Symposium, NASA Marshall Space Flight Center, Huntsville, Alabama, May 14-16, 1997

Stella, D., Pedrazzoli, G., Secci, G. and Portelli, C.(1991), SMA Applications in an Innovative Multishot Deployment Mechanism, 25th Aerospace Mechanisms Symposium, Jet Propulsion Lab, Pasadena, CA, pp 275-290

Stoeckel, D.(1991), Shape memory actuators for Automotive Applications, Materials & Design, Vol. 11, No. 6, pp 302-307

Sun, G. and Sun, C. T.(1993), One-Dimensional Constitutive Relation for Shape-Memory Alloy-Reinforced Composite Lamina, Journal of Materials Science, Vol. 28, pp 6323-6328

Sun, Q. P. and Hwang, K. C.(1993a), Micromechanics Modelling for the Constitutive Behavior of Polycrystalline Shape Memory Alloys-I: Derivation of General Relations, Journal of the Mechanics and Physics of Solids, Vol. 41, No. 1, pp 1-17

Sun, Q. P. and Hwang, K. C.(1993b), Micromechanics Modelling for the Constitutive Behavior of Polycrystalline Shape Memory Alloys-II: Study of the Individual Phenomena, Journal of the Mechanics and Physics of Solids, Vol. 41, No. 1, pp 19-33

Tanaka, K.(1985), A Phenomenological Theory of Transformation Superplasticity, Engineering Fracture Mechanics, Vol. 21, No. 4, pp 709-720

Tanaka, K.(1986), A Thermomechanical Sketch of Shape Memory Effect: One-Dimension Tensile Behavior, Res Mechanica, 18, pp 251-263

Tanaka, K., Nishimura, F. and Tobushi, H.(1995), Transformation Start Lines in TiNi and Fe-Based Shape Memory Alloys after Incomplete Transformations Induced by Mechanical and/or Thermal Loads, Mechanics of Materials, Vol. 19, No. 4, pp 271-280

Thrasher, M. A., Shahin, A. R., Meckl, P. H. and Jones, J. D.(1992), Thermal Cycling of Shape Memory Alloy Wires Using Semiconductor Heat Pump Modules, SPIE Vol. 1777, pp 197-200

Timoshenko, S.(1956), Strength of materials, D. Van Nostrand Company, Inc.

Tong, H. C. and Wayman, C. M.(1975), Thermodynamics of Thermoelastic Martensitic Transformations, Acta Metallurgica, Vol. 23, pp 209-215

Unda, J., Weisz, J., Rivacoba, J. and Urien, I.R.(1994), Family of Deployable/Retractable Structures for Space Application, Acta Astronautica, Vol. 32, No. 12, pp 767-784

Venison, G. S.(1986), A Practical Look at Shape Memory Alloys' Potential as a Thermal Actuator, Material & Design, Vol. 7, No. 3, pp 143-146

Wang, F. E.(1991), Recent Advances in Nitinol Technology, ADPA/AIAA /ASME/SPIE Conference on Active Materials and Adaptive Structures-Session 10, pp 177-183

Waram T.(1988), Design Principles for Ni-Ti Actuators, Engineering Aspects of Shape Memory alloys, Edited by: Duerig, T. W. *et al.*, Butterworth-Heinemann, pp 234-244

Wayman, C. M. and Duerig, T.W.(1988), An Introduction to Martensite and Shape Memory, Engineering Aspects of Shape Memory alloys, Edited by: Duerig, T. W. *et al.*, Butterworth-Heinemann, pp 3-20

Whitcher, F. D.(1997), Simulation of in Vivo Loading Conditions of Nitinol Vascular Stent Structures, Computers & Structures, Vol. 64, No. 5/6, pp 1005-1011

Witting, P. R. and Cozzarelli, F. A.(1992), Shape Memory Structural Dampers: Material Properties, Design and Seismic Testing, Technical Report NCEER-92-0013

Yaeger, J. R.(1984), A Practical Shape-Memory Electromechanical Actuator, Mechanical Engineering, pp 51-55

Yang, H., Liu, Z. C. and Tang, L. L.(1985), Antenna Made by Shape Memory Alloy for TW-1 Satellite, unpublished paper

Appendix A

Properties of Commercially Available Nitinol

We summarise the properties of commercially available Nitinol that are relevant to the design of space actuators in the following tables[1].

Transformation temperature (M_s)§	-200 $\sim$ 110°C
Latent heat of transformation †	$\approx$ 28,000 J/Kg
Hysteresis	2 $\sim$ 50°C
Transformation Strain (for polycrystalline material)	
One-way memory	max 8 % (for 1 cycle) 6 % (for 100 cycles) 4 % (for 100,000 cycles)
Normal two-way memory	3.2 %

Table A.1: Transformation properties of Nitinol.

§ Transformation temperature of Nitinol is extremely sensitive to the precise Ti/Ni ratio, and to alloying additions (for example, $\approx$10% of Pt or Pd tends to increase M_s to as high as $350°C$) (Duerig and Pelton 1994).

† Latent heat of transformation depends on the transformation temperature and stress rate (Duerig and Pelton 1994).

[1]Mainly based on data sheets from Advanced Materials and Technologies (Belgium), Dynalloy, Inc. (USA), and Duerig and Pelton (1994). For the properties of other SMAs, see WWW at http://www.mtm.kuleuven.ac.be/Research/Physical/ShapeMem/smatab.htm.

Melting point	$1{,}240 \sim 1{,}310^{o}$C
Density	$6{,}450 \sim 6{,}500$ Kg/m^3
Thermal conductivity	
Austenite	18 W/m^{o}C
Martensite	$8.6 \sim 10$ W/m^{o}C
Coefficient of thermal expansion	
Austenite	$11\times10^{-6}/^{o}$C
Martensite	$6.6\times10^{-6}/^{o}$C
Specific heat	490 J/Kg^{o}C
Electrical resistivity	
Austenite	0.82×10^{-6} Ωm
Martensite	0.76×10^{-6} Ωm
Damping capacity	$\approx$ 20 SDC

Table A.2: Physical properties of Nitinol.

Young's Modulus	
Austenite	$75 \sim 83$ GPa
Martensite	$28 \sim 41$ GPa
Poisson's ratio	0.33
Ultimate tensile strength	
Fully annealed	895 MPa
Work hardened	1900 MPa
Fatigue strength (N=10^6)	350 MPa
Hot workability	quite good
Cold workability	difficult due to rapid work hardening
Machinability	difficult, abrasive techniques are preferred
Jointing#	
Welding to other materials‡	extremely difficult
Welding to itself¶	relatively easy by resistance and TIG method

Table A.3: Mechanical properties of Nitinol.

Readers may refer several papers in Pelton *et al.* (1997) for more information.

‡ Solid state welding process is suggested by The Welding Institute (TWI) to avoid formation of intermetallics problem in fusion related welding process.

¶ Laser welding has been reported by Schlobmacher *et al.* (1994), and TWI has successfully welded Nitinol wires together, using a number of other processes, including percussive arc, capacitor discharges resistance welding.

Volume Change in Phase Transformation

Refer Section 2.1.1 for crystal structure data. We have the volume of austenite crystal

$$V_A = \ a_o^3 = 0.3015^3$$

and volume of martensite crystal

$$V_M = \ abc\,\cos(\beta - 90^o) = \ 0.2889 \times 0.4120 \times 0.4622 \times \cos(96.8^o - 90^o)$$

Hence, the percentage of volume change

$$\frac{\triangle V}{V_A} = \ \frac{V_A - V_M/2}{V_A} = \ 0.034\%$$

Appendix B

Temperature Distribution

B.1 Electrical Heating

We study the temperature distribution along a uniform wire, which is held in air between two clamps at temperature T_1 and T_2. The wire is heated by passing an electric current through it, Fig. B.1.

We define the following parameters (typical values for Nitinol are given in brackets, see Appendix A):

k= thermal conductivity of the material ($10 \sim 18$ W/m^{o}C);
A= cross-sectional area of the wire;
l= perimeter of the section of the wire;
T_o= ambient temperature;
ρ= density (6450 Kg/m^3);
c= specific heat (490 J/Kg^{o}C);
h= convection heat-transfer coefficient (in air: ≈ 4.5 W/m^{2o}C;
in water: ≈ 890 W/m^{2o}C);
L= length of the wire;
V= volume ($V = A \times L$);
R= resistance (resistivity$\approx 0.79 \times 10^{-6}$ Ωm);
I= electrical current.

The only quantities that are allowed to vary are T_1, T_2 and I.

B.1.1 Steady-State Analysis

If the electric current changes slowly, the temperature distribution may be calculated by steady-state analysis. In this case

$$I = I_o = \text{constant}$$

The steady-state heat conduction equation in one dimension is (Carslaw and

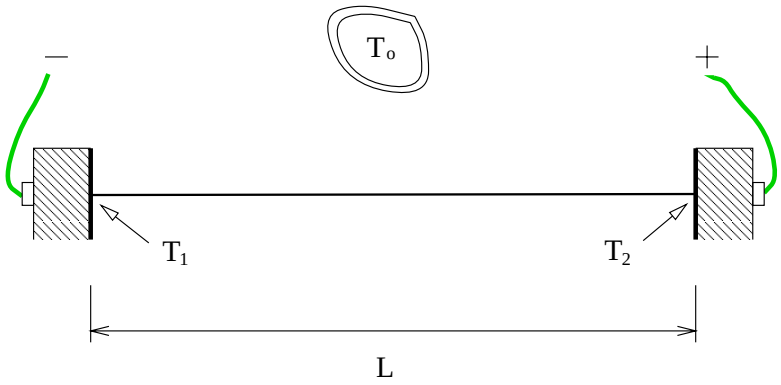

Figure B.1: Wire heated by passing an electric current through it.

Jaeger 1959)

$$\frac{\partial^2 T}{\partial x^2} - \frac{hl}{Ak}(T - T_o) = -\frac{I^2 R}{kV} \tag{B.1}$$

with the boundary conditions

$$T(0) = T_1 \tag{B.2}$$
$$T(L) = T_2 \tag{B.3}$$

The solution of Eqn. B.1 has the form

$$T = C_1 \mathrm{e}^{-mx} + C_2 \mathrm{e}^{mx} + C_3 \tag{B.4}$$

where,

$$\begin{aligned} C_1 &= \frac{(T_1 - T_2) - C_2(1 - \mathrm{e}^{mL})}{1 - \mathrm{e}^{-mL}} \\ C_2 &= \frac{(T_1 - T_o + B/m^2)(1 - \mathrm{e}^{-mL}) - (T_1 - T_2)}{\mathrm{e}^{mL} - \mathrm{e}^{-mL}} \\ C_3 &= T_o - \frac{B}{m^2} \end{aligned}$$

and

$$\begin{aligned} m^2 &= \frac{hl}{kA} \\ B &= -\frac{I^2 R}{kV} \end{aligned}$$

Figure B.2 shows the temperature distribution in wires of different lengths, 0.1 m, 0.25 m, 0.5 m and 1 m, but with the same diameter of 1 mm. It is assumed that $T_1 = T_2 = T_o = 0^o$C for different values of the electric currents.

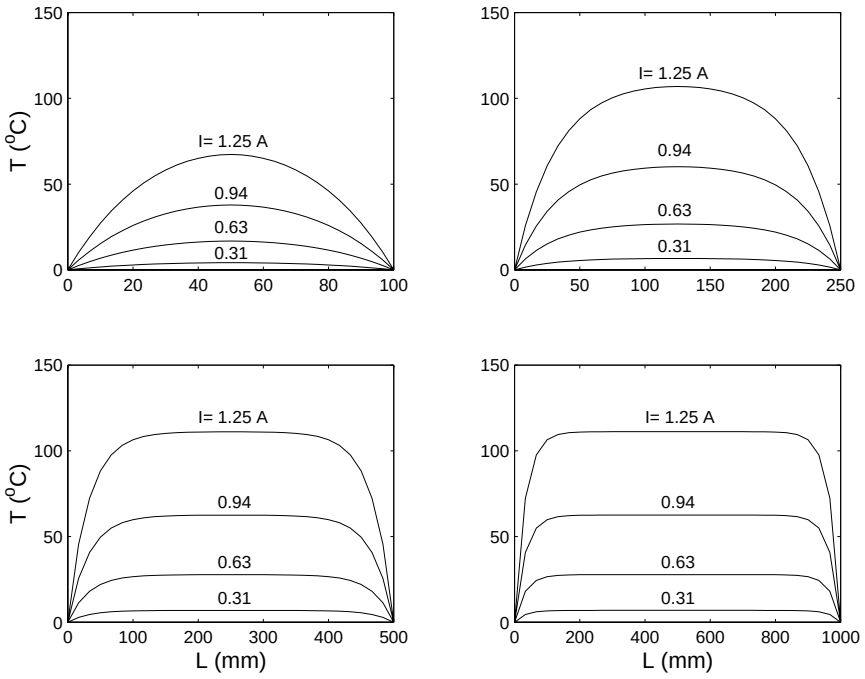

Figure B.2: Temperature distribution (steady-state analysis).

B.1.2 Unsteady-State Analysis

In this case, the electric current is a function of t

$$I = I(t)$$

The general heat conduction equation has the form (Carslaw and Jaeger 1959)

$$\rho c \frac{\partial T}{\partial t} - k \frac{\partial^2 T}{\partial x^2} = \frac{I^2 R}{V} - \frac{hl}{A}(T - T_o) \tag{B.5}$$

with the boundary conditions

$$T(t,0) = T_1(t) \tag{B.6}$$
$$T(t,L) = T_2(t) \tag{B.7}$$

and the initial condition

$$T(0,x) = f(x) \tag{B.8}$$

where $f(x)$ is the initial temperature distribution.

We may expand $f(x)$ in series

$$f(x) = \sum_{n=1,2,3\cdots} \left[a_n \sin \frac{n\pi x}{L} \right] + T_1(0) + \left[T_2(0) - T_1(0) \right] \frac{x}{L} \tag{B.9}$$

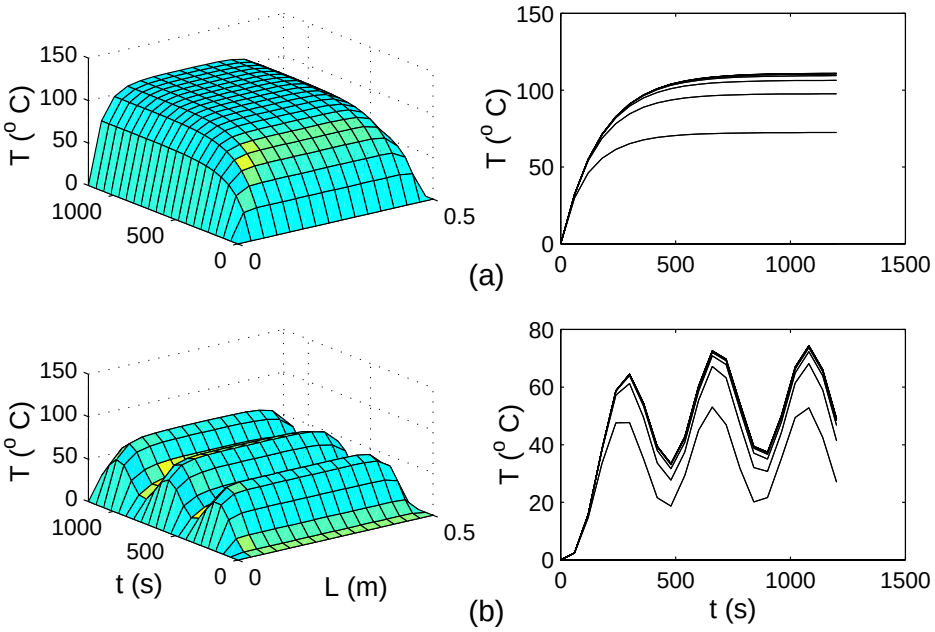

Figure B.3: Temperature distribution (unsteady-state analysis). (a) I= 1.25 A; (b) I= 1.25 $\sin(t/1200)$ A.

Thus we have

$$
\begin{aligned}
T(t,x) = \sum_{n=1,3,5\cdots} \frac{4}{B_1 n\pi} \int_0^t \mathrm{e}^{(B_2 - \frac{n^2\pi^2}{L^2})(t-\tau)/B_1} \Big\{ Q(\tau) - B_2 T_0 - B_1 \frac{dT_1}{d\tau} \\
+ B_2 T_1(\tau) \Big\} \sin(\frac{n\pi x}{L}) d\tau + T_1(t) + \Big[T_2(t) - T_1(t) \Big] \frac{x}{L} \\
+ \sum_{n=1,2,3\cdots} (-1)^{n+1} \frac{2}{B_1 n\pi} \int_0^t \mathrm{e}^{(B_2 - \frac{n^2\pi^2}{L^2})(t-\tau)/B_1} \Big\{ B_1 (\frac{dT_2}{d\tau} \\
- \frac{dT_1}{d\tau}) - B_2 \Big[T_2(\tau) - T_1(\tau) \Big] \Big\} \sin(\frac{n\pi x}{L}) d\tau \\
+ \sum_{n=1,2,3\cdots} \Big[a_n \sin(\frac{n\pi x}{L}) \Big] \mathrm{e}^{(B_2 - \frac{n^2\pi^2}{L^2}) t/B_1}
\end{aligned}
\tag{B.10}
$$

where,

$$
\begin{aligned}
B_1 &= \frac{\rho c}{k} \\
B_2 &= -\frac{hl}{Ak} \\
Q(t) &= \frac{I^2 R}{kV}
\end{aligned}
$$

Figure B.3 shows the temperature distribution in a wire of diameter 1 mm, $L = 0.5$ m, and $f(x)= 0^oC$, for the following two cases:

- $I= 1.25$ A, $T_1= T_2= T_o= 0^oC$
- $I= 1.25 \sin(t/1200)$ A, $T_1= T_2= T_o= 0^oC$

B.2 Heating Induced by a Phase Transformation

To calculate the temperature distribution along a wire with any kind of heating source we solve the following equation (see Fig. 4.14)

$$\rho c\frac{\partial T}{\partial t} - k\frac{\partial^2 T}{\partial x^2} = \tilde{Q}(x) - \frac{hl}{A}(T - T_o) \tag{B.11}$$

with boundary conditions as

$$T(t,0) = T_1(t) \tag{B.12}$$
$$T(t,L) = T_2(t) \tag{B.13}$$

and initial condition

$$T(0,x) = f(x) \tag{B.14}$$

where L is the length of the wire and $\tilde{Q}(x)$ is heat source. Expanding $\tilde{Q}(x)$ as a Fourier sine series

$$\tilde{Q}(x) = k \sum_{n=1,2,\cdots} d_n \sin(\frac{n\pi x}{L}) \tag{B.15}$$

Letting

$$\begin{aligned} B_1 &= \frac{\rho c}{k} \\ B_2 &= -\frac{hl}{Ak} \end{aligned}$$

and

$$f(x) = \sum_{n=1,2,\cdots} \left(a_n \sin\frac{n\pi x}{L}\right) + T_1(0) + \left[T_2(0) - T_1(0)\right]\frac{x}{L}$$

The solution of Eqn. B.11 can be written in the form

$$T(t,x) = \sum_{n=1,2,\cdots} \frac{1}{B_1} \int_0^t \mathrm{e}^{(B_2 - \frac{n^2\pi^2}{L^2})(t-\tau)/B_1} d_n \sin(\frac{n\pi x}{L}) d\tau + T_1(t) + \left[T_2(t) - T_1(t)\right]\frac{x}{L}$$

$$+\sum_{n=1,3,\cdots}\frac{4}{B_1 n\pi}\int_0^t \mathrm{e}^{(B_2-\frac{n^2\pi^2}{L^2})(t-\tau)/B_1}\left\{B_2\left[T_1(\tau)-T_o\right]-B_1\frac{dT_1}{d\tau}\right\}\sin(\frac{n\pi x}{L})d\tau$$

$$+\sum_{n=1,2,\cdots}(-1)^{n+1}\frac{2}{B_1 n\pi}\int_0^t \mathrm{e}^{(B_2-\frac{n^2\pi^2}{L^2})(t-\tau)/B_1}\left\{B_1(\frac{dT_2}{d\tau}-\frac{dT_1}{d\tau})-B_2\Big[T_2(\tau)\right.$$

$$\left.-T_1(\tau)\Big]\right\}\sin(\frac{n\pi x}{L})d\tau+\sum_{n=1,2,\cdots}\Big[a_n\sin(\frac{n\pi x}{L})\Big]\mathrm{e}^{(B_2-\frac{n^2\pi^2}{L^2})t/B_1} \tag{B.16}$$